JOTCS A
Journal of the Turkish Chemical Society
Section: A
Chemistry

TURKISH CHEMICAL SOCIETY

Determination of Copper in Hydroponic Nutrient Solutions by UV-Visible Spectrophotometry and Flow Injection Analysis

Seda Karapınar[1*], Seda Deveci[2], Ebru Çetinkaya[2], Birsen Demirata Öztürk[1]

[1]Istanbul Technical University, Department of Chemistry, Faculty of Science and Letters, Istanbul, 34485, Turkiye.
[2]Department of Chemistry Research, Mir Research and Development, Istanbul, 34517, Turkiye.

Abstract: Copper (Cu) is a micronutrient that plays an important role in the growth of plants. A spectrophotometric analysis method has been developed to determine Cu^{2+} in hydroponic nutrient solutions. 4-(2-pyridylazo)-resorcinol (PAR), 1-(2 pyridylazo)-2-naphthol (PAN) and 1-(2-thiazolylazo)-2-naphthol (TAN) ligands were studied as co-complexants that will enable determination of Cu^{2+}. Each microelement has an optimum pH value at which it forms a complex with the ligand. By studying the effect of pH on the metal-ligand complex, the optimum pH values at which maximum absorbances were obtained were determined. The interference effects of foreign ions in the nutrient solution were examined. 4-(2-pyridylazo)-resorcinol (PAR) complexes were found to be more resistant to foreign ion interference. For this reason, validation studies of the method developed for 4-(2-pyridylazo)-resorcinol (PAR) complexes were carried out. Afterwards, the developed method was adapted to the flow injection analysis system. The procedure is simple, rapid and reliable. This method was successfully applied to the determination of copper in hydroponic nutrient solutions.

Keywords: Micronutrients, Hydroponic nutrient solution, Spectrophotometry, Flow injection analysis.

Submitted: January 1, 2025. **Accepted:** March 6, 2025.

Cite this: Karapınar S, Deveci S, Çetinkaya E, Öztürk B. Determination of Copper in Hydroponic Nutrient Solutions by UV-Visible Spectrophotometry and Flow Injection Analysis. JOTCSA. 2025;12(2): 53-64.

DOI: https://doi.org/10.18596/jotcsa.1611640

***Corresponding author's E-mail:** babacanse@itu.edu.tr

1. INTRODUCTION

Hydroponic farming is a type of soilless farming system, and the most distinctive feature that distinguishes it from conventional farming is that it directly uses mineral-rich solutions to feed plants (1). The nutrient supply notably influences plant growth in many ways. The growth of plants is influenced both by macronutrients such as N, P, and K and by micronutrients (2). For this reason, it is important that the nutrient solution, which is one of the primary factors in the growth of plants, contains all the necessary nutrients that plants need (2). Today, using nutrient solutions to optimize crop nutrition (fertilization or liquid fertilization) is a popular practice in soil-grown greenhouse crops as well as in hydroponic cultures (3). Agricultural research in the world is focused on "in situ and specific application". The aim of the studies is to increase the agricultural quality, capacity, and yield, to make an accurate and optimum application (such as fertilization, pesticide, irrigation, harvest time estimation), and thus to add value to the agricultural economy. In most national and international greenhouse enterprises, the ion control of the nutrient solution is done by automatic measurement of pH and electrical conductivity (EC), the solution content is followed according to the EC change (4). However, since EC is the total electrical conductivity value, it cannot give information about the concentration of each ion in the system. Therefore, it is not possible to make individual and real-time corrections for nutrients. With such a determination method, more or less fertilization will be made than the ion needed by the plant, in this case, sufficient yield will not be obtained from the plant.

Copper is one of the vital trace elements needed for plant development (5). It serves as a key component of various proteins. It plays several important roles, including in cell wall metabolism, photosynthetic electron transport, responses to oxidative stress, protein synthesis, hormone regulation, and mitochondrial respiration (6). Although copper is essential for plants in small

amounts to support cellular functions as a micronutrient, excessive copper can be harmful, leading to negative impacts on plant growth and survival. Plants are capable of surviving and tolerating conditions with a deficiency in Cu^{2+}. However, when the concentration of Cu^{2+} surpasses the optimal level, it interferes with the plant's metabolism and becomes harmful. An excess of copper significantly hampers photosynthesis by stunting plant growth and development, limiting nutrient uptake from the soil, decreasing pigment levels, and inhibiting root growth and leaf expansion (7). Furthermore, excessive copper disturbs the proper functioning of essential cellular components (8).

Various techniques, including graphite furnace atomic absorption spectrometry (GF-AAS), inductively coupled plasma optical emission spectrometry (ICP-OES), and ion-selective electrode (ISE), have been established to measure copper (II) ions in solutions based on their concentration. However, many of these methods involve procedures that are either time-intensive or require complex equipment. Additionally, certain spectrophotometric approaches previously used for the determination of copper (II) present drawbacks, such as being time-consuming, labor-intensive, and relying on significant quantities of organic solvents, which can contribute to environmental pollution (9).

In recent years, flow injections have emerged as a popular analytical method, extensively utilized with spectrophotometric detection due to its widespread availability in laboratories worldwide. It offers advantages such as low cost, minimal reagent consumption, reduced waste generation, cost efficiency, small sample volume requirements, and ease of automation. Additionally, flow injections are widely applied in quantitative analysis and enable experiments under dynamically non-equilibrated conditions, thereby reducing analysis time and increasing sample throughput (10).

When planning a procedure (from sampling, extraction, purification to instrument analysis) in analytical chemistry, the green chemistry factor must be taken into consideration. There are various tools developed to assess the environmental impacts of analytical methods. These tools aim to increase the sustainability of analytical methods by assessing the toxicity of chemicals used in the analysis processes, energy consumption, waste amount and overall environmental impact (11).

The environmental sustainability of the method was assessed using the AGREE, AGREEprep and MoGAPI tools (12).

Many studies have developed methods for measuring copper in various samples (13-20). In this study, however, a spectrophotometric method was developed that will enable the measurement of copper elements in hydroponic nutrient solutions. With the developed method, the amounts of copper in hydroponic nutrient solutions can be determined specifically. In this way, faulty analyses based on electrical conductivity measurements made with EC meters in greenhouses will be prevented, correct and controlled fertilization will be made, and productivity and quality will be increased in production.

2. EXPERIMENTAL SECTION

2.1. Instrumentation

Shimadzu-1800 model UV-Vis spectrophotometer (Kyoto, Japan) for absorbance measurements and wavelength scanning for method optimization and analysis of metal ligand complexes in still environment studies, KERN-PFB 1200 2 model precision balance (Balingen, Germany) for chemical weighing, ALEX Machine ultrasonic bath (Istanbul, Turkey) for solution mixing and dissolving processes, MILLIPORE- Direct Q UV 3 model deionized pure water device (Burlington, Massachusetts, USA) for the preparation of ultrapure water used in solution preparation and cleaning of glassware, WTW-7310 model desktop pH meter (Weilheim, Germany) for pH measurements of solutions, IKA-VORTEX 3 model vortex (Staufen, Germany) for mixing solutions, Eppendorf Research series 10 µL, 100 µL, 100-1000 µL, 1000-5000 µL automatic pipettes (Hamburg, Germany) were used for solution transfers. For flow injection analysis; Ismatec-REGLO ICC peristaltic pump (SA, Switzerland) to transfer the solutions to the flow system, Rheodyne sample injection valve (Northbrook, Illinois, USA) to allow the sample to enter the flow system, Ocean Optics flame spectrometer (Massachusetts, USA) to detect the formed species, Ocean Optics beam source (Massachusetts, USA) to provide the beam to be sent to the flow cell, Biotech Degassi Classic degaser (Kungsbacka, Sweden) to remove air from the mobile phase, Saint Gobain Tygon™ S3™ E-3603 tubes (Courbevoie, France) for the solutions to advance in the flow system, plexiglass flow cell (Istanbul, Turkey) to pass enough light through the path were used. AGILENT- 240 FS AA model Atomic Absorption Spectrophotometer (Santa Clara, United States) was used for method validation tests.

2.2. Materials and Reagents

4-(2-pyridylazo)-resorcinol (PAR) (≥97.5% purity) and 1-(2-pyridylazo)-2-naphthol (PAN) (99.0%) were purchased from Sigma-Aldrich (Munich, Germany). 1-(2-thiazolylazo)-2-naphthol (TAN) (≥97.5%) was purchased from Alfa Aesar (Massachusetts, USA). Potassium chloride (KCl) (≥ 99.5%), ammonium chloride (NH_4Cl) (≥ 99.8%), sodium acetate ($NaCH_3COO$) (≥ 99.0%), ammonium acetate (NH_4CHOO) (≥ 98.0%), ammonium sulfate ($(NH_4)_2SO_4$) (≥ 99.5%), boric acid (H_3BO_3) (99.5 - 100.5%), glacial acetic acid (CH_3COOH) (≥ 99.8%), hydrochloric acid fuming 37% (HCl) (36.5 - 38.0%), sodium hydroxide (NaOH) (≥ 97.0%), ethanol (≥99.9%), nitrate standard (1000 µg/mL) in water (H_2O), calcium standard (1000 µg/mL) in 0.5 M nitric acid (HNO_3), potassium standard (1000 µg/mL) in 0.5 M nitric acid (HNO_3), Triton X 100 (90.0 - 110.0%) were purchased Merck (Rahway, NJ USA). Zinc standard (1000 µg/mL) in 0.5 M nitric acid (HNO_3), cupper

standard (1000 µg/mL) in 0.5 M nitric acid (HNO_3), iron standard (1000 µg/mL) in 0.5 M nitric acid (HNO_3), manganese standard (1000 µg/mL) in 0.5 M nitric acid (HNO_3), boron standard (1000 µg/mL) in 0.5 M nitric acid (HNO_3), phosphate standard (1000 µg/mL) in 0.5 M nitric acid (HNO_3), magnesium standard (1000 µg/mL) in 0.5 M nitric acid (HNO_3) were purchased from Reagecon (Clare, Ireland). Ultrapure water (Milli-Q RG, Merck Millipore, Burlington, Massachusetts) was used throughout this study.

2.3. Preparation Stock and Standard Solutions

For the stock solution of 4-(2-pyridylazo)-resorcinol (PAR), 1-(2-pyridylazo)-2-naphthol (PAN) and 1-(2-thiazolylazo)-2-naphthol (TAN) were prepared in ethanol (≥99.9%) and were further diluted in ethanol (≥99.9%) as required. These solutions were freshly prepared. All standard solutions were diluted with ultrapure water.

2.4. Determination of pH Conditions

Complex formations Cu^{2+} ions with 4-(2-pyridylazo)-resorcinol (PAR), 1-(2-pyridylazo) 2-naphthol (PAN) and 1-(2-thiazolylazo)-2-naphthol (TAN) were studied at different pH values (pH 3-pH 11). For pH 3 buffer solution, 0.657 g of solid KCl is dissolved in some ultrapure water and 11.9 mL of HCl is added. Final volume is made up to 100 mL with ultrapure water. Acetate buffers (16 mL of 0.1 M sodium acetate and 84 mL of 0.1 M acetic acid, 67.8 mL of 0.1 M sodium acetate and 32.2 mL of 0.1 M acetic acid, respectively) were used for the pH 4 and pH 5. For pH 6 buffer solution 0.82 mL of glacial CH_3COOH was added to 20 g of solid NH_4CH_3COO salt and dissolved in a little amount of ultrapure water after it was made up to 100 mL with ultrapure water. For pH 7 41.3 mL of 1/15 M (9.073 g/L) KH_2PO_4 and 58.7 mL of 1/15 M (11.87 g/L) Na_2HPO_4 solution were mixed. Solution A: (0.05 M Boric acid); 1.237 g solid H_3BO_3 was dissolved with 1 M NaOH, and the final volume was made up to 100 mL with 1 M NaOH. Solution B: (0.1 M HCl); 0.2 mL of 37% HCl was made up to 25 mL with ultrapure water. 55.4 mL of solution A and 44.6 mL of solution B were mixed for pH 8. (0.25 M) 1.55 g of solid H_3BO_3 was dissolved in some 0.05 M KCl and made up to 100 mL with 0.05 M KCl for pH 9, for pH 10 2.64 g of solid H_3BO_3 was dissolved in 90 mL of ultrapure water. The pH was adjusted to 10 with 10 M NaOH. The final volume was made up to 100 mL with ultrapure water. 6.75 g of solid NH_4Cl was dissolved in ammonia and made up to 100 mL with ammonia for pH 11. When necessary, the pH of the buffers was adjusted to the required values with HCl and NaOH solutions.

2.5. Spectra and The Complex Formation

The reagent and standard solutions were prepared according to the descriptions below. Shortly, 1.2 mg 4-(2-pyridylazo)-resorcinol (PAR) dissolved in a little amount of ethanol was transferred to an amber volumetric flask and made up to 25 mL with ethanol. The solution was stored at 4°C until analysis and prepared freshly for daily investigation. In the same way, 1 mg of 1-(2 pyridylazo)-2-naphthol (PAN) in 25 mL ethanol and 1 mg of 1-(2-thiazolylazo)-2-naphthol (TAN) in 25 mL of ethanol solution were prepared. Prior to analysis, standard solutions of Cu^{2+} diluted from 1000 ppm to 10 ppm with ultrapure water. To prepare the calibration chart of Cu-PAR complexes, appropriate volumes were taken from 10 ppm Cu^{2+} solution with final concentrations 0.125; 0.25; 0.5; 0.75, and 1 ppm. $2.23x10^{-4}$ M, 1.2 mL 4-(2-pyridylazo)-resorcinol (PAR), 25 µL of 10% Triton X-100, and 1 mL of buffer solution were added in this order. The final volume was made up to 5 mL with ethanol. Afterward, standard solutions were mixed for 10 seconds with a vortex. Absorbance values were read against the blank solution at a wavelength of 512 nm. The same procedure was applied to prepare the calibration graphs of TAN and PAN complexes. For TAN complexes, $1.56x10^{-4}$ M 4.4 mL 1-(2-thiazolylazo)-2-naphthol (TAN) was used and absorbance values were read at 576 nm wavelength. For PAN complexes, $1.6x10^{-4}$ M 1-(2-pyridylazo)-2 naphthol (PAN) was used and absorbance values were read at 553 nm wavelength.

2.6. Flow Injection Analysis

Figure 1 shows the absorbance schematic diagram of the flow system. The four-channel peristaltic pump was fitted for pumping the solutions. The tubes with 0.76 mm i.d. were used for delivery of the solutions. The ultrapure water was used as carrier. Sample and standard solutions were injected into a carrier stream with a sample injector. While the flame spectrometer was used to detect the species formed, the beam source was used to send the beam to the flow cell. The degasser removed air from the mobile phase and the plexiglass 2 mm flow cell to pass enough light through the path used. Three channels of the pump were used for the analysis of Cu^{2+} microelement in the flow injection analysis system. Sample/standard (2 mL/min), carrier (2 mL/min) and 4-(2 pyridylazo)-resorcinol (PAR) / buffer (1 mL/min) pass through these channels, respectively. The liquids that move along the line and mix in the reaction coil are detected (512 nm) by moving towards the flow cell after turning into the detectable species here.

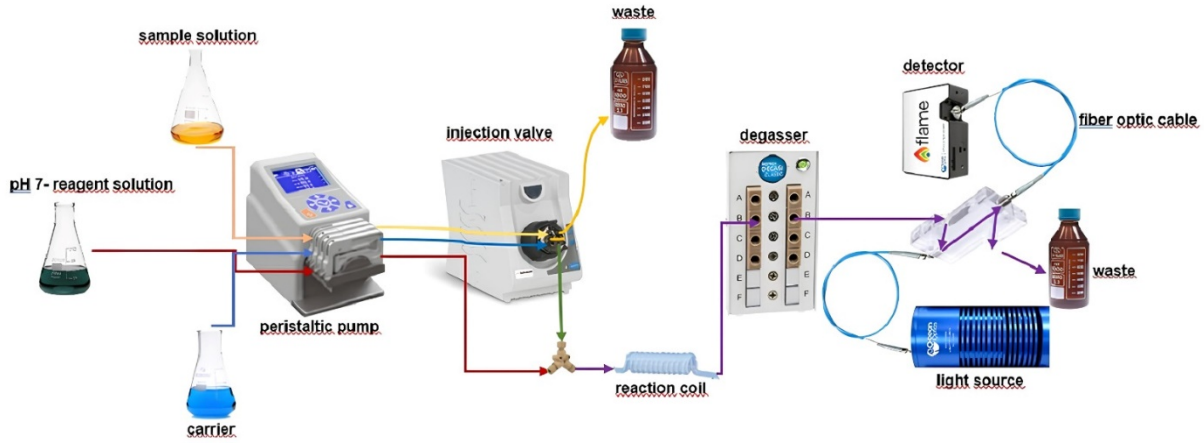

Figure 1: Schematic diagram of the flow injection system used for spectrophotometric determination of copper (II). Sample solutions / standard solutions, carrier (deionized water), pH7-R; reagent solution (pH 7 buffer solution - 4-(2-pyridylazo)-resorcinol (PAR) - deionized water), peristaltic pump, injection valve, waste, sample loop (200 µL), reaction coil (300 cm), degasser, flow cell (2 mm), source of light, detector (λ:512 nm).

3. RESULTS AND DISCUSSION

3.1. Effect of pH

Firstly, the effect of the pH on 4-(2-pyridylazo)-resorcinol (PAR), 1-(2-pyridylazo)-2 naphthol (PAN) and 1-(2-thiazolylazo)-2-naftol (TAN) complexes of Cu^{2+} have been investigated individually. Metal ligand complexes were formed using buffer solutions between pH 3 and pH 11 to determine the optimum pH range. The pH values and wavelengths at which Cu^{2+} gave maximum absorbance were determined. Table 1 shows the wavelengths at which Cu^{2+} gives maximum absorbance and Figure 2 shows absorbance values of the Cu^{2+} complexes between pH 3 and pH 11. Considering the spectrum results, the complex formed by Cu^{2+} and 4-(2-pyridylazo)-resorcinol (PAR) gave maximum absorbance between pH 7 and pH 9. However, 1-(2-pyridylazo)-2 naphthol (PAN) complexes give maximum absorbance at pH 8 and 9, while 1-(2-thiazolylazo)-2-naphthol (TAN) complexes give maximum peak at pH 5. pH values at which Cu^{2+} gives maximum absorbance with the 4-(2-pyridylazo)-resorcinol (PAR), 1 (2-pyridylazo)-2-naphthol (PAN) and 1-(2-thiazolylazo)-2-naphthol (TAN) were selected for further studies.

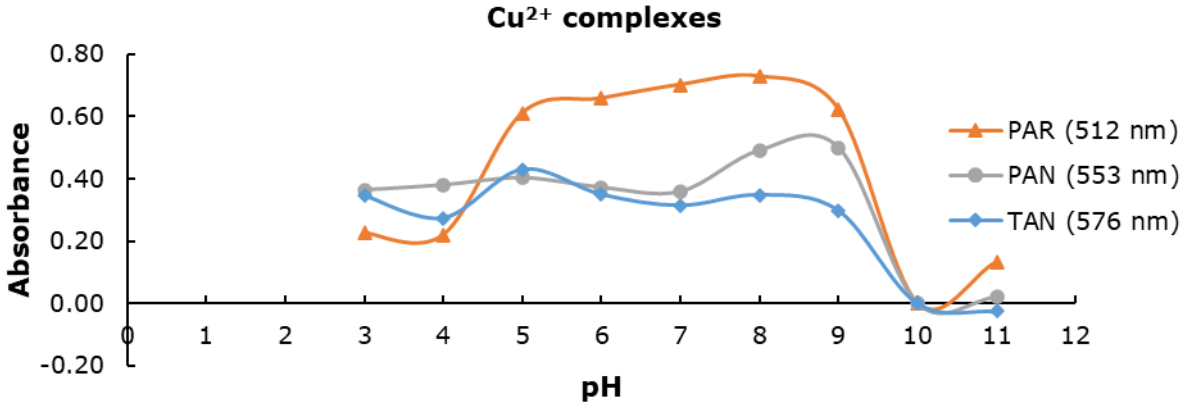

Figure 2: Between pH 3 - pH 11, absorbance values of the Cu^{2+} complexes. Cu-PAR complex, $C_{Cu=}$ 1 µg/mL, $C_{PAR=}$ 4.4 x10^{-5} M, Λ: 512 nm). Cu-PAN complex ($C_{Cu=}$ 1 µg/mL, $C_{PAN=}$ 7.4 x10^{-5} M, Λ: 553 nm). Cu-TAN complex ($C_{Cu=}$ 1 µg/mL, $C_{TAN=}$ 3.9 x10^{5} M, Λ:576 nm).

Table 1: Summarized data of absorption maxima of Cu^{2+} with PAR, PAN and TAN complexes.

Ligand	pH 3	pH 4	pH 5	pH 6	pH 7	pH 8	pH 9	pH 10	pH 11
PAR	540	520	513	514	513	510	512	513	513
PAN	561	559	555	553	551	553	554	554	-
TAN	583	579	577	575	574	583	583	-	-

3.2. Spectrophotometric Analysis of Cu^{2+} Ions

Absorption spectra of PAR, PAN, and TAN ranging from 300 to 800 nm were first scanned, and the absorption maxima were determined under all pH conditions. Then, the formation of complexes between the Cu^{2+} ions and PAR, PAN, and TAN were

tested. Absorption spectra versus the blank were recorded over the same wavelength range. The blank for the metal complex was composed of the buffer, water, ethanol, and chromogenic reagent solution. 10 mm path length, 3500 µL quartz glass high performance macro cells (Hellma Analytics, Müllheim, Germany) and A UV-1800 model UV–vis spectrophotometer equipped with UV Probe 2.43 version (Shimadzu, Kyoto, Japan) were used for analysis. Full scan spectra were recorded from 800 to 300 nm with a slit width of 1.0 nm and fast scanning speed. Spectral properties of the complexes formed by Cu^{2+} with PAR, PAN, and TAN are given in Figure 3. The rapid reaction between the metal and the ligand allows the reaction circle to be shorter in flow injection analysis, thus allowing more sample analysis in a shorter time. In this sense, all three ligand sources are suitable for use in flow injection analysis for Cu^{2+} analysis.

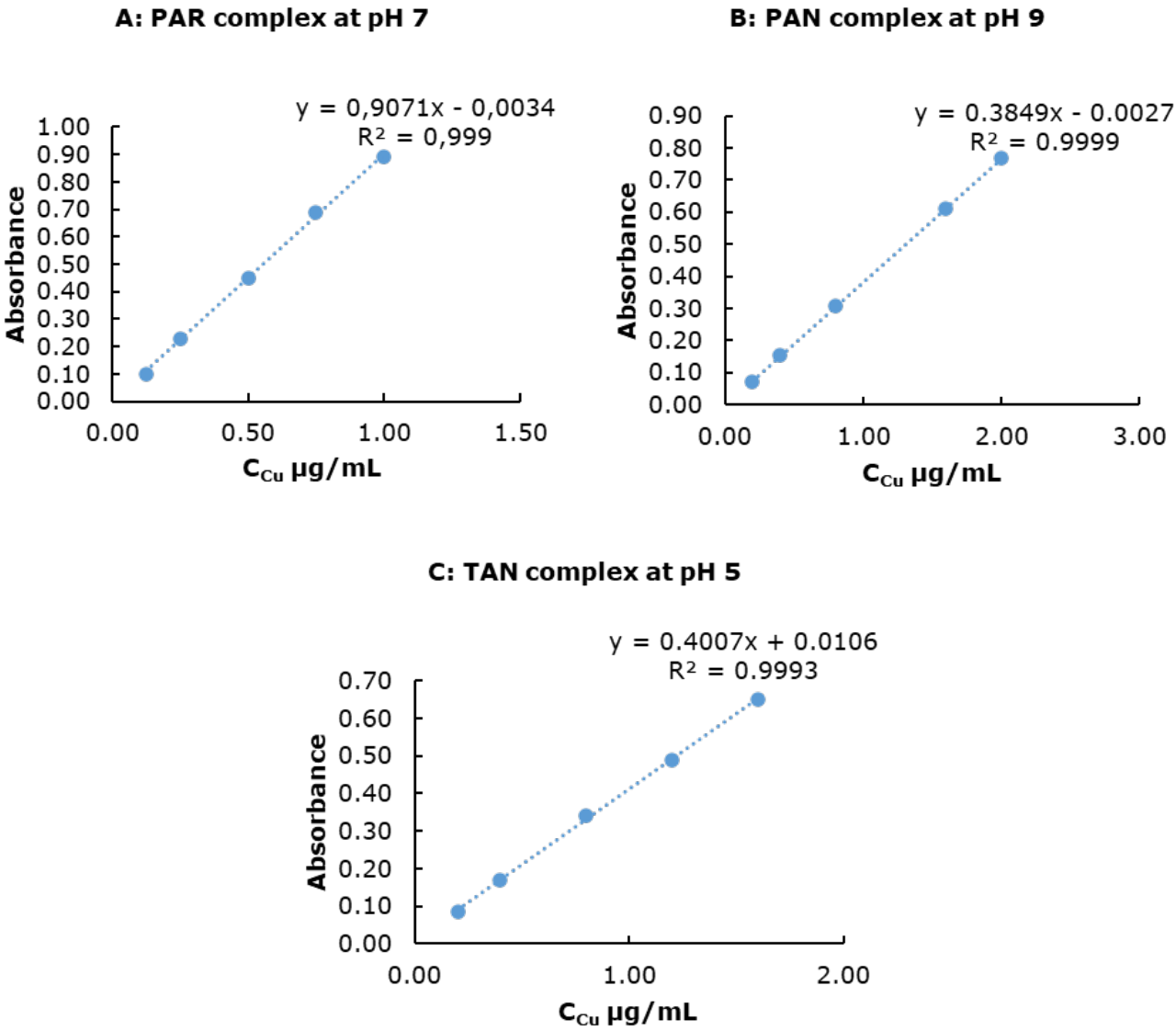

Figure 3: Calibration charts of Cu^{2+}. A) PAR complex at pH 7, Λ: 512 nm B) PAN complex at pH 9, Λ: 553 nm C) TAN complex at pH 5, Λ: 576 nm.

3.3. Interference Studies

The interference effects of K^+, NH_4^+, Zn^{2+}, Fe^{2+}, Mn^{2+}, Ca^{2+}, Mg^{2+}, BO_3^{3-}, NO_3^-, SO_4^{2-} and PO_4^{3-} ions for each metal ligand complex of other anions and cations in the matrix were investigated. While forming a fixed concentration metal-ligand solution, foreign ion solution at varying concentrations was added to the environment. The absorbance value with the least interference effect was determined by measuring the absorbance against the blank. PAR complexes were found to be more resistant to foreign ion interference. The % relative error values calculated from the determined absorbance value are given in Table 2.

Table 2: The effects of matrix ions on the determination of PAR, PAN and TAN complexes (n=3, 1 µg/mL Cu^{2+}).

Interferent	Supply of ion	Ligand of complex	Add ion concentration, µg/mL	Recovery, % Cu^{2+}
K^+	Standard KNO_3	PAR	210	-9.6
		PAN	400	-10.4
		TAN	50	-19.9
NH_4^+	NH_4CH_3COO	PAR	50	-5.6
		PAN	20	-2.5
		TAN	50	-9.9
Ca^{2+}	Standard Ca^{2+}	PAR	200	-9.4
		PAN	200	-7.2
		TAN	25	-13.8
Mg^{2+}	Standard Mg^{2+}	PAR	25	-4.8
		PAN	200	-1.4
		TAN	25	-16.6
Fe^{2+}	Standard Fe^{2+}	PAR	3	+5.3
		PAN	2.5	+54.1
		TAN	5	-74
Mn^{2+}	Standard Mn^{2+}	PAR	0.5	+0.1
		PAN	1	-1.0
		TAN	4	-3.3
Zn^{2+}	Standard Zn^{2+}	PAR	5	+0.1
		PAN	5	+0.3
		TAN	5	+0.4
BO_3^{3-}	Standard BO_3^{3-}	PAR	10	+4.4
		PAN	10	+0.2
		TAN	20	-5.4
NO_3^-	Standard NO_3^-	PAR	100	+9.1
		PAN	200	+10.5
		TAN	200	-7.2
SO_4^{2-}	Standard SO_4^{2-}	PAR	50	+4.2
		PAN	50	+5.2
		TAN	50	-6.3
PO_4^{3-}	Standard PO_4^{3-}	PAR	50	+1.3
		PAN	200	+6.7
		TAN	50	-4.7

3.4. Optimization of Spectrophotometric FIA System

It was determined that PAR complexes were more resistant to foreign ion interference compared to PAN and TAN complexes, therefore adaptation of the method to flow injection analysis was performed only for 4-(2-pyridylazo)-resorcinol (PAR) complexes. The effect of PAR concentration, carrier and reagent flow rates, sample injection volume, and reaction cell length on analytical signals was investigated and optimized one by one, to create optimum conditions for determination of Cu^{2+} by FIA method.

3.4.1. Influence of the PAR concentration

For Cu-PAR complexes, PAR in amounts ranging from 39 µM to 781 µM was added to 0.5 µg/mL Cu^{2+} at pH 7, and absorbance values were read at 512 nm. Previous studies on determining the ligand concentration in stagnant media were effective in determining this range. In Figure 4, absorbance values corresponding to PAR concentration are given for Cu^{2+} ions. It was decided to use 156 µM PAR in subsequent studies.

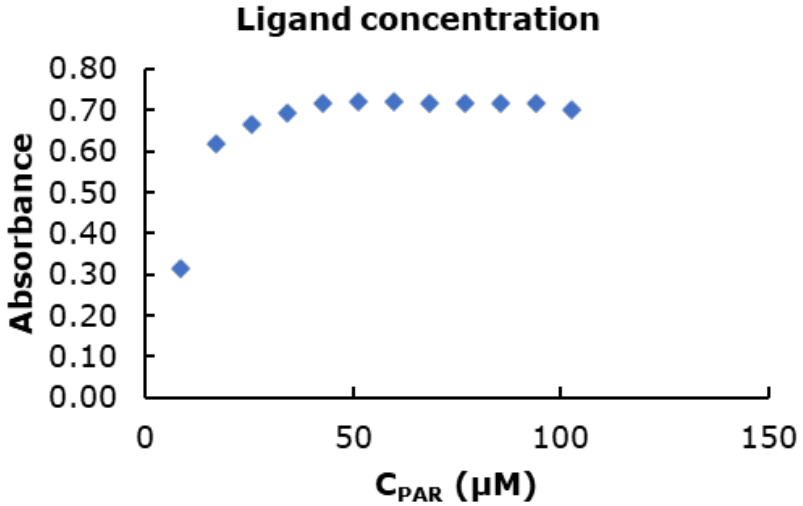

Figure 4: Plot of absorbance versus ligand concentration in flow injection analysis.

3.4.2. Determination of carrier and reagent flow rates, sample injection volume, and reaction cell length

The experiments in which PAR was used as the reagent for Cu^{2+}, 0.5 µg/mL Cu^{2+} in the sample channel, 156 µM PAR, 10 % Triton X-100, and pH 7 buffer solution in the reagent channel and deionized water in the carrier channel were passed through the system and absorbance measurements were made at 512 nm. Working ranges and selected values for each parameter are given in Table 3. When determining the working ranges, the reaction time of the analytes and the ligand in the stationary environment studies were considered. In stationary environment studies, it was observed that the analyte and the ligand reacted immediately and changed color. We can list the advantages of this situation for flow injection analysis such as keeping the reaction circle short, keeping the flow rates high, and allowing more samples to be read in a shorter time.

Table 3: Working ranges and selected values for FIA parameters.

Optimized parameters	Worked range	Max. value for pH 7
mixing coil length	100-500 cm	300 cm
carrier flow rate	1-3 mL/min	2 mL/min
reactant flow rate	0.5-1.5 mL/min	1 mL/min
injected sample volume	100-500 µL	200 µL

3.5. Method Validation

In order to determine the suitability of the method for the purpose, precision, linear range, limit of detection (LOD), limit of quantification (LOQ) parameters was examined. For the linear range, 10 standard solutions were prepared at increasing concentrations and the absorbance values read against these solutions were transferred to the calibration chart. Calibration curve for Cu^{2+} at pH 7 had a good linear relationship in the range 0.125-1 µg/mL with a correlation coefficient R^2 of 0.999. For Cu^{2+} the LOD (S/N = 3) and LOQ (S/N = 10) were 0.04 µg/mL and 0.1 µg/mL respectively. The proposed method has been applied to the determination of Cu (II) hydroponic nutrient solutions. The results obtained compared favorably with those obtained by FAAS. The paired T-test verified the accuracy. T-test value (1.89) less than the critical value at a confidence level of 95% (P value of 0.118). There is agreement between the results obtained with the proposed method and the FAAS method. Five repeated measurements were taken with Cu working solutions of known concentration on the same day, and the same process was repeated on three different days. The calculated intraday and interday precision values, relative standard deviations were ≤ 4.0%. Precision and accuracy evaluation was performed to verify the accuracy of the LOQ (Limit of Quantification) value of the method. The standard deviation (SD) and the relative standard deviation (RSD, %) for repeatability of LOQ were 0.01 and 1.39 respectively. (RSD, %) is 12.4 for intermediate precision. To test the accuracy at LOQ level, recovery was calculated at 95%. The absolute t value (5.9) calculated according to the t test (95% confidence level) result is greater than the critical t value (2.26) for d.f=8.9≈9. There is a statistically significant difference between the blank and LOQ values.

3.6. Determination of Copper in Hydroponic Nutrient Solutions

The recommended method was applied to hydroponic nutrient solutions. The results are shown in Table 4.

Table 4: Accuracy of the proposed method compared with FAAS method for determination of Cu^{2+} in hydroponic nutrient solutions samples.

Sample	Spiked, µg/mL	Found, µg/mL	Recovery, %	FAAS	Recovery, %
S1	0.20	0.19±0.02	96.48	0.20±0.01	100.00
	0.40	0.39±0.01	96.57	0.42±0.01	105.00
S2	0.20	0.20±0.02	100.35	0.21±0.00	105.00
	0.40	0.38±0.00	95.36	0.42±0.00	105.00
S3	0.20	0.21±0.00	104.27	0.19±0.01	95.00
	0.40	0.38±0.02	95.97	0.41±0.01	102.5

The analytical efficiency reported in the present study was also compared to other studies in the literature that investigated copper determination spectrophotometric methods. This comparison is shown in Table 5.

Akmese et al. (9) reported a flow injection analysis which was able to determine copper in river water and sea water. However, this work focused only on low metal ion concentrations. Although the linear working range values reported in the study of Granado-Castro M.D. et al. (16) are similar to our research, the method includes sample preconcentration as an extra analysis step. Despite its simplicity, the spectrophotometric flow injection analysis method developed by Purachat B. et al. (17) does not have the desired low LOD level and linear working range for our sample. The developed system by Youngvises N. et al. (18) was utilized for the analysis of Cu (II) ions in natural water. However, in hydroponic nutrient solutions, the matrix environment is formed by more types of ions at higher concentration levels. For example, macronutrients (N, P, K, Ca, Mg) are at much higher concentrations in hydroponic solutions because they are the main growth elements of plants. Ni Y. et al. (19), who used PAR as a chromogenic reagent in their studies, achieved a similar LOD level and linear working range. However, in our study, the analytical performance of PAN and TAN reagents was evaluated together with PAR as a chromogenic reagent. Optimization studies of the flow injection analysis system were also carried out for the method developed with PAR reagent. The disadvantage of the technique developed by Ghasemi et al. (20) is that it allows the detection of trace amounts of analyte.

Table 5: Findings reported from studies that examined the analysis of Cu^{2+}.

Analyte	Sample	Technique	Reagent	LOD	Linear range	Ref.
Cu(II)	River water and Sea water	FIA	Alizarin Red S	0.6 µg/L	2-110 µg/L	9
Cu(II)	Saline water	FIA	PABH	1.8 µg/L	6.9-984.5 µg/L	16
Cu(II)	Waste water, copper ore samples	FIA	Nitroso-R	0.68 µg/mL	1.0-7.0 µg/mL	17
Cu(II), Mn(II), Fe(II), Fe(III)	River water	FIA	Zincon	12 µg/L	0.050–1.0 mg/L	18
Fe(II), Cu(II), Zn(II), Mn(II)	Pharmaceutical preparations, chicken feedstuff, water samples	UV-VisS	PAR	0.015 µg/mL	0.05–0.8 µg/mL	19
Cu(II), Zn(II), Hg(II)	Natural waters	MCPE, UV-VisS	PAR	9.8 µg/L	0.02-0.10 mg/L	20
Cu(II)	Hydroponic nutrient solution	UV-VisS and FIA	PAN, TAN, PAR	0.04 µg/mL	0.125-1 µg/mL	This study

Abbreviations: FIA, flow injection analysis; Alizarin Red S, (3,4-dihydroxy-9,10-dioxo-2-anthracenesulfonic acid sodium salt); PABH, pyridine-2-acetaldehyde benzoylhydrazone; Nitroso-R, disodium 1-nitroso-2-napthol-3,6-disulfonate; Zincon, 2-carboxy-2′-hydroxy-5′-sulfoformazylbenzene; MCPE, micro cloud point extraction; UV-VisS, UV-*vis* spectrophotometry.

3.7. Green Profile Assessment

The environmental sustainability of the method was assessed using the AGREE, AGREEprep and MoGAPI tools.

3.7.1 Modified green analytical procedure index (MoGAPI)

MoGAPI visually assesses the environmental impact of a method, while also allowing direct comparison of different methods by assigning a total score. In the MoGAPI index, the different stages of the chemical analysis process are shown in a pentagram, with each section marked in green, yellow or red (12).

The data obtained because of the evaluation of the method with the MoGAPI tool are shown in Table 6 and Figure 5.

Table 6: Evaluation of the method with the MoGAPI tool.

Category	Method	Color (Point)
Collection (1)	Online or at-line	Yellow (2)
Preservation (2)	None	Green (3)
Transport (3)	Required	Yellow (2)
Storage (4)	Under normal conditions	Yellow (2)
Type of method: direct or indirect (5)	Simple procedures, e.g., filtration and decantation	Yellow (2)
Scale of extraction (6)	Not applicable	-
Solvents/reagents used (7)	Non-green solvents/reagents used	Red (1)
Additional treatments (8)	None	Green (3)
Reagents and solvents		
Amount (9)	<10 mL(<10 g)	Green (3)
Health hazard (10)	Moderately toxic; could cause temporary incapacitation; NFPA=2 or 3	Yellow (2)
Safety hazard (11)	Highest NFPA flammability or instability score is 2 or 3, or a special hazard is used.	Yellow (2)
Instrumentation		
Energy (12)	≤0.1 kWh per sample	Green (3)
Occupational hazard (13)	Emission of vapors to the atmosphere	Red (1)
Waste (14)	1–10 mL (1–10 g)	Yellow (2)
Waste treatment (15)	Degradation, passivation	Yellow (2)

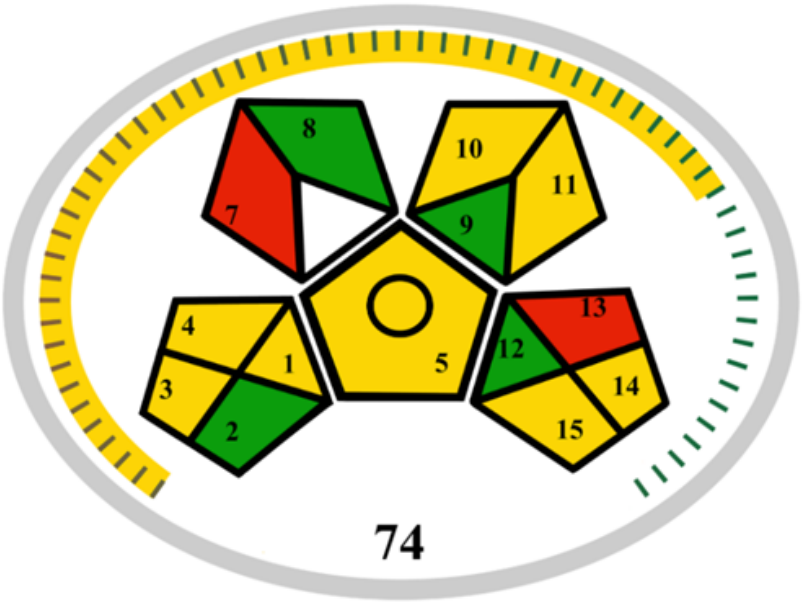

Figure 5: MoGAPI assessment scores for developed method.

3.7.2 Analytical GREEnness Metric approach (AGREE) and AGREEprep

The Agree model responds to the 12 principles of green analytical chemistry. It includes many parameters that have not been considered before, and it is complete compared to other methods. The software interface has 12 windows where green analytical chemistry is explained. Thanks to an algorithm that evaluates all inputs, a pictogram of the procedure is obtained.

Similar to AGREE, AGREEprep is based on the 10 principles of Green Sample Prepare. Therefore, the software is divided into 10 windows with different sizes related to the weighting of the sectors in the pictogram (11).

Table 7 shows the principles of Green Analytical Chemistry and Green Sample Preparation (11).

The total scores of AGREE and AGREE prep shown in Figure 6.

Table 7: Principles of green analytical chemistry and green sample preparation.

	Green Analytical Chemistry (GAC)	Green Sample Preparation (GSP)
1	Direct analytical techniques should be applied to avoid sample treatment	Favor in situ sample preparation
2	Integration of analytical processes and operations saves energy and reduces the use of reagents	Use safer solvents and reagents
3	Generation of a large volume of analytical waste should be avoided, and proper management of analytical waste should be provided	Target sustainable, reusable, and renewable materials
4	Minimal sample size and minimal number of samples are goals	Minimize waste
5	Automated and miniaturized methods should be selected	Minimize sample, chemical and material amounts
6	Reagents obtained from renewable sources should be preferred	Maximize sample throughput
7	The safety of the operator should be increased	Integrate steps and promote automation
8	In situ measurements should be performed	Minimize energy consumption
9	Derivatization should be avoided	Choose the greenest possible post-sample preparation configuration for analysis
10	The use of energy should be minimized	Ensure safe procedures for the operator
11	Multi-analyte or multi-parameter methods are preferred versus methods using one analyte or parameter at a time	
12	Toxic reagents should be eliminated or replaced	

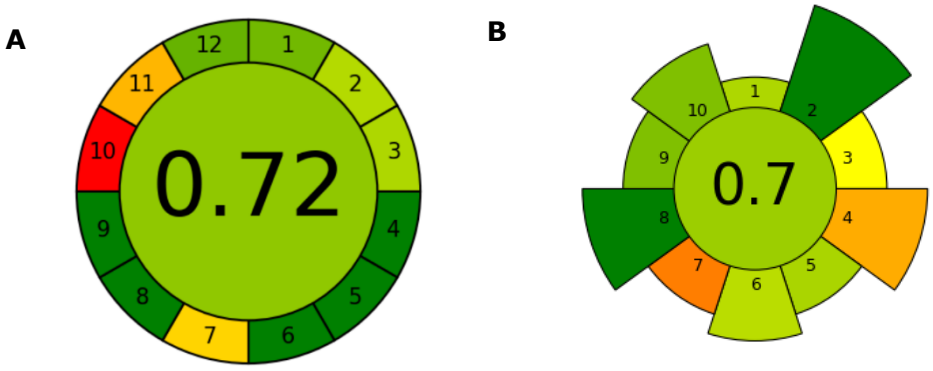

Figure 6: AGREE(A) and AGREE prep (B) assesment scores for developed method.

4. CONCLUSION

The present work deals with the spectrophotometric determination of copper using a UV spectrophotometer and flow injection analysis. This method uses PAR, PAN, and TAN, depending on the ambient pH based on complexities. These ligand types were studied to determine the complexing agent to copper microelement that gave maximum absorbance (Table 1). Complexes formed by Cu^{2+} ions with PAR, PAN and TAN ligands give characteristic absorption peaks in the UV-Vis region. The wavelength of the complexes generally shows a maximum absorption in the region between 500-600 nm. Parameters important for complex formation studies (ligand type, concentration, pH, etc.) have been optimized. The effect of pH on the metal-ligand complex was studied and the optimum pH at which maximum absorbance was obtained was determined. While PAR complexes give maximum absorbance at pH 7 and 8, PAN complexes give maximum absorbance at pH 9 and TAN complexes at pH 5. At the view of these results, the interaction between PAR and Cu^{2+} ions is pH dependent. While PAR's hydroxyl groups can be protonated (H^+ bonded) in acidic environments, they can be deprotonated at higher pHs and bind more strongly with the Cu^{2+} ion. Neutral or slightly basic pH ranges are generally preferred for complex formation. The complexation between PAN and Cu^{2+}

ions is pH sensitive. In acidic medium, the naphthol group can be protonated and this can prevent complex formation. In slightly basic medium (pH 8 and 9), the naphthol group is deprotonated and forms a stronger bond with the Cu^{2+} ion. The interactions between TAN and Cu^{2+} ions are weaker than those between PAR and PAN ligands. According to the results of interference analyses for metals (Table 2), the complexes formed with PAR are more resistant to foreign ion interference compared to PAN and TAN complexes. Detection limits of 0.04 µg/mL were reached for copper. The method uses EtOH as the reagent solvent, significantly reducing contamination and health hazards associated with the use of concentrated acids. Another advantage of this method is that it is suitable for determining the concentrations of copper ions in the nutrient solution, which are of great importance in hydroponic nutrient solutions. However, it should be emphasized that there are very few studies examining the spectrophotometric analysis of copper in hydroponic nutrient solutions. Although this study is simpler and faster compared to some of the existing methods, it also filled a gap in literature.

5. CONFLICT OF INTEREST

The authors declare that they have no known competing financial interests or personal relationships that could have appeared to influence the work reported in this paper.

6. ACKNOWLEDGMENTS

Seda Karapinar acknowledges the grant provided to her by The Scientific and Technological Research Council of Turkey (TUBITAK) in the frame of 2244 Industrial PhD Fellowship Program for PhD Students. This research was supported by the Istanbul Technical University Research Foundation under the PhD thesis (Seda Karapınar) Project; grant number 42999 ITU-BAP".

7. REFERENCES

1. Lei C, Engeseth NJ. Comparison of growth characteristics, functional qualities, and texture of hydroponically grown and soil-grown lettuce. LWT [Internet]. 2021 Oct;150:111931. Available from: <URL>.

2. Savvas D, Ntatsi G, Passam HC. Plant nutrition and physiological disorders in greenhouse grown tomato, pepper and eggplant. Eur J Plant Sci Biotechnol [Internet]. 2008;2(1):45–61. Available from: <URL>.

3. Putra PA, Yuliando H. Soilless culture system to support water use efficiency and product quality: A review. Agric Agric Sci Procedia [Internet]. 2015;3:283–8. Available from: <URL>.

4. Li H, Cheng Z. Hoagland nutrient solution promotes the growth of cucumber seedlings under light-emitting diode light. Acta Agric Scand Sect B — Soil Plant Sci [Internet]. 2015 Jan 2;65(1):74–82. Available from: <URL>.

5. Nazir F, Hussain A, Fariduddin Q. Hydrogen peroxide modulate photosynthesis and antioxidant systems in tomato (*Solanum lycopersicum* L.) plants under copper stress. Chemosphere [Internet]. 2019 Sep;230:544–58. Available from: <URL>.

6. Zhang D, Liu X, Ma J, Yang H, Zhang W, Li C. Genotypic differences and glutathione metabolism response in wheat exposed to copper. Environ Exp Bot [Internet]. 2019 Jan;157:250–9. Available from: <URL>.

7. Lillo F, Ginocchio R, Ulriksen C, Dovletyarova EA, Neaman A. Evaluation of connected clonal growth of Solidago chilensis as an avoidance mechanism in copper-polluted soils. Chemosphere [Internet]. 2019 Sep;230:303–7. Available from: <URL>.

8. Ameh T, Sayes CM. The potential exposure and hazards of copper nanoparticles: A review. Environ Toxicol Pharmacol [Internet]. 2019 Oct;71:103220. Available from: <URL>.

9. Akmese B, Aydin R, Asan A. A simple flow injection spectrophotometric procedure for direct determination of copper(II) in environmental samples. Asian J Chem [Internet]. 2014;26(12):3653–6. Available from: <URL>.

10. Prasertboonyai K, Liawraungrath B, Pojanakaroon T, Liawraungrath S. Mercury(II) determination in commercial cosmetics and local Thai traditional medicines by flow injection spectrophotometry. Int J Cosmet Sci [Internet]. 2016 Feb 2;38(1):68–76. Available from: <URL>.

11. Locatelli M, Kabir A, Perrucci M, Ulusoy S, Ulusoy HI, Ali I. Green profile tools: Current status and future perspectives. Adv Sample Prep [Internet]. 2023 May;6:100068. Available from: <URL>.

12. Mansour FR, Płotka-Wasylka J, Locatelli M. Modified GAPI (MoGAPI) tool and software for the assessment of method greenness: Case studies and applications. Analytica [Internet]. 2024 Sep 6;5(3):451–7. Available from: <URL>.

13. Teshima N, Gotoh S, Ida K, Sakai T. One-shot flow injection spectrophotometric simultaneous determination of copper, iron and zinc in patients' sera with newly developed multi-compartment flow cell. Anal Chim Acta [Internet]. 2006 Jan;557(1–2):387–92. Available from: <URL>.

14. Páscoa RNMJ, Tóth I V., Rangel AOSS. Spectrophotometric determination of zinc and copper in a multi-syringe flow injection analysis system using a liquid waveguide capillary cell: Application to natural waters. Talanta [Internet]. 2011 Jun;84(5):1267–72. Available from: <URL>.

15. Santos IC, Mesquita RBR, Rangel AOSS. Micro solid phase spectrophotometry in a sequential injection lab-on-valve platform for cadmium, zinc, and copper determination in freshwaters. Anal Chim Acta [Internet]. 2015 Sep;891:171–8. Available from: <URL>.

16. Granado-Castro MD, Díaz-de-Alba M, Chinchilla-Real I, Galindo-Riaño MD, García-Vargas M, Casanueva-Marenco MJ. Coupling liquid membrane and flow-injection technique as an analytical strategy for copper analysis in saline water. Talanta [Internet]. 2019 Jan;192:374–9. Available from: <URL>.

17. Purachat B, Liawruangrath S, Sooksamiti P, Rattanaphani S, Buddhasukh D. Univariate and simplex optimization for the flow-injection spectrophotometric determination of copper using nitroso-R salt as a complexing agent. Anal Sci [Internet]. 2001 Mar 23;17(3):443–8. Available from: <URL>.

18. Youngvises N, Suwannasaroj K, Jakmunee J, AlSuhaimi A. Multi-reverse flow injection analysis integrated with multi-optical sensor for simultaneous determination of Mn(II), Fe(II), Cu(II) and Fe(III) in natural waters. Talanta [Internet]. 2017 May;166:369–74. Available from: <URL>.

19. Ni Y, Wang Y, Kokot S. Application of multivariate calibration methods for the simultaneous multiwavelength spectrophotometric determination of Fe(II), Cu(II), Zn(II), and Mn(II) in mixtures. Anal Lett [Internet]. 2007 May;40(6):1209–26. Available from: <URL>.

20. Ghasemi E, Kaykhaii M. Determination of zinc, copper, and mercury in water samples by using novel micro cloud point extraction and UV-Vis spectrophotometry. Eurasian J Anal Chem [Internet]. 2016 Dec 27;12(4):313–24. Available from: <URL>.

JOTCS A Journal of the Turkish Chemical Society Section: A Chemistry

TURKISH CHEMICAL SOCIETY

Kinetic Modeling of Vitamin C Degradation in Lettuce (*Lactuca sativa L*) under Room and Cold Temperatures Using Computer Simulation Analysis

Awagu Emenike, Chinedu Okoroafor*

Nigerian Stored Products Research Institute

Abstract: This study investigates the kinetic modeling of vitamin C degradation in lettuce under room and cold temperatures of 17.5 °C, 19.5 °C, 21 °C and 6.5 °C, 7.5 °C, and 9.5 °C respectively using computer simulation analysis. High-Performance Liquid Chromatography is employed to assess the vitamin C concentrations in the lettuce samples, utilizing an isocratic elution procedure of flow rate of the mobile phase at 1.2cm^3 min^{-1} and an injection volume of 20 µL. The temperature of the analytical column is kept constant at 25 °C coupled with ultraviolet-visible detection set at 245 nm. The lettuce kept at room and cold temperatures for nine days show a reduction in vitamin C with increasing temperature and time. The degradation of vitamin C followed a first-order kinetic model as the average coefficient of determination (R^2-value) for room and cold temperatures tending to 1: 0.922843 and 0.940793 respectively. The integrated law method of first order kinetics gave rate constants of 0.855, 0.925, 0.991 and 0.497, 0.51, 0.546 k (min^{-1}) for the room and cold temperatures with corresponding half-lives of 0.8107, 0.7493, 0.6994 and 1.3947, 1.3591, 1.2695 days respectively. A mathematical model is created on the computer and the model's behavior is explored by running the simulation (forecast). The predicted kinetic models formulated gives the best prediction at $\ln(C) = \ln(C_0) - 0.497t$. The activated energy (EA) yielded values of 10.2220 and 30.4706 kcal/mol for both temperatures respectively. The experimental and computer simulation analysis indicates that lettuce at 6.5 °C retain higher vitamin C concentration.

Keywords: Vitamin C, lettuce, degradation, modeling, computer simulation analysis.

Submitted: November 04, 2023. **Accepted:** February 18, 2025.

Cite this: Emenike A, Okoroafor C. Kinetic Modeling of Vitamin C Degradation in Lettuce (Lactuca sativa L) under Room and Cold Temperatures Using Computer Simulation Analysis. JOTCSA. 2025;12(2):65–76.

***Corresponding author. E-mail:** okoroaforch@nspri.gov.ng

1. INTRODUCTION

Vegetables are rich in carbohydrates and fiber and low in fat and energy. They also include considerable amounts of micronutrients (1). Cultivated Lettuce (Lactuca sativa L.) is a widely grown and popularly consumed leafy vegetable because it contains vitamin C, polyphenols, and dietary fiber, which contribute to weight loss (due to its low caloric content), lower the risk of cardiovascular diseases (via reducing low-density lipoprotein (LDL) cholesterol and blood pressure), and reduce the risk of diabetes (by improving glucose metabolism) and colon cancer (due to protective role of dietary fiber) (2).The major traditional use of lettuce is as a sleep inducer. An investigation into lettuce extracts led to the discovery of a depressive compound. Significant sedative effects were observed in experimental animals when this drug was given to them (3).

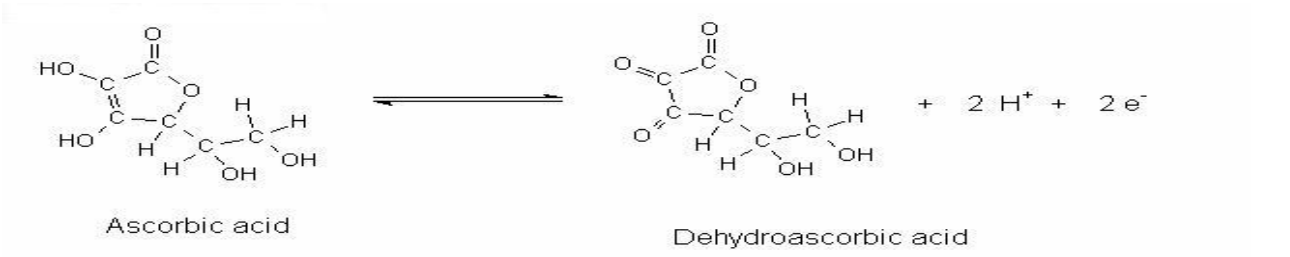

Scheme 1: Reduced (left) and oxidized (right) forms of Vitamin C.

Natural vitamin C is mostly found in fruits and vegetables, where it can be found in both reduced (L-ascorbic acid, AA) and oxidized (L-dehydroascorbic acid monomer, DHA) forms. According to Scheme 1, both AA and DHA have vitamin C activity, and during processing and storage, AA may be oxidized both enzymatically and non-enzymatically to produce DHA (1,3). Ascorbic acid (AA), also known as vitamin C, is an essential part of our diet. It guards against oxidative stress, which can cause cancer, inflammation, heart disease, asthma, and arteriosclerosis, and it also keeps scurvy at bay (4). Plants can make it themselves as can some animals, but humans do not have the right enzyme (gulonolactone oxidase) to synthesize this vitamin, hence, ascorbic acid has to be supplemented mainly through fruits and vegetables. Ascorbic acid is known to be a vitamin sensitive to several factors, including pH, moisture content, light, oxygen, and temperature (5). Its degradation proceeds in both aerobic and anaerobic pathways and depends upon many factors, such as oxygen, light, heat, storage temperature and storage time (6, 7). Anaerobic breakdown of ascorbic acid mostly manifests during storage, while oxidation mostly takes place during juice processing (8). The nutrient quality of food during processing has become increasingly important. Since the vitamin C content of fruits is destroyed during storage, the processing-induced deterioration of certain elements, including vitamin C, may be a crucial component in the shelf life of products, like juice concentrate (9).

The main factors that cause food to deteriorate and spoil have mechanical, physical, chemical, and microbiological influences. Foods that are mishandled during harvest, processing, and distribution might cause damage right away, which could ultimately shorten their shelf life. Fruits and vegetables are living organs of plants that undergo biological and biochemical activity even after they are separated from their plants. Respiration is a sequence of reactions whereby sugars and other substrates, for example, organic acids, are oxidized to carbon dioxide and steam, and energy is released (10). The rate of deterioration of harvested products is proportional to their rate of respiration. Hence, the higher the rate of respiration, the shorter the shelf life (10). Discoloration occurs at the cut surface of fruits and vegetables as a result of the disruption of compartmentation that occurs when cells are broken, allowing substrates and oxidase enzymes to come in contact with each other (11). Pretreatments are common in most of the drying process to improve product quality, storage stability, and processing efficiency. Temperature is the most important factor during drying and many researchers explored the relationship between vitamin C retention and temperatures and the degradation kinetics. Kuljarachanan et al. researched the loss of vitamin C in lime residues during drying at 60-120 degrees and observed that vitamin C decreased significantly with the drying time (12). On the other hand, lower temperatures have been reported to be more effective in reducing the degradation of vitamin C (13). The effect of light on the degradation of vitamin C has been reported. However, the reports are equivocal. While some researchers have reported the negative impact of light on vitamin C content (14, 15) during processing, some have reported higher retention of ascorbic acid content upon exposure to light treatment during storage (16). Meanwhile, Martinez-Sanchez et al. (17) reported that light did not affect the vitamin C content of Romaine lettuce during storage. Oxygen has been linked to vitamin C degradation due to its indispensability in the oxidative degradation pathway of vitamin C (18).

In recent times, an increase in quality retention of dried products by modifying processing method and pretreatment has attracted great attention. Therefore, defining the shell life of fruit juice and comparable products requires a thorough understanding of vitamin C degradation, including the kinetic order and rate constants (19). Numerous analytical techniques are available for the determination of the vitamin C content in various fruits and vegetables, amongst them are HPLC, iodometric titration, chromatographic methods, enzymatic methods, and electrochemical methods (20-23). Kinetics can be defined as the rate at which a reaction occurs. Changes occur at certain reaction rates. Kinetic modeling enables us to describe these changes and their rates

quantitatively. Understanding the fundamental reaction mechanisms that are essential for quality modelling and control is another benefit of kinetic modelling. In food systems, the kinetics of ascorbic acid degradation are more complicated, although in model systems, they follow first-order kinetics (24). Since the design of mechanistic models is hampered by the complexity of the degradation mechanisms, pseudo-kinetic models—such as zero-, first-, or second-order kinetics—are frequently used to get an ideal coordinate with the experimental data. The model that gives the highest coefficient of determination value (R^2 value) is regarded as the best fit for the analysis (25).

The simulation technique is the process of designing a model of a real system and conducting experiments with the purpose either of understanding the behavior of the system or evaluating various strategies for the operation of the system. Simulation has also been defined as the broad collection of methods used to study and analyze the behavior and performance of actual or theoretical systems. In simulation analysis, we build a mathematical model of a system, process, or other entity, usually on a computer, and then use a simulation to examine the model's behavior. A time series is a chronological sequence of observations on a particular variable. Usually, the observations are taken at regular intervals (minutes, days, months, years), but the sampling could be irregular. A time series analysis consists of two steps: (1) building a model that represents a time series, and (2) using the model to predict (forecast) future values. The objectives of this study were (i) to determine the rate of degradation of vitamin C in lettuce under pretreatment conditions of room and cold temperatures, to recommend the best; (ii) to develop kinetic models for predicting vitamin C degradation in the lettuce under the studied conditions. (iii) to predict the future values (forecast) (26).

2. MATERIALS AND METHODS

2.1 Reagents and chemicals

L-ascorbic acid (AA), metaphosphoric acid (MPA), orthophosphoric acid, and acetonitrile (HPLC grade) were all purchased from Merck (Darmstadt, Germany). For chromatographic analysis, de-ionized water of 18 $M\Omega cm^{-1}$ resistivity purified with a milli-Q system (Millipore, Bedford, USA) was used. The ascorbic acid stock standard solution was prepared in water and stored in a glass-stopper bottle at 4 °C in the dark (27).

2.2 Sample preparation

Fresh and matured lettuce was sourced from fruits and vegetable market located in Yankaba market, Nasarawa local Government of Kano state, Nigeria which lies between Longitude 70 54' and 90 06' East and Latitude 110 37' and 120 21' north. The fresh and matured lettuce vegetable of about 3 kg was washed under running tap water for about 2 min; the stems were removed by cutting with a sharp and pre-washed stainless steel knife to avoid contamination. The leaves of about 100 g each for the six (6) sets of temperatures; 17.5 °C, 19.5 °C, and 21 °C for room temperatures and 6.5 °C, 7.5 °C, and 9.5 °C for cold temperatures were made set for the experiment by draining them differently using muslin cloth for 5 min and the initial samples were blended in a Kenwood blender (Philips, HR 1702, Borehamwood, England, UK) and filtered with cheese-cloth. At two-day intervals, the samples were analyzed for vitamin C using high-performance liquid chromatography (HPLC). On the first day, initial unaltered samples maintained at specified room and cold temperature served as control. The remaining lots were spread evenly on trays and dried under room mild temperatures and the other half kept under cold temperatures. The temperature and relative humidity were measured using thermometer and hygrometer respectively. The lettuce vegetable wastes are bio-degradable in nature; they were disposed by putting in the soil where microbes acted on them enriching the soil. The experiments were carried out in 3 replications and the average of measurement was reported (28).

2.3 Instrumentation

The HPLC system consists of Waters liquid chromatography (Milford, MA, USA) equipped with a 600E multisolvent delivery system, an in-line degasser, a manual injection with 20 µL loop (Rheodyne 7125), and Waters 2487ʎ dual absorbance detector. Empowers software was used for controlling the analytical system and data processing.

2.3.1 Extraction of ascorbic acid

2.3.2. Mild-temperature-drying procedure

This procedure is a modification of Rahman's method (29). About 100 g of salad vegetable samples in each maturity stage were separately weighed and dried under mild temperature (15–20 °C) and ground to fine powder dust before extraction. The obtained powder were weighed (1.0 g for each sample and subsequently extracted with 25 mL of extractant solution, containing 5% MPA, at 10 °C and in the dark. The extraction process was performed using a shaker for 4 hours. All extractions were carried out in triplicate and obtained solutions were then filtered and stored at 4 °C before analysis. The injection of the extracts into the HPLC system was performed twice.

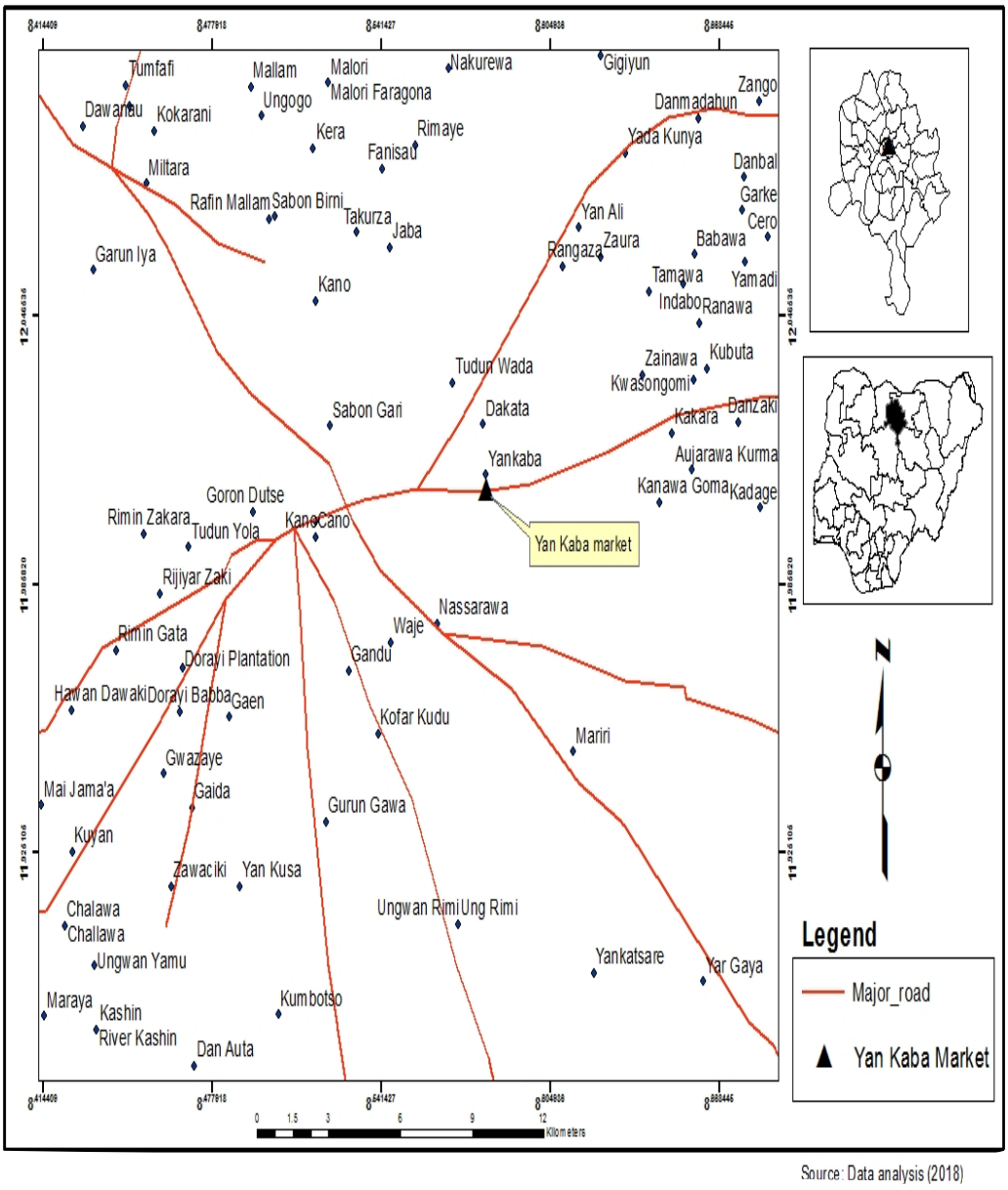

Source: Data analysis (2018)

2.3.3. HPLC analysis

Ascorbic acid was determined using a liquid chromatographic technique that included an isocratic elution process and UV-visible detection at 245 nm. Separations were carried out on a 5 µm RP C18 column of 250 mm × 4.6 mm (Spherical, Optimals ODS-H, Capital HPLC, UK) fitted with a 5 µm RP C18 guard column of 20 mm × 4.6 mm (Spherical, Optimals ODS-H, Capital HPLC, UK). The mobile phase employed was a mixture of 0.5% NaH_2PO_4 (pH 2.25 with H_3PO_4)–acetonitrile (93:7). The Flow rate of the mobile phase was 1.2 mL min^{-1} and an injection volume of 20 µL was used in quantitative analysis. The desired flow rate was set on the HPLC pump, then a known volume container was used to collect the eluent for a specific time. The flow rate was now calculated by dividing the collected volume by the time elapsed. The temperature of the analytical column was kept constant at 25 °C. The calibration curve and quantitative evaluations were accomplished at 245 nm. Standard solutions and extracts were filtered through a prefilter and then a 0.45 µm Millipore membrane before their injection. To prevent the loss of AA, standard solutions and extracted samples were protected from light using amber flasks. Quantitation was performed by comparing the chromatographic peak area with that of the external standard. The calibration curve was

plotted in the concentration range of 0.5–200 mg L^{-1} and based on a 10-point calibration (28).

2.4 Kinetic modeling

Using the integrated rate law, the breakdown of vitamin C was modeled. Using the integral approach of analysis, various models were created. As shown in the following integral law equation:

$$\frac{dC}{dt} = -K[C]^n \quad - \quad (1)$$

was utilized to create three concentration-based models with corresponding half-lives ($t_{1/2}$) for reaction orders n = 0, 1, and 2.
Zero order model (n = 0):

$$C = C_0 - kt \quad - \quad - \quad (2a)$$

$$t_{\frac{1}{2}} = \frac{C_O}{2k} \quad - \quad - \quad (2b)$$

First order model (n = 1):

$$\ln(Ckt) = \ln(C_0) - kt \quad - \quad (3a)$$

$$(t_{\frac{1}{2}}) = \ln\frac{(2)}{k} \quad -- \quad - \quad - \quad (3b)$$

Second order model (n = 2):

$$\frac{1}{C} = \frac{1}{C_0} + kt \quad - \quad - \quad - \quad (4a)$$

$$t_{\frac{1}{2}} = \frac{1}{kC_O} \quad - \quad - \quad (4b)$$

where k = rate constant, C_o = initial concentration of vitamin C in the sample, C = concentration of vitamin C in the sample at time t, and $t_{1/2}$= half-life of vitamin C in the sample.

2.4.1 Arrhenius equation

$$K = A_\rho \frac{E_A}{RT} \quad -- \quad - \quad (5a)$$

k = Rate Constant, A = Frequency Factor or Pre-experimental Factor, e = Mathematical quantity (e), R = the gas Constant, T = Kelvin Temperature, E_A = Activation Energy

Arrhenius's equation shows the effect of temperature on the rate constant and therefore on the rate of the reaction. The frequency factor, A, in the equation is approximately constant. The validity of the Arrhenius equation can be tested by taking the (ln) of both sides of the equation.

$$\ln K = \ln A - \frac{Ea}{Rt} \quad - \quad - \quad (5b)$$

A plot of lnK Vs 1/T at 3 different points was plotted to evaluate Ea and A

Computer simulation via Time-series Analysis
Regression Equation - - - (6)

i. $Y_t = S_t * I_t$
ii. Deforming moving average {MAD [4]}
iii. Deforming central moving average {CMA}
iv. Deforming seasonal and irregular components = $\{Y_t / _{CMA} * S_t I_t\}$
v. Deforming only seasonal component $\{S_t\}$
vi. Deseasonalized $\{Y_t / S_t\}$
vii. Deforming T_t = {I + slope *t) - Regression analysis to determine I and slope
viii. Plot graph

3. RESULTS AND DISCUSSION

The variations in vitamin C concentration of the lettuce vegetable at room and cold temperatures are presented in Table 1. At room temperature range of 17.5 to 21 °C and cold temperature of 6.5 to 9.5 °C, the lettuce degrades within two (2) day intervals from 898.41 mg/100 g to 0.80, 0.7085. 0.4085 mg/100 g and 895 mg/100 g to 18.98, 16.89, and 12.76 mg/100 g on the 9th day respectively. As can be observed, the concentration of vitamin C decrease steadily as storage time and temperature increase in all the vegetable samples. Injury to the plant tissues affects both the rate and the extent of water loss, this is the reason why leafy vegetables such as lettuce lose water at a higher rate than potatoes and apples (27). This confirms the fact that vitamin C in fruits and vegetables degrade during processing and storage. Therefore, ascorbic acid is usually selected as the most frequently measured nutrient to evaluate nutrient loss during storage. With so many important roles, the retention of vitamin C in products is regarded as a reliable and representative index during processing (28). A visual inspection of the kinetic plots of models (Fig. 1) from integral law equation (1) and order of reaction n = 0, 1 and 2 ;(2a), (3a) (4a) at both temperature ranges shows that the first order model fitted the kinetic data best in all the temperatures concerned. This shows that the first-order model fits the kinetic data best in all the vegetable samples stored at room and cold temperatures.

Table 1: Vitamin C (mg) in lettuce at various room and cold temperatures.

Time (day)	17.5 °C	19.5 °C	21 °C	6.5 °C	7.5 °C	9.5 °C
1	898.41	898.41	898.41	895.75	895.75	895.75
3	578.22	541.22	490.45	578.47	470.25	440.68
5	65.28	57.81	47.94	331.30	297.89	256.93
7	26.84	7.95	5.75	61.78	48.87	38.78
9	0.80	0.7085	0.4085	18.98	16.89	12.76

This is confirmed by the goodness of fit data (Table 2), where the first order kinetics exhibited R^2 values; 0.922843, R^2 adjusted 0.897124, P-value; 0.009316, R^2 value; 0.966717, R^2 adjusted 0.955623 P-value; 0.002603, R^2 value; 0.967654, R^2 adjusted 0.956872, P-value; 0.002493 for lettuce stored at room temperatures of 17.5 °C, 19.5 °C and 21 °C, respectively. From Table 3, R^2 values; 0.940793, R^2 adjusted 0.921057, P-value; 0.006227, R^2 value; 0.948852, R^2 adjusted 0.931802, P-value; 0.004987, R^2 value; 0.955274, R^2 adjusted 0.940365, P-value; 0.00407, for lettuce stored at cold temperatures of 6.5 °C, 7.5 °C and 9.5 °C respectively. The R^2 values are the highest and P - values the lowest.

Thus, the vitamin C degradation kinetics in lettuce under various temperature ranges is best described by first-order kinetics. This implies that the rate of degradation at any time is dependent on the initial concentration of vitamin C in the salad vegetables. The model with maximum R^2 and minimum P-value is adjudged the best (28). However, according to Barbara et al. (30), it is possible to have a low R^2 for both linear and logistic regression and still have a model that is correctly specified in every respect. And vice versa, you can have a very high R^2 and yet have a model that is grossly inconsistent with the data.

At room temperature (Table 4), lettuce at 17.5 °C has the lowest rate constant of 0.855 day^{-1} and the highest half-life of 0.8107 day compared with at 19.5 °C and 21 °C with a rate constant of 0.925 day^{-1}, half-life of 0.7493 day and 0.991 day^{-1}, half-life of 0.6994 day respectively. On the other hand, a cold temperature at 6.5 °C has least rate constant of 0.497 day^{-1} and the highest half-life of 1.3947 day compared with at 7.5 °C and 9.5 °C has rate constant of 0.51 day^{-1}, half-life of 1.3591 day and rate constant of 0.546 day^{-1}, half-life of 1.2695 day respectively. Again, comparing the least rate constants and highest half-lives (Table 4), it was deduced that at temperature of 6.5°C, the rate constant was 0.497 day^{-1} and half-life of 1.3947day while at temperature 17.5 °C, the rate constant was 0.855 day^{-1} and half-life of 0.8107 day. Invariably, the degradation of vitamin C at a temperature of 6.5 °C gave the lowest rate constant and highest half-life, which made it preferred over other temperatures.

Vitamin C belongs to the heat-sensitive substance. It is believed that the higher the storage temperature, the higher losses of vitamin C in the products (8,32,33). It is reported that drying temperature was the major factor controlling the degradation of vitamin C in lime residues and the higher drying temperature results in lower vitamin C content. The rate of deterioration is generally proportional to their respiration rate, which is often a good index to the storage potential of a crop. The higher the respiration rate, the shorter the shelf life and vice versa. Respiration rate can be used as a criterion to compare the perishability of fruits and vegetables (33).

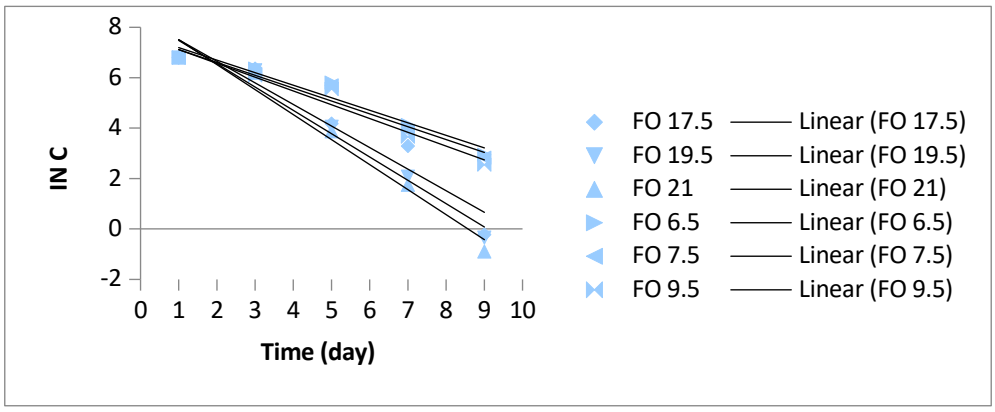

Figure 2: Plot of first-order kinetics for the lettuce at room and cold temperatures. FO: First-order, LN C: natural logarithm of the concentration of lettuce.

Table 2: Zero, first and second-order kinetic models at different room temperatures for lettuce.

KM ORDER	17.5 °C			19.5 °C			21 °C		
	R^2	R^2Adj	P- Value	R^2	R^2Adj	P- Value	R^2	R^2Adj	P- Value
ZO	0.842281	0.789708	0.02796	0.834523	0.779364	0.030128	0.820977	0.761303	0.034062
FO	0.922843	0.897124	0.009316	0.966717	0.955623	0.002603	0.967654	0.956872	0.002493
SO	0.524614	0.366152	0.1664	0.569261	0.425682	0.140523	0.555043	0.406725	0.148512

Table 3: Zero, first and second-order kinetic models at different cold temperatures.

KM ORDER	6.5 °C			7.5 °C			9.5 °C		
	R^2	R^2Adj	P- Value	R^2	R^2Adj	P- Value	R^2	R^2Adj	P- Value
ZO	0.955634	0.940846	0.00402	0.919219	0.892292	0.009991	0.89842	0.86456	0.014184
FO	0.940793	0.921057	0.006227	0.948852	0.931802	0.004987	0.955274	0.940365	0.00407
SO	0.71502	0.620027	0.071126	0.737742	0.650323	0.062248	0.729436	0.639248	0.065435

ZO – zero order, FO – first order, SO – second order, RT – Room Temperature, RT – room temperature, CT- Cold Temperature, KM – kinetic model.

Table 4: Rate constants, kinetic energies, and proposed models at RT and CT.

PT	T °C	k (day^{-1})	Half-life	Proposed Model	T (1/F)°C	E_A kcal/mol
RT	17.5	0.855	0.8107	$\ln(C) = \ln(C_0) - 0.855t$	0.015748031	10.2220
RT	19.5	0.925	0.7493	$\ln(C) = \ln(C_0) - 0.925t$	0.01490313	
RT	21	0.991	0.6994	$\ln(C) = \ln(C_0) - 0.991t$	0.014326648	
CT	6.5	0.497	1.3947	$\ln(C) = \ln(C_0) - 0.497t$	0.022883295	30.4706
CT	7.5	0.51	1.3591	$\ln(C) = \ln(C_0) - 0.51t$	0.021978022	
CT	9.5	0.546	1.2695	$\ln(C) = \ln(C_0) - 0.546t$	0.020366599	

Table 5: First-order kinetics trendline equation and R squared value for lettuce at room and cold temperatures.

Lettuce at room and cold temperatures (℃)	Y intercept	R square
17.5	-0.8559x + 8.3606	0.9228
19.5	-0.9256x + 8.4038	0.9667
21	-0.9919x + 8.5034	0.9677
6.5	-0.4973x + 7.6919	0.9408
7.5	-0.5103x + 7.6242	0.9489
9.5	-0.5467x + 7.6611	0.9553

The degradation rate of vitamin C is less for all the samples at cold temperatures; in particular, the degradation rate is the lowest in lettuce with a rate constant of 0.497 day^{-1} and a half-life of 1.3947 day. As shown in Table 4, storage is best done at a cold temperature of 6.5 °C, according to the established model. Lowering temperature during handling, transportation, and storage is the most effective means of extending the shelf life and reducing the loss of quality by lowering the metabolic processes such as respiration, transpiration, and ethylene production. However, vitamin C can be easily degraded because of its sensitive to various external factors, especially high temperature, oxygen, and light.

This indicates that the magnitude of the rate constant reflects the rate of reaction; the inference is that degradation of vitamin C occurred lower in lettuce vegetables stored at 6.5 °C under the same conditions. The half-life is longer for all analytical salad vegetable samples at cold temperatures implying that the rate of degradation of vitamin C is less as compared to storing at room temperature. Furthermore the kinetic models were developed based on the predicted initial contents, measured contents and storage time, from Table 4, the proposed models at 17.5 °C, 19.5 °C and 21 °C were: $In(C) = ln\ (C_0)$ -0.855t, $ln(C) = ln\ (C_0)$ - 0.925t, $ln(C) = ln(C_0)$ - 0.991t and at 6.5 °C, 7.5 °C and 9.5 °C were; $ln(C) = ln\ (C_0)$ - 0.497t, $ln(C) = ln(C_0)$ - 0.51t, $ln(C) = ln(C_0)$ - 0.546t. The first order model kinetics forecasted on the 21st day show:-9.61288, -11.0329, -12.3264 for room temperatures and -2.75068, -3.09208, -3.81868 for cold temperatures respectively indicating forecast at 6.5°C the best, through mathematical model created on the computer and behavior of the model explored by running the simulation (forecast). The keeping quality of lettuce at a cold temperature of 6.5 °C is better than the rest. From Table 4 and Fig.4 and 5, lettuce room temperatures of 17.5 °C, 19.5 °C and 21 °C had activation energy of 10.2220 kcal/mol while lettuce cold temperatures of 6.5 °C, 7.5 °C and 9.5 °C had activation energy of 30.4706 kcal/mol. The activation energy for ascorbic acid degradation in lettuce concurs with the range reported by Mauri et al. (32). The activation energy represents the minimum energy required for a chemical reaction to occur. For vitamin C degradation in lettuce, the reaction involved the conversion of ascorbic acid (vitamin C) to dehydroascorbic acid (an inactive form). This process required a certain energy threshold to overcome the energy barrier, represented by the activation energy (Ea). Elevated temperatures reduce Ea, increasing the degradation rate (33).

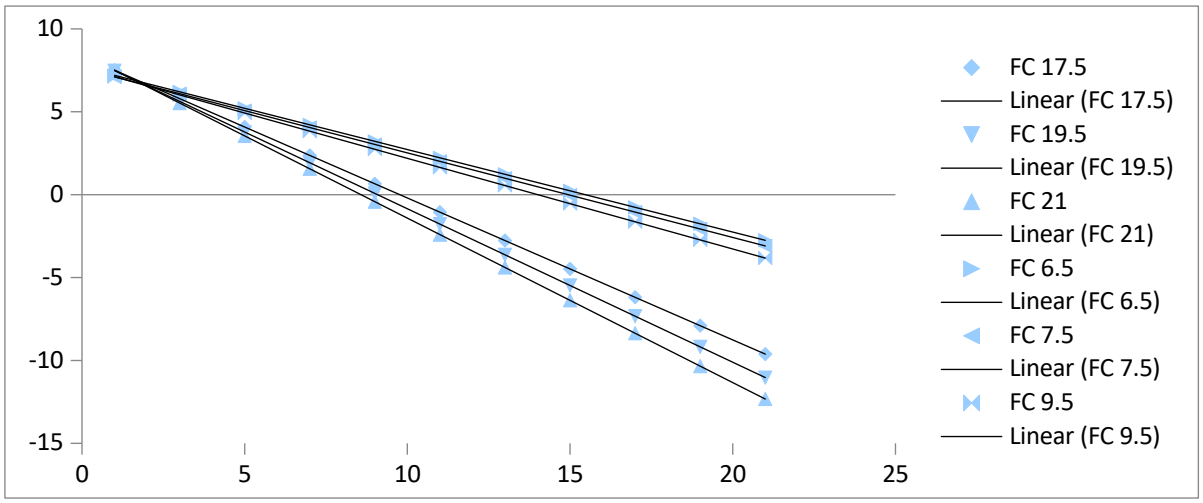

Figure 3: Computer simulation analysis (forecast) for lettuce at room and cold temperatures.

Table 6: First-order kinetics forecast Trendline equation and R Squared value for lettuce at room and cold temperatures.

Lettuce at room and cold temperatures (°C)	Y intercept	R square
17.5	-0.8559x + 8.3606	1.0
19.5	-0.9256x + 8.4038	1.0
21	-0.9919x + 8.5034	1.0
6.5	-0.4973x + 7.6919	1.0
7.5	-0.5103x + 7.6242	1.0
9.5	-0.5467x + 7.6611	1.0

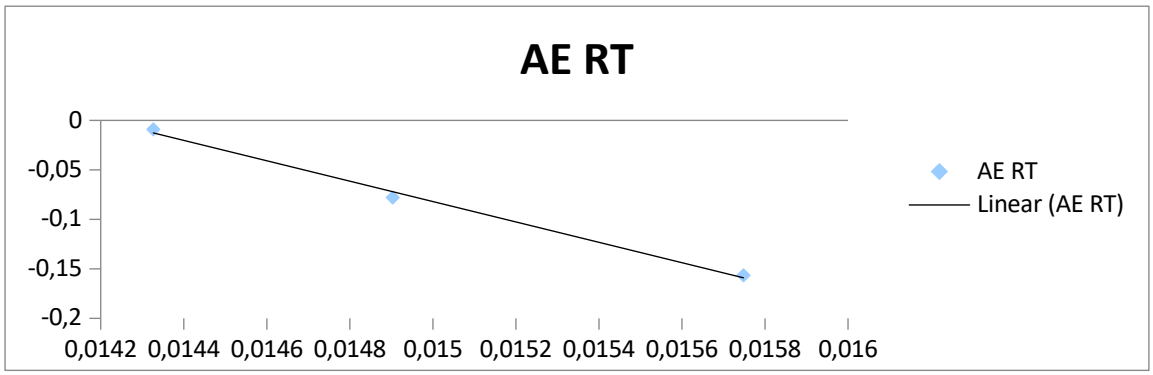

Figure 4: Arrhenius plot for lettuce at room temperature.

Table 7: Arrhenius trendline equation and R squared value for lettuce at room and cold temperatures.

Lettuce at room and cold temperatures (°C)	Y intercept	R square
RT	-103.06x + 1.4639	0.9951
CT	-37.942x + 0.1657	0.9912

RT: room temperature; CT: cold temperature

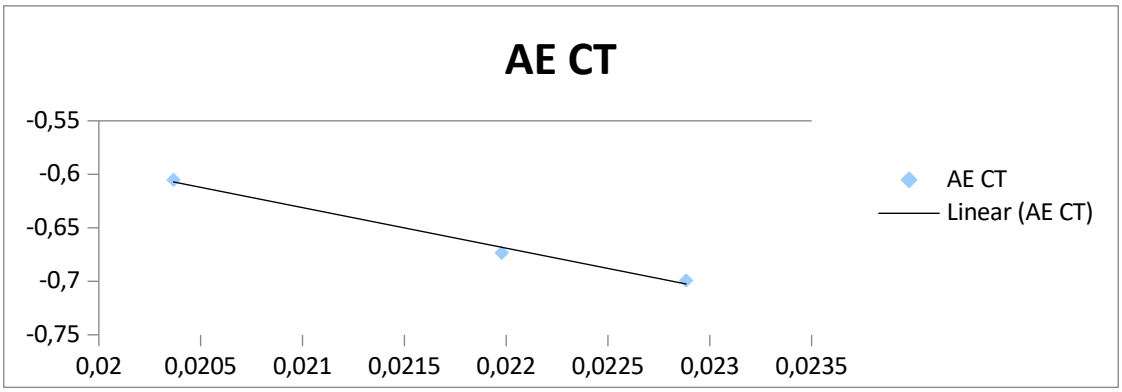

Figure 5: Arrhenius plot for the lettuce vegetable at cold temperature.

Among the temperatures and storage conditions studied, lettuce at cold temperatures has the highest activation energy, implying a lower degradation rate.

4. CONCLUSION

The rate of vitamin C degradation in the lettuce under room, cold temperatures and defined storage methods investigated in this study followed the first-order reaction kinetics. This indicated that the rate of degradation is dependent on the vitamin C concentration in the vegetable. There was a lower rate of vitamin C degradation at cold temperature storage of 6.5 °C compared to other temperatures. This implied that temperature is the major factor controlling the degradation of vitamin C. This is reflected in its lower rate constant, longer half-life, higher forecast, and activation energy values. This impresses the fact that the storage of lettuce at cold temperatures is preferable in terms of vitamin C retention.

5. CONFLICT OF INTEREST

The authors declare that they do not have any conflict of interest.

6. REFERENCES

1. Ariahu CC, Abashi DK, Chinma CE. Kinetics of ascorbic acid loss during hot water blanching of fluted pumpkin (Telfairia occidentalis) leaves. J Food Sci Technol [Internet]. 2011 Aug [cited 2025 Mar 29];48(4):454–9. Available from: <URL>

2. Kim MJ, Moon Y, Tou JC, Mou B, Waterland NL. Nutritional value, bioactive compounds and health benefits of lettuce (Lactuca sativa L.). Journal of Food Composition and Analysis [Internet]. 2016 Jun [cited 2025 Mar 29];49:19–34. Available from: <URL>

3. Sadino A, Renggana H, Suwendar S, Apriani R, Nurhandayani Y. HYPNOTIC-SEDATIVE ACTIVITY TEST OF 70% ETHANOL EXTRACT OF LETTUCE (Lactuca sativa L.) IN MALE WHITE MICE SWISS WEBSTER STRAIN. JIFB [Internet]. 2024 Jul 31 [cited 2025 Mar 29];15(2):113–20. Available from: <URL>

4. Cioroi M. Study on L-ascorbic acid contents from exotic fruits. 2006;

5. Lee HS, Coates GA. Vitamin C in frozen, fresh squeezed, unpasteurized, polyethylene-bottled orange juice: a storage study. Food Chemistry [Internet]. 1999 May [cited 2025 Mar 29];65(2):165–8. Available from: <URL>

6. Johnson Jr, Braddock RJ, Chen CS. Kinetics of Ascorbic Acid Loss and Nonenzymatic Browning in Orange Juice Serum: Experimental Rate Constants. Journal of Food Science [Internet]. 1995 May [cited 2025 Mar 29];60(3):502–5. Available from: <URL>

7. Fellers PJ. Shelf Life and Quality of Freshly Squeezed, Unpasteurized, Polyethylene-Bottled Citrus Juice. Journal of Food Science [Internet]. 1988 Nov [cited 2025 Mar 29];53(6):1699–702. Available from: <URL>

8. Abioye AO, Abioye VF, Ade-Omowaye BI, Adedeji AA. Kinetic modeling of ascorbic acid loss in baobab drink at pasteurization and storage temperatures. IOSR J Environ Sci Toxicol Food Technol. 2013;7(2):17–23.

9. Burdurlu HS, Koca N, Karadeniz F. Degradation of vitamin C in citrus juice concentrates during storage. Journal of Food Engineering [Internet]. 2006 May [cited 2025 Mar 29];74(2):211–6. Available from: <URL>

10. Salunkhe DK, Desai BB. Postharvest biotechnology of vegetables. Boca Raton, Fla: CRC Press; 1984. 2 p.

11. Stringer M, Dennis C, editors. Chilled foods: a comprehensive guide. 2. ed. Cambridge: Woodhead [u.a.]; 2000. 486 p. (Woodhead Publishing in food science and technology).

12. Kuljarachanan T, Devahastin S, Chiewchan N. Evolution of antioxidant compounds in lime residues during drying. Food Chemistry [Internet]. 2009 Apr [cited 2025 Mar 29];113(4):944–9. Available from: <URL>

13. Barbosa J, Borges S, Amorim M, Pereira MJ, Oliveira A, Pintado ME, et al. Comparison of spray drying, freeze drying and convective hot air drying for the production of a probiotic orange powder. Journal of Functional Foods [Internet]. 2015 Aug [cited 2025 Mar 29];17:340–51. Available from: <URL>

14. El-Beltagy A, Gamea GR, Essa AHA. Solar drying characteristics of strawberry. Journal of Food Engineering [Internet]. 2007 Jan [cited 2025 Mar 29];78(2):456–64. Available from: <URL>

15. Santos PHS, Silva MA. Retention of Vitamin C in Drying Processes of Fruits and Vegetables—A Review. Drying Technology [Internet]. 2008 Nov 21 [cited 2025 Mar 29];26(12):1421–37. Available from: <URL>

16. Zhan L, Hu J, Ai Z, Pang L, Li Y, Zhu M. Light exposure during storage preserving soluble sugar and l-ascorbic acid content of minimally processed romaine lettuce (Lactuca sativa L.var. longifolia). Food Chemistry [Internet]. 2013 Jan [cited 2025 Mar 29];136(1):273–8. Available from: <URL>

17. Martínez-Sánchez A, Tudela JA, Luna C, Allende A, Gil MI. Low oxygen levels and light exposure affect quality of fresh-cut Romaine lettuce. Postharvest Biology and Technology [Internet]. 2011 Jan [cited 2025 Mar 29];59(1):34–42. Available from: <URL>

18. Zhang M, Bhandari B, Fang Z. In: Handbook of Drying of Vegetables and Vegetable Products. 1st ed. Portland: Taylor & Francis Group; 2017. (Advances in Drying Science and Technology).

19. Derossi A, De Pilli T, Fiore AG. Vitamin C kinetic degradation of strawberry juice stored under non-isothermal conditions. LWT - Food Science and Technology [Internet]. 2010 May [cited 2025 Mar 29];43(4):590–5. Available from: <URL>

20. Tadese A, Subramanian P, Woldu A, Pal R. Electrochemical determination and comparison of ascorbic acid in freshly prepared and bottled fruit juices: A cyclic voltammetric study. Journal of Chemical and Pharmaceutical Research. 2014;6(5):880–8.

21. Gunjan K, Mangla D. Analysis of vitamin C in commercial and natural substances by iodometric titration found in Nimar and Malwa region. J Sci Res Phar. 2012;1(2):8.

22. Iwase H. Use of nucleic acids in the mobile phase for the determination of ascorbic acid in foods by high-performance liquid chromatography with electrochemical detection. Journal of Chromatography A [Internet]. 2000 Jun [cited 2025 Mar 29];881(1–2):327–30. Available from: <URL>

23. Vermeir S, Hertog MLATM, Schenk A, Beullens K, Nicolaï BM, Lammertyn J. Evaluation and optimization of high-throughput enzymatic assays for fast l-ascorbic acid quantification in fruit and vegetables. Analytica Chimica Acta [Internet]. 2008 Jun [cited 2025 Mar 29];618(1):94–101. Available from: <URL>

24. Liao ML, Seib PA. Chemistry of L-ascorbic acid related to foods. Food Chemistry [Internet]. 1988 [cited 2025 Mar 29];30(4):289–312. Available from: <URL>

25. Nwakaudu M, Nkwocha A, Madu I, Enwereji C, Ireaja I. Kinetic modeling of vitamin C (ascorbic acid) degradation in tomato and pawpaw under market storage conditions. International Journal of Current Research. 2015;7(6):16783–8.

26. Awagu E, Ekanem E, Kolo A, Adamu M. Kinetic modeling of vitamin C (ascorbic acid) degradation in blanched commonly consumed salad vegetables using computer simulation analysis. Journal of Applied Chemistry. 2017;10:59–66.

27. Nojavan S, Khalilian F, Kiaie FM, Rahimi A, Arabanian A, Chalavi S. Extraction and quantitative determination of ascorbic acid during different maturity stages of Rosa canina L. fruit. Journal of Food Composition and Analysis [Internet]. 2008 Jun [cited 2025 Mar 29];21(4):300–5. Available from: <URL>

28. Bozan B, Sagdullaev BT, Kozar M, Aripov KhN, Baser KHC. Comparison of ascorbic and citric acid contents inRosa canina L. fruit growing in the Central Asian region. Chem Nat Compd [Internet]. 1998 Nov [cited 2025 Mar 29];34(6):687–9. Available from: <URL>

29. Rahman MS. Food Properties. In: Users' Handbook. Dhaka: ORC; 2006.

30. Barbara FR, Thomas AR, Brian L. Minitab 17.3.1. Pennsylvania State University; 2017.

31. Silva EM, Da Silva JS, Pena RS, Rogez H. A combined approach to optimize the drying process of flavonoid-rich leaves (Inga edulis) using experimental design and mathematical modelling. Food and Bioproducts Processing [Internet]. 2011 Jan [cited 2025 Mar 29];89(1):39–46. Available from: <URL>

32. Mauri LM, Alzamora SM, Chirife J, Tomio MJ. Review: Kinetic parameters for thiamine degradation in foods and model solutions of high water activity. Int J of Food Sci Tech [Internet]. 1989 Feb [cited 2025 Mar 29];24(1):1–9. Available from: <URL>

33. Tian J, Chen J, Lv F, Chen S, Chen J, Liu D, et al. Domestic cooking methods affect the phytochemical composition and antioxidant activity of purple-fleshed potatoes. Food Chemistry [Internet]. 2016 Apr [cited 2025 Mar 29];197:1264–70. Available from: <URL>

JOTCSA Journal of the Turkish Chemical Society Section: A Chemistry

TURKISH CHEMICAL SOCIETY

Screening of Primary and Secondary Metabolites Profile of Different Extracts of *Cassia fistula* Flowers and its Perspectives on the Antimicrobial and Antidiabetic Potential of Active Extract

Nivetha Arunprakash[1*], Christina Ruby Stella[1], Angel Praba[1], Vijayavilas Sathyan Sangeetha[2]

[1]Holy Cross College, Bharathidasan University, Department of Chemistry, Tiruchirappalli, India
[2]Dhanalakshmi Srinivasan College of Arts and Science for Women, Department of Chemistry, Perambalur, India.

Abstract: This article provides an overview of the pharmacological activity and phytochemical constituents found in *Cassia fistula* flower extract. Some phytonutrients and antioxidants of plant extract may be compromised due to the relatively high concentration of organic solvents. The main goal of this study was to find out how well an aqueous extract from *Cassia fistula* flowers fights diabetes and germs in a lab setting. The maceration extract yielded the best results among others. The antimicrobial activity of the extract was evaluated using bacterial and fungal strains, while the anti-diabetic activity was assessed at different concentrations, ranging from 10 to 50 µg/mL. The maximum inhibition of 54.07% was observed at a concentration of 50 µg/mL, compared to the standard acarbose, which showed an inhibition of approximately 62.23%. The IC_{50} value of the flower extract was 49.3494 µg/mL, while that of the standard acarbose was 42.1726 µg/mL. The presence of phytochemicals in the extract was determined using UV and FTIR spectral studies, which are effective methods for extracting a broad range of chemical constituents. The results show that *Cassia fistula* flower extract has promising anti-diabetic and antimicrobial activity. It can be concluded that *Cassia fistula* has high alpha-amylase inhibitory activity, and these extracts have the potential to be effective antimicrobial agents against pathogenic microorganisms.

Keywords: Phytochemicals, *Cassia fistula*, Anti-microbial, Anti-diabetic, FTIR.

Submitted: February 14, 2024. **Accepted:** January 18, 2025.

Cite this: Arunprakash N, Stella CR, Praba A, Sangeetha VS. Screening of Primary and Secondary Metabolites Profile of Different Extracts of *Cassia fistula* Flowers and its Perspectives on the Antimicrobial and Antidiabetic Potential of Active Extract. JOTCSA. 2025;12(2): 77-84.

DOI: https://doi.org/10.18596/jotcsa.1436181

***Corresponding author's E-mail:** nivethaarun1717@gmail.com

1. INTRODUCTION

The present study aims to evaluate the antidiabetic effect of flowers of *Cassia fistula*. *Cassia fistula* is a small tree or shrub found in many western countries like Indonesia, Vietnam, Thailand, and India. Traditional folk medicine has a long history of utilizing all parts of the *Cassia fistula* plant. Studies have quantitatively evaluated the plant's antioxidant content, which has a direct impact on regulating blood sugar levels. Diabetes, a chronic and serious disease that affects people worldwide, poses a significant risk to the function of major organs such as the heart and kidneys. As a result, it is considered a dangerous illness (2,3). Currently, over 500 million people worldwide are affected by type 1 and type 2 diabetes mellitus. Medications, including insulin, are critical for people with diabetes to survive. The high cost of treatment and the serious nature of the disease have led to a growing awareness of the need for efficient, economical, and safe substitute medications (4).

Researchers have investigated the use of herbs and isolated compounds, such as glucosides, alkaloids, and steroids, to treat different stages of diabetes. Due to its greater accessibility, the focus of research has been on plant-based alternative medicines (5). In vitro and animal tests have been conducted to evaluate the effectiveness of plants and their extracts in regulating blood sugar levels. Given the rising number of people affected by diabetes in recent years, it is essential to explore alternative remedies. Investigating the effectiveness of

medicinal plants known to be useful in many traditional systems of medicine is a promising approach to discovering new antidiabetic drugs (6,7).

To address the critical issue of growing bacteria resistance against conventional antibiotics, it is essential to find novel antimicrobial chemicals or extracts. Biodiversity in plant chemicals is a rich potential resource. The flowers were studied with polar and non-polar solvents like hexane, chloroform, methanol, and ethanol, which exhibit good antibacterial activity, especially for gram-positive bacteria. Hence, the floral part of the *Cassia fistula* can be used for good antimicrobial drug formation (8). The pod of *Cassia fistula* was evaluated for its antidiabetic activity in rats with various concentrations of ethanolic extract, which exhibited a significant lowering of the blood sugar level. It is well recognized that the plant components of *Cassia fistula* constitute a significant source of secondary metabolites, particularly phenolic compounds (9,10). The current investigation examines the various techniques for extracting *Cassia fistula* flowers and assesses the antimicrobial and antidiabetic properties of the resulting active extract.

2. EXPERIMENTAL SECTION

2.1. Materials

Ferric chloride, glacial acetic acid, ammonia, Dragendroff's reagent, ethanol, hydrochloric acid, sulfuric acid, sodium hydroxide, and double distilled water were purchased from SRL chemicals and Merck. All chemicals utilized in the research were of superior quality and high purity, with a minimum purity level of ≥99.0%. The flowers of *Cassia fistula* were collected from Trichy district, India, in May.

2.2. Preparation of Flower Extracts

The fresh flowers of *Cassia fistula* were collected and dried at room temperature. To prepare the extract, the dried flower samples were ground into a fine powder. Each of the four portions of the 200g flower sample was extracted using maceration, digestion, infusion, and decoction methods with 1000 mL of double-distilled water. The methods chosen have been devised to achieve effectiveness in removing a wide range of chemical constituents. These techniques facilitate both heating and heatless extraction that enable the isolation of compounds with varying solubility. The maceration extraction method involved soaking the flower sample (200g) in 1000 mL of double distilled water for 72 hours, with periodic shaking and subsequent filtration for further use. For the digestion method, 200g of the flower sample was mixed with 1000 mL of double distilled water and heated in a water bath at 50C for 30 minutes, followed by filtration of the extract for further studies. The infusion method involved the same solvent-to-sample ratio as the maceration process, with a shorter soaking time of up to 4 hours, followed by filtration. Finally, the decoction method entailed heating 200 g of the flower sample with 1000 mL of double distilled water continuously for 30 minutes, with the concentrated extract then filtered for further analysis. (5,11).

2.3. Phytochemical Screening of Plant Extracts

The qualitative evaluation of phytoconstituents in the four different extracts was carried out using some standard procedures. The most crucial chemical analyses are those that examine the specific physiological advantages of the phytochemicals. Four extracts were examined qualitatively for the presence of such significant phytochemicals as flavonoids, alkaloids, phenolic compounds, tannin, terpenoids, saponin, carbohydrates, and steroids; outcomes were compared (7,12).

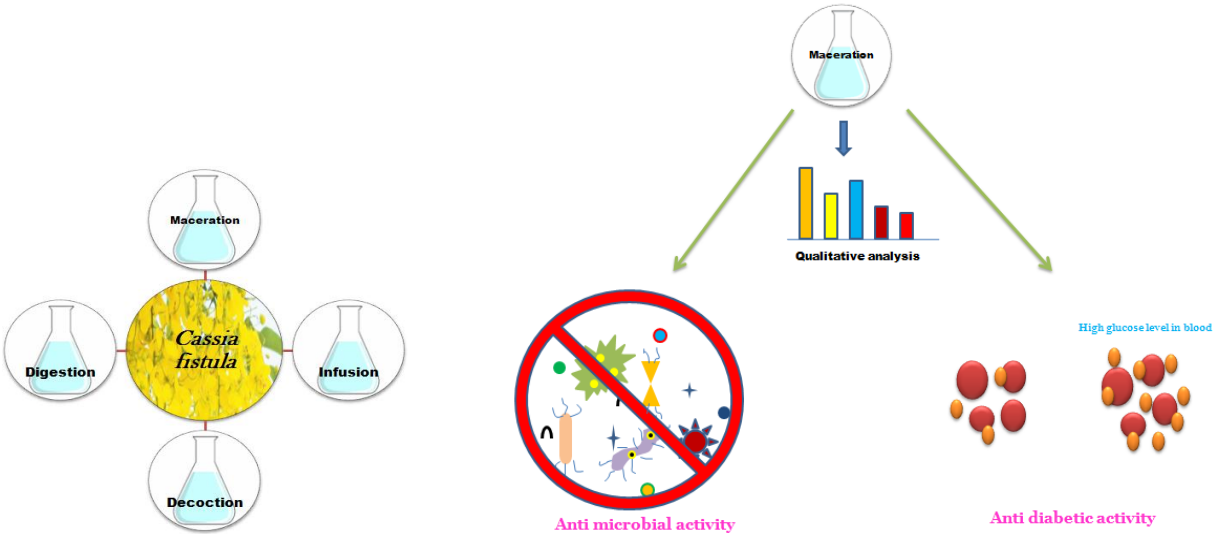

Figure 1: Schematic diagram of antimicrobial and antidiabetic activity of *Cassia fistula*.

2.4. Characterization of Flower Extract

The best outcomes of the phytochemical constituents were selected from the screening, and the extract obtained by the maceration technique was further analyzed. The macerated extract of *Cassia fistula* was subjected to spectral analysis, like UV-Vis and Fourier transform infrared spectroscopy. The aqueous extract of *Cassia fistula* was studied by a

UV-Vis spectrometer (Perkin Elmer, Lambda 35 model) with a wavelength range of 200–800 nm (13,14). The flower extract was subjected to the FTIR spectrometer (Perkin Elmer, range 4000-400 cm^{-1}) for the functional groups (15).

2.5. Antimicrobial Activity of Flower Extract

The agar well diffusion method was used to assess the flower extract's antibacterial and antifungal properties. The microbial test employed bacterial and fungal strains of *Bacillus subtilis, Staphylococcus aureus, Escherichia coli, Pseudomonas aeruginosa, Candida albicans, and Aspergillus niger*. Gentamicin was used as a control for these antimicrobial tests. The strains were subcultured in the nutrient broth, which was prepared just before the test. The nutritional agar medium was prepared, and the petri plates were prepared with wells (16,17). Each well was treated with the flower extract at a different concentration. The inhibition rate was calculated using the diameter of the zone of inhibition formed by the flower extract (18).

2.6. Antidiabetic Activity of Flower Extract

200µL of alpha-amylase solution was mixed with various concentrations of aqueous flower extract (10, 20, 30, 40, and 50 µL) and incubated for 10 mins (19). 200 mL dinitrosalicylic acid reagent was prepared using 12 g of sodium potassium tartrate tetrahydrate in 8.0 mL of 2 M NaOH and 20 mL of 96 mM of 3,5-dinitrosalicyclic acid solution, and the mixture was boiled, cooled and diluted for the absorbance of 540 nm. Acarbose was used as the standard reference. The inhibition rate and IC_{50} values were calculated (20).

3. RESULTS AND DISCUSSION

The occurrence of phytochemicals in the four different extracts was studied. The maceration method of extraction was found to be the most effective, as it is a low-tech technique that requires minimal equipment. This method does not involve heat, which may contribute to the preservation of bioactive compounds. In contrast, the decoction method, which involves continuous heating, is commonly used for extracting compounds from tough plant materials. This method is particularly useful for extracting less soluble compounds. The majority of the phytochemicals were present in all of the extracts since polar solvents were used. In comparison to other extracts, the maceration extraction process produced significantly better results. Some phytochemicals were absent or showed mild occurrence in the digestion and infusion processes, which may be due to the heating process of the plant extract.

Table 1: Phytochemical screening of aqueous flower extract of *Cassia fistula.*

S.No.	Phytochemicals	Extraction method			
		Maceration	Infusion	Digestion	Decoction
1	Flavonoid	+++	++	++	++
2	Alkaloid	+++	+	+	++
3	Phenols	++	-	+	+
4	Tannin	++	-	+	+
5	Terpenoid	++	+	+	+
6	Saponin	-	+	-	+
7	Carbohydrates	+++	++	++	++
8	Steroid	++	++	+	+

(+ : slightly present, ++ : moderately present, +++ : strongly present, - : absent)

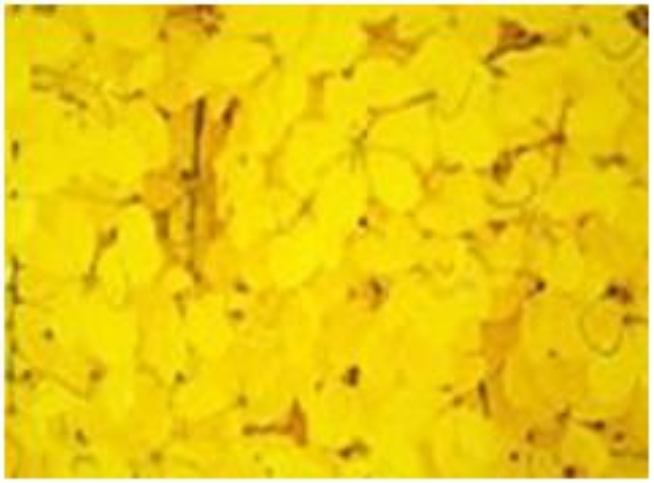

Figure 2: Flower of *Cassia fistula*.

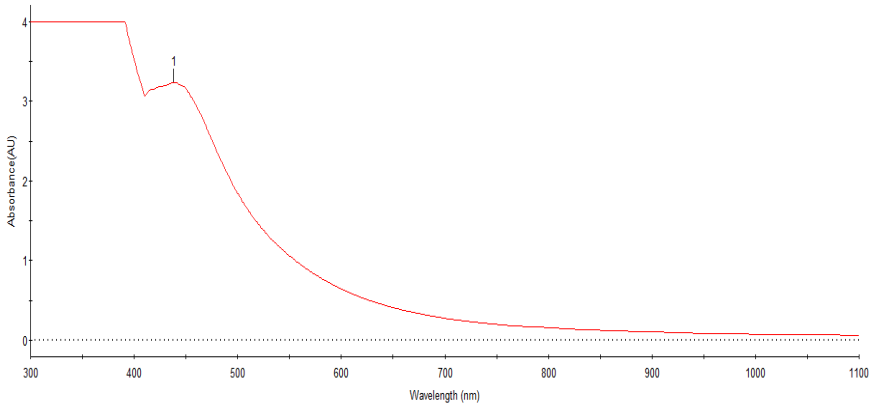

Figure 3: UV-Vis spectrum of flower extract of *Cassia fistula.*

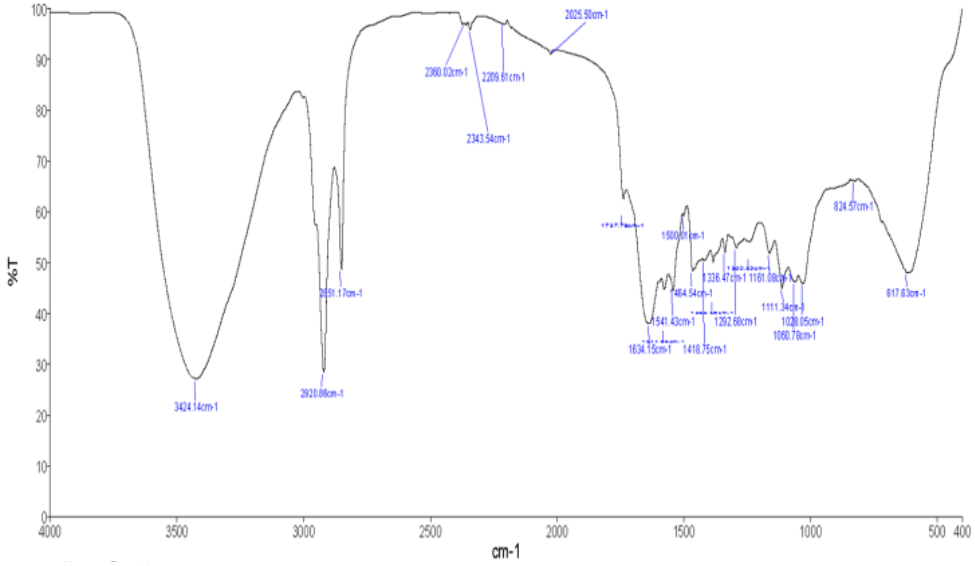

Figure 4: FTIR spectrum of flower extract of *Cassia fistula.*

The extract made using the maceration and decoction methods included significant amounts of flavonoids and phenolic substances. These phytochemicals have antioxidant properties, supporting several therapeutic qualities (7,39). Flavonoids are one of the major antioxidant agents present in most plant species. It is significantly present in maceration and decoction extracts. This plays a vital role in antimicrobial and antidiabetic activity. This secondary metabolite is widely studied for anticancer and anti-inflammatory activity (21,22). Many flavonoids were successfully isolated, and their structures were identified. The polyphenolic compounds and functional groups are responsible for the chelation of metals by scavenging free radicals and acting as the best antioxidant agents (12,36).

All different kinds of extracts contain substantial amounts of tannin. Typically, tannin is found in the tree's bark, protecting it from microbes. As a result, tannins have built-in antibacterial properties. These specific tannins, which were extracted from plant samples, have antiviral and antibacterial properties (7,21,35). Previous studies back up the claim that it slows tumor growth, which has a positive impact on numerous cancer types, like breast and lung cancer. Steroid content in *Cassia fistula* flower extracts is noticeable. These phytosterols are very beneficial for lowering cholesterol and blood sugar. Important phytosterols like stigmasterol and sitosterol have reduced the absorption of cholesterol (23,27,34). The maceration technique-adapted extract had the highest concentration of phytoconstituents of all the extracts. Hence, this extract was used for further antimicrobial and antidiabetic studies. The process of digestion necessitates high temperatures, which may cause the degradation of heat-sensitive compounds, resulting in the loss of biological activity. Furthermore, this extraction method exhibits reduced efficiency in extracting non-polar compounds. The infusion method displays limited extraction efficiency and possesses a brief shelf-life with aqueous extracts, allowing for microbial growth and oxidation. The decoction technique may cause the evaporation of volatile compounds in the extract, which are responsible for numerous medicinal properties. Each of these methods has its unique advantages and disadvantages, and the study assists in selecting the most appropriate extraction procedure for further research based on the specific requirements of biological studies.

The *Cassia fistula* flower extract was subjected to UV-Vis spectroscopy. The spectrum gives the details of σ and π bonds, chromophores, and other lone pairs of electrons (13,28). Hence, this information can help

identify the phytocompounds present in the plant extract. The aqueous extract shows absorption at a wavelength range of 438 nm, which indicates the presence of unsaturated groups (35,40). The peaks formed may be due to the presence of tannin, flavonoids, and carotenoids. This absorption range indicates the π – π* transition in the aromatic ring (24,29).

The FTIR spectrum of the flower extract of *Cassia fistula* is shown in figure 4. The well-defined absorbance peaks indicate the presence of many alkyl and alkane groups, as well as some hydroxyl groups. The absorption peaks at 3424 cm^{-1} and 2920 cm^{-1} indicated stretching of the hydroxyl group and symmetric stretching of saturated compounds in the extract. The peak that appears at 2209 cm^{-1} indicates the alkyne group. The peaks at 1541 and 1292 cm^{-1} may be due to the C=C stretching and C=O stretching (15,30). Hence, this FTIR spectrum proved the presence of phenolic compounds, aromatic compounds, amines, and alkanes in the aqueous extract of *Cassia fistula* flowers.

The aqueous extract of *Cassia fistula* flower was tested at various concentrations (25, 50, 75, and 100 µL) in gram-positive, gram-negative, and fungal strains. The microorganisms chosen for this study were selected based on their clinical relevance, specifically *Staphylococcus aureus* and *Escherichia coli*, which are the most common causes of skin infections and pneumonia, respectively, and are known to exhibit heavy antibiotic-resistant strains. Furthermore, these microorganisms represent a diverse range of organisms, including both gram-negative and gram-positive bacteria, as well as fungal strains, which allows for a broader understanding of the antimicrobial activity of *Cassia fistula* flowers. These microorganisms are ideal for studying antimicrobial resistance mechanisms and can be easily cultivated with well-defined growth requirements. Collectively, the pathogens responsible for a wide range of human diseases are these microorganisms and studying them can provide valuable insights into treatment strategies for various types of infections. The growth of *Staphylococcus aureus* bacteria and *Aspergillus niger* fungi was inhibited better than that of other microorganisms. On increasing the concentration of the flower extract, the zone of inhibition increased. The *Bacillus subtilis* and *Pseudomonas aeruginosa* have less inhibition at 100µl of the extract when compared to other microorganisms. Urinary tract infections caused by *Escherichia coli* can be treated with the *Cassia fistula* flower extract (25,31,33). Hence, the extract can be used as an alternative antimicrobial medicine and for further drug discovery studies. This kind of plant-based alternative medicine has been well appreciated in recent years for its less toxic and more effective antimicrobial behavior. Lethal diseases like pneumonia were caused by *Bacillus subtilis*, which can be treated by the *Cassia fistula* flower extract (17,32,41). Natural antioxidant agents like flavonoids and phenolic compounds may be responsible for the good antimicrobial activity of the *Cassia fistula* extract, which could be a suitable alternative to synthetic medicine.

Table 2: Antimicrobial activity of aqueous extract of *Cassia fistula* flower.

Microorganisms	Concentration of extract and zone of inhibition (mm/mL)				
	25 µL	**50 µL**	**75 µL**	**100 µL**	**Control**
Bacillus subtilis	14	16	19	22	20
Staphylococcus aureus	16	18	21	25	20
E. coli	15	18	20	23	20
Pseudomonas aeruginosa	15	18	20	22	25
Candida albicans	15	18	21	24	23
A. Niger	16	19	22	26	23

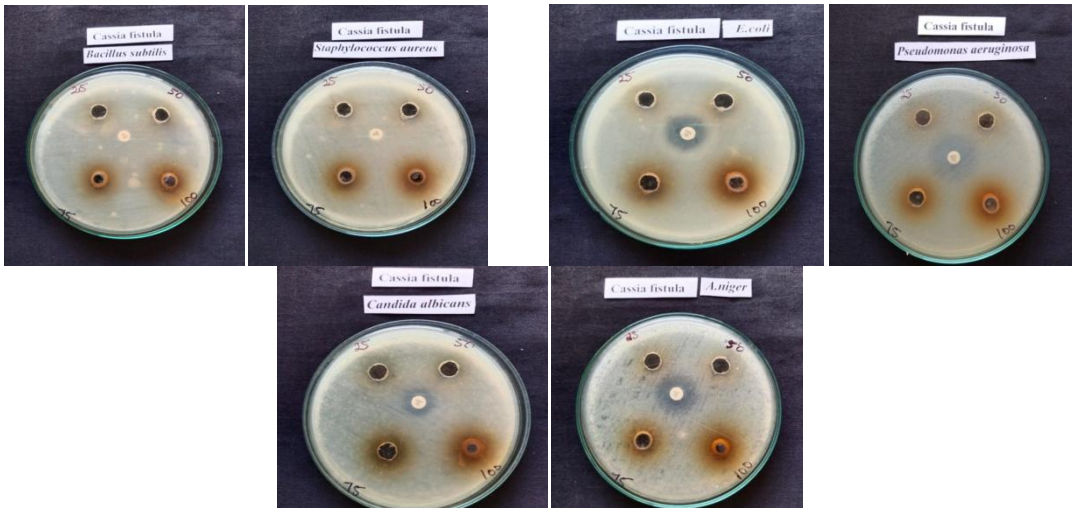

Figure 5: Antimicrobial activity of flower extract of *Cassia fistula.*

Table 3: Antidiabetic activity of aqueous extract of *Cassia fistula* flower.

Volume of the extract (µg/mL)	Absorbance at 540 nm		Percentage inhibition (%)	
	Standard	Extract	Standard	Extract
10	0.215	0.222	7.7253	4.7210
20	0.188	0.208	19.3133	10.7296
30	0.153	0.182	34.3347	21.8884
40	0.129	0.146	44.6351	37.3390
50	0.088	0.107	62.2317	54.0772

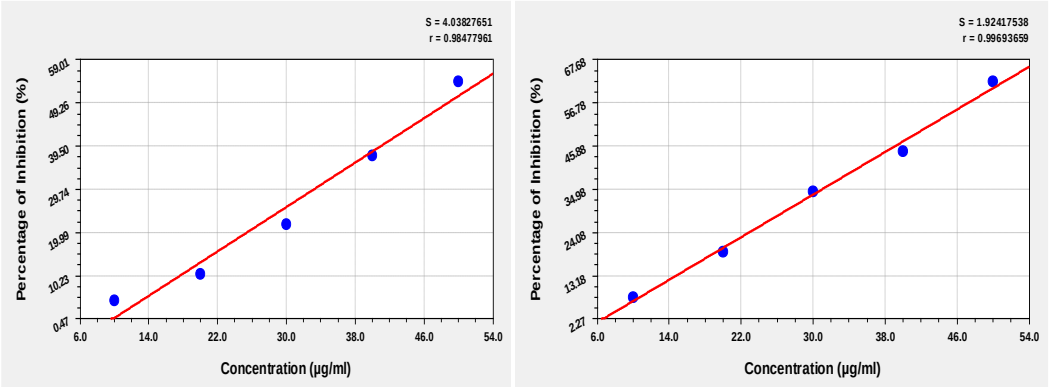

Figure 6: Graph of concentration of flower extract/standard and percentage of inhibition.

Various concentrations of *Cassia fistula* flower extract were evaluated for their antidiabetic activity using the α-amylase enzyme inhibition method. An *in vitro* α-amylase assay was carried out using 10, 20, 30, 40, and 50 µg/mL of *Cassia fistula* flowers and acarbose as a standard drug. The aqueous extract of *Cassia fistula* flower exhibits an inhibitory activity of α-amylase as IC_{50} 49.3494 µg/mL, whereas acarbose exhibits an IC_{50} 42.1726 µg/mL. Maximum inhibition of 54.07% was found at a concentration of 50 µg/mL of extract, which is compared with standard acarbose, which shows 62.23%. The IC_{50} value serves as a crucial parameter for assessing the efficacy of substances in biological functions. The IC_{50} value obtained for *Cassia fistula* extract is considered decent, indicating a high potency to inhibit 50% achievement at a lower concentration. While IC_{50} is a valuable metric, it is only one aspect of an extract's profile. It should be evaluated in conjunction with other factors to assess its therapeutic potential for antidiabetic treatment fully. Therefore, the obtained IC_{50} value for *Cassia fistula* flower is essential for understanding the extract's potency, effectiveness, and potential for development into therapeutic agents. Diabetes can be treated by reducing the production and absorption of glucose in the body. This can be done through the inhibition of enzymes like α-amylase, which helps digest carbohydrates. The results show that a significant amount of flower extract inhibits the a-amylase enzymes; hence, it can be used for the therapeutic approach to diabetes mellitus (37,38). The flowers of *Cassia fistula* could be used as an alternative natural antidiabetic agent as the disease is genetic, and a high number of cases have been recorded in recent years. Future research could focus on isolating and characterizing bioactive compounds from *Cassia fistula* extract and elucidating their mechanism of action. Additionally, optimizing the extraction method and formulating *Cassia fistula* for pharmacological uses could be explored.

4. CONCLUSION

Cassia fistula flower contains a significant source of bioactive compounds. The traditional medicinal system is becoming increasingly apparent as a global concern. Because of its low toxicity and widespread usage of its therapeutic properties, *Cassia fistula* could be one of them. UV and IR characterization of the aqueous extract of *Cassia fistula* flowers was used to predict the absorbance pattern and functional present groups. The antimicrobial activity of the *Cassia fistula* flower extract shows a maximum zone of inhibition against tested microbes, especially against fungi. The findings show that the anti-diabetic activity of the aqueous extract reveals high alpha-amylase inhibitory activity. It can be used as a green medicine for diabetes mellitus. It can be concluded that the aqueous extract of *Cassia fistula* flower can be used as a better alternative for treating diabetes mellitus and is also effective for pathogenic disorders.

5. CONFLICT OF INTEREST

The authors declare that they have no conflict of interest in this work.

6. ACKNOWLEDGMENTS

The authors are thankful to the Holy Cross College management for providing facilities to conduct this research work.

7. REFERENCES

1. Abubakar A, Haque M. Preparation of medicinal plants: Basic extraction and fractionation procedures

for experimental purposes. J Pharm Bioallied Sci [Internet]. 2020 Jan 1;12(1):1–10. Available from: <URL>.

2. Ambadiang MMM, Atontsa BCK, Tankeo SB, Nayim P, Wamba BEN, Bitchagno GTM, et al. Bark extract of *Cassia sieberiana* DC. (Caesalpiniaceae) displayed good antibacterial activity against MDR gram-negative phenotypes in the presence of phenylalanine-arginine β-naphthylamide. BMC Complement Med Ther [Internet]. 2020 Dec 12;20(1):342. Available from: <URL>.

3. Capetti F, Cagliero C, Marengo A, Bicchi C, Rubiolo P, Sgorbini B. Bio-Guided Fractionation Driven by In Vitro α-Amylase Inhibition Assays of Essential Oils Bearing Specialized Metabolites with Potential Hypoglycemic Activity. Plants [Internet]. 2020 Sep 21;9(9):1242. Available from: <URL>.

4. Chinnathambi A, Alharbi SA, Joshi D, V S, Jhanani GK, On-uma R, et al. Synthesis of AgNPs from leaf extract of *Naringi crenulata* and evaluation of its antibacterial activity against multidrug resistant bacteria. Environ Res [Internet]. 2023 Jan 1;216:114455. Available from: <URL>.

5. Daisy P, Saipriya. Biochemical analysis of *Cassia fistula* aqueous extract and phytochemically synthesized gold nanoparticles as hypoglycemic treatment for diabetes mellitus. Int J Nanomedicine [Internet]. 2012 Mar 7;7:1189–202. Available from: <URL>.

6. Dedvisitsakul P, Watla-iad K. Antioxidant activity and antidiabetic activities of Northern Thai indigenous edible plant extracts and their phytochemical constituents. Heliyon [Internet]. 2022 Sep 1;8(9):e10740. Available from: <URL>.

7. Duraipandiyan V, Ignacimuthu S. Antibacterial and antifungal activity of *Cassia fistula* L.: An ethnomedicinal plant. J Ethnopharmacol [Internet]. 2007 Jul 25;112(3):590–4. Available from: <URL>.

8. Grover M, Behl T, Sehgal A, Singh S, Sharma N, Virmani T, et al. In vitro phytochemical screening, cytotoxicity studies of *Curcuma longa* extracts with isolation and characterisation of their isolated compounds. Molecules [Internet]. 2021 Dec 11;26(24):7509. Available from: <URL>.

9. Gutiérrez-Grijalva E, Picos-Salas M, Leyva-López N, Criollo-Mendoza M, Vazquez-Olivo G, Heredia J. Flavonoids and phenolic acids from oregano: Occurrence, biological activity and health benefits. Plants [Internet]. 2017 Dec 26;7(1):2. Available from: <URL>.

10. Hameed B, Ali Q, Hafeez MM, Malik A. Antibacterial and antifungal activity of fruit, seed and root extracts of *Citrullus colocynthis* plant. Biol Clin Sci Res J [Internet]. 2020;2020(1):33. Available from: <URL>.

11. Jain PK, Soni A, Jain P, Bhawsar J. Phytochemical analysis of *Mentha spicata* plant extract using UV-VIS, FTIR and GC/MS technique. AvailableJournal Chem Pharm Res [Internet]. 2016;8(2):1–6. Available from: <URL>.

12. Jangir RN, Jain GC. Evaluation of antidiabetic activity of hydroalcoholic extract of *Cassia fistula* Linn. pod in streptozotocin-induced diabetic Rats. Pharmacogn J [Internet]. 2017 Jul 15;9(5):599–606. Available from: <URL>.

13. Jani DK, Goswami S. Antidiabetic activity of *Cassia angustifolia* Vahl. and *Raphanus sativus* Linn. leaf extracts. J Tradit Complement Med [Internet]. 2020 Mar 1;10(2):124–31. Available from: <URL>.

14. Karpagasundari C, Kulothungan Sjj. Analysis of bioactive compounds in Physalis minima leaves using GC MS, HPLC, UV-VIS and FTIR techniques. J Pharmacogn Phytochem. 2014;3(4):196–201.

15. Kifle ZD, Abdelwuhab M, Melak AD, Genet G, Meseret T, Adugna M. Pharmacological evaluation of medicinal plants with antidiabetic activities in Ethiopia: A review. Metab Open [Internet]. 2022 Mar 1;13:100174. Available from: <URL>.

16. Mechchate H, Es-safi I, Louba A, Alqahtani AS, Nasr FA, Noman OM, et al. In vitro alpha-amylase and alpha-glucosidase inhibitory activity and in vivo antidiabetic activity of *Withania frutescens* L. foliar extract. Molecules [Internet]. 2021 Jan 8;26(2):293. Available from: <URL>.

17. Moteriya P, Padalia H, Chanda S. Characterization, synergistic antibacterial and free radical scavenging efficacy of silver nanoparticles synthesized using *Cassia roxburghii* leaf extract. J Genet Eng Biotechnol [Internet]. 2017 Dec 1;15(2):505–13. Available from: <URL>.

18. Nandhini S, Geethalakshmi S, Selvam S, Radha R, Muthusamy P. Preliminary phytochemical and anti-diabetic activity of *Cassia sophera* Linn. J Pharmacogn Phytochem. 2016;5(1):87–91.

19. Oirere EK, Anusooriya P, Raj CA, Gopalakrishnan VK. Phytochemical analysis of N-hexane leaf extract of *Alpinia purpurata* (Vieill.) K. Schum using Uv-Vis, FTIR and GC-MS. Int J Pharm Pharm Sci [Internet]. 2015;7(8):387–9. Available from: <URL>.

20. Oliveira ESC, Acho LDR, Morales-Gamba RD, do Rosário AS, Barcellos JFM, Lima ES, et al. Hypoglycemic effect of the dry leaf extract of *Myrcia multiflora* in streptozotocin-induced diabetic mice. J Ethnopharmacol [Internet]. 2023 May 10;307:116241. Available from: <URL>.

21. Pham DQ, Pham HT, Han JW, Nguyen TH, Nguyen HT, Nguyen TD, et al. Extracts and metabolites derived from the leaves of *Cassia alata* L. exhibit *in vitro* and *in vivo* antimicrobial activities against fungal and bacterial plant pathogens. Ind Crops Prod [Internet]. 2021 Aug 1;166:113465. Available from: <URL>.

22. Rehana D, Mahendiran D, Kumar RS, Rahiman AK. In vitro antioxidant and antidiabetic activities of zinc oxide nanoparticles synthesized using different plant extracts. Bioprocess Biosyst Eng [Internet]. 2017 Jun 30;40(6):943–57. Available from: <URL>.

23. Paulraj MS, Rajkumar RJ, Thanapaul S. Phytochemicals as a potential source for anti-microbial, anti-oxidant and wound healing - a review. MOJ Bioorganic Org Chem [Internet]. 2018;2(2):61–70. Available from: <URL>.

24. Tanveer S, Latif A, Ashiq K, Qayyum M, Bajwa MA. A comprehensive review on pharmacological and phytochemical potential of *Cassia fistula* Linn: A Magical Herb. IJBPAS [Internet]. 2019;8(6):1134–57. Available from: <URL>.

25. Solikhah TI, Setiawan B, Ismukada R. Antidiabetic Activity of Papaya Leaf Extract (*Carica Papaya* L.) Isolated with Maceration Method in Alloxan-Induces Diabetic Mice. Syst Rev Pharm [Internet]. 2020;11(9):774–8. Available from: <URL>.

26. Stevens-Barrón JC, de la Rosa LA, Wall-Medrano A, Álvarez-Parrilla E, Rodríguez-Ramirez R, Robles-Zepeda RE, et al. Chemical composition and *in vitro* bioaccessibility of antioxidant phytochemicals from selected edible nuts. Nutrients [Internet]. 2019 Sep 27;11(10):2303. Available from: <URL>.

27. Mwalimu RJ, Packirisamy ASB. Phytochemical assessment and evaluation of the anti-oxidant, anti-microbial, anti-cholesterol, and anti-diabetic activities of *Triumphetta Pentandra* methanol based green leaf extract. J Inorg Organomet Polym Mater [Internet]. 2023 Dec 30;33(12):3779–93. Available from: <URL>.

28. Jangid R, Jain S, Sharma MK, Chatterjee S. In vitro antioxidant and antidiabetic activity of ethanolic extract of *Prosopis* species growing in Rajasthan, India. Vegetos [Internet]. 2022 Sep 28;36(1):62–9. Available from: <URL>.

29. Deepthi K, Renjith PK, Shameem K, Habeeb Rahman K, Chandramohanakumar N. Phytochemical screening of leaves and flower extracts of *Sesbania grandiflora* (L.) Pers. and its antimicrobial activity against fish pathogens. Vegetos [Internet]. 2022 Aug 4;36(2):626–33. Available from: <URL>.

30. Shekwa W, Maliehe TS, Masoko P. Antimicrobial, antioxidant and cytotoxic activities of the leaf and stem extracts of *Carissa bispinosa* used for dental health care. BMC Complement Med Ther [Internet]. 2023 Dec 15;23(1):462. Available from: <URL>.

31. Oloya B, Namukobe J, Ssengooba W, Afayoa M, Byamukama R. Phytochemical screening, antimycobacterial activity and acute toxicity of crude extracts of selected medicinal plant species used locally in the treatment of tuberculosis in Uganda. Trop Med Health [Internet]. 2022 Dec 17;50(1):16. Available from: <URL>.

32. KC BM, Gauchan DP, Khanal SN, Lamichhane J. Phytochemical screening, antioxidant and antibacterial activity of bamboo leaf collected from agroecosystem of the Central Siwalik region, Nepal. Vegetos [Internet]. 2023 Nov 28;37(6):2600–6. Available from: <URL>.

33. Sousa BCM de, Gomes D do A, Viana AF da S, Silva BA da, Barata LES, Sartoratto A, et al. Phytochemical analysis and antioxidant activity of ethanolic extracts from different parts of *Dipteryx punctata* (S. F. Blake) amshoff. Appl Sci [Internet]. 2023 Aug 24;13(17):9600. Available from: <URL>.

34. Tavanappanavar AN, Mulla SI, Shekhar Seth C, Bagewadi ZK, Rahamathulla M, Muqtader Ahmed M, et al. Phytochemical analysis, GC–MS profile and determination of antibacterial, antifungal, anti-inflammatory, antioxidant activities of peel and seeds extracts (chloroform and ethyl acetate) of *Tamarindus indica* L. Saudi J Biol Sci [Internet]. 2024 Jan 1;31(1):103878. Available from: <URL>.

35. Kattil A, Hamid, Dash KK, Shams R, Sharma S. Nutritional composition, phytochemical extraction, and pharmacological potential of mulberry: A comprehensive review. Futur Foods [Internet]. 2024 Jun 1;9:100295. Available from: <URL>.

36. Azmat F, Safdar M, Ahmad H, Khan MRJ, Abid J, Naseer MS, et al. Phytochemical profile, nutritional composition of pomegranate peel and peel extract as a potential source of nutraceutical: A comprehensive review. Food Sci Nutr [Internet]. 2024 Feb 8;12(2):661–74. Available from: <URL>.

37. Kasali FM, Kadima JN, Peter EL, Mtewa AG, Ajayi CO, Tusiimire J, et al. Antidiabetic medicinal plants used in Democratic Republic of Congo: A critical review of ethnopharmacology and bioactivity data. Front Pharmacol [Internet]. 2021 Oct 27;12:757090. Available from: <URL>.

38. Shahzad N, Alzahrani AR, Aziz Ibrahim IA, Shahid I, Alanazi IM, Falemban AH, et al. Therapeutic strategy of biological macromolecules based natural bioactive compounds of diabetes mellitus and future perspectives: A systematic review. Heliyon [Internet]. 2024 Jan 30;10(2):e24207. Available from: <URL>.

39. Iglesias-Guevara D, Sánchez-Torres P. Characterization of antifungal properties of avocado leaves and majagua flowers extracts and their potential application to control *Alternaria alternata*. Int J Food Microbiol [Internet]. 2024 Mar 2;413:110579. Available from: <URL>.

40. Chau TP, Devanesan S, Ayub R, Perumal K. Identification and characterization of major bioactive compounds from *Andrographis paniculata* (Burm. f.) extracts showed multi-biomedical applications. Environ Res [Internet]. 2024 Feb 1;242:117763. Available from: <URL>.

41. Oke-Altuntas F, Ipekcioglu S, Sahin Yaglioglu A, Behcet L, Demirtas I. Phytochemical analysis, antiproliferative and antioxidant activities of *Chrozophora tinctoria*: A natural dye plant. Pharm Biol [Internet]. 2017 Jan 5;55(1):966–73. Available from: <URL>.

JOTCSA
Journal of the Turkish Chemical Society Section: A Chemistry
TURKISH CHEMICAL SOCIETY

Evaluation of Different Types of Paracetamol Active Pharmaceutical Ingredients' Effects on the Release System

Sebnem Senol[1*]

[1]Yildiz Technical University, Department of Chemical Engineering, Istanbul, Turkey.

Abstract: The primary purpose of this study was to investigate the effect of active pharmaceutical ingredients (APIs) with varying particle sizes and properties on drug release and to develop matrix-type tablets based on poly(acrylic acid sodium salt) (PAANa) with different gelatin ratios for enhanced paracetamol release. Micronized, superfine, and purified paracetamol APIs were selected as model drugs to assess the impact of these APIs on drug release. Paracetamol is a frequently used medication in healthcare, so it is crucial to select the API with the optimal release rate and an economical, environmentally friendly production method. The direct compression method was employed in the preparation of the tablets due to its simplicity and ease of integration on an industrial scale. The release studies, release kinetics, scanning electron microscope (SEM), Fourier transform infrared spectroscopy (FT-IR), physical properties, and microbial analyses (*Escherichia coli*, total mold, yeast) were investigated. The release studies at pH 1.2 and pH 7.4 revealed that the type of active pharmaceutical ingredient, especially micronized paracetamol API and superfine API, affects the paracetamol release ratio. Microbial analyses showed that produced tablets were convenient for health. In addition, prepared tablets with added gelatine can be used to deliver paracetamol with the desired release profile.

Keywords: Matrix-type tablets, Paracetamol, Release kinetics, Release properties, Antimicrobial properties.

Submitted: December 22, 2024. **Accepted:** March 24, 2025.

Cite this: Senol S. Evaluation of Different Types of Paracetamol Active Pharmaceutical Ingredients' Effects on the Release System. JOTCSA. 2025;12(2): 85-98.

DOI: https://doi.org/10.18596/jotcsa.1605601

***Corresponding author's E-mail:** sebnemsenol_@hotmail.com

1. INTRODUCTION

A controlled drug delivery system involves a wide variety of scientific approaches, which are an important part of science and contribute to healthcare. These scientific approaches enhance efficiency, improve patient compliance, and minimize side effects (1-4). Furthermore, designed drug delivery has been progressing for overwhelming problems, including targeting specific sites and controlling drug release rates (5-7). Some drug release systems have major limitations, including poor *in vitro* release and bioavailability, high doses, and adverse side effects (8,9). However, controlled drug delivery systems have been developed to release APIs in a predictable, desired time, release rate, and quantity (10-15).

Controlled-release drug delivery offers a cost-effective solution for formulations, such as swelling matrix-type tablets, which have been widely used in the pharmaceutical industry (16,17). Matrix-type tablets are useful materials for releasing dosage forms and provide the lowest-cost solution for various applications.

Direct compression is one of the selected tablet preparation methods when mixed powders (active pharmaceutical ingredients, or APIs, and excipients) are compressible and stable under high-pressure conditions (18, 19). Additionally, direct compression is favored due to its simplicity, environmental friendliness, time, and cost-effectiveness, which is the most straightforward route for manufacturing matrix-type tablets, offering advantages such as large-scale and continuous production (20-24).

The addition of the drug to the polymer ingredient is a common method used in drug release (25-28). Hydrophilic polymers and polymer combinations are attractive for controlled-release studies, and these combinations have been used to formulate dosage forms for many years due to their unique features for efficient and specific drug delivery. Different types of polymers are used in release dosage forms. Mucoadhesive polymers are extensively selected in

tablet formulations due to their ability to adhere to the required sites for a prolonged period of time in the prepared formulation. Carbomers, commonly referred to as Carbopols, are weakly cross-linked polymers of acrylic acid with effective mucoadhesive properties, making them attractive for use in release systems. Additionally, Carbopol is a hydrophilic, cross-linked polyacrylic acid polymer with a high molecular weight. Additionally, drug dissolution and diffusion through the polymer are significant phenomena that influence the controlled release properties of the drug formulation. PAA and PAANa are among the materials preferred in many industries due to their properties, including hydrophilicity, non-toxicity, dispersion, and binding capacity (29-31).

Gelatin is a type of natural hydrophilic polymer and non-toxic material derived from the acid or alkaline hydrolysis of collagen, which has a variety of effective advantages, including good biocompatibility, solubility, easy acquisition, and biodegradability (32).

Paracetamol (acetaminophen) is probably the most common, widely available, and important analgesic and antipyretic active pharmaceutical ingredient, commonly used to relieve pain such as headaches, toothaches, and sprains. Furthermore, paracetamol is available in various dosage forms, including tablets, intravenous solutions, suspensions, capsules, and suppositories (29). The direct compression method for the oral solid form of paracetamol is mostly selected (24).

The current work aims at creating a release system through the preparation and characterization of prepared tablets. The effects of gelatine and paracetamol types on *in vitro* release of drugs have also been studied. As a result, different particle sizes, types of APIs, and kinetic models were significant determiners for drug delivery studies. Characterization and microbial analyses were evaluated, and all results were promising for the effective delivery of paracetamol.

2. EXPERIMENTAL SECTION

2.1. Materials

J.T. Baker provided sodium hydroxide (99.0%) and monobasic potassium phosphate. Sodium chloride (≥99.5%) and hydrochloric acid (37.0%) were supplied by Merck. Atabay Pharmaceutical Company kindly provided paracetamol APIs (assay: 100.5-100.7%). Gelatine (microbial grade) was purchased from Carlo Erba. Poly (acrylic acid sodium salt) with an average Molecular Weight of ~2,100 (for R&D usage) was supplied by Sigma Aldrich. Sabouraud 4% Dextrose Digest Agar (SDA) and Tryptic Soy Agar were provided by Merck. All chemical materials used were of analytical grade.

Table 1: API's sieve properties.

	Specification	**Results**	**Method**
Micronized API	325 Mesh (45 µm) =0	0	
Superfine API	80 Mesh (180 µm) = Max. 2	1	
	140 Mesh (106 µm) = Max. 5	3	Air jet sieving
Purified API	80 Mesh (180 µm) = Max 2	1	
	140 Mesh (106 µm) = Max. 5	4	

2.2. Preparation of Matrix Types of Tablets

Gelatine and poly(acrylic acid sodium salt) were prepared using a clean and dry mortar. All the ingredients were weighed accurately, as shown in Table 1, and then mixed thoroughly. API and excipient were completely blended in a mortar. A total of nine formulations were prepared using gelatin and various paracetamol APIs. A direct compression method was employed to prepare paracetamol-loaded tablets. The method used is simple and lacks critical manufacturing and formulation levels, making it easy to standardize for industrial-scale production. A 0.5±0.02 g mixture was manually added to the pellet (tablet) pressing device. A pressure of 160 kPa was applied for 5 minutes to produce tablets. A desiccator was used for storing the prepared tablets until further studies.

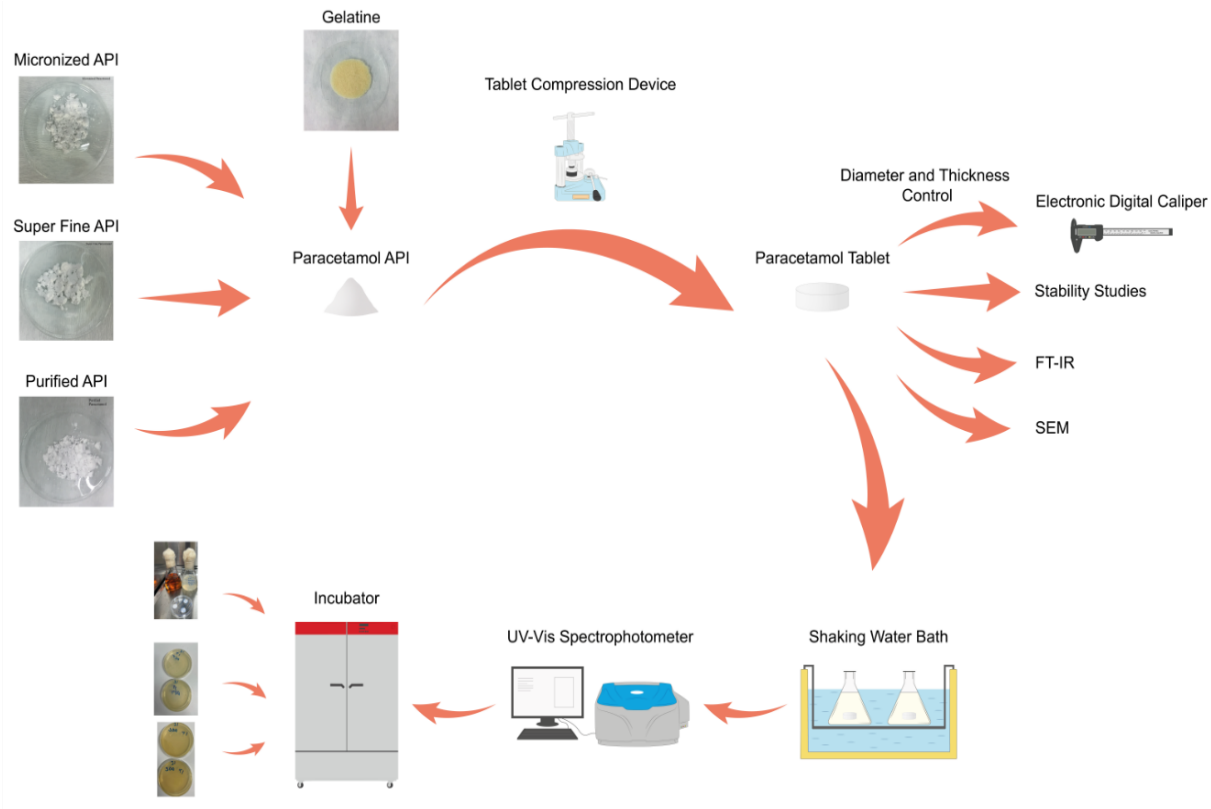

Figure 1: Experimental setup.

2.3. Characterization of The Tablets

A digital caliper was used to measure the diameter and thickness of the tablets (Carbon Fiber Composites Digital Caliper). Fourier Transform Infrared Spectroscopy (FT-IR, PerkinElmer Spectrum 100) was used for the characterization of chemical groups present in the tablets. A spectrum is obtained using the ATR technique with a diamond internal reflection element mounted on a holder, at a resolution of 4 cm-1, in the range of 4000-650 cm-1, with a total of 16 scans for each tablet. SEM photographs were taken with a JEOL JSM 6335F.

2.4. *In vitro* Drug Release of The Tablets

pH 1.2 and pH 6.8 buffer solutions were prepared for *in vitro* drug release tests at 37 ± 0.5 °C and 50 rpm. 50 mL of dissolution medium was used, and 2 mL of the same medium was taken for analysis. The quantity of paracetamol released over time was obtained by withdrawing samples at predetermined time intervals for 4-6 hours. The withdrawn volume was replaced with the same amount of additional buffer. The measurements were performed three times at 270 nm by using a UV-Vis spectrophotometer (Analytik Jena Specord 200/Plus). The reproducibility of this approach is 1 to 3%. A pH 1.2 buffer is prepared according to USP 29. The drug concentrations in the sample were validated using a standard calibration curve. The complete experimental procedures, including details of the buffer solution, were reported previously (3).

2.5. Kinetic Evaluation

First-order, Zero-order, Hixson-Crowell, and Korsmeyer-Peppas kinetic models were studied to examine the kinetic mechanism. The data from the *in vitro* studies were analysed using Korsmeyer-Peppas models to determine the release profile. Korsmeyer and Peppas's empirical equation was used to understand the dissolution mechanisms from the matrix-type tablets (31,33,34).

The equation represents the release of the drug,

$$\text{Korsmeyer – Peppas model: } M / Mt = K_{KP}t \qquad (1)$$

In the equation, M/Mt is the fraction of the drug released at time t, K_{KP} is the drug release rate constant, and n is the diffusional exponent (31,32).

2.6. Stability Studies

Tablets were subjected to stability studies by storing them at 25 ± 2 °C and 65 ± 5% relative humidity for a period of 3 months. At the end of the analysis, the formulation was evaluated for *in vitro* release profile. It was determined from the stability analyses that there were no significant differences in the drug quantity of the tablets. The physical appearance also showed no difference in tablet formulation.

3. RESULTS AND DISCUSSION

3.1. Characterization of the tablets

The produced tablets were characterized with the digital microscope, Fourier Transform Infrared spectroscopy (FT-IR), and Scanning Electron Microscopy (SEM). Figure 2 shows the images of tablets taken with the digital microscope. The diameter and thickness were 2.40 ± 0.05 and 0.20 ± 0.03 cm, respectively.

Table 2: Type of the prepared tablets.

	Content, w/w %				
	Poly(acrylic acid sodium salt)	**Micronized Paracetamol API**	**Superfine Paracetamol API**	**Purified Paracetamol API**	**Gelatine**
Tablet 1 (T1)	90	10	-	-	-
Tablet 2 (T2)	90	-	10	-	-
Tablet 3 (T3)	90	-	-	10	-
Tablet 4 (T4)	85	10	-	-	5
Tablet 5 (T5)	80	10	-	-	10
Tablet 6 (T6)	85	-	10	-	5
Tablet 7 (T7)	80	-	10	-	10
Tablet 8 (T8)	85	-	-	10	5
Tablet 9 (T9)	80	-	-	10	10

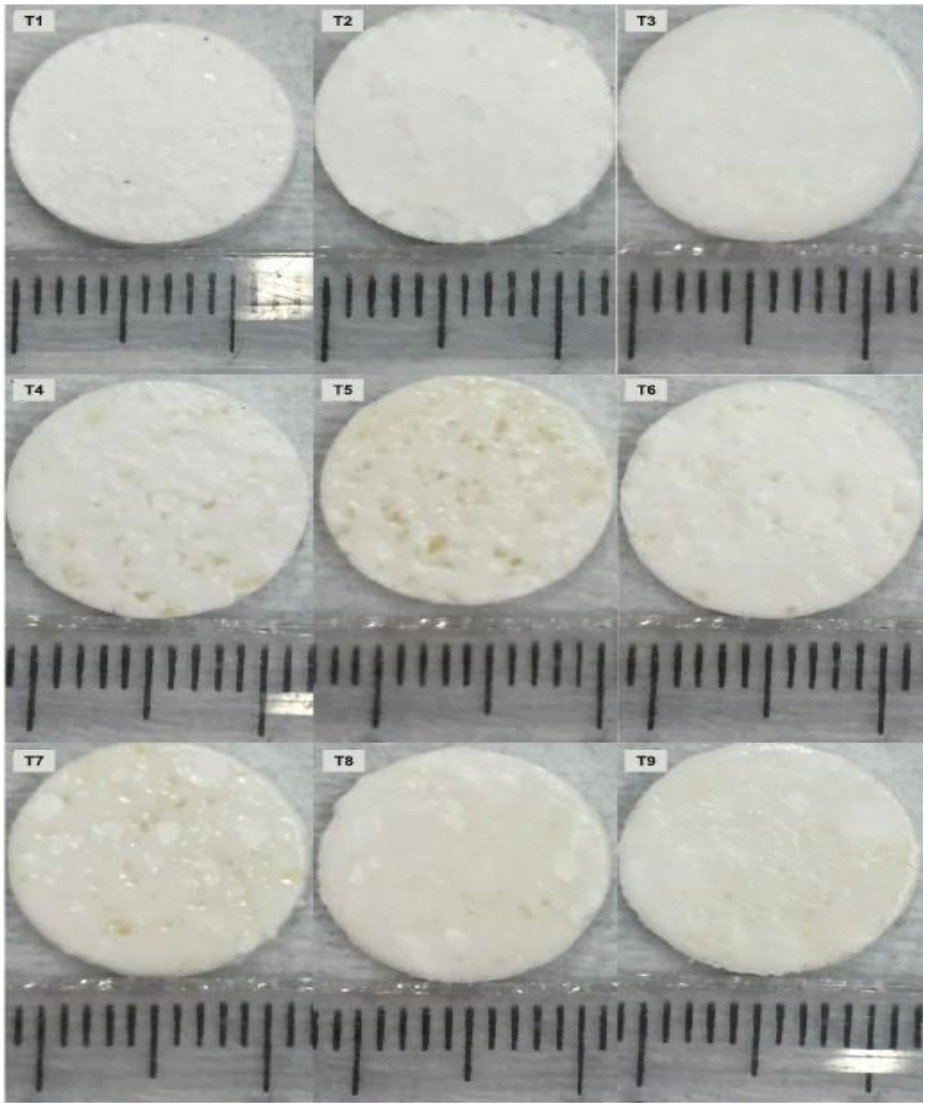

Figure 2: Image of tablets.

FT-IR was applied to determine the intact functional groups of samples. The position of the band in the FT-IR spectra of paracetamol APIs was compared with that in the FT-IR spectra of different types of paracetamol APIs with gelatin. The characteristic peaks of paracetamol were intact in the FT-IR spectrum of different kinds of paracetamol APIs with gelatin used in the formulations. The data showed no changes in the characteristic peaks of the tablet formulations compared to the APIs. When the FT-IR spectrum of PAANa is examined, the peaks related to the asymmetric and symmetric stretching vibrations of the carboxylate group occur at wavenumbers of 1543 cm^{-1} and 1400 cm^{-1} (35). The characteristic

bands around 2940 cm^{-1} and 1107 cm^{-1} can be assigned to the -CH_2 stretching and C-H bending of PaaNa (36). Vibrational peaks for O-H and -CH_3 stretching appeared at 3318 cm^{-1} and 3161 cm^{-1}, respectively. Vibrational peaks at 1649 and 1609 cm^{-1} were assigned to C=O and C=C stretching, respectively, for the paracetamol spectrum (37). The amide II peak was observed at 1547 cm^{-1} in the spectrum of gelatin (38). The N-H amide II bonding, asymmetrical C-H band, and C-C stretching peak appeared at 1562 cm^{-1}, 1503 cm^{-1}, and 1416 cm^{-1} in the spectrum of Paracetamol, respectively (37). The absorption peaks at 1369-1321 cm^{-1} and 1258-1223 cm^{-1} were examined for symmetrical banding C-H and C-N (aryl) stretching. Additionally, absorption peaks at 1171 cm^{-1} and 966 cm^{-1} were assigned to C-O stretching and C-N (amide) stretching, respectively. Vibrational peaks for the para-disubstituted aromatic ring and out-of-plane ring deformation of the phenyl ring were observed at 835 and 671 cm^{-1}, respectively (37).

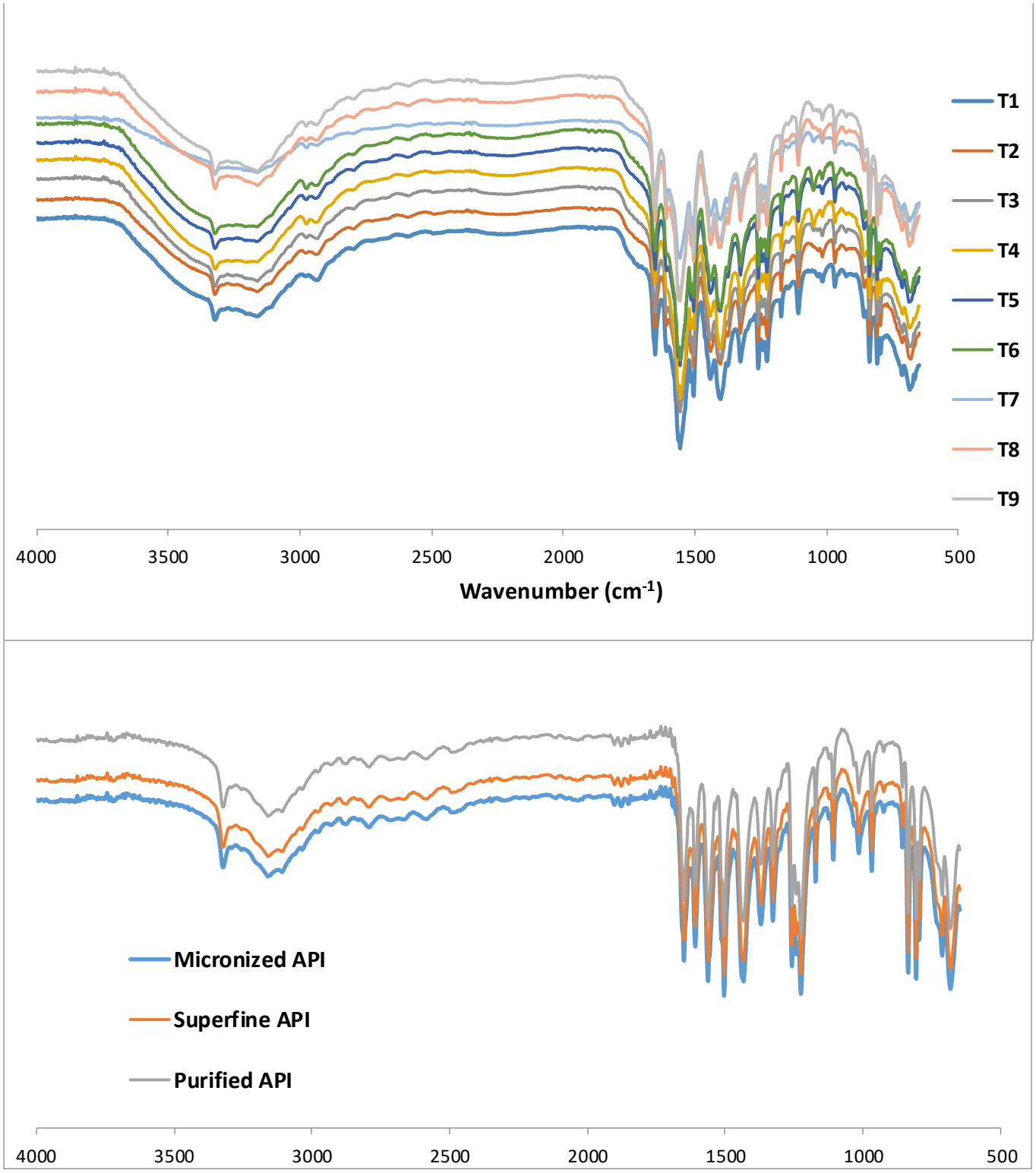

Figure 3: FT-IR analyses of matrix types of tablets and Paracetamol's APIs.

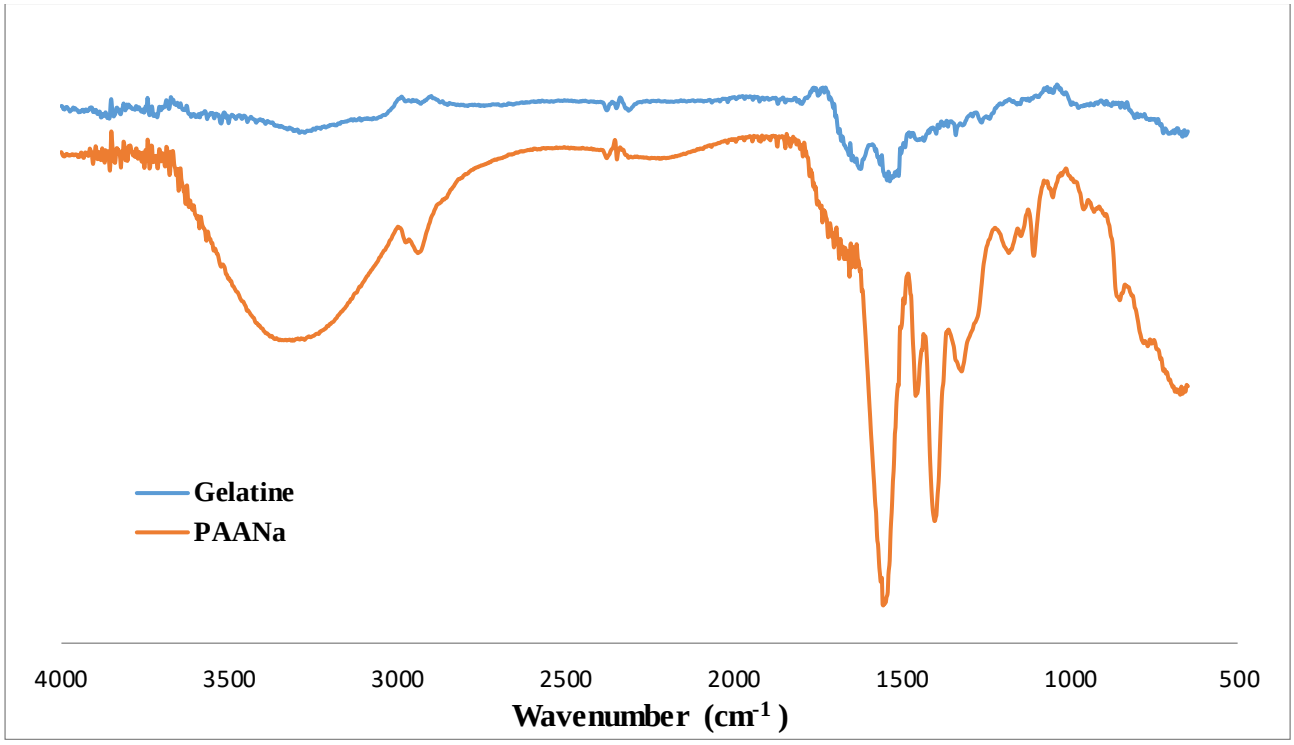

Figure 4: FT-IR analyses of gelatine and PAANa.

3.2. SEM Analysis

A Scanning Electron Microscope (SEM) was used to determine the morphology of the samples. SEM photographs of tablets are given in Fig. 4. T1 (a) and T5 (c) SEM images are powder forms of the tablet before pressing the tablet. T1 (b) and T5 (d) are tablet forms after pressing. T1 tablet has a large, channel-like, and open structure. The presence of gelatine in the T5 tablet exhibits a less porous structure. SEM images demonstrated that the tablet surface became nearer with the addition of gelatine (T5).

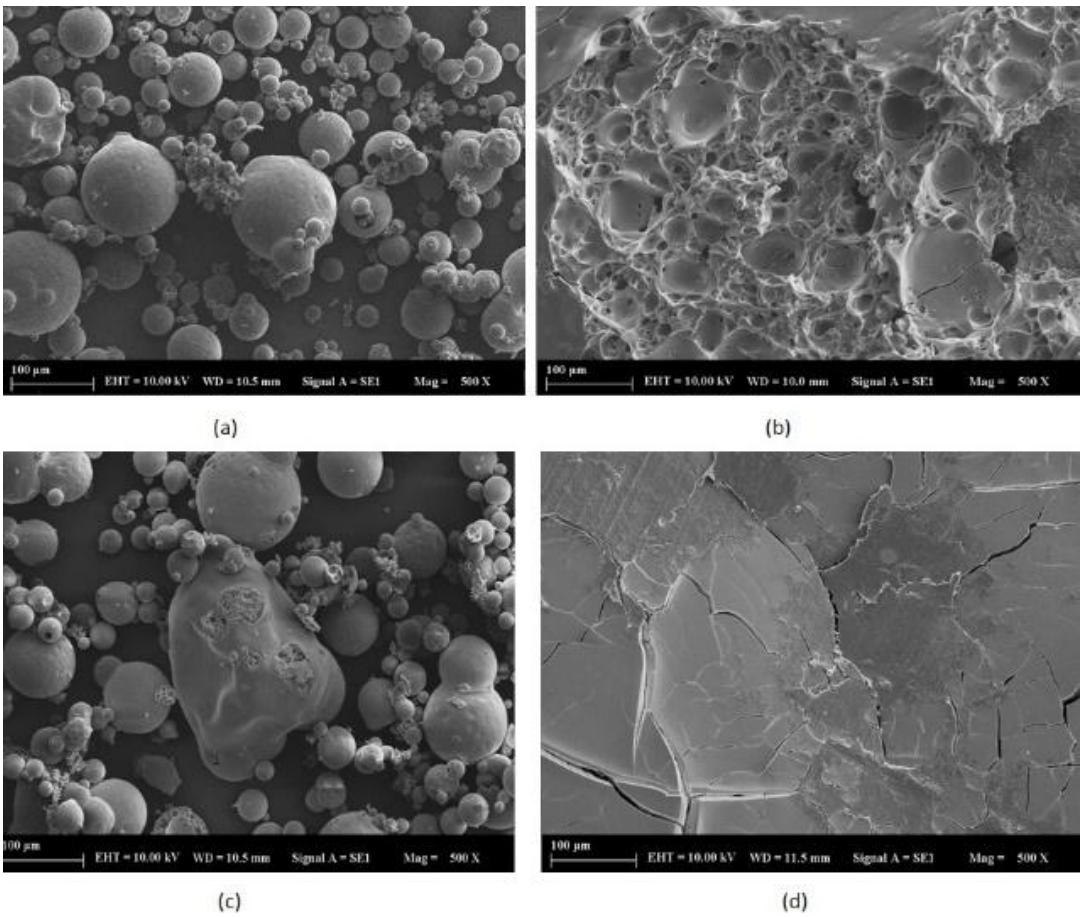

Figure 5: SEM images of tablets (a) T1 powder form before pressing, (b) T1 tablet form, (c) T5 powder form before pressing, (d) T5 tablet form.

3.3. In vitro Drug Release Studies

3.3.1. In pH 1.2 media (simulated gastric fluid)

Figure 6 shows the percent cumulative release of paracetamol at a pH 1.2 medium. Micronized API exhibited a significant effect on release enhancement. Additionally, the T2 tablet with superfine API exhibited high paracetamol release, reaching 94.02%. The *in vitro* drug release data for formulations T1 and T5, containing micronized API, showed a maximum percent cumulative release of paracetamol of 96.72% and 93.39% after 4 hours, respectively (39-41). The addition of gelatine in tablet formulation resulted in a decrease in the amount of drug released. The percentage of paracetamol release of T8 reached 58.78% within 4 h at pH 1.2.

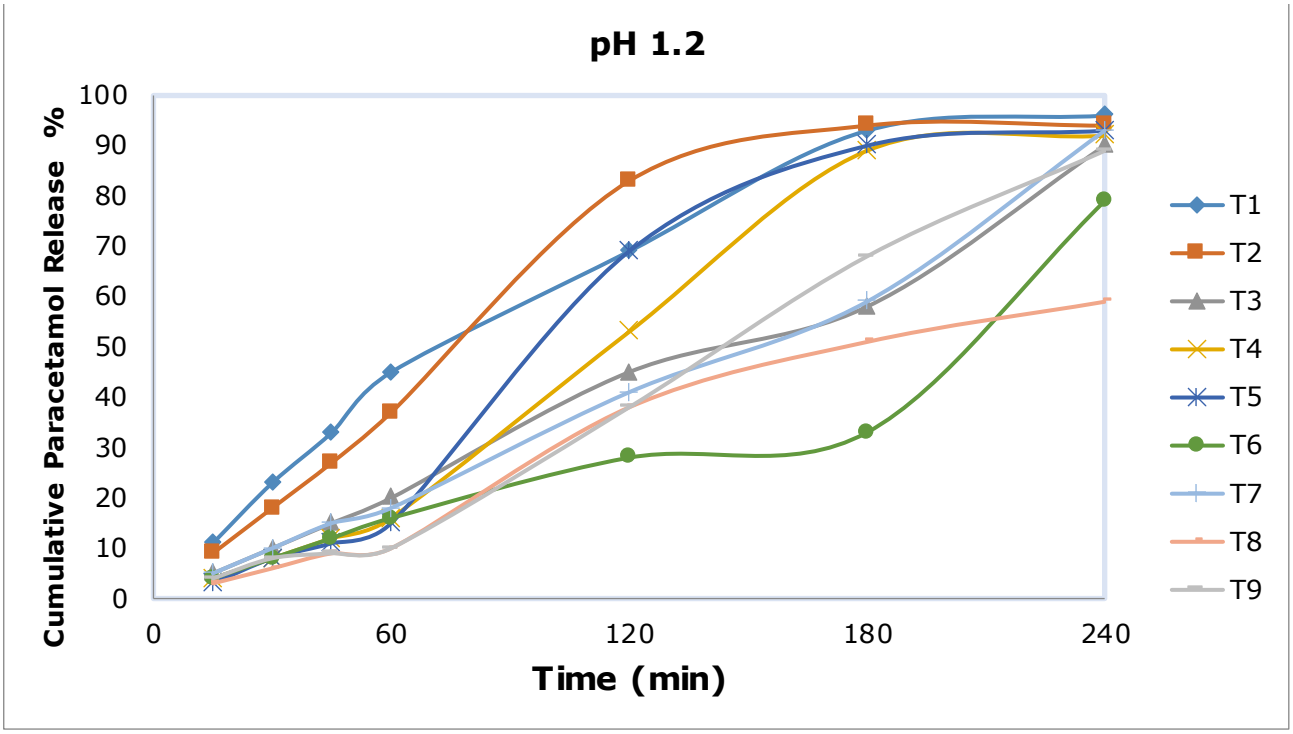

Figure 6: Paracetamol release profiles of matrix tablets at pH 1.2.

3.3.2. In pH 6.8 media (simulated intestinal fluid)
The release of paracetamol from matrix-type tablets was studied for 6 hours in simulated intestinal fluid. The T1 tablet (micronized API) showed 97.03% paracetamol release at the end of 6 hours. T5 and T4 tablets with micronized API showed good performance with 96.40% and 91.54% paracetamol release, respectively. Additionally, the T2 tablet with superfine API showed a percent cumulative release of paracetamol of 91.58%.

T8 exhibited the minimum percent cumulative release of paracetamol with 81.19% in 6 h. The release rate of tablets with gelatine was slower at both pH 1.2 and pH 6.8. Also, as shown in Figs. Results 7 and 8 indicate that the presence of gelatin in tablets causes a lower drug release ability. In general, matrix-type tablets exhibit higher cumulative paracetamol release in a pH 6.8 medium (39,42).

T1 is a tablet containing micronized API, and T4 and T5 are versions of this tablet with added gelatin. T2 is a tablet containing superfine API, while T6 and T7 are tablets with added gelatin. T3 is a tablet containing purified API, and T8 and T9 are tablets with added gelatin. Figure 8 shows the highest release rates of the tablets at pH 1.2 and pH 6.8. In Figure 8, it is observed that tablets with added gelatin have a lower release rate than those without gelatin.

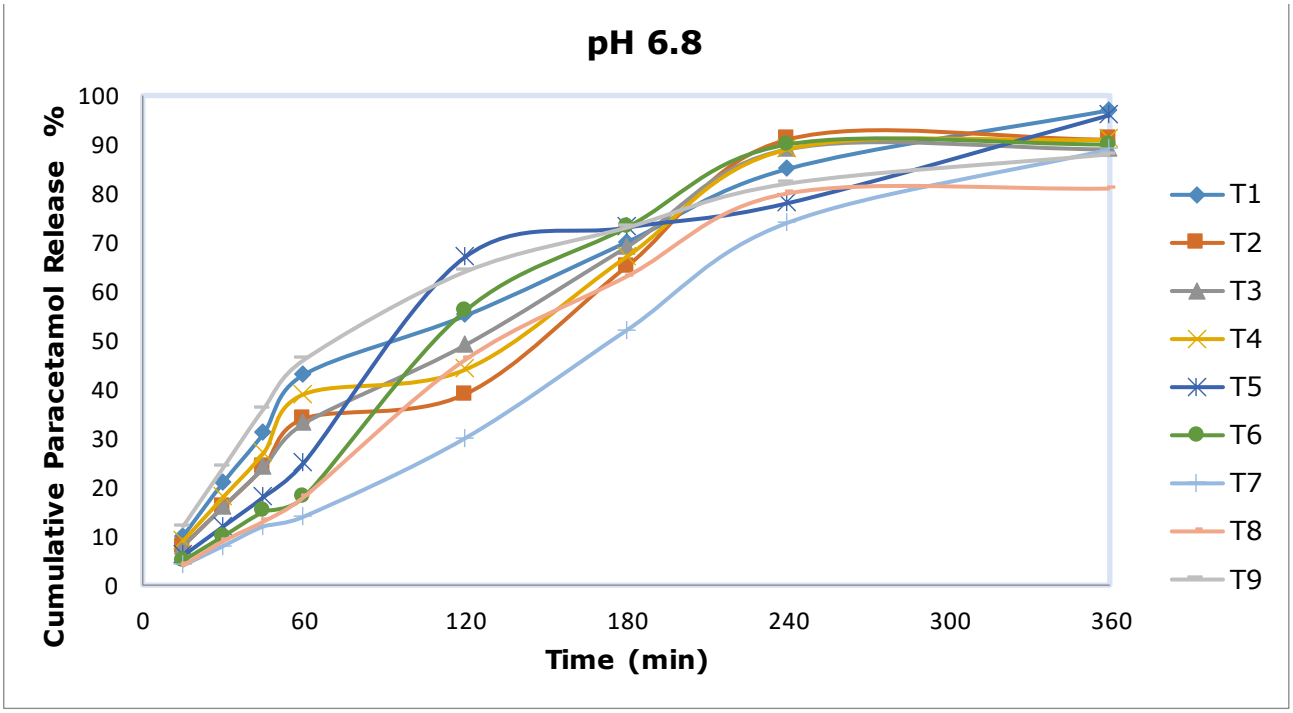

Figure 7: Paracetamol release profiles of matrix tablets at pH 6.8.

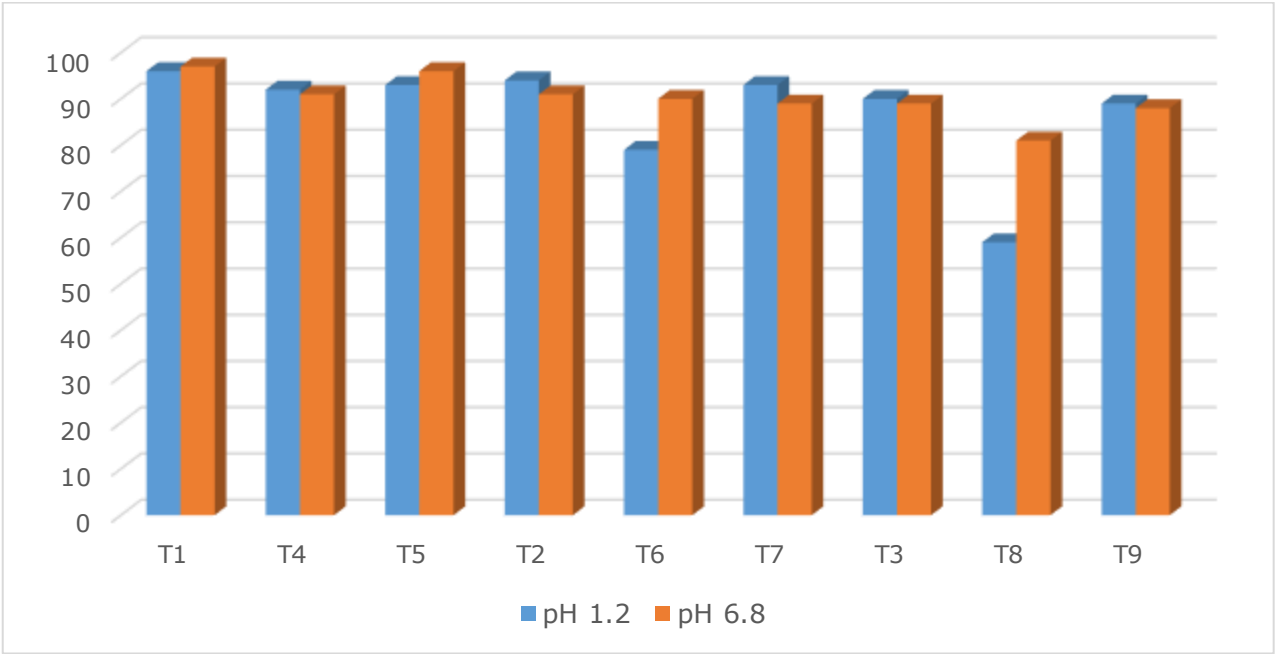

Figure 8: Paracetamol maximum release profiles at pH 1.2 and pH 6.8.

3.4. Microbial Analyses

In this section, microbial analyses were conducted to assess the compatibility of the produced tablets with their health properties. The pour-plate method was used according to the European Pharmacopoeia (EP) 2.6.12 and the United States Pharmacopoeia (USP) 61-62 (43, 44). Microbial analysis procedures consisted of the following steps: 10.0 g of product was weighed, and 100 mL (1/10) of N/Peptone was added. 10 mL of this dilution was taken, and 100 mL (1/100) was completed. 1 mL was poured into two pieces of Tryptic Soy Agar-Sabouraud 4% Dextrose Agar (TSA-SDA) medium. They were incubated at 30 – 35°C for 3-5 days for total aerobic bacteria and incubated at 20-25°C for 5-7 days for molds and yeasts.

For specific microorganism analysis, 10 mL of a 1:10 dilution was added to 90 mL of Tryptic Soy Broth (TSB) medium in a beaker. They were incubated for 18-24 hours at 30-35 °C.

Microbiological contamination limits follow as:
Total aerobic microbial count: Not more than 1,000 colony-forming units (CFU) per gram.
-Total molds and yeast counts: Not more than 100 CFU per gram.
-Pathogens: No *Escherichia coli (E. coli)* per gram.

Table 3 represents the acceptance criteria for the microbiological quality of tablets. The total aerobic microbial count, total mold, and yeast count were found to be less than 100 colony-forming units (CFU). *E. coli* must be absent in oral drugs, and E. coli was not found in the tablets. According to the specifications presented in Table 3, the formulations comply with the required microbiological standards for pharmaceutical preparations. These findings provide strong evidence supporting the quality and safety of the T1–T9 formulations.

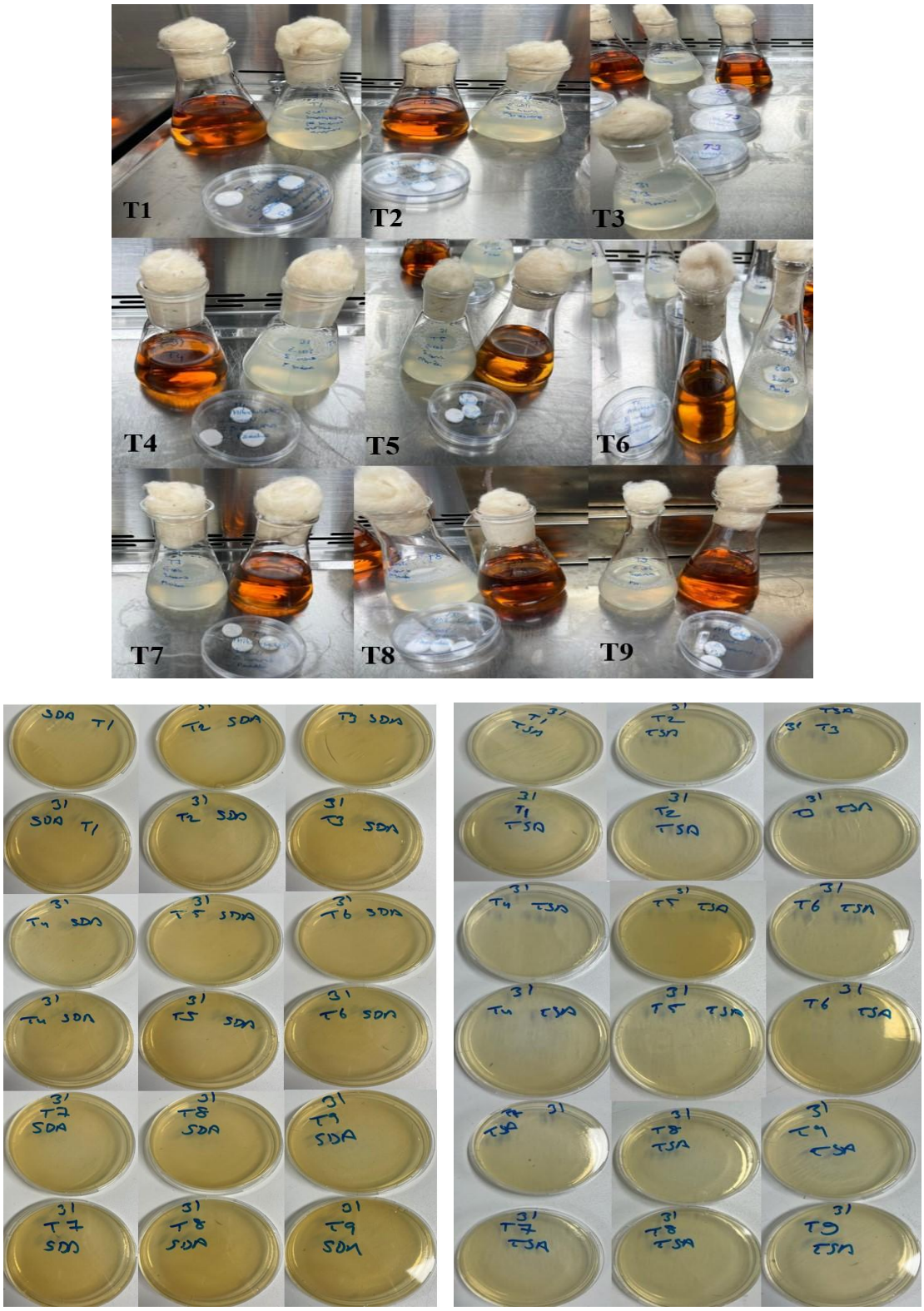

Figure 9: Images of microbial analyses.

Table 3: Microbial limit test results.

	T1-T9
Method	Pour Plate Method
Media	Sabouraud Casein Digest Agar Medium
Incubator temperature and time	32.5 ± 2.5 °C, 5 days
Number of samples	3
Total Aerobic Microbial Count	<1000 CFU / g
	T1-T9
Method	Pour Plate Method
Media	Sabouraud Dextrose Digest Agar Medium
Incubator temperature and time	22.5 ± 2.5 °C, 7 days
Number of samples	3
Total Aerobic Microbial Count	<100 CFU / g
Escherichia coli (*E. coli*)	0 CFU / g

3.5. Paracetamol Release Kinetic Tests

The release data were fitted into the Korsmeyer-Peppas kinetic model to understand the release mechanism. The model with the higher R-squared value is considered optimal for the release data. The kinetic values obtained for different formulations are indicated in Table 4. The release data were investigated using the Korsmeyer-Peppas equation; the n values for the prepared tablet formulations ranged from 0.9470 to 0.9901 in pH 1.2 and pH 6.8 media. It was observed that the drug release data for all formulations fit well to the Korsmeyer-Peppas kinetic model (R^2 values ranged from 0.9470 to 0.9901). Most tablet formulations exhibit a non-Fickian mechanism, as indicated by their n-release exponent values within the range of 0.45 < n <, as shown in Table 4. These values support the notion that the drug release mechanism may be related to polymer relaxation and drug diffusion. Drug release, erosion, and swelling processes can affect the non-Fickian release mechanism. Moreover, non-Fickian release kinetics can facilitate the development of controlled-release formulations that modulate the drug release rate over an extended period. The development of the formulation can also increase patient compliance and treatment efficacy (45-47).

Table 4: Release kinetic studies of tablets.

	pH	**Zero order**		**First order**		**Hixson-Crowell**		**Peppas**		**Best Fit Model**
		R^2	K_0 [mg / h] $*10^{-4}$	R^2	K_1 [h^{-1}]	R^2	K_s	R^2	n	
T1	1.2	0.8061	7.720	0.6583	1.4583	0.7222	0.0138	**0.9667**	0.6228	Korsmeyer-Peppas
	6.8	0.9219	7.345	0.7098	1.5815	0.7978	0.0137	**0.9669**	0.6073	
T2	1.2	0.6950	7.995	0.6241	1.6187	0.6615	0.0151	**0.9652**	0.7683	
	6.8	0.9110	7.695	0.7644	1.8652	0.8383	0.0152	**0.9698**	0.6768	
T3	1.2	0.9232	8.270	0.7891	2.3233	0.8589	0.018	**0.9901**	0.8523	
	6.8	0.9007	7.540	0.2914	1.7789	0.8135	0.015	**0.9851**	0.6882	
T4	1.2	0.8376	9.135	0.7463	2.4958	0.7939	0.0201	**0.9753**	0.9886	
	6.8	0.9071	7.370	0.7360	1.7268	0.8144	0.0143	**0.9685**	0.6374	
T5	1.2	0.7974	9.275	0.7024	2.5732	0.7511	0.0207	**0.9629**	1.0642	
	6.8	0.8787	8.160	0.7230	2.075	0.7884	0.0170	**0.9798**	0.8140	
T6	1.2	0.9045	7.114	0.8388	2.6196	0.8982	0.0173	**0.9632**	0.8331	
	6.8	0.8765	8.49	0.753	2.3011	0.8096	0.0184	**0.9779**	0.8846	
T7	1.2	0.9283	8.635	0.8118	2.3638	0.8771	0.0185	**0.9789**	0.8618	
	6.8	0.9768	7.955	0.8491	2.6292	0.9195	0.0187	**0.9789**	0.8864	
T8	1.2	0.8554	5.690	0.7476	2.8178	0.7965	0.0166	**0.9663**	0.9268	
	6.8	0.8994	7.580	0.2782	2.3366	0.8219	0.0178	**0.9880**	0.8974	
T9	1.2	0.9047	8.790	0.8173	2.7221	0.8608	0.0204	**0.9470**	0.9692	
	6.8	0.8382	6.320	0.6476	1.4076	0.7211	0.0118	**0.9513**	0.5411	

4. CONCLUSION

A direct compression method was successfully applied to prepare the matrix-type tablet. According to experimental data, a greater quantity of the drug was released from the tablet as the environmental pH increased. The results of *the in vitro drug release study revealed that the type of gelatin and APIs,*

especially micronized active pharmaceutical ingredients, played a crucial role in enhancing drug release. Gelatine decreased the release ratio of paracetamol in both media. It was indicated that the release of paracetamol was slower in formulation T8, which contained gelatin with purified paracetamol. Additionally, the T1 tablet exhibited the maximum percent cumulative release of paracetamol in both pH 1.2 and pH 6.8 media. The present study demonstrated that matrix-type tablets with added gelatin can be formulated for the controlled delivery of paracetamol, achieving the desired release profile *in vitro*. Microbial analyses showed that produced tablets were suitable for health. From this perspective, the current study and its results were promising for paracetamol drug delivery. However, it should be taken into consideration that in vivo studies are required to determine whether the prepared and chosen formulation(s) will be accurate.

5. CONFLICT OF INTEREST

The author of the manuscript declares no conflicts of interest.

6. ACKNOWLEDGMENTS

The author is also thankful to Assoc. Prof. Dr. Emel Akyol and Merve Gülter Ak for their kind support. This research did not receive any specific grant from funding agencies in the public, commercial, or not-for-profit sectors.

7. REFERENCES

1. Nowaczyk G, Kempka M, Wereszczyńska B, Flak D, Gapiński J. Viscoelasticity, morphology, and molecular diffusion in structurally controlled ternary poly(acrylic acid) and nonionic surfactant-based hydrogels. Polym Test [Internet]. 2024 Aug 1;137:108505. Available from: <URL>.

2. AL-Fawares O, Alshweiat A, Abuawad A. Development of chitosan-polyacrylic acid complex systems for enhanced oral delivery of *Lactobacillus gasseri* and *Bifidobacterium bifidum* probiotics. Drug Des Devel Ther [Internet]. 2025 Jan 25;Volume 19:585–98. Available from: <URL>.

3. Senol S, Akyol E. Synthesis and characterization of hydrogels based on poly(2-hydroxyethyl methacrylate) for drug delivery under UV irradiation. J Mater Sci [Internet]. 2018 Nov 20;53(21):14953–63. Available from: <URL>.

4. Eslami H, Ansari M, Darvishi A, Pisheh HR, Shami M, Kazemi F. Polyacrylic acid: A biocompatible and biodegradable polymer for controlled drug delivery. Polym Sci Ser A [Internet]. 2023 Dec 25;65(6):702–13. Available from: <URL>.

5. Walker J, Albert J, Liang D, Sun J, Schutzman R, Kumar R, et al. In vitro degradation and erosion behavior of commercial PLGAs used for controlled drug delivery. Drug Deliv Transl Res [Internet]. 2023 Jan 7;13(1):237–51. Available from: <URL>.

6. Guan Y, Yu C, Zang Z, Wan X, Naeem A, Zhang R, et al. Chitosan/xanthan gum-based (Hydroxypropyl methylcellulose-co-2-Acrylamido-2-methylpropane sulfonic acid) interpenetrating hydrogels for controlled release of amorphous solid dispersion of bioactive constituents of *Pueraria lobatae*. Int J Biol Macromol [Internet]. 2023 Jan 1;224:380–95. Available from: <URL>.

7. Kriangkrai W, Puttipipatkhachorn S, Sriamornsak P, Sungthongjeen S. Design and evaluation of new gel-based floating matrix tablets utilizing the sublimation technique for gastroretentive drug delivery. Gels [Internet]. 2024 Sep 9;10(9):581. Available from: <URL>.

8. Lee YJ, Kim JE. In vitro–In vivo correlation of tianeptine sodium sustained-release dual-layer tablets. Molecules [Internet]. 2022 Apr 29;27(9):2828. Available from: <URL>.

9. Senol S, Akyol E. Preparation and characterization of pH-sensitive hydrogels from photo-crosslinked poly(ethylene glycol) diacrylate incorporating titanium dioxide. Mater Sci [Internet]. 2020 Sep 1;38(3):443–9. Available from: <URL>.

10. Heng PWS. Controlled release drug delivery systems. Pharm Dev Technol [Internet]. 2018 Oct 21;23(9):833. Available from: <URL>.

11. Nanda A, Das S, Sahoo R, Nandi S, Swain R, Pattanaik S, et al. Aspirin-hydrogel ocular film for topical delivery and ophthalmic anti-inflammation. J Serbian Chem Soc [Internet]. 2022 Apr 28;87(7–8):829–43. Available from: <URL>.

12. Şenol Ş, Akyol E. Preparation of photopolymerizable HEMA/PEG-DA based hydrogels filled with low concentrations of nanoparticle titanium dioxide for release of donepezil HCl. El-Cezeri Fen ve Mühendislik Derg [Internet]. 2021 May 4;8(2):887–96. Available from: <URL>.

13. Zhang A, Jung K, Li A, Liu J, Boyer C. Recent advances in stimuli-responsive polymer systems for remotely controlled drug release. Prog Polym Sci [Internet]. 2019 Dec 1;99:101164. Available from: <URL>.

14. Layek B. A comprehensive review of xanthan gum-based oral drug delivery systems. Int J Mol Sci [Internet]. 2024 Sep 21;25(18):10143. Available from: <URL>.

15. Lee JH, Yeo Y. Controlled drug release from pharmaceutical nanocarriers. Chem Eng Sci [Internet]. 2015 Mar 24;125:75–84. Available from: <URL>.

16. Abou-Yousef H, Dacrory S, Hasanin M, Saber E, Kamel S. Biocompatible hydrogel based on aldehyde-functionalized cellulose and chitosan for potential control drug release. Sustain Chem Pharm [Internet]. 2021 Jun 1;21:100419. Available from: <URL>.

17. Siamidi A, Konstantinou A, Pavlou P, Siamidis I, Vlachou M. Modified release of acetaminophen from matrix tablet formulations: Influence of tablet

geometry. Lett Drug Des Discov [Internet]. 2024 Mar 20;21(3):568–74. Available from: <URL>.

18. Sanchez-Ballester NM, Bataille B, Soulairol I. Sodium alginate and alginic acid as pharmaceutical excipients for tablet formulation: Structure-function relationship. Carbohydr Polym [Internet]. 2021 Oct 15;270:118399. Available from: <URL>.

19. Anwar S, Zafar F, Yasmin R, Ali H, Jabeen S, Tahir Y. Formulation development of mouth dissolving lornoxicam tablets by direct compression method. Lat Am J Pharm [Internet]. 2024;43(9):1925–34. Available from: <URL>.

20. Pourmadadi M, Tajiki A, Abdouss M, Beig Mohammadi A, Kharaba Z, Rahdar A, et al. Novel carbon quantum dots incorporated polyacrylic acid/polyethylene glycol pH-sensitive nanoplatform for drug delivery. Inorg Chem Commun [Internet]. 2024 Jan 1;159:111814. Available from: <URL>.

21. Barimani S, Šibanc R, Tomaževič D, Meier R, Kleinebudde P. 100% visual inspection of tablets produced with continuous direct compression and coating. Int J Pharm [Internet]. 2022 Feb 25;614:121465. Available from: <URL>.

22. Khan A, Khan A, Nazir S, Khan NR, Ullah M, Shahbaz N, et al. An evaluation of the effect of aging on the quality attributes of orodispersible tablets prepared by the direct compression technique. Drug Dev Ind Pharm [Internet]. 2025 Apr 3;51(4):309–18. Available from: <URL>.

23. Kokott M, Lura A, Breitkreutz J, Wiedey R. Evaluation of two novel co-processed excipients for direct compression of orodispersible tablets and mini-tablets. Eur J Pharm Biopharm [Internet]. 2021 Nov 1;168:122–30. Available from: <URL>.

24. Piponski M, Bakovska Stoimenova T, Topkoska M, Stefov S, Piponska M, Trendovska Serafimovska G. Development and validation of a fast and simple RP-HPLC method for the determination of diosmin and hesperidin in combined tablet dosage form. Maced J Chem Chem Eng [Internet]. 2018 Nov 7;37(2):127–34. Available from: <URL>.

25. Langer R, Peppas N. Chemical and physical structure of polymers as carriers for controlled release of bioactive agents: A review. J Macromol Sci Part C [Internet]. 1983 Jan 19;23(1):61–126. Available from: <URL>.

26. Şenol Ş, Akyol E. Study on the preparation and drug release property of modified PEG-DA based hydrogels. J Turkish Chem Soc Sect A Chem [Internet]. 2019 May 15;6(1):1–14. Available from: <URL>.

27. Langer R. Invited review polymeric delivery systems for controlled drug release. Chem Eng Commun [Internet]. 1980 Jan 30;6(1–3):1–48. Available from: <URL>.

28. van der Merwe J, Steenekamp J, Steyn D, Hamman J. The role of functional excipients in solid oral dosage forms to overcome poor drug dissolution and bioavailability. Pharmaceutics [Internet]. 2020 Apr 25;12(5):393. Available from: <URL>.

29. Ambarish S, Shirsand S, Anandkumar Y, Shirsand S. To study the effect of HPMC and carbopol in mucoadhesive buccal tablets of meclizine hydrochloride using central composite design: In-vitro characterization. Ger J Pharm Biomater [Internet]. 2024;3(1):3–18. Available from: <URL>.

30. Al-Dubai ASAE, Akyol E. Polyacrylic acid and polyacrylic acid sodium salt as ınhibitors of calcium oxalate crystal formation. Bulg Chem Commun [Internet]. 2023;55(3):278–82. Available from: <URL>.

31. Lin HR, Sung K. Carbopol/pluronic phase change solutions for ophthalmic drug delivery. J Control Release [Internet]. 2000 Dec 3;69(3):379–88. Available from: <URL>.

32. Rashid TU, Sharmeen S, Biswas S, Ahmed T, Mallik AK, Shahruzzaman M, et al. Gelatin-based hydrogels. In: Cellulose-Based Superabsorbent Hydrogels [Internet]. Springer Cham; 2018. p. 1–41. Available from: <URL>.

33. Paarakh MP, Jose PA, Setty C, Peter Christoper GV. Release kinetics – concepts and applications. Int J Pharm Res Technol [Internet]. 2019 Jan 1;8(1):12–20. Available from: <URL>.

34. Korsmeyer RW, Gurny R, Doelker E, Buri P, Peppas NA. Mechanisms of solute release from porous hydrophilic polymers. Int J Pharm [Internet]. 1983 May 1;15(1):25–35. Available from: <URL>.

35. Liu J, Ran Q, Miao C, Zhou D. Synthesis and characterization of comb-like copolymer dispersant with methoxy poly (Ethylene oxide) side chains. Polym Plast Technol Eng [Internet]. 2011 Jan 6;50(1):59–66. Available from: <URL>.

36. Prabhakar R, Kumar D. Investigation on poly(acrylate-co-acrylamide)/polyaniline conducting hydrogel. Am J Polym Sci Eng [Internet]. 2014;3:201400534. Available from: <URL>.

37. Trivedi M, Patil S, Shettigar H, Bairwa K, Jana S. Effect of biofield treatment on spectral properties of paracetamol and piroxicam. Chem Sci J [Internet]. 2015;6(3):3. Available from: <URL>.

38. Jain D, Carvalho E, Banthia AK, Banerjee R. Development of polyvinyl alcohol–gelatin membranes for antibiotic delivery in the eye. Drug Dev Ind Pharm [Internet]. 2011 Feb 12;37(2):167–77. Available from: <URL>.

39. Obeidat WM, Nokhodchi A, Alkhatib H. Evaluation of matrix tablets based on Eudragit®E100/Carbopol®971P combinations for controlled release and improved compaction properties of water soluble model drug paracetamol. AAPS PharmSciTech [Internet]. 2015 Oct 28;16(5):1169–79. Available from: <URL>.

40. Didacus Nnamani N, Okhuelegbe Eraga S. Evaluation of the compression properties of co-

processed paracetamol, gelatin and microcrystalline cellulose formulation prepared via melt-in agglomeration. Trends Pharm Sci [Internet]. 2022 Dec 1;8(4):243–52. Available from: <URL>.

41. Tarawneh OA, Madi AM, Hamed R, Qirem R, Qerem W, Alhusban A, et al. In vitro characterization and evaluation of commercialized paracetamol products in Jordan. Dissolution Technol [Internet]. 2019;26(1):36–44. Available from: <URL>.

42. Jain V, Singh R. Design and characterization of colon-specific drug delivery system containing paracetamol microsponges. Arch Pharm Res [Internet]. 2011 May 9;34(5):733–40. Available from: <URL>.

43. United States Pharmacopeia (USP) <61>, Microbiological examination of non-sterile products & microbial enumeration tests & USP <62>, Microbiological examination of non-sterile products: Tests for specified microorganisms, (United States Pharmacopeial Convention. 2016; Available from: <URL>.

44. European Pharmacopeia (EP) <2.6.12> Microbiological examination of non-sterile products: Microbial enumeration tests, (European Directorate for the Quality of Medicines and Healthcare). 2017; Available from: <URL>.

45. Mutlu H, Akyol E. Development of transdermal cellulose-based patches for Alzheimer's treatment and investigation of penetration behavior. Bulg Chem Commun [Internet]. 2024;56(3):342–7. Available from: <URL>.

46. Rezk AI, Obiweluozor FO, Choukrani G, Park CH, Kim CS. Drug release and kinetic models of anticancer drug (BTZ) from a pH-responsive alginate polydopamine hydrogel: Towards cancer chemotherapy. Int J Biol Macromol [Internet]. 2019 Dec 1;141:388–400. Available from: <URL>.

47. Senol S, Akyol E. In-vitro evaluation of co-excipients for release of donepezil hydrochloride from Carbopol 974P based tablets. Rev Roum Chim [Internet]. 2022 Oct 23;67(10–12):515–23. Available from: <URL>.

JOTCS A
Journal of the Turkish Chemical Society
Section: A
Chemistry

TURKISH CHEMICAL SOCIETY

Essential Oil from Lime Peel (*Citrus aurantifolia*) Grown in Long an Province, Vietnam: Chemical Composition and Biological Activities

Le Pham Tan Quoc[1*], Lam Bach Bao Phuong[1]

[1]Institute of Biotechnology and Food Technology, Industrial University of Ho Chi Minh City, Ho Chi Minh City, 700000, Vietnam.

Abstract: The present study evaluated *Citrus aurantifolia* essential oil (CaEO) from lime peel grown in Long An province, Vietnam. Gas chromatography–mass spectrometry analysis identified six bioactive compounds, of which D-limonene (69.99%), β-Pinene (10.28%), and α-Pinene (13.08%) were the most abundant. Physicochemical properties, including relative density (0.9295), absolute density (0.9267 g/mL), acid value (0.5481 mg KOH/g), ester value (0.3123 mg KOH/g), and saponification value (0.8604 mg KOH/g), were determined. The antioxidant activity was evaluated using DPPH and ABTS assays, with IC_{50} values of 13.99 ± 1.84 and 1.52 ± 0.09 mg/mL, respectively, indicating significant free radical scavenging potential. The antibacterial effect against *Staphylococcus aureus* (S. aureus), *Bacillus subtilis* (B. subtilis), *Escherichia coli* (E. coli), and *Salmonella enteritidis* (S. enteritidis) was confirmed using the disk diffusion method. The inhibition zones were minimal (approximately 8 mm). In addition, CaEO exhibited a long-lasting aroma, making it suitable for industrial applications. These findings highlight the potential application of CaEO in food preservation, pharmaceuticals, and cosmetics, providing a sustainable approach to utilizing lime peel waste.

Keywords: Antioxidant activity, Antibacterial activity, *Citrus aurantifolia*, Essential oil.

Submitted: January 20, 2025. **Accepted:** March 26, 2025.

Cite this: Quoc LPT, Phuong LBB. Essential Oil from Lime Peel (*Citrus aurantifolia*) Grown in Long an Province, Vietnam: Chemical Composition and Biological Activities. JOTCSA. 2025;12(2): 99-106.

DOI: https://doi.org/10.18596/jotcsa.1623631

***Corresponding author's E-mail:** lephamtanquoc@iuh.edu.vn

1. INTRODUCTION

Lime (*Citrus aurantifolia*) is one of the most widely grown citrus fruits in Vietnam, thriving in the tropical and subtropical climates of the region. The major lime-growing areas include Dong Thap, Tien Giang, and Ben Tre, which are known for their fertile soil and favorable climatic conditions (1).

Lime essential oil (CaEO), primarily extracted from the peel, is a valuable by-product rich in bioactive compounds such as D-limonene, β-pinene, and citral, which exhibit antibacterial, antioxidant, and antifungal properties (2). However, these properties depend on many factors, especially the extraction method. The extraction method significantly influences the yield and composition of essential oils. Jiang et al. (2011) reported that steam distillation, reflux extraction, and ultrasound-assisted extraction yielded at 0.16%, 2.18%, and 2.34%, respectively (3). Among these, D-limonene was the predominant component, accounting for 25.5% of the total composition, which plays a crucial role in the oil's bioactivity. Mohammed et al. (2014) also demonstrated that CaEO exhibits antibacterial activity against *P. aeruginosa*, *S. aureus*, *B. subtilis*, and *E. coli* with inhibition zones ranging from 12 to 16 mm (4). Furthermore, CaEO exhibits strong antioxidant potential, with $IC_{50\text{-}DPPH}$=3.03 ± 0.019 mg/mL and $IC_{50\text{-}ABTS}$=4.27 ± 0.023 mg/mL, reinforcing its potential applications in various industries (5).

Due to these bioactive properties, CaEO is highly suitable for applications in food preservation, cosmetics, and pharmaceuticals (6). Despite being a popular refreshing beverage, particularly in Vietnam's hot climate, lime peels are frequently thrown away, raising environmental concerns. Utilizing these peels for essential oil extraction not only minimizes waste but also contributes to local development by creating value-added products from agricultural by-products (7).

Recent studies have further highlighted the antimicrobial and preservative properties of CaEO.

For example, Freche et al. (2022) demonstrated that CaEO effectively inhibits microbial growth, thereby extending the shelf life of food products (8). These findings underscore the need to characterize CaEO from different regions to optimize its applications. However, no studies have specifically investigated the physicochemical properties, chemical composition, and bioactive properties of CaEO derived from Long An. Given the unique soil and climate conditions of this region, an in-depth study on the biological properties of CaEO from Long An is essential for fully exploiting its potential in the food, pharmaceutical, and cosmetic industries.

To address this gap, the present study aims to analyze the chemical composition and biological properties of CaEO extracted from limes grown in Long An. This research not only provides new insights into the value of CaEO but also promotes the utilization of lime by-products, contributing to sustainable development in the citrus industry.

2. MATERIALS AND METHODS

2.1. Plant Extraction

CaEO was extracted from the peel of *Citrus aurantifolia*, a lime variety grown and harvested in Long An province, Vietnam (Coordinates: 10°25′21″N, 106°28′45″E). The essential oil extraction was according to the procedure described by Long et al. (2023) (9). After being processed into powder and juice, the peel essential oil (EO) was obtained by steam distillation at 100 °C for 3 h. The extraction efficiency of EO in this process was about 0.5% (w/w). The EO obtained after extraction was stored in dark glass bottles at room temperature to maintain its quality and long-term effectiveness.

2.2. Bacterials Strains

In this study, four bacterial strains were used: two Gram-positive bacteria, *S. aureus* (ATCC 33591) and *B. cereus* (ATCC 11778); and two Gram-negative bacteria, *E. coli* (ATCC 25922) and *S. enteritidis* (ATCC 13072). These bacterial strains were provided by the Institute of Biotechnology and Food Technology, Industrial University of Ho Chi Minh City.

2.3. Chemicals

The chemicals used in the study included 2,2-diphenyl-1-picrylhydrazyl (DPPH, ≥97%, Sigma, USA), 2,2'-azinobis (3-ethylbenzothiazoline-6-sulfonic acid) (ABTS, ≥98%, Sigma, USA), and dimethyl sulfoxide (DMSO, ≥99.5%, China). Also, the media used for growing cultures and testing antibacterial properties, like Mueller–Hinton agar and nutrient broth from HiMedia in India, along with other chemicals, were of analytical grade.

2.4. Evaluation of The Physicochemical Properties of CaEO

According to ISO 279 (1998) (10), the relative density (RD) was determined by the proportion of the mass of a given volume of the EO to the mass of an equal volume of distilled water at 20 °C, while the absolute density (AD) was determined by the proportion of the mass of a given volume of the EO to the same volume. In addition, the freezing point (FP) was determined following ISO 1041 (1973) (11), 5 mL of the obtained CaEO was added to the test tube, which was then placed into a freezing container. The temperature of the freezing container was gradually lowered until the EO appeared to crystallize. The FP was recorded at that moment.

The acid value (AV) was determined according to the procedure of ISO 1242 (2023) (12). The obtained CaEO (1 g) was dissolved in 5 mL of 96% ethanol, and a few drops of 1% phenolphthalein were added to the mixture. The KOH solution (0.1 M) was used to titrate this mixture until it turned pink. The AV was calculated using the equation below:

$$\mathrm{AV} = \frac{\mathrm{V_{KOH}} \times 0.1 \times 56.1}{\text{Mass of essential oil}} \quad (12)$$

For the determination of the saponification value (SV), 2 g of EO and 25 mL of the ethanol solution of KOH (0.5 M) were mixed in a glass flask (250 mL). The mixture was then heated for 60 min in the condenser system. Subsequently, 25 mL of distilled water and a few drops of 1% phenolphthalein were added to the mixture. The HCl solution (0.5 M) was used to titrate this mixture until it turned colorless (13). The SV was calculated using the following formula:

$$\mathrm{SV} = \frac{(\mathrm{V_{Blank}} - \mathrm{V_{Sample)}} \times 0.5 \times 56.1}{\text{Mass of essential oil}} \quad (13)$$

The difference between SV and AV represents the ester value (EV):

$$\mathrm{EV} = \mathrm{SV} - \mathrm{AV} \quad (14)$$

2.5. Fragrance Retention (FR) of CaEO

The fragrance retention (FR) of the EO was determined based on the concentration and FR duration following the methods described by Mahajan (2022) with minor modifications (14). The EO was diluted in 96% ethanol to 20%, 40%, 60%, 80%, and 100% (v/v). The three drops of solution were applied to a scent test paper and left to distribute evenly. The time until the scent fully disappeared under normal conditions was recorded to evaluate fragrance retention.

2.6. Gas Chromatography–Mass Spectrometry (GC-MS) Analysis

The chemical composition of CaEO was analyzed using gas chromatography–mass spectrometry (GC-MS). An aliquot of 1 µL CaEO was injected into the instrument (Agilent Technology 5977E MSD) using an autosampler and an Agilent 7890A GC system. Analysis was performed using a Carbowax 20MTM column (30 m × 0.25 mm × 0.25 µm) and helium carrier gas at a constant flow rate of 10 mL/min, with a split ratio of 10:1. The injection rate was set to 250°C. The individual heating program was as follows: hold at 50 °C for 2 min, increase to 250 °C at a rate of 10 °C/min, hold at this temperature for

5 min, increase to 280 °C, and hold for 3 min. Mass spectra were recorded in electron ionization (EI) mode at an energy of 70 eV.

2.7. Determination of The 2,2-diphenyl-1-picrylhydrazyl (DPPH) Antioxidant Activity of CaEO

The antioxidant capacity of CaEO was evaluated by the free radical scavenging activity (RSA) using the DPPH method, following the procedure described by Quyen and Quoc (2024), with minor modifications (15). The EO was dissolved in ethanol (96%) to create different concentrations. Then, 0.3 mL of EO solution was mixed with 2.7 mL of 0.1 mM DPPH solution and left to rest at room temperature in the dark for 30 min. The color loss of DPPH was measured using a Thermo Scientific™ Genesys™ 20 Visible Spectrophotometer (USA) at 517 nm. Vitamin C was used as a control. The percentage of inhibition was calculated based on the CaEO concentration to estimate the 50% inhibitory concentration (IC_{50}). The antioxidant capacity (AC) was calculated using the following formula:

$$\%\mathrm{DPPH}_{\mathrm{RSC}} = \frac{\mathrm{A}_{\mathrm{control}} - \mathrm{A}_{\mathrm{sample}}}{\mathrm{A}_{\mathrm{control}}} \times 100 \quad (15)$$

where $\mathrm{A}_{\mathrm{control}}$ is the absorbance of the DPPH solution; and $\mathrm{A}_{\mathrm{sample}}$ is the absorbance of CaEO solution in the presence of DPPH solution.

2.8. Determination of Antioxidant Activity in CaEO Using ABTS

The experiments were performed based on the method described by Biskup et al. (2013) with minor modifications (16). The ABTS solution was standardized by dissolving 7 mM ABTS and 2.45 mM potassium persulphate in stored water. This service was mixed in a 1:1 ratio and reacted in the dark at room temperature for 16 h to form ABTS radicals (ABTS radical cation). After 16 h, the ABTS solution was diluted with stored water until an absorbance of 0.70 ± 0.02 was obtained at 734 nm. Then, 0.1 mL of EO solution was prepared at various concentrations and mixed with 3 mL of ABTS solution. The solution was adjusted to a final volume of 5 mL using ethanol and then kept in the dark at room temperature for 6 min. After this period, the absorbance was measured at 734 nm. The percentage of inhibition was determined based on the CaEO concentration, and the IC_{50} value (the concentration required to achieve 50% inhibition) was subsequently calculated. The antioxidant capacity (AC) was calculated using the following formula:

$$\%\mathrm{ABTS}_{\mathrm{RSC}} = \frac{\mathrm{A}_{\mathrm{control}} - \mathrm{A}_{\mathrm{sample}}}{\mathrm{A}_{\mathrm{control}}} \times 100 \quad (16)$$

where $\mathrm{A}_{\mathrm{control}}$ is the absorbance of the ABTS solution; and $\mathrm{A}_{\mathrm{sample}}$ is the absorbance of CaEO solution in the presence of ABTS solution.

2.9. Determination of The Antibacterial Activity (AA) of CaEO

The antibacterial activity (AA) was determined using the paper disk diffusion method based on the method described by Carović-Stanko et al. (2010) with some modifications (17). First, 100 µL of bacterial suspension (0.5 McFarland standard concentration, equivalent to approximately 1.5×10^8 CFU/mL) was evenly spread onto Mueller–Hinton agar (MHA) medium using an inoculating loop. Sterile paper disks (6 mm in diameter) were inoculated with 5 µL of the EO and then they were placed on MHA medium surface, while gentamicin (10 µg/disc) and 5% (v/v) dimethyl sulfoxide (DMSO) solution were used as positive and negative controls, respectively. The plates were incubated at 37°C for 24 h. The antibacterial activity was evaluated by measuring the diameter of the inhibition zone around the paper disk.

2.10. Data Analysis

Analysis of variance (ANOVA) and comparison of means were performed using Statgraphics Centurion 20 (StatPoint Technologies, Inc.) software, with a 95% confidence level ($p \leq 0.05$) determined using the least significant difference (HSD) method. The results are shown as the mean ± standard deviation.

3. RESULTS AND DISCUSSION

3.1. Determination of Physicochemical Properties of CaEO

The physicochemical properties of CaEO are summarized in Table 1. The CaEO was a pale yellow, transparent liquid with a characteristic aroma and slight flame. The physicochemical parameters of CaEO were measured as follows: pH value, 3.47; RD, 0.9295 ± 0.0021; AD, 0.9267 ± 0.0021 g/mL; AV, 0.5481 ± 0.0211 mg KOH/g; SV, 0.8604 ± 0.0095 mg KOH/g; and EV, 0.3123 ± 0.0084 mg KOH/g. These characteristics indicate that CaEO belongs to the group of light EOs, is rich in terpenes, and has a very low free acid content. Ester compounds also account for a negligible proportion (18).

Compared to the Algerian CaEO, the pH value was 6.0, which was much higher than the pH of 3.47 for CaEO in this study. In terms of RD, the Algerian EO had a mass of only 0.894 g/mL, which was lower than the 0.9267 g/mL observed for CaEO. The AV value of the Algerian EO reached 2.10 mg KOH/g, which was higher than the 0.5481 mg KOH/g observed for CaEO (19). Also, a different study on CaEO (*Citrus aurantifolia*) from Nigeria found an SV value of 130.37 mg KOH/g, which is much higher than the 0.8604 mg KOH/g found for CaEO in this study. These differences may be caused by differences in chemical composition, plant origin, and environmental conditions.

CaEO stands out for its outstanding ability to retain fragrance. The FR duration ranged from 5.75 (with 20% EO) to 57.21 hours (pure EO). This characteristic makes CaEO a priority choice in the fragrance and cosmetic industries, where the ability to retain a long-lasting scent plays an important role.

Moreover, compared to other EOs in the same group, CaEO has shown advantages in terms of stability, pleasant scent, and versatility, making it suitable for many applications.

Table 1: Physicochemical properties of *Citrus aurantifolia*.

No.	Physicochemical properties	Value
1	pH	3.47 ± 0.12
2	Freezing point (FP, °C)	< −18°C
3	Relative density (RD)	0.9295 ± 0.0021
4	Absolute density (AD, g/mL)	0.9267 ± 0.0021
5	Acid value (AV, mg KOH/g EO)	0.5481 ± 0.0211
6	Saponification value (SV, mg KOH/g EO)	0.8604 ± 0.0095
7	Ester value (EV, mg KOH/g EO)	0.3123 ± 0.0084
8	Fragrance retention (FR, h):	
	20% EO	5.75 ± 0.47
	40% EO	18.66 ± 0.98
	60% EO	29.76 ± 1.45
	80% EO	41.12 ± 2.61
	100% EO	57.21 ± 3.27

3.2. Chemical Composition of CaEO

GC-MS detected 6 main components in CaEO (Table 2). The analysis indicated that CaEO was mainly comprised of monoterpene hydrocarbons. The main component was D-Limonene (69.99%), a monoterpene ring with a characteristic citrus scent. Similar to previous studies, such as Miller et al. (2011), this ratio ranged between 60 and 75% (21). They play an important role in antibacterial, anti-inflammatory, and antioxidant properties and are widely used in the food and pharmaceutical industries. The second most abundant component was α-Pinene (13.08%), followed by β-Pinene (10.28%), which are monoterpenes with high antibacterial and anti-inflammatory properties commonly found in EOs derived from the Rutaceae family (22). The α-Pinene and β-Pinene content in this lime peel EO sample was superior to that of some CaEOs from the Mediterranean region, which typically range from 5 to 10% (23). The Sabinene (3.63%) and α-Myrcene (2.00%) contents in the sample were also consistent with other studies, contributing to the complex aroma and anti-relaxant properties (24). Although present in low proportions, γ-Terpinene (1.02%) plays a significant role in the antioxidant activity of EO (25).

Table 2: Chemical composition of *Citrus aurantifolia* essential oil.

No.	Compounds	Molecular formula	RT (min)	Content (%)
1	α-Pinene	$C_{10}H_{16}$	3.27	13.08
2	β-Pinene	$C_{10}H_{16}$	3.92	10.28
3	Sabinene	$C_{10}H_{16}$	4.00	3.63
4	α-Myrcene	$C_{10}H_{16}$	4.25	2.00
5	D-Limonene	$C_{10}H_{16}$	4.60	69.99
6	γ-Terpinene	$C_{10}H_{16}$	4.94	1.02

3.3. Determination of The Antioxidant Activity

Table 3 shows that the antioxidant activity of CaEO was significantly lower than that of vitamin C when determined using both the DPPH and ABTS methods. Specifically, with the DPPH method, the IC_{50} of CaEO was 13.99 mg/mL, while that of vitamin C was only 6.04 µg/mL, indicating a significant difference. Similarly, using the ABTS method, the IC_{50} of CaEO was 1.52 mg/mL, whereas vitamin C exhibited a much lower value of 3.12 µg/mL, confirming its superior antioxidant activity compared to CaEO.

When compared to other studies, the $IC_{50\text{-DPPH}}$ value of CaEO in this study (13.99 mg/mL) was higher than that of Algerian CaEO (7.41 mg/mL) (26), indicating lower antioxidant activity. However, the $IC_{50\text{-ABTS}}$ of our CaEO (1.52 mg/mL) was significantly lower than that of Algerian CaEO (53.6 mg/mL) (26), suggesting a higher ABTS inhibitory ability. Additionally, CaEO from Tunisia also exhibited a lower $IC_{50\text{-DPPH}}$ value of 4.1 mg/mL (27), suggesting it had a stronger DPPH scavenging ability than that of CaEO in this study. Differences in antioxidant activity could be attributed to variations in chemical composition influenced by geographic location, climate, and extraction methods (28). Differences in the content of bioactive compounds, particularly D-limonene, γ-terpinene, α-pinene, etc., strongly affect antioxidant activity. The higher IC_{50} value in our study suggests that the CaEO from Long An (Vietnam) may have a different chemical composition compared to those from Tunisia and Algeria.

Overall, although CaEO exhibits weaker antioxidant activity than vitamin C, it still holds potential as a natural antioxidant source. Further studies should investigate the impact of extraction methods and environmental factors on its bioactive composition to optimize its application in the food and pharmaceutical industry.

Table 3: Antioxidant activity using DPPH and ABTS methods.

Test sample	$IC_{50\text{-DPPH}}$	$IC_{50\text{-ABTS}}$
Vitamin C (µg/mL)	$6.04^{a} \pm 0.35$	$3.12^{b} \pm 0.26$
CaEO (mg/mL)	$13.99^{b} \pm 1.84$	$1.52^{a} \pm 0.09$

Different letters (a, b) in the same column indicate significant differences ($p \leq 0.05$) between samples.

3.4. Determination of The Antibacterial Activity (AA) of CaEO

Table 4 shows that CaEO exhibited significantly lower antibacterial efficacy than gentamicin against both Gram-negative and Gram-positive bacteria. For Gram-negative bacteria, the inhibition zone diameters of CaEO against *E. coli* (8.52 ± 0.62 mm) and *S. enteritidis* (8.45 ± 0.29 mm) were much smaller than those of gentamicin (16.11 ± 0.56 mm and 10.67 ± 0.27 mm, respectively). Similarly, for Gram-positive bacteria, CaEO demonstrated weaker antibacterial activity, with inhibition zones of 8.11 ± 0.73 mm for *S. aureus* (compared to 14.48 ± 0.83 mm for gentamicin) and 7.99 ± 0.55 mm for *B. cereus* (compared to 20.04 ± 0.98 mm for gentamicin). Overall, the antibacterial sensitivity of CaEO in this study was classified as "not sensitive" due to its inhibition zones being approximately 8 mm (29).

Compared to some raw materials from other regions, there are notable differences in antibacterial properties, with Egyptian CaEO demonstrating significantly higher antibacterial activity, showing inhibition zone diameters of 32 mm for *S. aureus* and 49 mm for *P. aeruginosa* (30). Similarly, Ben Hsouna et al. (2017) reported higher inhibition zones for *S. enteritidis* (18 mm), *B. cereus* (24 mm), *E. coli* (15 mm), and *S. aureus* (22 mm) using essential oils from Tunisia, suggesting variations in antibacterial efficacy based on plant origin, extraction method, and chemical composition (27). The lower antibacterial activity of CaEO in this study may be attributed to its chemical composition. Limonene, the dominant compound in CaEO, has been reported to exhibit antibacterial properties, but its efficacy depends on concentration and interactions with other bioactive compounds (31).

The antibacterial activity of EOs is primarily linked to their hydrophobicity, allowing them to penetrate bacterial cell membranes, disrupt lipid bilayers, and increase membrane permeability. This process leads to ion leakage, loss of intracellular components, and ultimately, bacterial cell death (32). These mechanisms explain why EOs are widely applied in food preservation despite variations in their antibacterial potency.

Table 4: Antibacterial zones of CaEO.

Test strains	Diameter of the inhibitory zones of gentamicin (mm)	Diameter of the inhibitory zones of CaEO (mm)
E. coli	$16.11^{Ca} \pm 0.56$	$8.52^{Db} \pm 0.62$
S. enteritidis	$10.67^{Ab} \pm 0.27$	$8.45^{Ca} \pm 0.29$
S. aureus	$14.48^{Bb} \pm 0.83$	$8.11^{Ba} \pm 0.73$
B. cereus	$20.04^{Db} \pm 0.98$	$7.99^{Aa} \pm 0.55$

Within a row (a–b) or a column (A–D), different letters denote significant differences ($p < 0.05$) between samples or microorganisms, respectively.

4. CONCLUSION

This study extracted and characterized *Citrus aurantifolia* essential oil (CaEO) from lime peels in Long An province, Vietnam, highlighting its chemical composition and bioactive potential. GC-MS analysis identified six key compounds, with D-limonene (69.99%), β-Pinene (10.28%), and α-Pinene (13.08%) as the predominant constituents. The physicochemical properties of CaEO, including relative and absolute density, acid value, ester value, and saponification value, were determined to assess its stability and quality. Antioxidant activity was confirmed through DPPH and ABTS assays, with IC_{50} values of 13.99 ± 1.84 and 1.52 ± 0.09 mg/mL, respectively, indicating strong free radical scavenging capacity. However, the antibacterial activities of CaEO were relatively low, with inhibition zones ranging from 7.99 to 8.52 mm against *S. aureus*, *B. subtilis*, *E. coli*, and *S. enteritidis*. Additionally, the long-lasting aroma of CaEO enhances its applicability in various industries. These findings suggest that CaEO could be a valuable natural additive in food preservation, pharmaceuticals, and cosmetics, offering an eco-friendly approach to utilizing lime peel waste while increasing the economic value of local lime products.

5. CONFLICT OF INTEREST

The authors declare that they have no conflicts of interest.

6. ACKNOWLEDGMENTS

The authors are thankful to the Institute of Biotechnology and Food Technology, Industrial University of Ho Chi Minh City, for providing the laboratory facility.

7. REFERENCES

1. Hien Tran T, Tien Nguyen V, Phat Dao T, Duc Lam T, Quoc Toan T, Duy Nguyen T, et al. New direction in research on extraction of *Citrus aurantifolia* (Lemon fruit) essential oil grown in Mekong Delta - Vietnam via microwave-assisted

hydrodistillation. IOP Conf Ser Mater Sci Eng [Internet]. 2019 Jun 1;542(1):012038. Available from: <URL>.

2. Lopresto CG, Meluso A, Di Sanzo G, Chakraborty S, Calabrò V. Process-intensified waste valorization and environmentally friendly d-limonene extraction. Euro-Mediterranean J Environ Integr [Internet]. 2019 Dec 23;4(1):31. Available from: <URL>.

3. Jiang M, Yang L, Zhu L, Piao J, Jiang J. Comparative GC/MS analysis of essential oils extracted by 3 methods from the bud of *Citrus aurantium* L. var. *amara* Engl. J Food Sci [Internet]. 2011 Nov 9;76(9):C1219–25. Available from: <URL>.

4. Mohammed IO, Alrasheid AA, Hussein Ayoub SM. GC-MS analysis and study of the antimicrobial activity of *Citrus paradisi*, *Citrus aurantifolia*, and *Citrus sinensis* peel essential oils as hand sanitizer. Drlica K, editor. Int J Microbiol [Internet]. 2024 Jan 2;2024(1):4957712. Available from: <URL>.

5. Permadi N, Nurzaman M, Doni F, Julaeha E. Elucidation of the composition, antioxidant, and antimicrobial properties of essential oil and extract from *Citrus aurantifolia* (Christm.) Swingle peel. Saudi J Biol Sci [Internet]. 2024 Jun 1;31(6):103987. Available from: <URL>.

6. Rasool N, Saeed Z, Pervaiz M, Ali F, Younas U, Bashir R, et al. Evaluation of essential oil extracted from ginger, cinnamon and lemon for therapeutic and biological activities. Biocatal Agric Biotechnol [Internet]. 2022 Sep 1;44:102470. Available from: <URL>.

7. Ivanov N V., Anikina DS, Navrov A V. Composition of essential oils in the peel of lemon, cv. tashkentskii, grown in protected ground in different natural and climatic zones. Russ J Plant Physiol [Internet]. 2024 Jun 13;71(3):94. Available from: <URL>.

8. Freche E, Gieng J, Pignotti G, Ibrahim SA, Feng X. Applications of lemon or cinnamon essential oils in strawberry fruit preservation: A review. J Food Process Preserv [Internet]. 2022 Sep 9;46(9):e16526. Available from: <URL>.

9. Long DM, Quoc LPT, Nhung TTP, Thy VB, Nhu NLQ. Chemical profiles and biological activities of essential oil of *Citrus hystrix* DC. peels. Korean J Food Preserv [Internet]. 2023 Jun;30(3):395–404. Available from: <URL>.

10. ISO 279. International Organization for Standardization. Essential oils - Determination of relative density at 20°C. Geneva, Switzerland [Internet]. 1998. Available from: <URL>.

11. ISO 1041. International Organization for Standardization. Essential oils - Determination of freezing point. Geneva, Switzerland [Internet]. 1973. Available from: <URL>.

12. ISO 1242. International Organization for Standardization. Essential oils - Determination of acid value by two titration methods, manual and automatic. Geneva, Switzerland [Internet]. 2023. Available from: <URL>.

13. ISO 7660. International Organization for Standardization. Essential oils - Determination of ester value of oils containing difficult-to-saponify esters. Geneva, Switzerland [Internet]. 1983. Available from: <URL>.

14. Mahajan VK. Perfumes and associated allergens: A brief review. Cosmoderma [Internet]. 2022 Feb 23;2:21. Available from: <URL>.

15. Quyen PT, Quoc LPT. Chemical composition and biological evaluation of tea tree (*Melaleuca alternifolia* L.) leaves essential oils. Rev Fac Nac Agron Medellín [Internet]. 2024 May 1;77(2):10743–50. Available from: <URL>.

16. Biskup I, Golonka I, Sroka Z, Gamian A. Antioxidant activity of selected phenols estimated by ABTS and FRAP methods. Postep Hig Med Dosw [Internet]. 2013;67:958–63. Available from: <URL>.

17. Carović-Stanko K, Orlić S, Politeo O, Strikić F, Kolak I, Milos M, et al. Composition and antibacterial activities of essential oils of seven *Ocimum* taxa. Food Chem [Internet]. 2010 Mar 1;119(1):196–201. Available from: <URL>.

18. Saini RK, Ranjit A, Sharma K, Prasad P, Shang X, Gowda KGM, et al. Bioactive compounds of citrus fruits: A review of composition and health benefits of carotenoids, flavonoids, limonoids, and terpenes. Antioxidants [Internet]. 2022 Jan 26;11(2):239. Available from: <URL>.

19. Benoudjit F, Maameri L, Ouared K, History A. Evaluation of the quality and composition of lemon (*Citrus limon*) peel essential oil from an Algerian fruit juice industry. Alger J Environ Sci Technol December Ed [Internet]. 2020;6(4):1575–81. Available from: <URL>.

20. Uahomo PO, Kpaduwa S, Daniel C, Ezerioha CE. Characterization and comparative assessment of the essential oil from lime (*Citrus aurantifolia*) exocarp using maceration and soxhlet extraction methods. Sch Int J Chem Mater Sci [Internet]. 2023 Jul 22;6(06):126–34. Available from: <URL>.

21. Miller JA, Thompson PA, Hakim IA, Chow HHS, Thomson CA. d-Limonene: A bioactive food component from citrus and evidence for a potential role in breast cancer prevention and treatment. Oncol Rev [Internet]. 2011 Mar 17;5(1):31–42. Available from: <URL>.

22. Michaelakis A, Papachristos D, Kimbaris A, Koliopoulos G, Giatropoulos A, Polissiou MG. Citrus essential oils and four enantiomeric pinenes against *Culex pipiens* (Diptera: Culicidae). Parasitol Res [Internet]. 2009 Aug 8;105(3):769–73. Available from: <URL>.

23. Boelens MH, Jimenez R. The chemical composition of some mediterranean citrus oils. J

Essent Oil Res [Internet]. 1989 Jul;1(4):151–9. Available from: <URL>.

24. Kfoury M, Auezova L, Greige-Gerges H, Fourmentin S. Promising applications of cyclodextrins in food: Improvement of essential oils retention, controlled release and antiradical activity. Carbohydr Polym [Internet]. 2015 Oct 20;131:264–72. Available from: <URL>.

25. Mollica F, Gelabert I, Amorati R. Synergic antioxidant effects of the essential oil component γ-terpinene on high-temperature oil oxidation. ACS Food Sci Technol [Internet]. 2022 Jan 21;2(1):180–6. Available from: <URL>.

26. Budiarto R, Khalisha A, Sari DN, Ujilestari T, Wahyono T, Azmi AFM, et al. Antioxidant properties of lemon essential oils: A meta-analysis of plant parts, extraction methods, dominant compounds, and antioxidant assay categories. Chem Biol Technol Agric [Internet]. 2024 Sep 27;11(1):147. Available from: <URL>.

27. Ben Hsouna A, Ben Halima N, Smaoui S, Hamdi N. *Citrus lemon* essential oil: Chemical composition, antioxidant and antimicrobial activities with its preservative effect against *Listeria monocytogenes* inoculated in minced beef meat. Lipids Health Dis [Internet]. 2017 Dec 3;16(1):146. Available from: <URL>.

28. Floegel A, Kim DO, Chung SJ, Koo SI, Chun OK. Comparison of ABTS/DPPH assays to measure antioxidant capacity in popular antioxidant-rich US foods. J Food Compos Anal [Internet]. 2011 Nov 1;24(7):1043–8. Available from: <URL>.

29. Ponce AG, Fritz R, del Valle C, Roura SI. Antimicrobial activity of essential oils on the native microflora of organic Swiss chard. LWT - Food Sci Technol [Internet]. 2003 Nov 1;36(7):679–84. Available from: <URL>.

30. Asker M, El-gengaihi SE, Hassan EM, Mohammed MA, Abdelhamid SA. Phytochemical constituents and antibacterial activity of *Citrus lemon* leaves. Bull Natl Res Cent [Internet]. 2020 Dec 19;44(1):194. Available from: <URL>.

31. Han Y, Sun Z, Chen W. Antimicrobial susceptibility and antibacterial mechanism of limonene against *Listeria monocytogenes*. Molecules [Internet]. 2019 Dec 20;25(1):33. Available from: <URL>.

32. Li YQ, Sun XX, Feng JL, Mo HZ. Antibacterial activities and membrane permeability actions of glycinin basic peptide against *Escherichia coli*. Innov Food Sci Emerg Technol [Internet]. 2015 Oct 1;31:170–6. Available from: <URL>.

JOTCS A
Journal of the Turkish Chemical Society
Section: A
Chemistry

TURKISH CHEMICAL SOCIETY

Preparation and *in Vitro* Adhesive Application of Visible Light-Activated Modified Sodium Alginate

Rumeysa TUTAR[1*]

[1]Department of Chemistry, Faculty of Engineering, Istanbul University-Cerrahpaşa, Avcılar, Istanbul 34320, Turkey.

Abstract: Materials that are responsive to visible light have been extensively used in biomedical applications, including tissue engineering. Tissue adhesives are among the most important applications of tissue engineering. In this study, different concentrations of Ruthenium (Ru) and sodium persulfate (SPS) photoinitiators (0.2/2, 0.5/5, and 1/10 mM) were prepared. Sodium alginate (Na-alginate) was modified with methacrylate (AlgMA) to render it photoactive. Photoactive materials prepared with different ratios of photoinitiators were physically, chemically, morphologically, and mechanically tested. The results of the different analyses supported each other. Ru/SPS concentrations of 0.2/2, 0.5/5, and 1/10 mM were used to evaluate the hydrogel structures. No physical, chemical, or mechanical differences were observed between the 0.5/5, and 1/10 mM. The in vitro adhesion properties of the hydrogels increased significantly from 0.2/2 mM to 1/10 mM Ru/SPS. As the Ru/SPS concentration was increased, a significant increase in cell viability was observed. In particular, 1/10 mM Ru/SPS showed the greatest effect and created the most statistically significant difference.

Keywords: AlgMA, Ru/SPS, Light-activation, Visible light, Tissue adhesives.

Submitted: January 22, 2025. **Accepted:** March 25, 2025.

Cite this: Tutar R. Preparation and *in Vitro* Adhesive Application of Visible Light-Activated Modified Sodium Alginate. JOTCSA. 2025;12(2): 107-16.

DOI: https://doi.org/10.18596/jotcsa.1624684

***Corresponding author's E-mail:** rumeysa.tutar@iuc.edu.tr

1. INTRODUCTION

Na-alginate is a natural anionic polysaccharide obtained from brown algae and is abundantly found on the seafloor (1-3). In brown algae, glycans include cellulose, fucans, and alginates (4). Na-alginate has excellent properties such as low cost, low cytotoxicity, and biodegradability, making it a highly attractive material for biomedical applications. Owing to these properties, it has been extensively investigated as a natural polysaccharide in various fields. Some modifications have been applied to Na-alginate structures to eliminate disadvantages, such as poor gelation and mechanical strength. In particular, hydroxyl and carboxyl groups within the molecular structure can be modified using physical, chemical, and biological methods (5). Na-alginate was processed using chemical and physical modifications. Therefore, it is possible to modify and create new alginate derivatives with controlled sequences and tailored structures.

Physical crosslinking was used to improve the properties of sodium alginate. The basic principle of physical crosslinking involves the use of hydrogen bonds and tangle points to form gel-network structures (6). In this context, ionic (Ca^{2+}) crosslinking is especially common and is formed by crosslinking and exchanging sodium ions with alginic acid. Alginate gluconate combines with gluconic acid blocks on adjacent alginic acid chains to form an eggshell pattern (7).

Chemical modification of Na-alginate can change its chemical structure. Methacrylamides and methacrylates, which are called functional labeling structures, are widely used as graft biomaterials for the photopolymerization process (8-10). Alginate has been modified with methacrylic anhydride (MA) to improve photosensitivity and adhesion strength (11). Ruthenium (Ru) is a transition metal. Ru-based transition metal complexes and sodium persulfate (SPS) have been widely used to prepare visible-light-initiation systems. Visible light at 400-700 nm has shown significant advantages in tissue-engineering applications. The Ru/SPS photoinitiator system with $\varepsilon \approx 14600\ m^{-1}\ cm^{-1}$ at 450 nm can be used most effectively in polymerization applications. In this

initiator system, Ru acted as an electron donor for SPS. Therefore, SPS accepts electrons from Ru^{2+}, which are then oxidized to Ru^{3+}. Because of these electron transfers, radicals were formed. The radicals formed here activate the photocrosslinking of methacryloyl groups in modified biomaterials (12-15).

The clinical application of tissue adhesives has gained significant attention for promoting tissue health. Suturing damaged tissue is highly challenging in terms of both patient comfort and long-term tissue healing. Furthermore, tissue adhesives have the advantages of being simple and time-saving, and can be alternatives to sutures (16-18). Understanding the chemistry of tissue materials is important for explaining the adhesion mechanisms of tissue adhesives. Therefore, Na-alginate was modified to improve its adhesion mechanism. Various tissue adhesives have been prepared and used for clinical applications. These adhesives are divided into various categories: cyanoacrylate adhesives, fibrin-based adhesives, proteins, polysaccharides, and polymer-based adhesives (18).

This study utilized the standardized test methodologies outlined by the American Society for Testing and Materials (ASTM) to perform burst pressure tests (19-20). Collagen sheets were used to mimic skin in vitro. Skin injury simulation was performed on these sheets. Tissue adhesives prepared with various photoinitiator concentrations were subjected to in vitro adhesion testing on simulated wounds. Thus, the adhesion between the material and tissue after injury and wound closure was tested in vitro. Additionally, cell viability of the tissue adhesives was tested in a cell culture study (20).

In this study, methacrylate-modified Na-alginate was prepared as a precursor material to physically and chemically crosslink the AlgMA hydrogels. The primary objective was to develop AlgMA hydrogels using varying concentrations of the Ru/SPS photoinitiator system (0.2/2, 0.5/5, and 1/10 mM) and evaluate their physical, chemical, morphological, and mechanical properties. Additionally, an in vitro skin model was simulated using collagen sheets to assess the adhesion properties of the hydrogels. These findings indicate that the concentration of the Ru/SPS photoinitiator system significantly influenced the characteristics of the resulting biostructures.

2. EXPERIMENTAL SECTION

2.1. Chemicals and Instruments

Sodium alginate, phosphate-buffered saline (PBS) tablets, methacrylic anhydride (MA), cellulose dialysis membranes (14 kDa molecular weight cut-off), tris(2,2-bipyridyl) dichlororuthenium (II) hexahydrate (Ru), and SPS were purchased from Sigma-Aldrich. The ATR-FTIR spectra of all the samples were obtained within the range of 4000 to 500 cm^{-1} using a Jasco FT/IR 6700 spectrophotometer. For NMR analysis, a JEOL ECZ500R (11.75 Tesla) spectrometer equipped with a high-performance Ultrashield™ 500 MHz superconducting magnet was utilized. Scanning electron microscopy (SEM) images were captured at various magnifications using a JEOL JSM 5600 microscope. A TA.XT Plus Texture Analysis Mechanical Tester was used for compression tests.

2.2. Synthesis of Na-Alginate-Methacryloyl (AlgMA)

Methacrylic anhydride was selected as the modification chemical to incorporate methacrylate groups into biopolymers. Sodium alginate (Na-alginate) was dissolved in DI water (2.5 wt %), and 15 ml of methacrylic anhydride per gram of alginate was added to the solution (11). The mixture was left to react for 3 h at room temperature. The reaction pH was adjusted to 7 using sodium hydroxide (NaOH). To stop the reaction, the solution was precipitated using ethanol. The precipitated polymer was then dissolved in water. Subsequently, dialysis against deionized water was performed to eliminate unreacted methacrylic anhydride. The AlgMA solution was then filtered through a filter. The purified polymer was then lyophilized under sterile conditions.

2.3. Fabrication of AlgMA Hydrogels

Dried and sterile 5 wt% AlgMA was weighed and dissolved with Ru and SPS photoinitiator systems (PI) which were prepared as 0.2mM/2mM, 0.5mM/5mM and 1mM/10mM, respectively. The prepared solutions were placed in PDMS molds (5 mm diameter × 1 mm thickness). They were then chemically crosslinked with visible light (VALO Visible Light Photocrosslinking device, Ultradent, USA) to chemically crosslink them (11-12). Various initiator concentrations at exposure times of 4 min were studied to optimize the irradiation conditions based on the PI concentrations. Then, 1M Ca^{+2} (7) was added to the crosslinked hydrogels to ionically crosslink them.

2.4. Chemical Characterization

Pristine Na-alginate, methacrylate-modified alginate, and crosslinked AlgMA hydrogels were chemically characterized by FTIR. Spectroscopic methods are preferred for defining the bonds of working molecules and elucidating their structures.

2.5. Physical Characterization

The swelling behavior of the prepared structures was determined according to a previously reported procedure (11). AlgMA solutions prepared with different photoinitiator concentrations were chemically crosslinked by curing under visible light for 240 s. It was then ionically cross-linked with 1M Ca^{+2}. The prepared structures were then frozen and lyophilized for drying. The lyophilized structures were weighed and recorded. The dry structures were then immersed in DPBS for swelling measurements. The swelling ratios at 24h and 48h were weighed and recorded. The swelling results were calculated using the following formula:

$$Swelling(\%) = (Ws - Wi)/Wi * 100 \quad (1)$$

where Wi is the initial weight and Ws is the swollen weight.

2.6. Morphological Characterization

The surface morphologies were analyzed by SEM. The samples and scaffolds were mounted on a double-sided graphite tape affixed to a metal surface and sputter-coated with gold for 10 s.

2.7. Mechanical Characterization

The materials for the mechanical characterization of the hydrogel structures were prepared as described in detail in Section 2.3. The pre-gel solution (200 µL) was used to perform the compression tests. Compression tests were applied at a strain rate of 0.6 mm min^{-1} until the failure point (maximum strain of 98%) was reached.

2.8. In vitro Burst Pressure Characterization

A standard test method was followed for the burst pressure test, ASTM standard test, F2392-04 (19). The in vitro burst pressure of the prepared hydrogels was measured using a specially designed burst pressure apparatus. Briefly, collagen sheets, which were commercially purchased and used as biological substrates, were prepared by washing with distilled water and DPBS. The wound was simulated by creating a defect in the prepared collagen sheets. Wound defects were created using a 3 mm medical punch. Next, the defective collagen sheets were placed in a burst pressure apparatus. Hydrogels with different Ru/SPS concentrations were prepared. Then, 100 µL of the prepared hydrogel was pipetted onto the defect site of the collagen sheets. The hydrogels were then cured with visible light for 4 min for chemical crosslinking and with $CaCl_2$ for 5 min for ionic crosslinking (21). The burst pressures of all the gels were recorded using a pressure sensor (PS-2017, PASCO; Roseville, CA, USA) by continuously pumping air using a flow pump (n = 4).

2.9. In vitro Cell Culture Studies

L929 Cell Line Propagation: L929 Cell Line, passage 18, was checked twice a day in T25 flasks in EMEM containing 10% FBS (Pan Biotech P30-1301) and expected to reach 70% confluency. (Doubling Time: 22-26 hours) (Cell line L929 is of ATCC CCL-1 origin). Preparation of Samples: Polymeric biogels prepared as dry samples were first kept in PBS containing 10% penicillin/streptomycin for 1 d. At the end of the waiting period, the samples were sterilized by keeping them under a UV lamp for 30 min. Cells in 96-Well Plates: 500 µL of trypsin-EDTA (Gibco, 15400054) was added to the cells that reached 70% confluence in T25 flasks and incubated at 37 °C in a 5% CO2 environment for 3-5 minutes. As soon as the cells dissociated under an inverted microscope (Zeiss Primovert, Germany), a medium containing 10% FBS was added. Centrifuge at 300xg for 5 min, and discard the medium. Add 1 mL of EMEM medium. Counting was performed on a Logos Luna II instrument using Trypan Blue (Gibco, 1525061). The polymers to be tested for cytotoxicity were added to the wells, and a medium containing 10% FBS was added so that 10^4 cells per well were added. Application of Cytotoxicity Test: Each group was made in the form of at least three replicate wells, and repeated analysis was ensured. After the material was applied, the cells waited for the time to be tested without being removed from the incubator. At the end of the hour, 10% of the well volume (equal to 20 µL of WST-8) was added to the WST-8 solution. The lights were turned off during this process. The cell culture dish was wrapped in aluminum foil and incubated for another 2 h. After 2 h, the absorbance was measured at 450 nm in a cell culture dish. The results were formulated and the percentage viability was determined (Equation 2).

$$\text{Cell Viability (\%)} = \frac{(Atreatment - Ablank)}{(Acontrol - Ablank)} * 100 \quad (2)$$

Where, A = absorbance.

2.10. Statistical Analysis

For each experiment, at least three samples were tested, and the data are presented as mean ± SD (*P < 0.05, **P < 0.01, ***P < 0.001, and ****P < 0.0001). One-way analysis of variance (ANOVA) and t-tests were performed, followed by Tukey's test for statistical analysis.

3. RESULTS AND DISCUSSION

The functional groups of Na-alginate and methacrylation-modified alginate (AlgMA) structure are shown in Figure 1. The chemical compositions of the pristine alginate and the fabricated samples were identified using FTIR spectra.

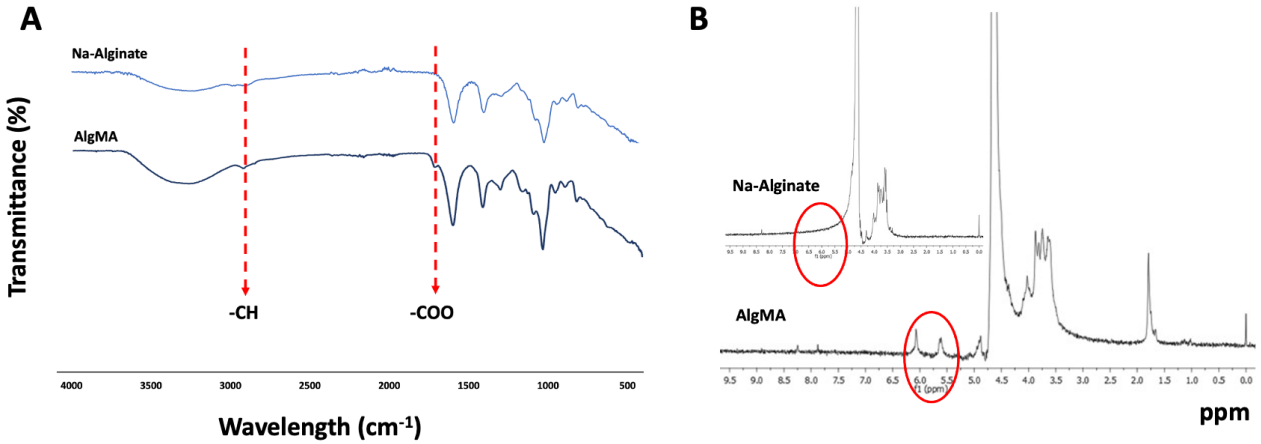

Figure 1: ATR-FTIR (A) and NMR (B) analyses of pristine alginate and AlgMA structures.

As shown in Figure 1 (A), the C=C stretching band at 1595 cm^{-1} and the C-H stretching band were observed at 2914 cm^{-1} identifying the substance. The C-H stretching peak at 2914 cm^{-1} indicated that it was an aldehyde.

When the two structures are compared in Figure 1 (A), it can be seen that the growth of the carbonyl (C=O) stretching vibration grafted with methacrylic anhydride groups showed a shoulder appearance around 1700 cm^{-1} in the AlgMA spectrum (11,21). This peak is characteristic of the methacrylate groups. In addition, νC-O bands were observed at 1296 cm^{-1}. This characteristic peak in the spectra confirms the successful modification of Na-alginate with methacrylate.

The ^{1}H-NMR spectra of Na-alginate and AlgMA are shown in Figure 1 (B). In the chemical structure formed after methacrylation, distinctive signals of groups reacting with methacrylate and vinyl groups, 5.20-6.30 ppm, were observed in the spectrum (11). In addition, Na-alginate itself does not have a significant methyl (-CH_3) group, so a significant signal around 1.75 ppm is not expected. However, for AlgMA, during the addition of the methacryloyl group, the -CH_3 (methyl) protons of the methacrylate group gave a signal around 1.75 ppm. This signal was due to the CH_3 (-C=CH_3) protons in the methacrylate group.

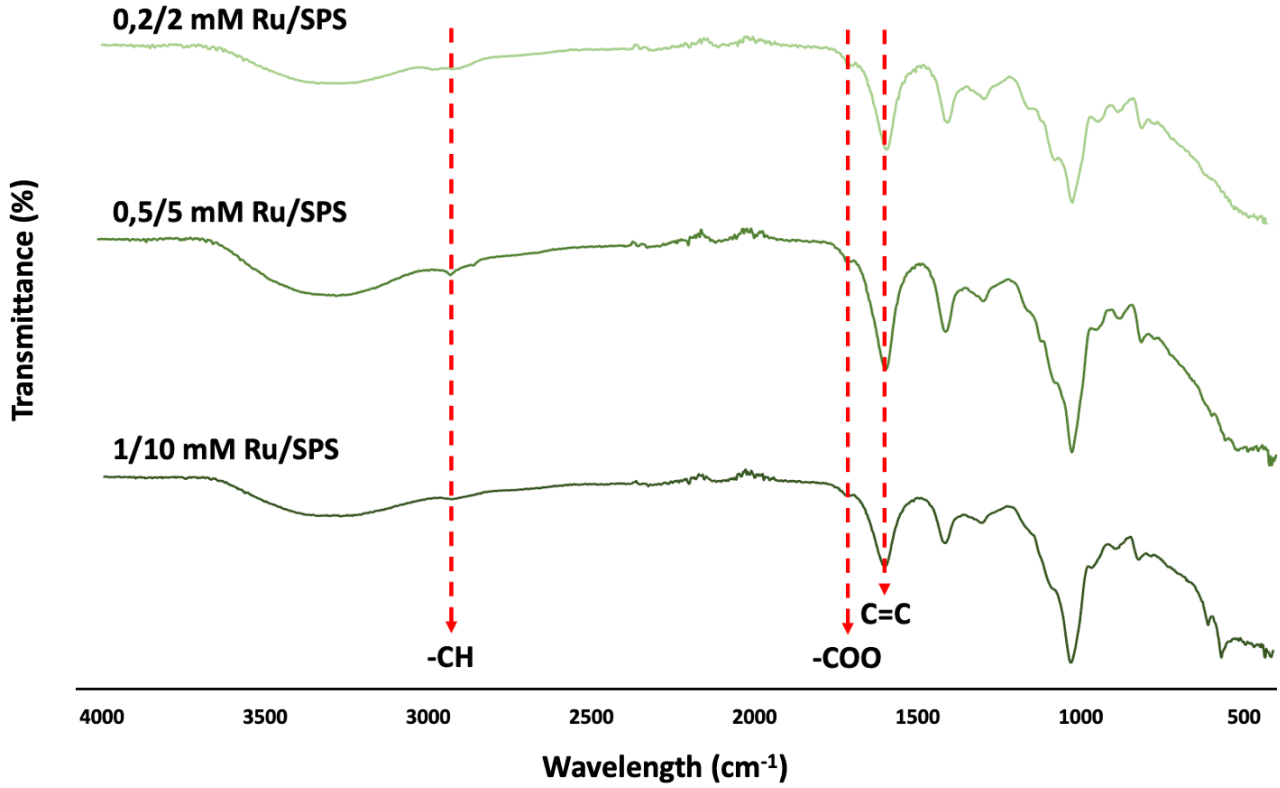

Figure 2: ATR-FTIR Analysis of AlgMA hydrogels fabricated with varying concentrations of the Ru/SPS photoinitiator.

As shown in Figure 2, the intensity of the C=C (1630-1650 cm^{-1}) peak decreased as the methacrylate groups polymerized and the double bonds opened. The C=O (1700-1750 cm^{-1}) peak does not change significantly but may become clearer as polymerization is completed. The other peak (-OH) remained constant.

The morphological characteristics of the freeze-dried hydrogel structures are shown in Figure 3. Increasing the Ru/SPS concentration increased the morphological properties of AlgMA hydrogels.

SEM images and composite elemental maps of the same structures obtained using EDS revealed that increasing the concentration of the photoinitiators influenced the porosity and pore size of the hydrogel structures. SEM analysis revealed that the AlgMA hydrogels with different photoinitiator concentrations had a homogeneous pore structure, moderately rough surface, distinct network formation, and minimal crack formation.

If the Ru ratio increases as the photoinitiator density decreases (Figure 3(A)), this may indicate that Ru is concentrated (tends to cluster) in certain regions. The decrease in the atomic value (%) of Ru from 12.7 (Figure 3(B)) to 2.4 (Figure 3(C)) indicates that the Ru concentration in the sample decreases. If the Ru ratio decreases as the photoinitiator density increases, this may indicate that Ru is more dispersed or that cross-linking increases.

For the scaffolds prepared with 0.5/5 mM and 1/10 mM Ru/SPS systems (Figure 3(B-C)), the pores are almost homogeneous and regular, which indicates that the material has undergone a controlled production process.

Alginate-based materials form a specific network structure as a result of crosslinking (ionic crosslinking with calcium and covalent bonding with visible light). The free-radical crosslinking reaction rate increases as the concentration of the Ru/SPS system increases, which increases the formation of covalent crosslink bonds (22).

The swelling properties of the AlgMA hydrogels are shown in Figure 4.

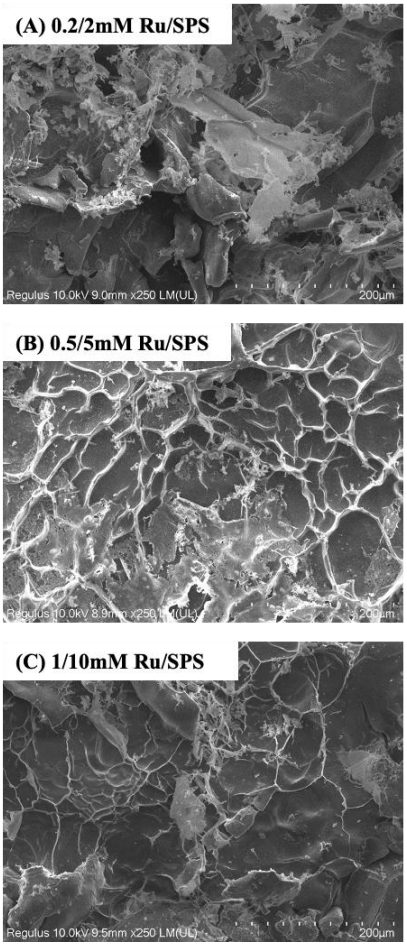

Element	Atomic %	Atomic % Error	Weight %	Weight % Error
C	8.7	0.0	4.4	0.0
N	1.3	0.1	0.8	0.1
O	80.3	0.2	53.9	0.2
S	0.1	0.0	0.1	0.0
Ru	9.6	0.0	40.8	0.1

Element	Atomic %	Atomic % Error	Weight %	Weight % Error
C	3.2	0.0	1.5	0.0
N	0.2	0.1	0.1	0.0
O	83.7	0.2	50.1	0.1
S	0.2	0.0	0.2	0.0
Ru	12.7	0.0	48.2	0.1

Element	Atomic %	Atomic % Error	Weight %	Weight % Error
C	30.0	0.1	21.4	0.1
N	3.5	0.2	2.9	0.2
O	63.7	0.2	60.6	0.2
S	0.3	0.0	0.6	0.0
Ru	2.4	0.0	14.5	0.0

Figure 3: SEM images and Energy Dispersive Spectroscopy (EDS) analysis of AlgMA hydrogels fabricated with varying concentrations of Ru/SPS photoinitiator. Scale bar: 200 μm.

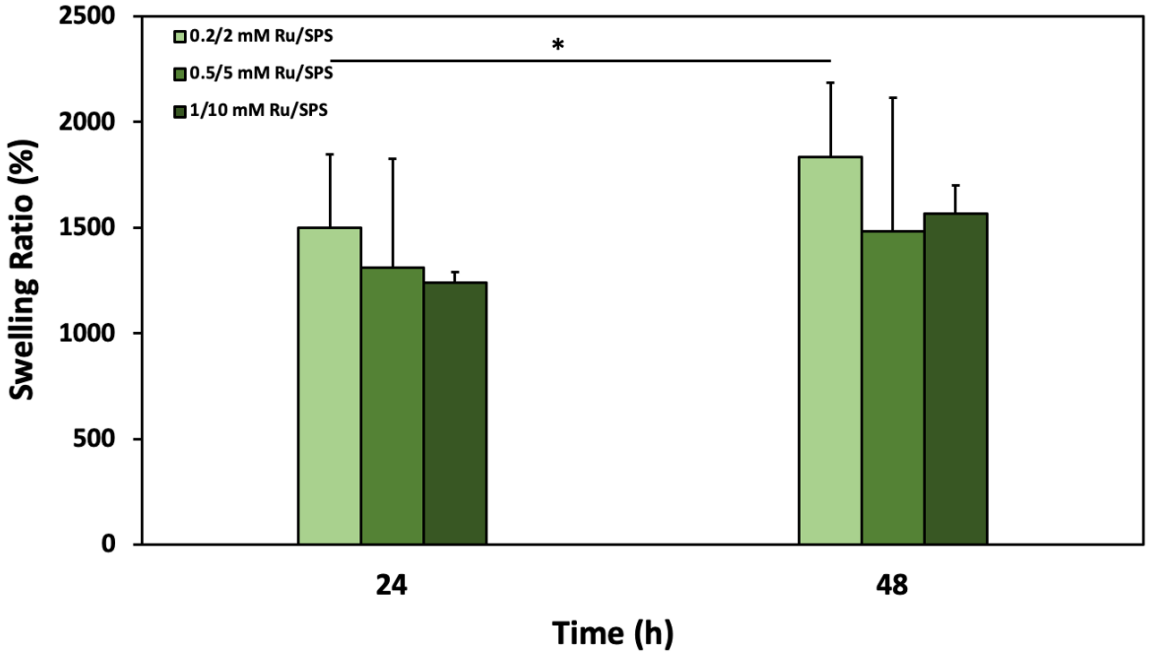

Figure 4: Swelling properties of AlgMA hydrogels fabricated with varying concentrations of the Ru/SPS photoinitiator (n=4).

Measurements at 24h and 48h showed that increasing the initiator concentration from 0.2/2 mM Ru/SPS to 0.5/5 or 1/10 mM Ru/SPS did not cause any significant difference in the swelling ratio. These results indicate that 0.2/2 mM Ru/SPS is sufficient to complete the cross-linking of the monomers. Again, the swelling behavior at 24h and 48h did not show any significant change for the 0.5/5 mM and 1/10 mM Ru/SPS systems. Moreover, the–OH groups in Na-alginate were transferred to -COO via a methacrylate modification reaction, which also limited the water absorption ability.

The stiffness of the fabricated AlgMA hydrogel was measured. The compressive modulus and compressive strength of AlgMA hydrogels synthesized with varying concentrations of the Ru/SPS photoinitiator system are presented in Figure 5.

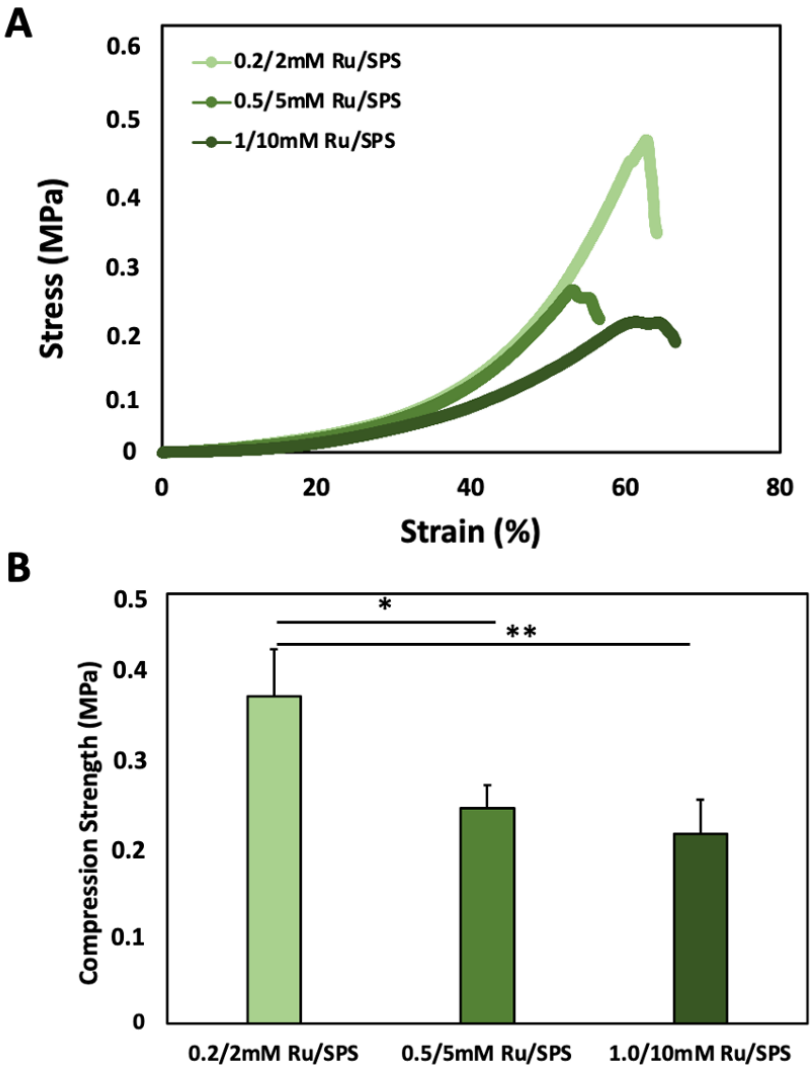

Figure 5: Compressive modulus (A) and strength (B) of AlgMA hydrogels fabricated using different concentrations of Ru/SPS (n=3).

As shown in Figure 5A, the 0.2/2 mM Ru/SPS sample appears to have a higher load-carrying capacity compared to the others, reaching the highest stress value (strength increase). All samples initially exhibited elastic deformation at low strains. Moreover, the 0.2/2 mM Ru/SPS sample shows a sudden fracture at approximately 60% strain, whereas the other samples break with lower strength or exhibit yielding behavior. In addition, it can be observed that as the Ru/SPS concentration increased, the material carried lower stress and exhibited earlier deformation.

Hydrogels prepared using 0.2/2 mM Ru/SPS (0.44 ± 0.05 MPa) exhibited a significantly higher compressive modulus than those fabricated with 0.5/5 mM (0.27 ± 0.03 MPa) and 1/10 mM (0.26 ± 0.04 MPa) Ru/SPS. However, no statistically significant differences were observed when the Ru/SPS concentration was increased to 0.5/5 mM or 1/10 mM. These findings suggest that a concentration of 0.2/2 mM Ru/SPS is sufficient to achieve complete crosslinking of the AlgMA macromers (Figure 5B).

These data show that a low concentration of 0.2/2 mM Ru/SPS offers the best mechanical performance; however, the elastic modulus and strength decrease as the concentration increases. If more strength is desired, it may be necessary to optimize the

crosslinking structure or improve the mechanical properties of the material through different modifications.

ASTM standards for biological adhesive hydrogels were used in the experiments. A collagen sheet, which was commercially purchased and used as the biological substrate, was prepared (Figure 6 (A)). The wound was then simulated by creating a defect in the prepared collagen sheets (Figure 6 (B)). Wound defects were created using a 3 mm medical punch. Next, the defective collagen sheets were placed in a burst pressure apparatus. AlgMA solutions prepared with different Ru/SPS concentrations were then added to the wound defects, as shown in Figure 6 (C). After the addition of the AlgMA solutions, they were covalently cross-linked with visible light (Figure 6 (D)). Then, ionic cross-linking with Ca^{+2} was performed to prepare the AlgMA hydrogel for the study.

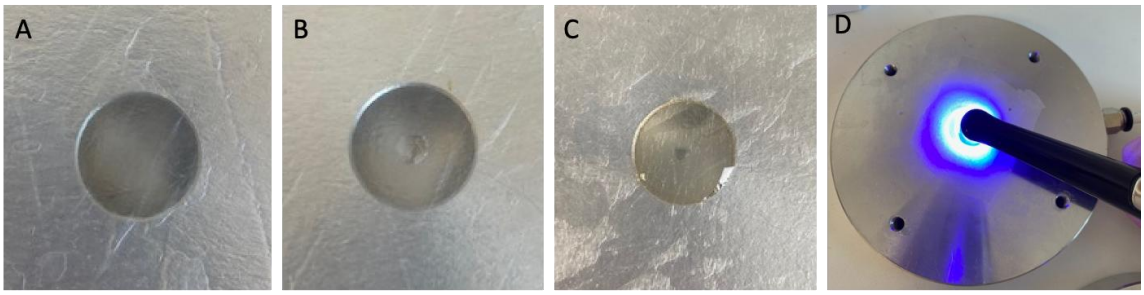

Figure 6: Images of AlgMA Hydrogels for adhesive application to a collagen sheet. Collagen sheet in the burst pressure apparatus (A), wound defect on the sheet (B), AlgMA solution (C), and cross-linking with visible light (D).

Various photoinitiator concentrations at an exposure time of 4 min. Then, 1M $CaCI_2$ was added to the crosslinked hydrogels to ionically crosslink them.

An in vitro burst pressure test was performed (Figure 7) to demonstrate how the adhesion properties changed with the different photoinitiator concentrations. A low photoinitiator concentration negatively affected AlgMA adhesion properties. After applying pressure, the material was separated from the collagen layer in a short time of 20 seconds.

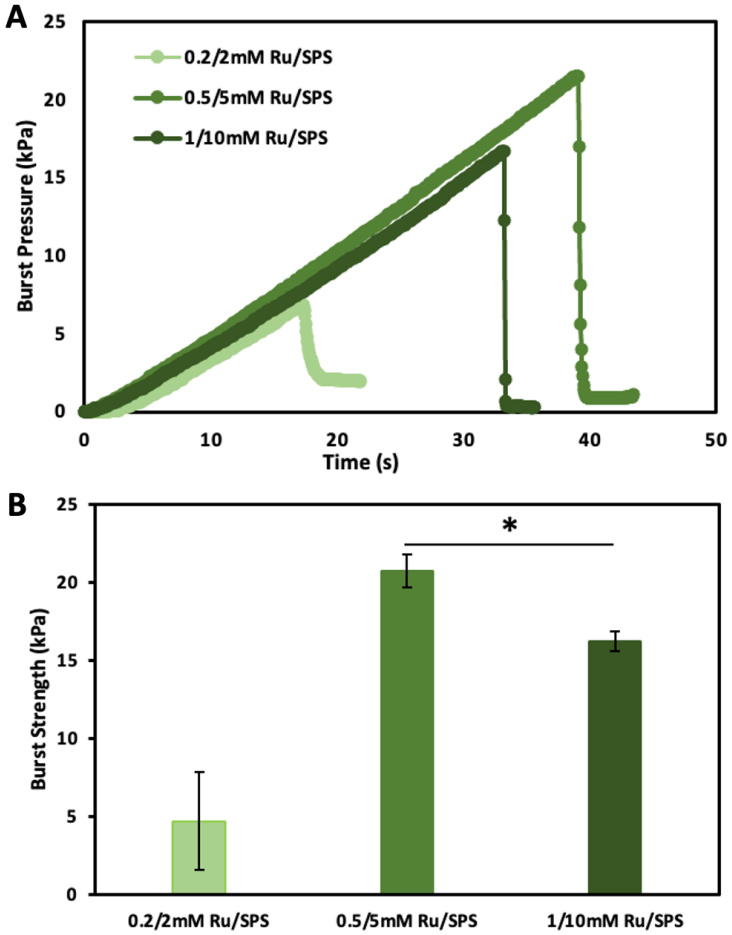

Figure 7: In vitro adhesive properties, burst pressure (A), and burst strength (B) of AlgMA hydrogels.

In Figure 7(A), 0.2/2 mM Ru/SPS reached the lowest burst pressure and failed in approximately 20 s, whereas 0.5/5 mM Ru/SPS and 1/10 mM Ru/SPS samples withstood higher pressures (around 20 kPa) and burst in approximately 30-40 seconds. In addition, the 1/10 mM Ru/SPS exhibited the highest strength. In all samples, the pressure increased linearly, and when it reached a certain threshold point, a sudden drop occurred, resulting in sample destruction. Higher burst pressures and longer durations were observed at higher concentrations.

This indicates that the interaction between the material and collagen was insufficient. As the photoinitiator concentration increased, the adhesion strength also increased. However, as the concentration increased, the material strength increased, as the AlgMA-cured areas were completely cured, which slightly reduced the adhesion strength with the collagen layer. The burst pressures of hydrogels significantly increased from 4.7 ± 3.11 kPa to 20.75 ± 1.06 kPa and 16.25 ± 0.6 kPa as the photoinitiator concentration was increased from 0.2/2 mM to 1/10 mM Ru/SPS concentration (Figure 7(B)).

As the Ru/SPS concentration increased, the resistance of the material to the burst pressure increased. Ru/SPS (1/10 mM) showed the best mechanical performance, whereas 0.2/2 mM Ru/SPS exhibited the lowest strength. This indicates that a higher degree of crosslinking or network density increased the mechanical strength of the material.

Different concentrations of the Ru/SPS system resulted in viability and abundance of live cells (Figure 8) at 24h.

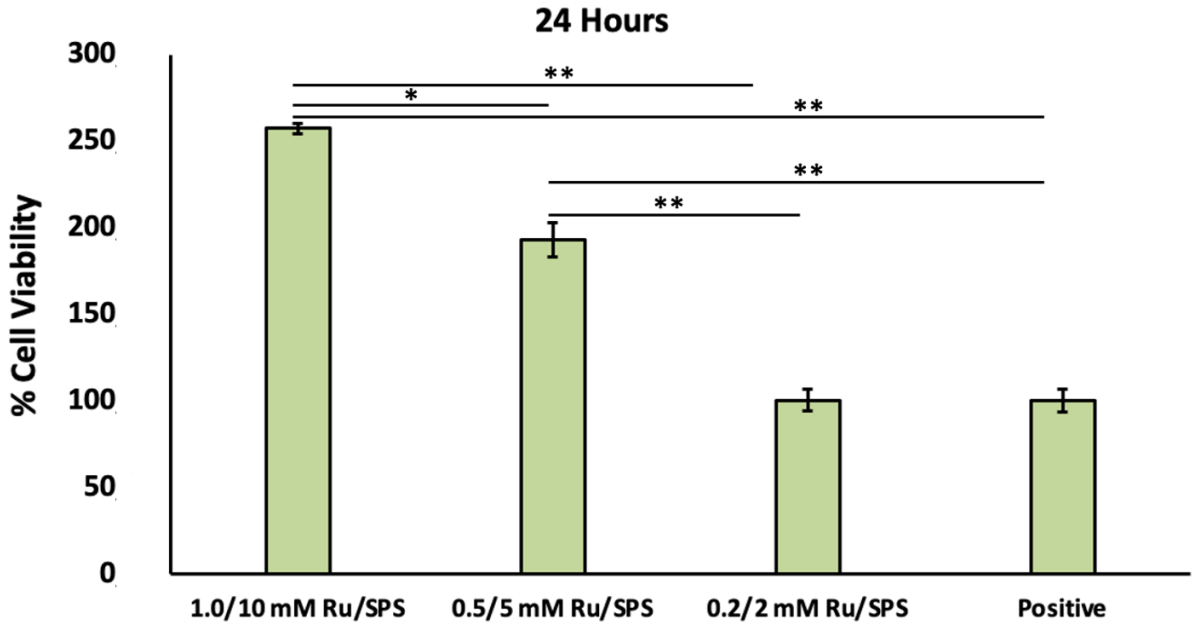

Figure 8: Viability and metabolic activity of fibroblasts cultured on AlgMA Hydrogels after 24h. (*p<0.05, mean±std, n=3) All analyses were performed in triplicate.

When the cell study results were evaluated, a significant increase in cell viability was observed with increasing Ru/SPS concentration. At the end of the 24-h incubation period, cell viability rates were at the highest level in the 1.0/10 mM Ru/SPS group, while a relatively lower but still high value was observed in the 0.5/5 mM Ru/SPS group. Cell viability in the 0.2/2 mM Ru/SPS group decreased significantly and fell to a level closer to the positive control (L929 Cell Line) group. These results reveal the dose-dependent effect of Ru/SPS concentration on cell viability (23).

4. CONCLUSION

In this study, different concentrations of the Ru/SPS photoinitiator (0.2/2, 0.5/5, and 1/10 mM) were prepared. Na-alginate was selected as the biomaterial and was modified with methacrylate to make it photoactive. Photoactive AlgMA hydrogels prepared using different ratios of photoinitiators were tested physically, chemically, morphologically, mechanically, and biologically. AlgMA hydrogels with 0.2/2 mM Ru/SPS and 0.5/5 or 1/10 mM Ru/SPS did not cause any significant differences in the swelling ratio. However, increasing the Ru/SPS concentration positively affects the homogeneity of the hydrogel structures. The scaffolds prepared with the 0.5/5 mM and 1/10 mM Ru/SPS systems exhibited homogeneity and regularity, indicating that the material underwent a controlled production process. The hydrogels prepared using 0.2/2 mM Ru/SPS exhibited a significantly higher compressive modulus, comparable to those fabricated with 0.5/5 mM and 1/10 mM Ru/SPS. However, no statistically significant differences were observed when the Ru/SPS concentration was increased to 0.5/5 mM or 1/10 mM. The in vitro adhesion properties of hydrogels significantly increased from 4.7 ± 3.11 kPa to 20.75 ± 1.06 kPa and 16.25 ± 0.6 kPa as the photoinitiator concentration was increased from 0.2/2 mM to 1/10 mM Ru/SPS concentration. As the Ru/SPS concentration was increased, a significant increase in cell viability was observed. In particular,

1/10 mM Ru/SPS showed the greatest effect and created the most statistically significant difference.

5. CONFLICT OF INTEREST

The author declares that she has no affiliations with or involvement in any organization or entity with any financial interest in the subject matter or materials discussed in this manuscript.

6. REFERENCES

1. Sellimi S, Younes I, Ayed H Ben, Maalej H, Montero V, Rinaudo M, et al. Structural, physicochemical and antioxidant properties of sodium alginate isolated from a Tunisian brown seaweed. Int J Biol Macromol [Internet]. 2015 Jan 1;72:1358–67. Available from: <URL>.

2. Rinaudo M. Main properties and current applications of some polysaccharides as biomaterials. Polym Int [Internet]. 2008 Mar 9;57(3):397–430. Available from: <URL>.

3. Ishikawa K, Miyamoto Y, Takechi M, Toh T, Kon M, Nagayama M, et al. Non-decay type fast-setting calcium phosphate cement: Hydroxyapatite putty containing an increased amount of sodium alginate. J Biomed Mater Res [Internet]. 1997;36(3):393–9. Available from: <URL>.

4. Rinaudo M. Seaweed polysaccharides, in Comprehensive Glycoscience, vol. 4, ed. by Kamerling JP. Elsevier. In Amsterdam, Netherlands; 2007. p. 691–735.

5. Szekalska M, Puciłowska A, Szymańska E, Ciosek P, Winnicka K. Alginate: Current use and future perspectives in pharmaceutical and biomedical applications. Int J Polym Sci [Internet]. 2016 Jan 1;2016(1):7697031. Available from: <URL>.

6. Paul UC, Manian AP, Široká B, Duelli H, Bechtold T. Sorption of iron(III)–alginate complexes on cellulose fibres. Cellulose [Internet]. 2013 Oct 6;20(5):2481–90. Available from: <URL>.

7. Dhamecha D, Movsas R, Sano U, Menon JU. Applications of alginate microspheres in therapeutics delivery and cell culture: Past, present and future. Int J Pharm [Internet]. 2019 Oct 5;569:118627. Available from: <URL>.

8. Sun F, Guo J, Liu Y, Yu Y. Preparation, characterizations and properties of sodium alginate grafted acrylonitrile/polyethylene glycol electrospun nanofibers. Int J Biol Macromol [Internet]. 2019 Sep 15;137:420–5. Available from: <URL>.

9. Vuocolo T, Haddad R, Edwards GA, Lyons RE, Liyou NE, Werkmeister JA, et al. A highly elastic and adhesive gelatin tissue sealant for gastrointestinal surgery and colon anastomosis. J Gastrointest Surg [Internet]. 2012 Apr 1;16(4):744–52. Available from: <URL>.

10. Lim KS, Klotz BJ, Lindberg GCJ, Melchels FPW, Hooper GJ, Malda J, et al. Visible light cross-linking of gelatin hydrogels offers an enhanced cell microenvironment with improved light penetration depth. Macromol Biosci [Internet]. 2019 Jun 26;19(6):1900098. Available from: <URL>.

11. Tutar R, Ceylan D, Çelebi-Saltik B. Preparation and characterization of conductive and multi-network nanocomposite hydrogels as potential scaffolds for electroactive tissues. New J Chem [Internet]. 2024 Aug 19;48(33):14736–45. Available from: <URL>.

12. Annabi N, Rana D, Shirzaei Sani E, Portillo-Lara R, Gifford JL, Fares MM, et al. Engineering a sprayable and elastic hydrogel adhesive with antimicrobial properties for wound healing. Biomaterials [Internet]. 2017 Sep 1;139:229–43. Available from: <URL>.

13. Lim KS, Ramaswamy Y, Roberts JJ, Alves M, Poole-Warren LA, Martens PJ. Promoting cell survival and proliferation in degradable poly(vinyl alcohol)–tyramine hydrogels. Macromol Biosci [Internet]. 2015 Oct 11;15(10):1423–32. Available from: <URL>.

14. Fancy DA, Denison C, Kim K, Xie Y, Holdeman T, Amini F, et al. Scope, limitations and mechanistic aspects of the photo-induced cross-linking of proteins by water-soluble metal complexes. Chem Biol [Internet]. 2000 Sep 1;7(9):697–708. Available from: <URL>.

15. Lim KS, Levato R, Costa PF, Castilho MD, Alcala-Orozco CR, van Dorenmalen KMA, et al. Bio-resin for high resolution lithography-based biofabrication of complex cell-laden constructs. Biofabrication [Internet]. 2018 May 11;10(3):034101. Available from: <URL>.

16. Bouten PJM, Zonjee M, Bender J, Yauw STK, van Goor H, van Hest JCM, et al. The chemistry of tissue adhesive materials. Prog Polym Sci [Internet]. 2014 Jul 1;39(7):1375–405. Available from: <URL>.

17. Duarte AP, Coelho JF, Bordado JC, Cidade MT, Gil MH. Surgical adhesives: Systematic review of the main types and development forecast. Prog Polym Sci [Internet]. 2012 Aug 1;37(8):1031–50. Available from: <URL>.

18. Spotnitz WD, Burks S. Hemostats, sealants, and adhesives: components of the surgical toolbox. Transfusion [Internet]. 2008 Jul 8;48(7):1502–16. Available from: <URL>.

19. ASTM F2392-04, 2015, ASTM International, West Conshohocken, PA [Internet]. Available from: <URL>.

20. Tutar R, Yüce-Erarslan E, İzbudak B, Bal-Öztürk A. Photocurable silk fibroin-based tissue sealants with enhanced adhesive properties for the treatment of corneal perforations. J Mater Chem B [Internet]. 2022 Apr 13;10(15):2912–25. Available from: <URL>.

21. Tavafoghi M, Sheikhi A, Tutar R, Jahangiry J, Baidya A, Haghniaz R, et al. Engineering tough, injectable, naturally derived, bioadhesive composite

hydrogels. Adv Healthc Mater [Internet]. 2020 May 24;9(10):1901722. Available from: <URL>.

22. Kim H, Jang JH, Han W, Hwang HJ, Jang J, Kim JY, et al. Extracellular matrix-based sticky sealants for scar-free corneal tissue reconstruction. Biomaterials [Internet]. 2023 Jan 1;292:121941. Available from: <URL>.

23. Murphy CM, Haugh MG, O'Brien FJ. The effect of mean pore size on cell attachment, proliferation and migration in collagen–glycosaminoglycan scaffolds for bone tissue engineering. Biomaterials [Internet]. 2010 Jan 1;31(3):461–6. Available from: <URL>.

JOTCSA Journal of the Turkish Chemical Society Section: A Chemistry

TURKISH CHEMICAL SOCIETY

Polymeric Nanoparticle Formulation, Characterization and Penetration Study for Topical Delivery of Timolol Maleate

Muhammad Sulaiman[1], Endang Lukitaningsih[2*], Ronny Martien[3], Retno Danarti[4], Yohanes Widodo Wirohadidjojo[4]

[1]Gadjah Mada University, Doctoral Program, Yogyakarta, 55281, Indonesia.
[2]Gadjah Mada University, Department of Pharmaceutical Chemistry, Yogyakarta, 55281, Indonesia.
[3]Gadjah Mada University, Department of Pharmaceutics, Yogyakarta, 55281, Indonesia.
[4]Gadjah Mada University, Department of Dermatology and Venereology, Yogyakarta, 55281, Indonesia.

Abstract: Infantile hemangioma (IH), while usually not life-threatening, often carries the risk of complications and causes anxiety due to changes in appearance. While regarded as an effective therapeutic choice, timolol maleate (TM) is mostly effective for mild and superficial lesions due to its limited absorption. The goal of this study was to examine the potency of natural polymers to be utilized as main ingredients in nanoparticle formulations to be used as a potential alternative for treating IH. The major ingredients chosen for nanoparticle production were chitosan and acacia gum. Different combinations of polymer concentrations were examined to improve the characteristics of an optimal formula. The nanoparticles obtained were assessed in terms of their physical properties, encapsulation efficiency, and skin permeation. The resulting nanoparticles (TMNP) exhibited a spherical morphology, had diameters of 175.417 ± 3.144 nm, a PDI of 0.346 ± 0.031 and ZP of 31.95 ± 1.09 mV. An encapsulation efficiency value of 17.42 ± 0.02% was considerably adequate to promote desirable activity towards IH. The nanoparticle exhibited enhanced penetration of drug compared to the unencapsulated form. This research is hoped to contribute to the expanding application of nanoparticle technology, particularly in the treatment of infantile hemangioma utilizing nanoparticles derived from natural sources.

Keywords: Nanoparticle, Pharmaceutical preparations, Biopolymer, Penetration Study, Infantile hemangioma.

Submitted: November 26, 2024. **Accepted:** April 7, 2025.

Cite this: Sulaiman M, Lukitaningsih E, Martien R, Danarti R, Wirohadidjojo YW. Polymeric Nanoparticle Formulation, Characterization and Penetration Study for Topical Delivery of Timolol Maleate. JOTCSA. 2025;12(2): 117-28.

DOI: https://doi.org/10.18596/jotcsa.1587817

***Corresponding author's E-mail:** lukitaningsih_end@ugm.ac.id

1. INTRODUCTION

Timolol maleate (TM) is a nonspecific beta receptor antagonist that has long been applied to treat cardiovascular diseases (1) and glaucoma (2,3). Recently, TM is also known as one of several potential drugs for the treatment of infantile hemangioma (IH) and has become a subject in many research studies (4). This trend has grown since the incidental finding of oral propranolol activity against IH back in 2008, while it was being used to treat cardiovascular abnormality in infants with IH (5). Regarding the fact that both drugs came from the same family, compared to its predecessor, TM is hypothesized to possess higher potency with lower side effects. Its inhibitory effects are mainly by controlling proliferation via vasoconstriction on hemangioma vascularization controlling angiogenesis (6) and apoptosis induction through beta adrenergic receptor signaling pathways (7) in IH management.

Despite its promising potential, most orally TM is eliminated shortly after being given due to the first pass effect; hence, the poor bioavailability profile (under 50%) (8). On the other hand, a relatively similar activity against IH but with lower side effects is observed in topically applied TM compared to oral propranolol (4) or topical corticosteroids (9). This is due to the fact that topical application can hinder the vast distribution of a drug and avoid many undesired systemic activities. In other research, it was also

proven that concurrent use with oral propranolol can enhance the effects while shortening the duration of medication at the same time (10).

Although timolol's topical dose form is highly effective, it has not been commercially accessible for treating IH. Thus far, numerous investigations and pharmacological trials have exclusively employed ocular drops or simple solutions (11). Moreover, common challenges in conventional topical delivery, such as poor resident time and penetration ability, are also present (12). The outermost layer of the skin, stratum corneum (SC) acts as an obvious obstacle in delivering drug substances, hence limiting the depth of penetration (13). That is why the majority of research regarding topically applied TM only applies to mild superficial and non-complicated conditions of IH. In other research, a topically applied TM still showed mild to medium side effects to the skin condition during treatment. Furthermore, a relatively long term cure is still observed in many cases treated with topical TM (14,15).

Nanotechnology offers a promising way out to solve problems that constantly join topical delivery. Although numerous studies have put forward the use of lipids and surfactants as superior choices due to skin barrier nature (16), natural polymers such as chitosan (CH) offer biocompatibility and penetration enhancing characteristics, which can turn out to be powerful substitutes (17). This research aims to explore the use of entirely natural materials instead of commonly used polyanions like tripolyphosphate (TPP) and poly (lactic-co-glycolic acid) (PLGA) in the production of nanoparticles through ionic gelation. The objective is to improve the effectiveness and safety of topically applied timolol maleate for the treatment of infantile hemangioma. Nanoparticles will be synthesized based on interactions between chitosan (CH) and acacia gum (AG) that occur upon simple stirring. Optimized formula will be obtained using simple lattice design with the help of Design Expert version 11.0 software. Based on the author's current understanding, while numerous studies have examined the application of nanoparticles for drug delivery in IH, this research makes complete use of environmentally friendly and readily obtainable materials and methods, while also employing comprehensive testing protocols as well as competitive results. This raises the possibility that basic nanoparticle technology could be utilized more frequently to improve the prognosis of treatment for infantile hemangiomas.

2. MATERIAL AND METHODS

2.1. Materials

Chitosan medium molecular weight (degree of deacetylation >75%) was purchased from local company CV Bio Chitosan Indonesia (Indonesia), Acacia gum was obtained from Fagron Pharmaceutical (Netherlands), Timolol maleate (99,98% analytical grade) was purchased from Octagon Chemical Limited (China). Acetic acid (99%, analytical grade) and anhydrous sodium acetate from Merck (New Jersey, USA). Ammonium acetate and Acetonitrile were of analytical grade, from Merck (New Jersey, USA) and Smartlab (Indonesia) subsequently.

2.2. Methods

2.2.1. Preliminary study

Each of the nanoparticle constituents was firstly prepared as a stock solution by accurate weighing and solubilizing with appropriate solvents (1% acetic acid for CH, water for AG and TM). Prior to the optimization process, a preliminary trial was conducted without the incorporated drug to find and appropriate working concentration range suitable for the formation of nanoparticles. This was done by creating a matrix table of nanoparticle formation according to the combination of five concentration variations of chitosan (CH) (0,1 - 0,8% w/v) and acacia gum (AG) (0,01- 0,08 % w/v). CH solution was poured into a magnetically stirred glass containing AG solution, both in acetate buffer pH 5 medium, followed by continuous stirring for 10 minutes. The resulting mixture was then observed by visual inspection and continued with size and polydispersity index measurements using particle size analyzer (PSA) Zetasizer Nano (Malvern Instrument, Malvern, UK) to ensure the desired formation of nanoparticles, and the lower and upper limits of working concentrations were determined based on that assessment.

2.2.2. Formula optimization

Optimization process was done by simple lattice mixture experimental method with the help of Design-Expert (Version 11, Stat-Ease Inc., MN, USA) software for further study regarding the effect of each polymer components of the nanoparticle. The two chosen independent variables were the percentage of CH and AG concentrations in the formula. The lower and upper concentrations of CH and AG were obtained from preliminary study results and inserted into the software. The concentration range of both components was then adjusted automatically by the software, as seen in Table I. A total of 11 formulas with five different combinations of CH and AG were acquired and used to synthesize the nanoparticle, this time with the addition of TM as an active component. As for formula F1, F2 and F5 were prepared thrice. A series concentration of AG in buffer pH 5 solution was mixed with drug substance and stirred for 5 minutes to complete the interaction and CH in acetate buffer solution was added subsequently, and the stirring continued for another 10 minutes. The final concentration of TM was fixed to 0,1% for each formula with total polymer of 0,42% (w/v). Desirability value was determined to attain best formula. The resultant formula was thereafter stored at a low temperature of 4º Celsius, while its stability was assessed to verify its suitability for the upcoming test. Assessment was made based on visual inspection (presence of sediment or turbid appearance) followed by size and polydispersity measurement using particle size analyzer instrument Zetasizer Nano (Malvern Instrument, Malvern, UK).

2.2.3. Characterization of optimum formula (TMNP)

Measurements of size and polydispersity index (PDI) can be conducted simultaneously by dynamic light scattering (DLS) method using PSA instrument

Zetasizer nano (Malvern instrument, Malvern, UK). Firstly, samples were prepared by diluting TMNP solution by 1:100 with acetate buffer pH 5. Subsequently, approximately 1 mL sample was put into a glass cuvette and measured at a scattering angle of 90º and a temperature 25º Celsius.

Zeta potential was measured based on the electrophoretic movement of particles upon the presence of electric current using Zetasizer Nano (Malvern instrument, Malvern, UK). Samples were prepared by mixing TMNP solution with acetate buffer at pH 5 in a ratio of 1:100 and placed into a dip cell cuvette for measuring zeta potential. The samples were later measured at a constant temperature of 25º Celsius. Data were collected in triplicate.

The size and morphology of the optimum nanoparticle formation were studied with photography technique using transmission electron microscopy (TEM) instrument (Jeol JEM-1400Flash, USA). This method is using a different technique in determining sizes, so it could also be complementary to size measurement by DLS method. Samples were prepared by a proper dilution of the optimum formula using water. A tiny amount of the sample solution was put on carbon coated copper grid and allowed to evaporate at ambient temperature. Measurement was conducted in vacuum conditions and read at appropriate magnification.

FTIR analysis was conducted to measure and study the possible interaction between components of nanoparticles. This can also be useful to make sure whether the obtained nanoparticles contain each component involved in the formation. For this, a Thermo-Nicolet iS 10 FTIR instrument equipped with a deuterated triglycines sulfate detector was used. A tiny amount of each pure CH, AG and TM powder and freeze-dried TMNP were milled with KBr powder to form a pellets and spectra were recorded between 4000 to 400 cm^{-1}.

Entrapment or encapsulation efficiency (%EE) was determined indirectly, in which the encapsulated drug can be hypothetically determined by measuring the concentration of free drug in the formula. In order to find the concentration of the free drugs, samples were first transferred into a 100 kDa MWCO ultrafiltration tube (Sartorius, Germany). The tube was later centrifuged at 2000 rpm until filtrate was separated and collected to be transferred into a different vial. The filtrate was mixed with mobile phase to reach proper dilution and filtered with 0.45 micron syringe filters and injected into an HPLC instrument with UV detectors. The HPLC system was run on Shimadzu LC-2050C instrument equipped with PDA detectors, using Phenomenex C18 (250 x 4,6 mm; 5 µm) column. A 20 µL diluted sample was injected to HPLC system using acetate buffer pH 3,5/acetonitrile 80:20 as mobile phase, 1 mL/min flow rate, and detection wavelength at 297 nm. All the measurements were done in triplicate and results were expressed in ± standard deviation. The result was marked as free drugs concentration in each formula and % Entrapment efficiency was calculated according to formula:

$$\%\ Entrapment\ Efficiency = \frac{Total\ weight\ of\ drug - Free\ drug}{Total\ weight\ of\ drug}\ x\ 100\ \% \quad (1)$$

2.2.4. Ex-vivo permeation study

To investigate the efficacy of the nano-formulation in facilitating the delivery of timolol maleate across the skin, a permeation study was conducted utilizing the PermeGear ILC07 automated diffusion system instrument (PermeGear, USA). The utilization of rat skin as a membrane barrier involved the collection of samples from euthanized animals, following the clearance of the Ethical Committee of the Faculty of Veterinary Medicine at Gadjah Mada University (EC no 72/EC-FKH/Eks./2023). The obtained skin was stretched onto a surgical tray, and the fat tissue was meticulously separated by the use of a scalpel and surgical blade. Subsequently, the skin was firmly affixed to the membrane bed, featuring a circular diffusion area of 1 cm in diameter. Clamping secured the attachment, orienting the stratum corneum towards the donor compartment. The receptor compartment was filled with a phosphate buffer solution at a constant flow rate, maintaining a pH of 5.5 and temperature at 32 ± 1 ºC. Prior to commencing the test, a 15-minute period was allocated for the purpose of running the instrument, so ensuring the saturation of the skin with a buffer solution. Subsequently, a series of samples (0.5 mL, 200 µg/mL) were subjected to exposure within the donor compartment, initiating the test at a time interval of 6 hours. A volume of 2.4 mL of the sample was collected at regular intervals of 30 minutes. Subsequently, the collected sample was diluted using the mobile phase, followed by filtration using a syringe filter with a pore size of 0.45 microns. Finally, the filtered sample was introduced into the High-Performance Liquid Chromatography (HPLC) system. The HPLC equipment was operated using identical parameters as those employed in the encapsulation efficiency assessment and has been verified to ensure the reliability. The data were subjected to analysis by producing a curve that depicted the accumulation of drugs per unit area as a function of time (18). The values of the steady state or maximum flux (Jss) and the lag time (Tlag) were determined by calculating the slope and x-intercept, respectively, from the linear section of the plot. All study were done in triplicate and data were served as mean ± standard deviation (SD). Statistical significance was determined by two sample T-test with P value < 0.05 was considered statistically significant.

3. RESULTS AND DISCUSSION

3.1. Orientation and Optimization

Timolol maleate nanoparticles (TMNP) were prepared using ionic gelation technique. In this method, nanoparticles are theoretically self-assembled due to ionic interaction between components with opposite charges, which in this case are CH and AG. This

technology has been utilized in the production of polymeric nanoparticles since it is simple and safe for the environment (19). An orientation study was conducted prior to optimization process to simplify the search for optimum concentration range in which nanoparticle was formed. This step was done by mixing CH and AG solutions in several variations of concentration. An acidic aqueous medium was used where the acetyl groups in chitosan's structure and the carboxylate groups of acacia gum are protonated and deprotonated subsequently to make sure the interaction (20). Furthermore, this state was maintained by the use of acetate buffer medium to avoid any pH change. The medium was adjusted to a pH of 5 so that it would be suitable for its intended purpose while avoiding any irritation to the skin's structure.

In the orientation study, nanoparticles were formed in a size of 125.9 to 256.0 nm with PDI between 0.071 and 0.420 (supplementary data). A visually good and desired result of nanoparticle characteristics was seen between the use of CH (0.2-0.4%) and AG (0.02-0.08%). On the contrary, the use of more than 0.4% CH in all ranges of AG resulted in undesirable characteristics such as more turbid solutions with higher size and/or polydispersity index results. It was also worth mentioning that the results became less predictable in that range of concentrations, making it much more difficult to control the outcome of the synthesis. It was concluded that increasing the concentration of CH in a formula produced lower-sized nanoparticles if the concentration of AG was fixed. This result was due to the formation of a more compact and enclosed structure being formed as CH more available. On the other hand, the higher the concentration of AG the bigger the size of the nanoparticle being produced. The reason behind this was because AG as a cross-linker with negative charge tend to be attached in the Np's surface when CH as a counter charge was no more available and apparently this could lead to a bigger size to be formed or trigger aggregation. As an outcome of this preliminary study, a range of 0.1 to 0.4% and 0.02 to 0.06 % for CH and AG subsequently were chosen to be the lower and upper limit working concentration on the next optimization step.

Table 1: Detailed characteristics (Size, polydispersity index (PDI) and zeta potentials (ZP)) of eleven formulas with different combination of chitosan (CH) and acacia gum (AG) in optimization process, n=3.

Formula code	Components (%w/v)			Characteristics		
	CH	AG	TM	Size (nm)	PDI	Zp (mV)
F1	0.4	0.02		172.6 ± 1.131	0.273 ± 0.003	34.1 ± 3.30
F2	0.34	0.08		210.9 ± 1.947	0.137 ± 0.032	39.0 ± 1.27
F3	0.355	0.065		204.3 ± 3.972	0.154 ± 0.004	35.9 ± 2.65
F4	0.4	0.02		175.3 ± 6.647	0.292 ± 0.004	31.0 ± 0.21
F5	0.37	0.05		196.8 ± 1.344	0.188 ± 0.007	40.5 ± 1.41
F6	0.4	0.02	0.1	177.8 ± 0.141	0.252 ± 0.022	34.6 ± 0.98
F7	0.37	0.05		194.1 ± 1.698	0.168 ± 0.004	39.3 ± 1.07
F8	0.385	0.035		189.2 ± 1.935	0.209 ± 0.024	35.5 ± 3.56
F9	0.34	0.08		210.8 ± 2.344	0.124 ± 0.009	40.7 ± 0.65
F10	0.37	0.05		194.3 ± 1.710	0.162 ± 0.018	38.3 ± 0.30
F11	0.34	0.08		211.6 ± 2.192	0.128 ± 0.029	39.7 ± 1.63

In the next step, the obtained lower and upper limits of concentration were used to find the optimum formula and to study the effect of each polymer in the formation of nanoparticles. A total of eleven formulas were determined by the Design-Expert software (Version 11, Stat-Ease Inc., MN, USA) with characteristics after synthesis, as shown in Table 1. A specific criterion was used to determine the most suitable formula: the lowest size and in-range PDI and zeta potential values were expected. Size was considered to be of a higher importance factor since, hypothetically, the lower the size, the better the penetration. Regarding the PDI and zeta potentials, it could be inferred that the optimal formula can be attained when both variables fall within their acceptable range values. The particle size (PS) values were obtained in nanometer range (172.6 ± 1.131 – 211.6 ± 2.192 nm) as seen in Table 1. Adequate precession was 37.96 with adjusted R2 (0.9770) was in reasonable agreement with predicted R2 (0.9684). A linear relationship was built with calculated equation for the PS analysis as seen on equation 1. Positive estimations of X1 (CH) and X2 (AG) suggested a rise in PS when CH and AG concentrations increased. It was also confirmed with the calculated equation that AG possessed much stronger effect on producing bigger size value than CH. The contour plot (Figure 1(a)) demonstrates that the incorporation of different polymer percentages has a direct effect on PS value. Greater CH concentrations yielded lower PS values, whereas higher AG concentrations tended to level up PS values, as determined by preliminary research.

$$PS = 392.38484 .X1 + 982.89766 .X2 \quad (2)$$

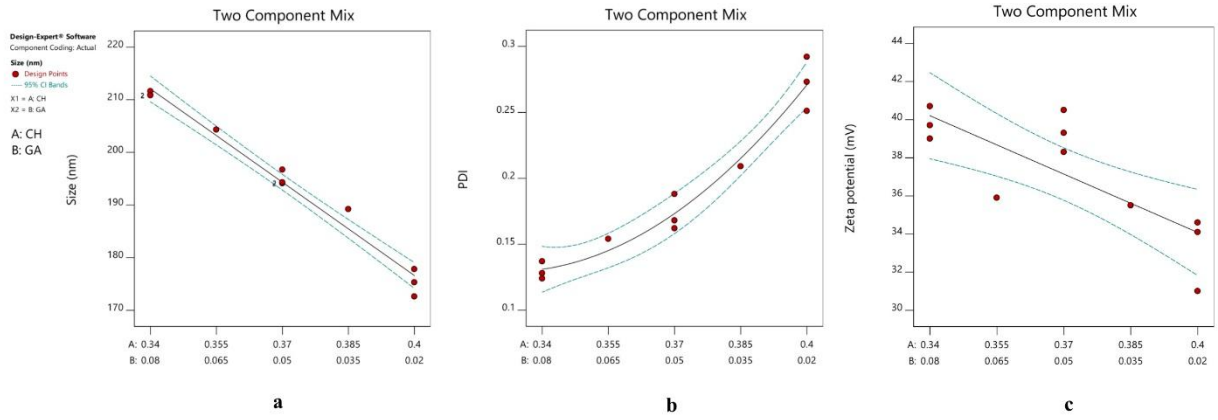

Figure 1: Result on chitosan and acacia gum (CH/AG) mixture at different concentration contour plot graph; Size (a), PDI (b) and Zeta potentials (c).

PDI analysis showed a good polydispersity value (0.124 ± 0.012 – 0.292 ± 0.004) as depicted in Table 1, meaning that the resulting eleven formulas were nearly uniform in size. Adequate precession was 20.05, and adjusted R^2 (0.9490) was in reasonable agreement with predicted R^2 (0.9187). Positive estimates of X_1 and X_2 indicated an increase in PDI as the amounts of CH and AG increased, while the interaction of both components tended to lower the PDI value. This conclusion is true because the interaction of two polymers with different charges tends to produce a more compact and homogenous nanoparticle structure. A quadratic relationship between polymer ratio and PDI was seen in equation 2. From the calculated equation, it can be concluded that AG possessed a stronger effect on producing a higher PDI value than CH and interaction between the two would lower PDI value. The contour plot depicted in Figure 1(b) illustrates the relationship between the inclusion of varying polymer fractions and the resulting impact on the PDI value. Preliminary step findings indicate that an increase in CH concentrations resulted in higher PDI values, while higher AG concentrations were seen to have a tendency to decrease PDI values. The accuracy of this outcome can be attributed to the pivotal role played by AG as the decisive factor in the enhanced production of nanoparticles.

PDI= 0.872862 .X1 + 8.36675 .X2-30.70205 X1.X2 (3)

Zeta potential measurement results can be observed in Table 1 where all the formulas showed varied positive charges (between 30.8 ± 1.00 and 40.7 ± 0.656 mV). These results were reasonable since CH dominates the charge of the formed nanoparticles. Adequate precession was 8.5063, and adjusted R2 (0.5824) was in reasonable agreement with predicted R2 (0.4713). The calculated linear equation was built for the particle size analysis, as seen in equation 3, and it should be highlighted that the interaction of both polymers resulted in a reduction in the positive charge of the nanoparticle core. The results were much more complicated when different combinations of CH and AG were being used, as observed in Figure 1(c). The resultant charge tends to rise and fall depending on the ratio between the two polymers, although all formulas possessed an acceptable range of surface charge.

ZP= 79.29260 .X1-178.34388 .X2 (4)

The results of the optimum formula prediction from the software yield one solution with concentrations of 0.4 and 0.02% (w/v) for CH and AG, respectively, and a desirability value of 0.897. The formula that demonstrates the highest level of efficiency was expected to yield a particle size (PS) value of 176.612 nm, a polydispersity index (PDI) of 0.271, and a zeta potential of 34.084 mV. The model's validity was confirmed through six replicated confirmation attempts of nanoparticle production, resulting in an average size of 175.417 ± 3.144 nm, a PDI of 0.346 ± 0.031, and a ZP of 31.95 ± 1.09 mV.

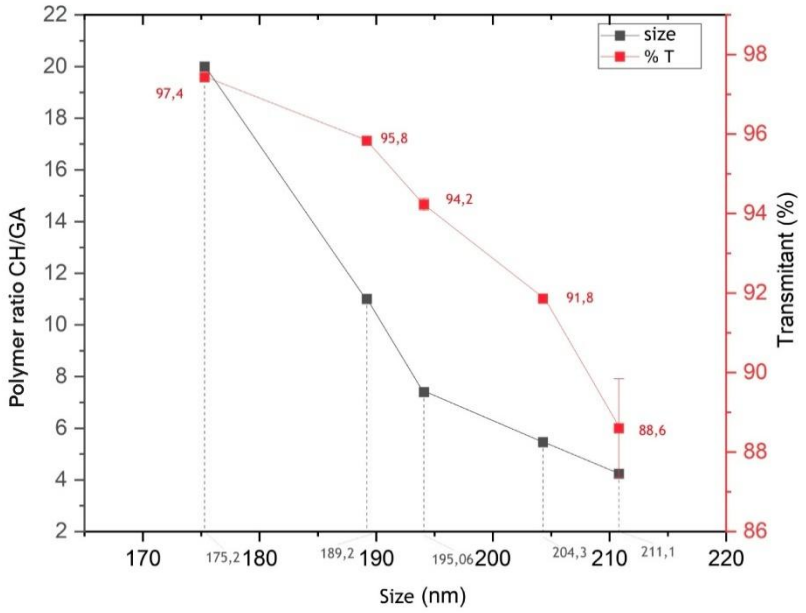

Figure 2: Graph depicting the correlation among polymer ratio, size, and transmittance during the optimization phase.

Visual observation showed a distinct dispersion of nanoparticles without sedimentation (data not shown). This outcome is attributable to the comparatively small amount and size of nanoparticles produced, rendering them invisible to the naked eye. Consequently, alongside ocular observation, transmittance values were obtained utilizing a spectrophotometer within the visible wavelength range of 650 nm. This measurement aims to guarantee the formation of particles in the carrier solution, as a theoretically clear and particle-free solution should yield a transmittance value approaching 100%, allowing nearly all light to pass through the examined solvent layer. The transmittance values measured using a spectrophotometer on nanoparticle samples including various polymer combinations are illustrated in Figure 2. The results indicate that the formation of nanoparticles is characterized by a transmittance value of less than 100%. Moreover, a reduced concentration ratio of CH/GA corresponds to a lower transmittance value. This can possibly be regarded as a consequence of the increased production of nanoparticles. The results indicate that GA is a significant variable in nanoparticle formation, as it serves as a cross-linker that interlinks the CH polymer framework, facilitating the creation of nanoparticles. Furthermore, a negative relationship exists between the size of the produced nanoparticles and the transmittance value; specifically, smaller particle sizes correspond to elevated transmittance values, a phenomenon that can be elucidated by a comparable premise.

Both the material and methods employed in this research offered several advantages. Chitosan and acacia gum in this study are both water-soluble polymers which come from natural sources; hence, they are much more economical and sustainable compared to other materials. Ionic gelation relies only on simple stirring while also avoiding the use of toxic organic solvents, making it known for its ease, cheapness and reproducibility in controlling the desired nanoparticle characteristics. The pH range selected was about 5 because at pH levels below 3.5, the carboxylic groups of GA became protonated, which inhibited the ionic interactions with CH. On the other hand, at pH values above 6.0, close to its pKa, the degree of ionization of Chitosan and its solubility dropped (20). In this study, chitosan and acacia gum were first dissolved in acetate buffer to minimize the pH change during mixing and storing since acidity has a direct effect on the formation of stable chitosan nanoparticles. Moreover, the slightly acidic pH is considered safe and compatible to the natural characteristic of human skin (21).

3.2. Formula Characterization

3.2.1. Size and morphology

In the beginning step of measurements using particle size analyzer, samples were first mixed with their medium (1:100) to reach proper dilution. An acetate buffer with pH 5 was the actual medium of the nanoparticles and has been chosen to dilute the samples; hence, the affecting factors, such as a change in medium viscosity or ionization can be neglected. After the dilution, samples were put in a glass cuvette and measured. The size distribution was obtained and serves as intensity distribution curve, as observed in Figure 3 (a). In addition, the zeta potential graph exhibits a single peak with a narrow band, as seen in Figure 3 (b) which showed ZP value for one of the samples during the optimization process was found to be +34 mV. Adequate stability can be attained, which was supported by the optimal ZP value. This result can later be compared with TEM result. As shown in Figure 4, the morphological properties of the optimized formula were studied using TEM and the photographic view revealed almost spherical particles. The surface of these vesicles looked to be smooth, non-aggregated, and evenly scattered. The

results suggested that such simple synthesis and interaction of two polymers can also creates formation of stable nanoparticles with spherical properties. The TEM micrograph and Zetasizer measurements were in good agreement regarding the mean particle size. As indicated previously, the reported PS was less than 200 nm, which may theoretically achieve good skin penetration and reach the dermis, where IH typically emerges. The dilution step prior to measurement is crucial since DLS method is based on measurement of particles Brownian motion, so it is sensitive to factors affecting the Brownian motion. A very dense particles in its medium can not move freely, thus rated as having a bigger size than the actual size. This can lead to false measurement. This is also applied to aggregated particles. Moreover, as previously explained, the formation of a more numerous and uniform particle population results in a lower PDI value when more AG is present.

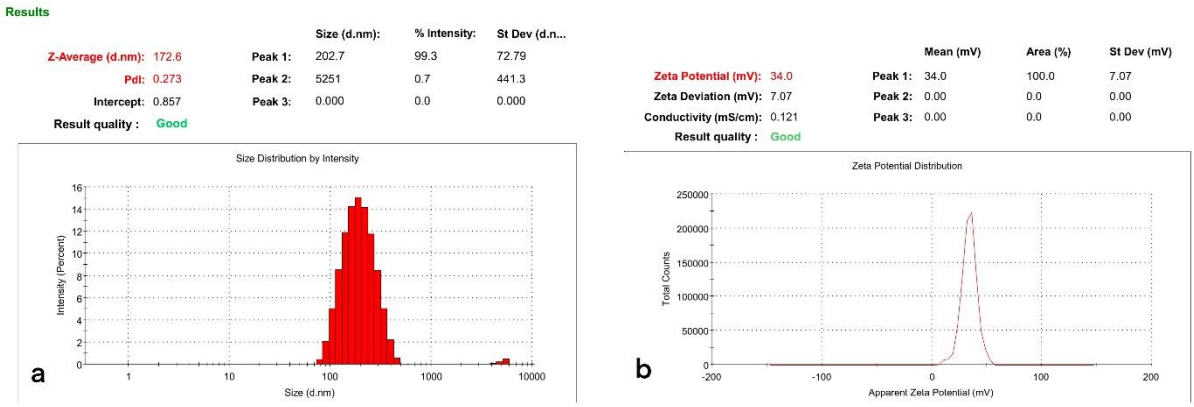

Figure3: Example of Particle size distribution (a) and zeta potential distribution (b) measurement of TMNP formula.

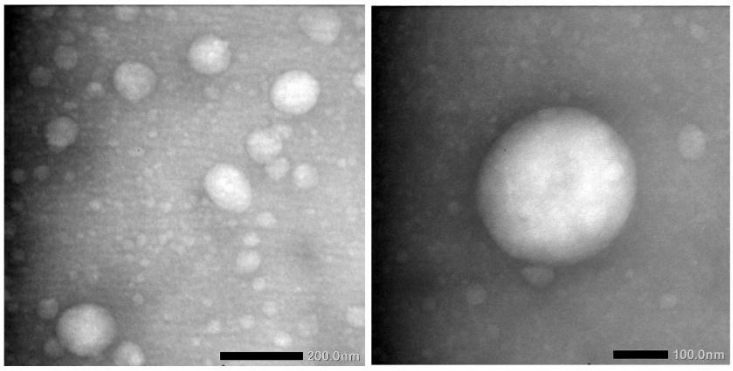

Figure 4: TEM micrograph of optimized formula (TMNP). The morphological properties showed smooth surface and evenly scattered particles with size under 200 nm.

Size is the most unique and important characteristic that defines nanoparticles compared to other delivery systems. Together with its distribution, they both can be determined using dynamic light scattering (DLS) method, which is a principal method employed by particle size analyzer instruments. DLS method collects signals, which are fluctuations of scattering light that happen upon collision between projected light and Brownian moving particles. The signals then transformed mathematically to produce a prediction size of the particle being measured. This definitive size is called hydrodynamic size, which represent hypothetical size of a spherical particle that has the same Brownian motion as the particle being measured (22). That is why results from DLS method are sometimes compared to other methods, such as photography method using Transmission Electron Micrograph (TEM) technique, to ensure the accuracy of the measurement. As for zeta potentials, PSA instrument works based on the measurement of particles' mobility in the event of electric current. In brief, this motion is depicting the surface charge of a nanoparticle and is affected by several factors such as charge of the inner core, ionization of the medium and attached constituent on nanoparticle's surface (23). As a result, zeta potential is a net charge measured as a resultant of those affecting factors. This theory confirms the result in this study where all the zeta potential were in positive value due to CH existence in the core and tend to be lower when more negatively charge AG entangled in the surface of the TMNP. Moreover, the use of acetate buffers as a medium negated the change of TMNP environment that can trigger different particle movements.

3.2.2. FTIR analysis

Each individual component of nanoparticles and TMNP formula itself were analyzed for their structural and possible interactions in nanoparticle formation (Figure 5). Chitosan (CH) powder showed the characteristics of symmetric vibrational bands of -OH and -NH groups at 3376 cm^{-1}. The bands at 2920 cm^{-1} and 2878 cm^{-1} represented C-H stretching vibrations. Since chitosan is not usually fully

deacetylated, there was still a band at 1654 cm^{-1} for the stretching vibrations of C=O (Amide I) followed by the presence of 1598 cm^{-1} band for N-H bending vibration (Amide II). Moreover, stretching vibration of C-O-C in chitosan structure were represented by bands 1077 and 1030 cm^{-1}. This result is in correspondence with another study (24). The acacia gum (AG) spectrum showed a typical band at 3398 cm^{-1} that corresponded to O-H stretching vibration of glycosidic ring, while the band at 2932 cm^{-1} showed the C-H stretching. The C-O stretching vibration of primary alcohol was present at 1070 cm^{-1}. This finding is further corroborated by the outcomes of prior studies conducted by other researchers (25). The CH-AG mixture compounds exhibited a peak at 3419 cm^{-1}, which can be attributed to the stretching vibration of overlapping -NH_2 and -OH groups. Analysis on the CH-AG ionic interaction showed a considerable shift in the carbonyl-amide area due to the interaction of both biopolymers. The N-H bending vibration of -NH_3^+ groups (band at 1598 cm^{-1}) and the asymmetric and symmetric -COO stretching vibrations at 1608 cm^{-1} and 1420 cm^{-1}, respectively, were slightly shifted to 1567 cm^{-1} and 1414 cm^{-1}, suggesting the presence of electrostatic interaction between the amine groups of CH and carboxyl groups of AG. Additionally, the C-N stretching vibration (band at 1154 cm^{-1}) was present but slightly shifted to 1152 cm^{-1}. This finding was also documented in other research publications (26).

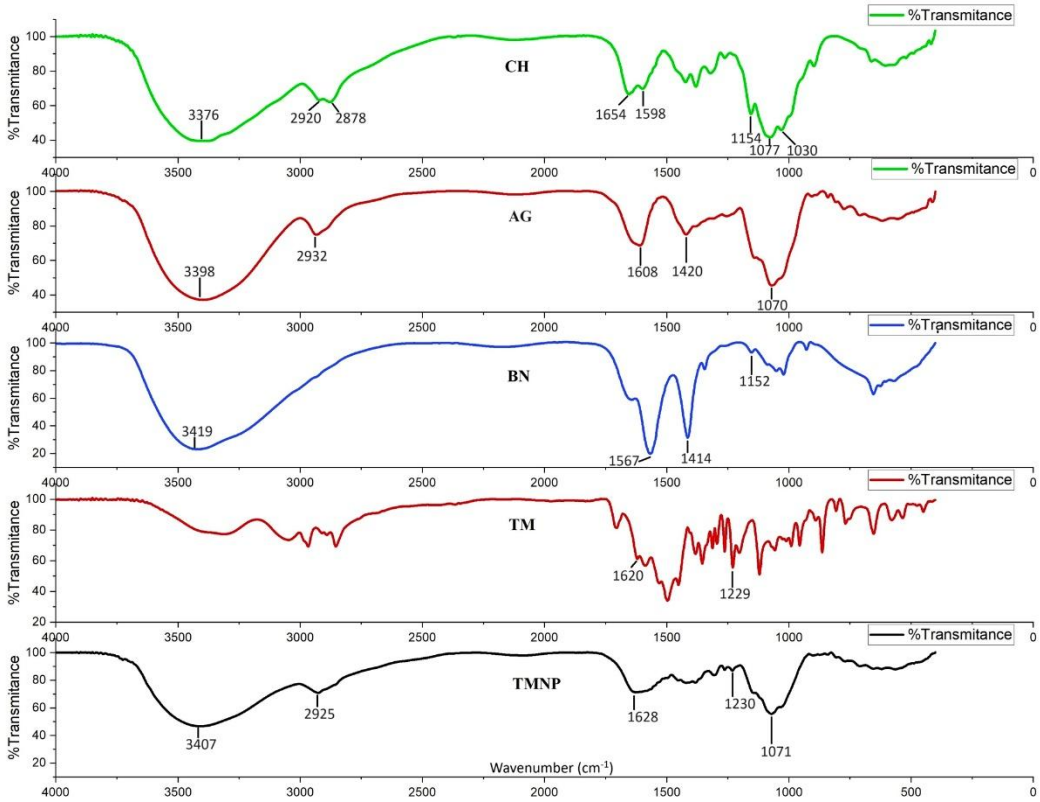

Figure 5: Infra red spectrum analysis of nanoparticles (TMNP) and constituents (CH: chitosan, AG: acacia gum, BN: blank nanoparticle, TM: timolol maleate)

The spectrum of pristine timolol maleate (TM) showed a characteristic broad band of N-H stretching vibration at 3310 cm^{-1} from the secondary amine group. The two weak broad bands at 3046 and 2966 cm^{-1} confirmed the presence of secondary alcohol's O-H stretching. Peaks at 2910 and 2853 cm^{-1} belonged to aliphatic C-H stretching vibration. A strong peak at 1705 cm^{-1} belonged to C=O stretching vibration of the aliphatic carbonyl group of maleic acid. C=N stretching vibration of imine group was observed by the presence of a peak at 1620 cm^{-1}. N-H bending vibration of the secondary amine appeared at 1496 cm^{-1}. A peak appeared at 1229 cm^{-1} belonged to C-N stretching vibration of the secondary amine, while 1202 and 1120 cm^{-1} corresponded to C-O stretching vibration of vinyl ether and secondary alcohol, respectively. Those peaks can also be observed and is comparable to that in several literatures (27). The IR spectra of the TMNP formula, which is a combination of all the analyzed components, exhibits characteristic bands that are also observed in the individual constituent molecules. In summary, the characteristic bands of CH and AG, which indicate the presence of overlapping O-H and N-H stretching vibrations, were observed at 3407 cm^{-1}. Additionally, a band at 2925 cm^{-1}, corresponding to C-H stretching vibrations of polysaccharide components, was observed due to the presence of both polymers. The presence of the C=N stretching vibration of the imine group in the TM structure was confirmed by a shift at 1628 cm^{-1}, compared to the previous value of 1620 cm^{-1}. The C-N stretching vibration of the secondary amine groups was observed at 1230 cm^{-1}, which is a shift from the previous value of from 1229 cm^{-1}. In addition, TMNP exhibited a band at 1071 cm^{-1}, indicating the stretching vibration of the C-O bond in the -OH group of both CH and AG structures.

3.3. Stability on Cold Temperature Storage

Throughout this research, the nanoparticle preparations under investigation were held at low temperatures, and simple stability testing was conducted to establish whether they were appropriate for future study. Table II displays the test results, based solely on two samples. The table shows that the characteristics of the nanoparticles held in the cooler (4 ºC) were similar to those of the freshly synthesized samples even after up to three months of storage (P value > 0.05).

Table 2: Detailed characteristics (size, polydispersity index (PDI) and zeta potentials (ZP)) of samples after 3 month 4 ºC storage.

Samples	Size (nm)		PDI		ZP (mV)	
	Initial	3 months	Initial	3 months	Initial	3 months
TMNP 1	173.7±1.021	174.9±4.743	0.284 ±0.031	0.329±0.064	30.4±1.93	29.9±5.44
TMNP 5	197.4±1.401	199.2±12.89	0.175±0.008	0.220±0.104	40.5±1.41	39.7±1.63

3.4. Entrapment Efficiency

In this study, the determination of %EE was conducted indirectly by measuring free (unentrapped) drug centrifugation technique. The process of isolating unbound drug molecules from nanoparticles is a pivotal stage in the calculation of the percentage encapsulation efficiency. The dialysis method employing a semi-permeable membrane and the centrifugation method utilizing a specific force are the two most commonly employed approaches. The dialysis method is characterized by a significant time requirement, whereas the centrifugation method carries the inherent danger of compromising nanoparticle stability and promoting drug leakage during the procedure. This work used a Vivaspin (Sartorius, Germany) porous tube with a pore size of 100 kDa to facilitate the utilization of low-speed centrifugation and reduce errors. The HPLC method employed in this study has undergone validation and demonstrated its selectivity, accuracy, and precision in quantifying the content of timolol maleate in our nanoparticle samples. Once the free drug has been meticulously extracted from the nanoparticle suspension and appropriately prepared before being introduced into the High-Performance Liquid Chromatography (HPLC) system, the concentration of the free drug may be determined by analyzing the collected samples. The %EE value for the optimal formula was determined to be 17.41 ± 0.015 % based on calculations utilizing the previously stated equation.

3.5. Ex-vivo Penetration Study

In many penetration studies, artificial membranes are frequently employed as substitutes for human skin in penetration tests, mostly driven by ethical considerations. In contrast, several animal models have been proposed as potential substitutes for human skin, encompassing porcine (28), rodent (29), guinea pig, and snake shading skin (30). Nevertheless, these choices present a limitation in relation to the anticipated variation in barrier composition (18). In this study, the ability of polymer nanoparticles to assist timolol maleate penetration was assessed using animal skin (Sprague Dawley rat). The percutaneous penetration profile of timolol maleate in nano-formulation (TMNP) and in solution (TMS) are depicted in Figure 6(a). The figure illustrates that the permeation of TM in nanoparticle group was always greater than that of the naked TM group. It is noteworthy that the disparity in the buildup of permeant became more apparent after a period of 2 hours until the end of the experiment. Moreover, Figure 6(b) clearly illustrates that the nanoparticle group exhibits a higher percentage of drug penetration at the end of experiment. However, the statistical analysis indicated that there were no significant differences between the two groups. This is likely because the test animals were inherently diverse, leading to a wide range of data for each replicate. Nevertheless, this outcome serves as evidence that the benefits of chitosan as a permeation enhancer, particularly in nanoparticle form, significantly contribute to the increased penetration of TM.

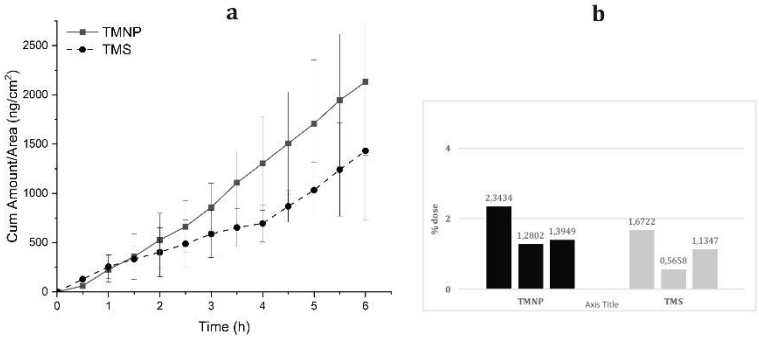

Figure 6: Rat skin penetration profile of timolol maleate nanoparticle (TMNP) and solution (TMS) (a), total penetration served as % dose between TMNP (mean = 1.67 ± 0.58 %) and TMS (mean = 1.12 ± 0.55 &) (b). Data were collected in triplicate and served as mean ± SD.

Timolol maleate, a type of beta blocker, is considered less suited for topical and transdermal application compared to other beta blockers like propranolol and betaxolol (31). A previous experiment has examined the permeation of timolol into human skin using a concentration of 10 mg/mL of timolol maleate. These experiments revealed a minimal penetration rate (1.06 +/- 0.75%) throughout a 4-hour testing period. In addition, the utilization of various permeation enhancers has the potential to significantly increase the absorption of timolol maleate into the epidermis, resulting in a rise from around one percent to multiple times that quantity throughout the 24-hour testing duration (32). In this study, chitosan was utilized as a delivery agent with permeation-enhancing properties. In recent years, significant research has been performed to evaluate the capacity of chitosan and its derivatives to improve permeability. This is accomplished through the use of both bio-adhesion and a transitory rupture of the cellular membrane's tight junctions. Chitosan's cationic nature enables its interaction with the anionic tight junctions of dermal cells, resulting in pore dilatation (33).

Table 3 displays the measured values for flux and lag time of the study. Although the statistical analysis does not show a significant difference between the results of the two samples, it is evident that the average lag time of the TMNP formula is smaller than that of TMS. The steady state flux value exclusively determines the rate at which the drug moves after it has reached a state of saturation in the skin layers, which may not vary significantly once the steady state has been attained. Nevertheless, the lag time value was greater in the TMNP formula, indicating the nanoparticle formula's capacity to enhance penetration. In combination with the shape of the penetration profile curve and the percentage of drug that was transported by the end of the study, it was evident that the nano-formulation improved the delivery of the drug. This study employed rat skin, which offers benefits such as comparable anatomical features to humans and cost-effectiveness and accessibility. Nevertheless, the permeability of mouse skin is comparatively greater than that of human skin so it would be good to conduct further studies using human skin as a comparison (34).

Table 3: Flux (Jss) and lag-time values in timolol maleate penetration study across rat skin in nanoparticle formulation (TMNP) and basic solution (TMS).

Formulation type	Jss ($ng/cm^2.h^{-1}$)	Lag time (h)
TMNP	619.54	0.77
	325.59	0.66
	376.12	0.88
Average	440.41 ± 157.17	0.77 ± 0.11
TMS	620.77	3.66
	166.33	0.68
	295.89	1.28
Average	360.69 ± 234.15	1.87 ± 1.58

4. CONCLUSION

This study demonstrates the successful synthesis of nanoparticles composed of chitosan and acacia gum, utilizing a straightforward technique that eliminates the need for toxic solvents. These nanoparticles were designed to serve as carriers for the drug timolol maleate, specifically for the topical treatment of infantile hemangioma. The effectiveness of this synthesis method was confirmed through various characterization techniques, which collectively provide consistent evidence. This study confirms the feasibility of using a safe biopolymeric incorporation for the treatment of infantile hemangioma, an illness that mostly affects a vulnerable group, mainly infants. Furthermore, the formula exhibits commendable stability for extended periods of storage and possesses an optimal size that facilitates both effective penetration and satisfactory retention inside the skin layer, so ensuring a safer therapeutic approach. The findings of this study provide evidence to endorse the utilization of natural components for enhancing nanotechnology's efficacy in addressing challenges related to medication delivery, particularly in the context of topical treatment for infantile hemangiomas.

5. CONFLICT OF INTEREST

The authors declared no conflict of interest.

6. ACKNOWLEDGMENTS

We expressed our gratitude for the implementation of this research which was carried out through a funding by The Final Project Recognition Grant Gadjah Mada University (Number 5075/UN1.P.II/Dit-Lit/PT.01.01/2023) in 2023.

7. REFERENCES

1. Satterfield KR, Chambers CB. Current treatment and management of infantile hemangiomas. Surv Ophthalmol [Internet]. 2019 Sep 1;64(5):608–18. Available from: <URL>.

2. Cuggino JC, Tártara LI, Gugliotta LM, Palma SD, Alvarez Igarzabal CI. Mucoadhesive and responsive nanogels as carriers for sustainable delivery of timolol for glaucoma therapy. Mater Sci Eng C [Internet]. 2021 Jan 1;118:111383. Available from: <URL>.

3. Negri L, Ferreras A, Iester M. Timolol 0.1% in Glaucomatous Patients: Efficacy, Tolerance, and

Quality of Life. J Ophthalmol [Internet]. 2019 May 2;2019(1):4146124. Available from: <URL>.

4. Wu HW, Wang X, Zhang L, Zheng JW, Liu C, Wang YA. Topical timolol vs. oral propranolol for the treatment of superficial infantile hemangiomas. Front Oncol [Internet]. 2018 Dec 18;8(DEC):605. Available from: <URL>.

5. Tiemann L, Hein S. Infantile hemangioma: A review of current pharmacotherapy treatment and practice pearls. J Pediatr Pharmacol Ther [Internet]. 2020 Sep 1;25(7):586–99. Available from: <URL>.

6. Liviskie CJ, Brennan CC, McPherson CC, Vesoulis ZA. Propranolol for the treatment of lymphatic malformations in a neonate – A case report and review of literature. J Pediatr Pharmacol Ther [Internet]. 2020 Mar 1;25(2):155–62. Available from: <URL>.

7. Macca L, Altavilla D, Di Bartolomeo L, Irrera N, Borgia F, Li Pomi F, et al. Update on treatment of infantile hemangiomas: What's new in the last five years? Front Pharmacol [Internet]. 2022 May 26;13:879602. Available from: <URL>.

8. Morsi NM, Aboelwafa AA, Dawoud MHS. Improved bioavailability of timolol maleate via transdermal transfersomal gel: Statistical optimization, characterization, and pharmacokinetic assessment. J Adv Res [Internet]. 2016 Sep 1;7(5):691–701. Available from: <URL>.

9. Danarti R, Ariwibowo L, Radiono S, Budiyanto A. Topical timolol maleate 0.5% for infantile hemangioma: Its effectiveness compared to ultrapotent topical corticosteroids - A single-center experience of 278 cases. Dermatology [Internet]. 2016 Jan 10;232(5):566–71. Available from: <URL>.

10. Gong H, Xu D peng, Li Y xiao, Cheng C, Li G, Wang XK. Evaluation of the efficacy and safety of propranolol, timolol maleate, and the combination of the two, in the treatment of superficial infantile haemangiomas. Br J Oral Maxillofac Surg [Internet]. 2015 Nov 1;53(9):836–40. Available from: <URL>.

11. Chen ZY, Wang QN, Zhu YH, Zhou LY, Xu T, He ZY, et al. Progress in the treatment of infantile hemangioma. Ann Transl Med [Internet]. 2019 Nov;7(22):692–692. Available from: <URL>.

12. Benson HAE, Grice JE, Mohammed Y, Namjoshi S, Roberts MS. Topical and transdermal drug delivery: From simple potions to smart technologies. Curr Drug Deliv [Internet]. 2019 May 29;16(5):444–60. Available from: <URL>.

13. Ghasemiyeh P, Mohammadi-Samani S. Potential of nanoparticles as permeation enhancers and targeted delivery options for skin: Advantages and disadvantages. Drug Des Devel Ther [Internet]. 2020 Aug 12;Volume 14:3271–89. Available from: <URL>.

14. Püttgen K, Lucky A, Adams D, Pope E, McCuaig C, Powell J, et al. Topical timolol maleate treatment of infantile hemangiomas. Pediatrics [Internet]. 2016 Sep 1;138(3):e20160355. Available from: <URL>.

15. Wu HW, Liu C, Wang X, Zhang L, Yuan W, Zheng JW, et al. Topical application of 0.5% timolol maleate hydrogel for the treatment of superficial infantile hemangioma. Front Oncol [Internet]. 2017 Jun 27;7:137. Available from: <URL>.

16. Zanela da Silva Marques T, Santos-Oliveira R, Betzler de Oliveira de Siqueira L, da Silva Cardoso V, Maria Faria de Freitas Z, Barros RCSA, et al. Development and characterization of a nanoemulsion containing propranolol for topical delivery. Int J Nanomedicine [Internet]. 2018 May 14;13:2827–37. Available from: <URL>.

17. Ma J, Wang Y, Lu R. Mechanism and application of chitosan and its derivatives in promoting permeation in transdermal drug delivery systems: A review. Pharmaceuticals [Internet]. 2022 Apr 10;15(4):459. Available from: <URL>.

18. Neupane R, Boddu SHS, Renukuntla J, Babu RJ, Tiwari AK. Alternatives to biological skin in permeation studies: Current trends and possibilities. Pharmaceutics [Internet]. 2020 Feb 13;12(2):152. Available from: <URL>.

19. Muhtadi WK, Novitasari L, Danarti R, Martien R. Development of polymeric nanoparticle gel prepared with the combination of ionic pre-gelation and polyelectrolyte complexation as a novel drug delivery of timolol maleate. Drug Dev Ind Pharm [Internet]. 2020 Nov 1;46(11):1844–52. Available from: <URL>.

20. Vuillemin ME, Michaux F, Muniglia L, Linder M, Jasniewski J. Gum Arabic and chitosan self-assembly: Thermodynamic and mechanism aspects. Food Hydrocoll [Internet]. 2019 Nov 1;96:463–74. Available from: <URL>.

21. Schafer N, Balwierz R, Biernat P, Ochędzan-Siodłak W, Lipok J. Natural ingredients of transdermal drug delivery systems as permeation enhancers of active substances through the *Stratum Corneum*. Mol Pharm [Internet]. 2023 Jul 3;20(7):3278–97. Available from: <URL>.

22. Modena MM, Rühle B, Burg TP, Wuttke S. Nanoparticle characterization: What to measure? Adv Mater [Internet]. 2019 Aug 30;31(32):1901556. Available from: <URL>.

23. Dukhin AS, Xu R. Zeta-potential measurements. In: Characterization of Nanoparticles [Internet]. Elsevier; 2020. p. 213–24. Available from: <URL>.

24. Akinluwade K, Oyatogun G, Alebiowu G, Adeyemi I, Akinwole I. Synthesis and characterization of polymeric nanoparticles formed from cowry shells and acacia gum extracts. J Adv Biol Biotechnol [Internet]. 2017 Jan 10;14(1):1–8. Available from: <URL>.

25. Ta Q, Ting J, Harwood S, Browning N, Simm A, Ross K, et al. Chitosan nanoparticles for enhancing drugs and cosmetic components penetration through

the skin. Eur J Pharm Sci [Internet]. 2021 May 1;160:105765. Available from: <URL>.

26. de Oliveira JL, Campos EVR, Pereira AES, Nunes LES, da Silva CCL, Pasquoto T, et al. Geraniol encapsulated in chitosan/gum arabic nanoparticles: A promising system for pest management in sustainable agriculture. J Agric Food Chem [Internet]. 2018 May 30;66(21):5325–34. Available from: <URL>.

27. Chavda D, Thakkar V, Soni T, Gandhi T. Formulation and in vitro-in vivo evaluations of timolol maleate viscous eye drops for the treatment of glaucoma. Eur J Biomed Pharm Sci [Internet]. 2016;3(9):573–85. Available from: <URL>.

28. Rahma A, Lane ME, Sinkó B. A comparative study of the in vitro permeation of 2-phenoxyethanol in the skin PAMPA model and mammalian skin. Int J Pharm [Internet]. 2023 Mar 25;635:122692. Available from: <URL>.

29. Todo H. Transdermal permeation of drugs in various animal species. Pharmaceutics [Internet]. 2017 Sep 6;9(3):33. Available from: <URL>.

30. Praça FSG, Medina WSG, Eloy JO, Petrilli R, Campos PM, Ascenso A, et al. Evaluation of critical parameters for in vitro skin permeation and penetration studies using animal skin models. Eur J Pharm Sci [Internet]. 2018 Jan 1;111:121–32. Available from: <URL>.

31. Chantasart D, Hao J, Li SK. Evaluation of skin permeation of β-blockers for topical drug delivery. Pharm Res [Internet]. 2013 Mar 4;30(3):866–77. Available from: <URL>.

32. Soni S, Jain SK, Jain NK. Effect of penetration enhancers on transdermal delivery of timolol maleate. Drug Dev Ind Pharm [Internet]. 1992 Jan 20;18(10):1127–35. Available from: <URL>.

33. Iyer A, Jyothi VGSS, Agrawal A, Khatri DK, Srivastava S, Singh SB, et al. Does skin permeation kinetics influence efficacy of topical dermal drug delivery system? J Adv Pharm Technol Res [Internet]. 2021 Oct 1;12(4):345–55. Available from: <URL>.

34. Supe S, Takudage P. Methods for evaluating penetration of drug into the skin: A review. Ski Res Technol [Internet]. 2021 May 23;27(3):299–308. Available from: <URL>.

JOTCS A
Journal of the Turkish Chemical Society
Section: A
Chemistry

TURKISH CHEMICAL SOCIETY

Determination of Antioxidant Capacities of Some Dietary Supplements by Spectrophotometric and Chromatographic Methods

Aslı Demir[1], Kevser Sözgen Başkan[1]*, Sema Demirci Çekiç[1]

[1]İstanbul University-Cerrahpaşa, Department of Chemistry, 34320 Avcılar, İstanbul, Türkiye.

Abstract: The main objective of this study is to propose standard analytical methods for the determination and comparison of plant-specific antioxidant components found in some herbal products (sold as dietary supplements). Numerous studies indicate that nutritional supplements can offer medical benefits due to their content of hydrophilic and lipophilic molecules as well as natural extracts or synthetic compounds with antioxidant properties. While these products are marketed as antioxidant boosters, there is a limited amount of data available on the antioxidant activity and bioactive compound content of commercially available formulations. Therefore, in our study, tablet and capsule forms of ground grape seed, rosemary, bitter melon, and ginkgo biloba plants containing polyphenol-type compounds known for their antioxidant properties were investigated. The total polyphenol contents (TPC) of these products were determined by the Folin-Ciocalteu method, and total antioxidant capacities (TACs) were determined by CUPRAC and ABTS methods. The HPLC system was used to detect and quantify the components responsible for antioxidant capacity, and the most appropriate chromatographic analysis methods were suggested for each sample. Total antioxidant capacity values as trolox (TR) equivalent (mmol TR/g) determined by CUPRAC and ABTS methods are 0.90 ± 0.07 and 0.72 ± 0.17 for grape seed, 0.79 ± 0.05 and 0.41 ± 0.09 for rosemary, 0.08 ± 0.006 and 0.11 ± 0.05 for bitter melon, 0.12 ± 0.01 and 0.14 ± 0.02 for ginkgo biloba, respectively. These findings were correlated with HPLC data, and components contributing to the antioxidant capacity were identified.

Keywords: Dietary supplements, grape seed, rosemary, bitter melon, ginkgo biloba.

Submitted: January 3, 2025. **Accepted:** April 15, 2025.

Cite this: Demir A, Sözgen Başkan K, Demirci Çekiç S. Determination of Antioxidant Capacities of Some Dietary Supplements by Spectrophotometric and Chromatographic Methods. JOTCSA. 2025;12(2): 129-40.

DOI: https://doi.org/10.18596/jotcsa.1506003

***Corresponding author's E-mail:** sozgen@iuc.edu.tr

1. INTRODUCTION

Food and good nutrition are the basis of human existence and healthy life (1,2). To live a quality life, the food we eat must have high nutritional quality. Recently, the consumption of commercially prepared and processed foods has become widespread because they are practical. These foods are exposed to physical and chemical transformations as a result of some processes (for example, refined sugar, bran-free flour, skimmed milk, margarine, etc.). These operations mean that their important properties are lost. As a result, wrong eating habits develop in society, and accordingly, health problems caused by malnutrition appear. Because the basic substances the body needs (vitamins, proteins, carbohydrates, minerals, oils, etc.) can only be met by a sufficient and balanced diet (3,4). The opposite situation causes the immune system to weaken gradually. Numerous epidemiological and clinical studies link the consumption of antioxidant-rich fruits, vegetables, plant-based drinks, and whole grains with lower incidence and mortality rates of chronic diseases such as diabetes, atherosclerosis, rheumatoid arthritis, neurodegenerative and coronary diseases, and cancer (5-12). In addition to fruits and vegetables, herbs of no specific nutritional value can also constitute an important source of antioxidants (13-15). The term herb includes not only herbaceous plants but also the leaves, bark, roots, seeds, fruits, and flowers of shrubs and trees. There are also products called nutraceuticals, which are often mixed with dietary supplements. The term "nutraceutical" is derived from the words "nutrition" and "drug" and is used for nutritional products that are also used as medicine. Nutraceuticals include probiotic and prebiotic food substances and foods for special medical purposes, either individually or in combination. In contrast, dietary supplements include minerals, vitamins, protein supplements, functional foods, and herbal products, either individually or in combination. It is stated in the

literature that nutraceuticals and nutritional supplements are collectively referred to as dietary supplements (16,17).

Due to the reasons we explained above and the environmental conditions, the decrease in the quality of most of the foods consumed has caused consumers to turn to products sold under the name of dietary supplements to maintain a healthy life. Dietary supplements are used worldwide and represent a broad category of ingestible products that are distinguishable from conventional foods and drugs (4). These are not medical medicines; they are used extensively to support a healthy life and to compensate for some nutritional elements not taken enough by diet. The US Food and Drug Administration (FDA) states that dietary supplements are beneficial for a healthy diet. It has been reported that until relatively recently, limited scientific research has been done on dietary supplements, and there is not much information on this subject. The same authors also pointed out that the prevalence of supplement use has increased significantly in the last 20 years (18). Dietary supplements are prepared from different parts of a plant, have different compositions, and have different concentrations of bioactive compounds; hence, it is to be expected that they will vary widely in their antioxidant powers. There is no information about antioxidant activities on the label of herbal supplement products sold on the market. In addition, there are very few studies in the world literature to determine the antioxidant activities of these products (19-22). Since humans use these products to support natural antioxidant intake, their activities should be known and standardized. Therefore, manufacturers should use standard analytical methods to standardize their products and determine effective doses and their antioxidant capacity so that they can market their products with confidence.

The dietary supplements we examined in our study were grape seed extract, rosemary, bitter melon, and ginkgo biloba, sold in capsule or tablet form. The grape seed extract is known as a powerful antioxidant that protects the body from premature aging and disease (23). Scientific studies have shown that the rosemary plant has antioxidant, antibacterial, antiviral, and immune system-enhancing effects due to its compounds (24). It is known that some of the bioactive substances found in bitter melon have hypoglycemic, antiulcer, antioxidant, antibiotic, antidiabetic, anticarcinogenic, and antimutagenic activities that are proven by clinical studies (25). The use of ginkgo biloba products has become widespread all over the world due to the effects of their components on the brain vessels in situations such as age-related memory impairment and dementia (26). Commercial herbal products are in tablet or capsule form but are often not standardized, and quality can vary from manufacturer to manufacturer and batch to batch (27,28). Assessments of the safety, quality, and efficacy of nutrients and other bioactive compounds are needed to provide the scientific information that regulators need (28,29). Indeed, data on the antioxidant activity of products currently on the market are scarce. These are called antioxidant boosters while recommending, but their labels lack information on effective antioxidant capacity values.

The main purpose of this study is to propose standard analytical methods to determine the originality and antioxidant capacities of selected dietary supplements, which are widely used for various reasons and are closely related to human health. Another purpose is to develop and apply chromatographic methods that will provide data that can be used to determine the bioactive components they contain and, thus, the effective dose to be used according to the needs of the person. Based on chromatographic data, plant-specific antioxidant components can be identified in plant products, and these can be compared with original plant samples.

2. EXPERIMENTAL SECTION

2.1. Chemicals and Instrumentation

Trolox (TR), quercetin (QUE), rosmarinic acid (RA), flavone, apigenin (APG), luteolin (LUT), kaempferol (KAM), rutin (RUT), caffeic acid (CA), carnosol (CAR), carnosic acid (CRA), catechin (CAT) hydrate, epicatechin (ECAT), gallic acid (GA), chlorogenic acid (CLA), copper(II) sulfate pentahydrate, Folin–Ciocalteu (FC) reagent, potassium sodium tartrate tetrahydrate ($KNaC_4H_4O_6.4H_2O$), neocuproin (2,9-dimethyl-1,10-phenanthroline) (Nc), sodium hydroxide (NaOH), sodium chloride (NaCl), hydrochloric acid (HCl) (37%) were supplied from Sigma-Aldrich (Steinheim, Germany); procyanidin B2, resveratrol (RES), cyanidin (CYD) chloride, ABTS {2,2′-azino-bis(3-ethylbenzthiazolin-6-sulfonic acid)} from Fluka Chemie AG (Buchs, Switzerland); copper(II) chloride dihydrate ($CuCl_2.2H_2O$), ortho-phosphoric acid (*o*-H_3PO_4), formic acid (HCOOH) from Merck KGaA (Darmstadt, Germany), ammonium acetate (NH_4Ac), sodium carbonate (Na_2CO_3), potassium persulfate ($K_2S_2O_8$), methanol (MeOH) (HPLC grade), ethanol (EtOH) (96%) from Honeywell Riedel-de Haën GmbH (Seelze, Germany). All chemicals used were of analytical reagent grade.

The instruments and equipment used were as follows: Radwag WAS 220/X (Bracka Poland) analytical balance for weighing chemicals and real samples**,** Bandelin Sonorex model ultrasonic bath for preparation of solutions and extracts (Bandelin electronic GmbH & Co. KG, Berlin, Germany), IKA HB4 Basic brand water bath (IKA-Werke Gmbh & Co. KG, Staufen, Germany), Elektro-Mag vortex (İstanbul, Turkey), Millipore brand bidistilled water device (EMD Millipore Corp., Burlington, MA, USA), Varian Cary 100 UV-visible spectrophotometer for absorbance measurements (Varian, Inc., Palo Alto, CA, USA), PerkinElmer Series 200 UV-Vis. HPLC System (detector, pump, vacuum degasser) (Shelton, USA) for chromatographic analysis.

2.2. Preparation of Solutions

Trolox, luteolin, kaempferol, rutin, caffeic acid, quercetin, rosmarinic acid, carnosic acid, carnosol, flavone, gallic acid, procyanidin B2, and chlorogenic acid stock solutions were prepared in 80% (v/v)

MeOH; apigenin in 0.2 M ethanolic sodium hydroxide. Catechin, epicatechin, resveratrol, and cyanidin chloride stock solutions were prepared in 80% (v/v) MeOH containing 2% (v/v) HCl. All antioxidant solutions were stored at −20 °C.

CUPRAC (Cupric Reducing Antioxidant Capacity) assay reagents; 1.0×10^{-2}M $CuCl_2$ solution was prepared by dissolving $CuCl_2{\cdot}2H_2O$ in water; 1.0 M ammonium acetate (NH_4Ac) buffer (pH 7.0) was prepared from NH_4Ac in water and 7. 5×10^{-3}M neocuproine (Nc) solution was prepared daily by dissolving Nc in 96% ethanol (EtOH).

ABTS (2,2′-azino-bis(3-ethylbenzthiazolin-6-sulfonic acid))/TEAC assay reagents; ABTS radical cation ($ABTS^{+\bullet}$) chromogenic reagent (7.0 mM) was prepared by dissolving this compound in water and adding $K_2S_2O_8$ to this solution such that the final persulfate concentration in the mixture is 2.45 mM. The resulting solution was left to mature at room temperature in the dark for 12-16 h and then used for ABTS/TEAC assays. The reagent solution was diluted with EtOH at a volume ratio of 1:10 before use.

Folin-Ciocalteu assay reagents; Lowry A solution: 2% (w/v) Na_2CO_3 was prepared in 0.1 M NaOH solution, Lowry B solution: 0.5 M $CuSO_4$ was prepared in 1% (w/v) $KNaC_4H_4O_6$ solution, Lowry C: 1 mL of Lowry B solution was added to 50 mL of Lowry A solution.

2.3. Preparation of Dietary Supplement Products for Analysis

2.3.1. Samples and extraction procedures

Grape seed extract, rosemary, and ginkgo biloba samples, which are sold in capsule or tablet form, and bitter melon samples in paste form (dried and in capsules) were obtained from companies selling such products in İstanbul (Türkiye) (Fig. 1).

Figure 1: Studied samples and their contents.

Aqueous solutions of methanol at 80, 70, and 50% (v/v) concentrations were used as the possible solvent for the extraction of powdered rosemary and ginkgo biloba samples in capsule form. The paste content of the bitter melon capsule was cut into pieces with a plastic knife and then extracted with the same solvents at 65 °C. For grape seed extract, the same solvents were used to contain 1% (v/v) HCl. 0.5 or 1.0-gram amount of the powder samples were extracted in stoppered flasks placed in an ultrasonic bath first with 10 mL solvent for 30 min, then with added 10 mL solvent for 30 min, and finally with 5 more mL solvent for 30 min, in conclusion overall extraction taking 90 min. The extracts were first filtered through a filter paper, then through a GF/PET (glass fiber/polyethylene terephthalate) 1.0/0.45 μm microfilter, and analyzed.

2.3.2. Hydrolysis of extract

The hydrolysis of all glycosides to aglycones provides convenience for the quantitative determination of flavonoids in samples. For this reason, grape seed extract containing 80% (v/v) MeOH and 1% (v/v) HCl was adjusted to 50% (v/v) MeOH and 1.2 M HCl in the final volume and then heated under reflux at 80 ºC for 4 h for hydrolysis (30). Extracts from other samples prepared with 80% (v/v) MeOH were diluted to 50% (v/v) MeOH. Hydrochloric acid was added to reach a final concentration of 1.2 M HCl, and the hydrolysis process was carried out as described above. At the end of the process, the resulting hydrolysates were filtered through a 1.0/0.45 μm GF/PET microfilter. The volumes of the filtered solutions were then adjusted with 50% (v/v) MeOH.

2.4. Spectrophotometric Total Antioxidant Capacity Assays

2.4.1. CUPRAC assay

The CUPRAC method, as described by Apak et al. (31) was applied as follows: A mixture comprised of 1 mL of 1.0×10^{-2} M $CuCl_2$ solution, 1 mL of 1 M NH_4Ac buffer at pH 7.0, and 1 mL of 7.5×10^{-3} M Nc solution was prepared, x mL sample solution and (1−x) mL distilled water were added, and well mixed (total volume: 4.0 mL). This final mixture in a stoppered test tube was stood at room temperature for 30 min. At the end of this period, the absorbance at 450 nm was measured against a reagent blank. This method was applied to the extracts and hydrolysate of the studied samples. The pH of the hydrolysate solution was first brought to pH 6.0 with the addition of NaOH solution, and then analysis was performed.

The total antioxidant capacity (TAC) values of the samples analyzed using this method were calculated as mmol TR/g of dry matter.

2.4.2. ABTS/TEAC assay

The blue-green solution prepared as described above was diluted 1:10 (v/v) with EtOH. The reference solution was prepared with diluted 1 mL of $ABTS^{\bullet+}$ solution and 4 mL of EtOH (total volume: 5.0 mL). The sample solutions were prepared as follows: x mL of extract, (4-x) mL of 80% (v/v) MeOH, and 1 mL of $ABTS^{\bullet+}$ solution. The absorbances of all solutions were recorded at 734 nm against EtOH at the end of the 6th min. (32) The absorbance of the reference diminished in the presence of antioxidants, the absorbance decrease (ΔA) being proportional to antioxidant concentration.

The total antioxidant capacity (TAC) values of the samples analyzed using this method were calculated as mmol TR/g of dry matter.

2.5. Determination of Total Phenolic Content by Folin-Ciocalteu Assay

According to the Folin-Ciocalteu (FC) method measuring total phenolic content (TPC), x mL of extract, (2-x) mL of distilled water, and 2.5 mL of Lowry C solution (the preparation is explained above) were added to a test tube. After 10 min, 0.25 mL FC reagent (diluted with water at a 1:3 (v/v) ratio) was added (total volume: 4.75 mL). The tubes were kept at room temperature for 30 min, and absorbance was measured at 750 nm against a reagent blank (33).

The TPC values of the samples analyzed using this method were calculated as mmol GA/g of dry matter.

2.6. Chromatographic Analyses

Different gradient elution programs were modified for chromatographic analysis of the polyphenolic compounds found in the studied samples. The elution programs were formed using the ACE 5 C18 (25 cm × 4.6 mm, 5 µm particle size) HPLC column (ACE Ltd, Aberdeen, Scotland) and one of the suitable binary mobile phase systems (0.2% (v/v) formic acid and MeOH or 0.2% (v/v) *o*-H_3PO_4 and MeOH).

The gradient elution program (I), which is modified for the analysis of grape seed capsule components and consisted of 0.2% formic acid (A) and MeOH (B) binary solvent system was applied as follows: initially and for 5 min 93% A, 10 min from 93% to 90% A (curve 6), 5 min from 90% to 87% A (curve 6), 5 min from 87% to 82% A (curve 6), 15 min from 82% to 79% A (curve 10), 10 min from 79% to 76% A (curve 10), 6 min from 76% to 73% A (curve 10), 12 min from 73% to 0% A (curve 10). Curve numbers in parentheses are the slope (change rate of solvent) codes of the Empower Software (Waters Corporation) program. The flow rate was 1 mL/min; analytical detection wavelengths were selected as 280 and 520 nm.

The gradient elution program (II), which is modified for the analysis of rosemary capsule components and consisted of 0.2% formic acid (A) and MeOH (B) binary solvent system was applied as follows: initially 80% A, 3 min from 80% to 65% A (curve 6), 10 min from 65% to 50% A (curve 6), 15 min from 50% to 40% A (curve 6), 10 min from 40% to 20% A (curve 6), 15 min from 20% to 0% A (curve 10). The flow rate was 1 mL/min, and the analytical detection wavelength was selected as 280 nm.

The gradient elution program (III), which is modified for the analysis of bitter melon capsule components and consisted of 0.2% *o*-H_3PO_4 (A) and MeOH (B) binary solvent system was applied as follows: initially and for 3 min 100% A, 17 min from 100% to 70% A (curve 6), 10 min from 70% to 45% A (curve 6), 10 min from 45% to 0% A (curve 6). The flow rate was 0.7 mL/min, and the analytical detection wavelength was selected as 320 nm.

The gradient elution program (IV), which is modified for the analysis of ginkgo biloba capsule components and consisted of 0.2% *o*-H_3PO_4 (A) and MeOH (B) binary solvent system was applied as follows: initially and for 1 min 20% A, 3 min from 20% to 35% A (curve 6), 5 min from 35% to 45% A (curve 6), 12 min from 45% to 50% A (curve 6), 3 min from 50% to 55% A (curve 6), 2 min from 55% to 60% A (curve 6), 2 min from 60% to 80% A (curve 6), 13 min from 80% to 100% A (curve 6). The flow rate was 1.0 mL/min; analytical detection wavelengths were selected as 280 and 320 nm.

In the HPLC analysis of studied sample extracts, retention times were compared with those of standards. Analysis results were evaluated according to the calibration graphs, which were drawn between peak areas and concentrations of standard compounds.

2.7. Combined HPLC-CUPRAC and HPLC-ABTS Methods

The contribution of the sample components determined by chromatographic analysis to the measured spectrophotometric total antioxidant capacity was calculated using the equation (1) (34-36). In this equation, the component concentrations were multiplied by the TEAC (Trolox equivalent antioxidant capacity) coefficients determined by the spectrophotometric methods, and by summing these values, the theoretical TACs of the samples were calculated. As a result, HPLC–CUPRAC refers to the capacity calculated by multiplying the concentrations determined in HPLC by the TEAC coefficients of the CUPRAC method.

$$Theoretical\ TAC = \sum_{i=1}^{n} C_i\,(TEAC)_i \qquad \text{(Eq. 1)}$$

C_i: concentration of ith component determined by HPLC; *(TEAC)i*: TEAC coefficient of ith component calculated by the selected TAC measurement method (i.e., CUPRAC and ABTS).

2.8. Statistical Analysis

Spectrophotometric assays were applied in three repetitions for each sample and standard. Descriptive statistical analyses were performed using Excel

software (Microsoft Office 2016) to calculate the mean and the standard error of the mean.

3. RESULTS AND DISCUSSION

3.1. Sample Preparation and Selection of Suitable Solvent for Extraction

The spectra of the extracts, which were prepared as specified in section 2.3.1 and diluted at appropriate rates, were taken in the range of 200-600 nm (the spectra were not given), and the solvent ratios that provided the highest extraction efficiency were determined. The most suitable solvents were determined according to spectra: 80% MeOH containing 1% (v/v) HCl for grape seeds sample and 80% (v/v) MeOH for rosemary, bitter melon, and ginkgo biloba samples.

3.2. The Results of Spectrophotometric Methods

Since the results obtained by applying the spectrophotometric methods (CUPRAC, ABTS, and Folin-Ciocalteu) to the samples will be given as TR and GA equivalents, firstly, calibration graphs were created with the related standard compounds. Thus, molar absorption coefficients were calculated for each compound (Table 1).

Table 1: Molar absorption coefficients of reference standard compounds used in spectrophotometric methods.

Spectrophotometric method	Reference standard compound	Molar absorption coefficient (mol/L.cm)
CUPRAC	TR	1.67×10^4
ABTS/TEAC	TR	2.60×10^4
Folin-Ciocalteu	GA	6.10×10^3

According to the literature data, the compounds with antioxidant properties expected to be found in the highest amount in grape seeds are CAT, ECAT, GA, flavone, procyanidin B2, RES, and CYD (37). The main antioxidant compounds that are likely to be found in our other studied samples are; CA, RA, CAR, and CRA in rosemary (38); GA, CAT, CA, and CLA in bitter melon (39,40); RUT, LUT, KAM, APG, and QUE in ginkgo biloba (41,42). Using the standards of these substances, calibration graphs (drawn as absorbance vs molar concentration) were created with spectrophotometric total antioxidant capacity measurement methods (CUPRAC and ABTS), and the molar absorption coefficients of each compound were calculated. As a result, the molar absorption coefficients of tested compounds were divided into the molar absorption coefficient of standard reference TR, and the TEAC coefficient of each compound was calculated (Table 2). The TEAC coefficient expresses the mM concentration of the TR solution, which is equivalent to the activity of a 1 mM solution of the antioxidant compound whose reducing power is to be measured (43).

Table 2: TEAC coefficients of antioxidants tested with CUPRAC and ABTS methods.

Antioxidant	$TEAC_{CUPRAC}$	$TEAC_{ABTS}$
CAT	3.13	3.14
ECAT	2.77	2.65
GA	2.97	3.84
Flavone	0.34	0.05
Procyanidin B2	7.72	5.45
RES	1.30	3.63
CYD	1.04	1.18
CA	3.00	1.39
RA	5.40	5.65
CAR	1.47	2.31
CRA	2.16	1.09
QUE	4.49	4.23
RUT	2.99	3.15
CLA	3.05	1.35
APG	0.25	0.65
LUT	2.83	1.58
KAM	2.00	1.12

3.3. Total Phenolic Contents and Total Antioxidant Capacities of Samples

The total antioxidant capacities of the sample extracts and their hydrolysates were determined spectrophotometrically using the CUPRAC and ABTS/TEAC methods. The total phenolic content of the same samples was determined using the Folin-Ciocalteu method. All results are listed in Table 3.

Although there are not many studies in the literature measuring the antioxidant activities of plant-based dietary supplements, when examining a few studies for this purpose, it has been found that DPPH (2,2-diphenyl-1-picrylhydrazyl), FRAP (Ferric Reducing Antioxidant Capacity), ORAC (Oxygen Radical Absorbance Capacity) and HORAC (Hydroxyl Radical Antioxidant Capacity) methods are used (19-21,40,44). Among these methods, ORAC and HORAC have a hydrogen atom transfer (HAT) mechanism, while FRAP and DPPH have a single electron transfer (SET) mechanism. The CUPRAC and ABTS methods used in our study are based on the SET mechanism. The main advantage of the CUPRAC method over other similar assays is that the reagent is more stable and easier to prepare than other chromogenic reagents (e.g., ABTS, DPPH). The TAC values of the antioxidants determined with CUPRAC are perfectly additive, i.e., the TAC of a mixture is equal to the sum of the TAC values of its components. The CUPRAC reagent is selective because it has a lower redox potential; accordingly, non-antioxidant reducing compounds, such as simple sugars and citric acid, are not oxidized with the CUPRAC reagent. The standard potential of the Cu(II, I)-Nc redox couple is about 0.6 V and thus close to that of $ABTS^{\bullet+}$/ABTS, i.e., 0.68 V (43). For this reason, ABTS was preferred as a comparison method. As can be seen in Table 3, the TAC values determined with both methods were close to each other. It can be seen that the highest TAC value among the analyzed products belongs to the acidic and non-acidic grape seed extracts. Özcan et al. (44) reported that the content of phenolic compounds in the skin and pulp of certain grape varieties grown in Turkey was lower than in the seeds. In this study, 15 mL of a methanol-water-formic acid mixture (5:4.85:1.5, v/v) was added to approximately 2 g of a grape seed sample. The mixture was sonicated for 2 minutes. The sample was then centrifuged at 4500 rpm for 15 minutes. After centrifugation, 10 mL of n-hexane was added to the separated supernatant and mixed with a vortex mixer. The extract was then concentrated using a rotary evaporator at 50 °C. The resulting residue was dissolved in methanol, and analytical methods were applied. The TACs of the samples were evaluated using the DPPH assay, the TPCs were determined using the Folin-Ciocalteu assay, and the chromatographic analyses were performed using an HPLC system with a PDA detector. The determined TAC and TPC values of the grape seeds were between 86.688-90.974% and 421.563-490.625 mg GAE/100 g, respectively. The phenolic compounds of the grape seeds were determined to be significantly higher compared to the other parts of the grapes. The major phenolic compounds quantified were 1,2-dihydroxybenzene, rutin, apigenin-7-glucoside, caffeic acid, (+)-catechin, gallic acid, quercetin, and resveratrol. The authors compared their results with those of similar studies and attributed the observed differences in the results to diversity, cultural factors, or analytical conditions. In a study by Krasteva et al. (45), the TPC, the compositions, and the antioxidant and antibacterial activities of four grape seed extracts (Cabernet Sauvignon, Marselan, Pinot Noir, and Tamyanka) were investigated. The antioxidant capacity of these extracts was analyzed using DPPH and ABTS assays. An HPLC system with a PDA detector was used for the chromatographic analysis of the extracts. The total phenol content was determined using the Folin-Ciocalteu assay. In this study, the samples were prepared as follows: 5 g of grape seed powder was mixed with 25 mL of 70% aqueous ethanol using a magnetic stirrer at a constant speed of 500 rpm at room temperature and pressure for 3 hours. This procedure was repeated twice, and the collected supernatants were centrifuged and concentrated to 1 mL in an evaporator. The total phenolic content of the extracts was determined in the range of 79.06–111.22 mg GAE/g DW. The total antioxidant capacity values of the same samples were determined in the range of 245.60 ± 3.23 - 597.23 ± 4.12 (μM TE/g DW) using the DPPH assay and in the range of 1907.24 ± 9.56 - 2273.92 ± 12.32 (μM TE/g DW) using the ABTS method. The differences between the results of the two assays were attributed to the different mechanisms used in the determination of antioxidant capacity. The components identified in the HPLC analysis of the same samples were gallic acid, gallic acid glucoside, (+)-catechin and (-)-epicatechin, procyanidins B1, B2, and B3, and procyanidin C1. The results of these two studies, which include analyses of grape seeds, are in close agreement with our findings on the phenolic compounds identified. The TEAC coefficient values of these components in Table 2 explain the high antioxidant capacities of the grape seed extracts. In addition, our results show that the grape seed extracts had the highest total phenolic component contents (Table 3). On the other hand, the values obtained with the ABTS method are relatively low compared to the results obtained with the CUPRAC method. This finding can be explained by the different responses of the components to these methods. Indeed, this is confirmed by the TEAC coefficients obtained (Table 2). The order of the other commercial products we examined according to their antioxidant capacity values from highest to lowest is rosemary > ginkgo biloba > bitter melon. This ranking also applies to the total phenolic content. The FC method is used to determine the total phenolic content of a sample, but it is not specific to phenolic compounds or antioxidants in general. This method suffers from several interfering substances (sugars, aromatic amines, sulfur dioxide, ascorbic acid, organic acids, Fe(II), etc.) (46). For this reason, the values obtained with this method are generally higher than the TAC values.

The antioxidant activity of rosemary is mainly attributed to its phenolic compounds, particularly phenolic diterpenes such as carnosol, carnosic acid, rosmanol, epirosmanol, and isorosmanol. Additionally, rosmarinic acid, a caffeic acid ester, is also recognized as an important component of

rosemary due to its superior antioxidant properties (24,38). Olah et al. (47) conducted a study on the polyphenol content and antioxidant capacity of three different rosemary extracts prepared from both fresh and dried plants. The phenolic compounds in these samples were identified using thin-layer chromatography (TLC) and an HPLC system with a diode array detector (DAD). The polyphenols were determined using sodium molybdate reagent at 505 nm, and the total antioxidant activity and capacity values were evaluated by DPPH, ABTS, FRAP, and CUPRAC assays. The analyzed extracts were prepared by cold extraction with 100 mL 70% EtOH (1:5 - dry plant: solvent) from dry and fresh plants. The TLC and HPLC analyses revealed that rosmarinic acid was the component with the highest concentration. The study showed that the total polyphenol content and rosmarinic acid content in the alcoholic extract of fresh plants were two to three times higher than in extracts from dried plants. From these results, the authors concluded that the drying process can lead to changes or degradation of the polyphenolic compounds. In this study, the high polyphenol content determined for the hydroalcoholic extract (0.601 mg/mL rosmarinic acid) was confirmed by the highest values determined for antioxidant activity. Namely, the IC_{50} values of the DPPH and ABTS methods were determined as 39.1 µL and 7.7 µL, respectively, while the values determined as TE µM/100 mL for the FRAP and CUPRAC methods were 698 and 1947, respectively.

The highest antioxidant capacity of rosemary capsules was also measured in our study using the CUPRAC method.

The main phenolic components found in bitter melon extracts are gallic acid, epicatechin, chlorogenic acid, catechin, and gentisic acid (40,48,49). Anilakumar et al. (50) reported that the products of bitter melon fruit and seed extracts in capsule or tablet form are widely used in many countries. Still, the Food and Drug Administration has not evaluated these products, and they need further validation. Various products made from bitter melon (in the form of powder, paste, capsules, or tablets) are sold on the market and are widely used in our country. In our previously published study, the total phenolic content and antioxidant capacity of some commercial bitter melon products (powder, packaged powder, capsule, paste in olive oil) and of unripe and ripe fruits were determined spectrophotometrically (Folin-Ciocalteu, CUPRAC, and ABTS) and chromatographically (51). In this study, the bitter melon samples were extracted with 80% MeOH. In addition, most research studies on bitter melon have found EtOH, MeOH, or water to be suitable extraction agents (52-54). In this study, the ranking of TAC (total antioxidant capacity) of the samples analyzed by CUPRAC and ABTS method was determined as follows: capsule (CUPRAC value, 140.8; ABTS/HRP value, 143.6 µmol TRE/g) > packaged powder (129.6; 126.1) > powder (52.3; 64.3) > unripe fruit (42.5; 36.3) > paste in olive oil (17.6; 14.4) > ripe fruit (8.7; 7.0). On the other hand, the order of phenolic content of the same samples was determined as follows: unripe fruit (193.2 µmol GAE (gallic acid equivalent)/g) > capsule (162.0) > packaged powder (160.6) > powder (83.6) > paste in olive oil (38.3) > ripe fruit (14.6) (51). The TAC and TPC values of the bitter melon extract examined in the present study (see Table 3) are also within the range of the values mentioned above.

Table 3: The total antioxidant capacity (TAC) and total phenolic content (TPC) values of the examined samples were determined by spectrophotometric methods.

Sample	CUPRAC (mmol TR/g)[a]	ABTS/TEAC (mmol TR/g)[a]	TPC (mmol GA/g)[a]
Grape seed extract	0.910±0.070	0.720±0.170	1.710±0.470
Grape seed extract hydrolysate	0.420±0.030	0.300±0.030	0.740±0.150
Acidic grape seed extract	1.240±0.050	0.710±0.210	2.040±0.430
Acidic grape seed extract hydrolysate	0.570±0.030	0.330±0.020	0.760±0.220
Rosemary extract	0.790±0.050	0.410±0.090	0.550±0.130
Rosemary extract hydrolysate	0.180±0.030	0.120±0.070	0.160±0.040
Bitter melon extract	0.080±0.006	0.110±0.050	0.240±0.030
Bitter melon extract hydrolysate	0.070±0.010	0.070±0.010	0.150±0.040
Ginkgo biloba extract	0.120±0.008	0.140±0.020	0.400±0.160
Ginkgo biloba extract hydrolysate	0.050±0.002	0.070±0.006	0.160±0.040

The results are presented as mean (n=3) ± standard deviation.

The results of the CUPRAC and ABTS assays results showed that the antioxidant capacity values of the Ginkgo biloba extract were close to each other. In a study, the total phenolic content and antioxidant capacity (FRAP method) of Ginkgo biloba L. leaves and various commercial Ginkgo teas were determined and compared. For this purpose, different water extracts (infusions and decoctions) were prepared by varying the steeping, boiling, and infusion times, while an aqueous ethanolic extract (water/ethanol 80/20, v/v) was also prepared. It was found that the total phenolic content and FRAP values of the collected ginkgo leaves were similar to those of commercial ginkgo teas. Contrary to the preparation methods recommended by the manufacturers, decoction was found to be more effective than infusion in extracting the antioxidant compounds. It was also reported that aqueous ethanolic extracts had significantly higher total phenolic content and antioxidant capacity than water extracts. The phenolic concentrations of the water extracts ranged from 21.11 to 34.22 mg/g GAE for leaf samples and from 15.84 to 27.31 mg/g GAE for commercial teas. The phenolic content of the

aqueous ethanol extracts for the collected ginkgo leaf samples was 75.74 mg/g GAE, while these values for the commercial ginkgo teas ranged from 85.51 to 98.28 mg/g GAE. It was found that the antioxidant capacity of the aqueous ethanol extracts of the ginkgo samples was about three times higher than that of the water extracts. FRAP values of the water extracts ranged from 16.68 to 31.91 mmol/g AAE for the collected leaf sample and from 14.10 to 31.34 mmol/g AAE for the commercial teas. The antioxidant capacity of the aqueous ethanolic extracts was 69.12 mmol/g AAE for the collected leaf sample, and its values ranged from 62.76 to 69.99 mmol/g AAE for commercial tea samples (55). Aybastier conducted a study on Ginkgo biloba samples available for sale in Türkiye, examining three different forms: medicine, food supplement, and leaf (56). The study involved the ultrasonic extraction of all three sample types in both acidic and non-acidic environments, and the antioxidant properties of the extracts were evaluated. The antioxidant capacities were measured using the ABTS method, while the total phenolic content was assessed using the Folin-Ciocalteu method. Additionally, HPLC was used to identify the antioxidant compounds present in the samples. In this study, the drug, Ginkgo biloba leaf, and food supplement products were each extracted using a 60% methanol solution. For the acidic extraction, a 60% methanol solution containing 2 M HCl was utilized. The extraction process was conducted in an ultrasonic bath at 50°C for 100 minutes. It has been stated that the extraction was also carried out in an acidic environment to facilitate the hydrolysis of antioxidant compounds in the glycoside structure and convert them into aglycones. It is known that a compound with a glycoside structure and its aglycone, which is formed through acidic hydrolysis, displays different antioxidant properties (57). The results indicated that the drug form exhibited superior antioxidant properties compared to both the food supplement and leaf forms. According to the Folin-Ciocalteu method, the total phenolic content of the drug sample was measured at 68.16 ± 1.83 mg GAE/g for the non-acidic extract and 80.27 ± 6.55 mg GAE/g for the acidic extract. Additionally, the antioxidant capacity value for the same sample, determined using the ABTS method, was found to be 59.75 ± 3.57 mg TE/g for the non-acidic extract and 56.48 ± 8.66 mg TE/g for the acidic extract. As a result of HPLC analyses, rutin (quercetin-3-rutinoside) was determined as the main phenolic substance in all extracts, while the others were protocatechuic acid, p-hydroxybenzoic acid, kaempferol-3-glucoside, kaempferol, and quercetin. The differences in antioxidant content among the Ginkgo biloba products studied can be attributed to several factors. First, the plants were sourced from different locations, which may have influenced their composition. Second, the methods used to prepare these products varied. Namely, the leaves were collected from the tree and dried; the dietary supplement was created by encapsulating the processed product; and the drug formulation underwent a standardized preparation method after verifying its composition. As a result, it was concluded that the most reliable form of Ginkgo biloba is the tablet sold as a pharmaceutical drug.

3.4. Chromatographic Analysis

In the chromatographic analysis of the studied samples, the phenolic compositions were determined by comparing the retention times of the standards and/or by adding standard solutions to the diluted sample extracts in an appropriate ratio.

Compounds detected in the methanol extract of the grape seed sample at 280 nm include epicatechin, resveratrol, and flavone, while the hydrolysate contains catechin, procyanidin B2, and resveratrol. In the acidic methanol extract and hydrolysate of the same sample, catechin, gallic acid, and resveratrol were detected at 280 nm, along with cyanidin chloride at 520 nm. The extract prepared from the rosemary capsule contained caffeic acid, rosmarinic acid, carnosol, and carnosic acid, as determined by HPLC at 280 nm. The phenolic compounds identified in the other studied samples are as follows: in the bitter melon extract (at 320 nm), chlorogenic acid, rutin, and quercetin; in the ginkgo biloba extract (at 340 nm), rutin, luteolin, kaempferol, apigenin, and quercetin.

Calibration graphs were created using the standards of the relevant phenolic substances, and the findings are reported in Table 4. In the calibration equations provided in Table 4, y refers to the peak area, c to the concentration, and r to the correlation coefficient. The individual antioxidant concentrations of the studied samples were determined using calibration curves in HPLC. The recovery percentage values of the HPLC methods were assessed by adding standard antioxidant compounds to the sample extracts and hydrolysates. These values ranged from 94.6% to 99.0% in grape seed extracts and hydrolysates, 97.0% to 99.7% in rosemary extract, 95.2% to 98.9% in bitter melon extract, and 92.0% to 99.8% in ginkgo biloba extracts.

3.5. Theoretical TAC Values Determined by HPLC-CUPRAC and HPLC-ABTS Methods

Concentration calculations for each component were conducted through chromatographic analysis, applying the calibration equations found in Table 4. The theoretical total antioxidant capacity (TAC) values for each sample were calculated using equation (1) from section 2.7. By leveraging the additivity property of TAC in complex samples, we determined the theoretical TAC by multiplying the concentration of each identified antioxidant by its corresponding Trolox Equivalent Antioxidant Capacity (TEAC) coefficient value, then summing all obtained values. The ratio of the theoretically calculated TAC values to those measured via spectrophotometric methods allowed us to assess the contribution of each component identified through chromatographic analysis to the overall antioxidant capacity. These contributions were expressed as percentages in parentheses in Table 5 and were found to range from 33% to 57%. These results suggest that when the analytical standards for antioxidant compounds in similar plant-based products are available, it is feasible to accurately determine the contribution of each compound to the total antioxidant capacity through chromatographic analysis.

Table 4: Calibration equations, correlation coefficients, and linear ranges of some phenolic compounds determined from HPLC chromatograms.

Phenolic compound	Retention time (min)	Detection wavelength (nm)	Calibration equation	r	Linearity range (mol/L)
GA[a]	6.0	280	$y = 6.8\times10^{9}\ c - 3.0\times10^{4}$	0.9684	1.0×10^{-5}–2.0×10^{-4}
CAT[a]	27.5	280	$y = 4.0\times10^{8}\ c - 2.7\times10^{3}$	0.9945	1.0×10^{-5}–2.0×10^{-4}
ECAT[a]	39.1	280	$y = 9.0\times10^{7}\ c - 5.6\times10^{2}$	0.9987	1.0×10^{-5}–2.0×10^{-4}
RES[a]	60.8	280	$y = 8.2\times10^{9}\ c - 5.0\times10^{3}$	0.9765	1.0×10^{-5}–2.0×10^{-4}
CYD[a]	61.5	520	$y = 8.0\times10^{9}\ c - 4.0\times10^{4}$	0.9413	1.6×10^{-5}–1.6×10^{-4}
Flavone[a]	64.1	280	$y = 7.4\times10^{9}\ c - 1.6\times10^{4}$	0.9984	1.6×10^{-5}–1.6×10^{-4}
Procyanidin B2[a]	32.0	280	$y = 5.0\times10^{8}\ c - 4.0\times10^{2}$	0.9898	1.6×10^{-5}–1.6×10^{-4}
CA[b]	9.0	280	$y = 9.0\times10^{8}\ c - 5.1\times10^{4}$	0.9728	1.0×10^{-5}–2.0×10^{-4}
RA[b]	14.2	280	$y = 9.2\times10^{8}\ c - 4.0\times10^{3}$	0.9992	1.0×10^{-5}–2.0×10^{-4}
CAR[b]	39.8	280	$y = 3.2\times10^{8}\ c - 2.7\times10^{3}$	0.9928	1.0×10^{-5}–2.0×10^{-4}
CRA[b]	46.3	280	$y = 1.4\times10^{8}\ c - 2.2\times10^{3}$	0.9824	1.0×10^{-5}–2.0×10^{-4}
CLA[c]	25.9	320	$y = 6.0\times10^{9}\ c - 3.9\times10^{4}$	0.9986	1.0×10^{-5}–2.0×10^{-4}
RUT[c]	36.8	320	$y = 7.0\times10^{9}\ c - 3.2\times10^{4}$	0.9958	1.0×10^{-5}–2.0×10^{-4}
QUE[c]	44.7	320	$y = 5.2\times10^{9}\ c - 1.1\times10^{4}$	0.999	1.0×10^{-5}–2.0×10^{-4}
LUT[d]	20.8	340	$y = 6.0\times10^{9}\ c - 1.3\times10^{4}$	0.9844	1.0×10^{-5}–2.0×10^{-4}
KAM[d]	23.8	340	$y = 7.2\times10^{8}\ c - 2.1\times10^{4}$	0.9830	1.0×10^{-5}–2.0×10^{-4}
APG[d]	25.5	340	$y = 6.4\times10^{9}\ c - 2.1\times10^{4}$	0.9749	1.0×10^{-5}–2.0×10^{-4}

a, b, c, and d indicate that the chromatograms of these compounds were taken by gradient elution programs called I, II, III, and IV, respectively.

Table 5: Theoretical total antioxidant capacity values (mmol TR/g) were determined by HPLC-CUPRAC and HPLC-ABTS methods.

Sample	HPLC-CUPRAC (mmol TR/g)	HPLC-ABTS (mmol TR/g)
Grape seed extract	0.42 (46%)	0.37 (51%)
Grape seed extract hydrolysate	0.18 (43%)	0.11 (37%)
Acidic grape seed extract	0.71 (57%)	0.34 (48%)
Acidic grape seed extract hydrolysate	0.32 (56%)	0.16 (48%)
Rosemary extract	0.31 (39%)	0.19 (46%)
Rosemary extract hydrolysate	0.04 (22%)	0.05 (42%)
Bitter melon extract	0.03 (38%)	0.04 (36%)
Bitter melon extract hydrolysate	0.03 (43%)	0.04 (57%)
Ginkgo biloba extract	0.04 (33%)	0.05 (36%)
Ginkgo biloba extract hydrolysate	0.02(40%)	0.03 (43%)

4. CONCLUSION

In our study, we examined dietary supplements that include grape seed extract, rosemary, bitter melon, and ginkgo biloba, all sold in capsule or tablet form. For the first time, we employed the CUPRAC and HPLC-CUPRAC methods to assess the antioxidant capacity of these products, comparing our findings with those obtained from the ABTS/TEAC method. The analytical techniques used to evaluate the specificity and antioxidant capacity of the selected dietary supplements can be recommended as standard methods.

To determine the effective dose based on human requirements, we can measure the types and amounts of bioactive substances using the methods developed or modified for the chromatographic analysis of the samples in our study. Furthermore, the chromatographic data obtained will allow us to identify plant-specific antioxidant compounds in raw plants and ascertain whether there is imitation or adulteration in products falsely claimed to contain these plants.

5. CONFLICT OF INTEREST

The authors declare there is no potential conflict of interest concerning the research, authorship, and/or publication of this article.

6. ACKNOWLEDGMENTS

This study was funded by the Scientific Research Projects Coordination Unit of Istanbul University-Cerrahpaşa. Project number: 18516.

7. REFERENCES

1. Binns CW, Lee MK, Lee AH. Problems and prospects: Public health regulation of dietary supplements. Annu Rev Public Health [Internet]. 2018 Apr 1;39(1):403–20. Available from: <URL>.

2. Gul K, Singh AK, Jabeen R. Nutraceuticals and functional foods: The foods for the future World. Crit Rev Food Sci Nutr [Internet]. 2016 Dec 9;56(16):2617–27. Available from: <URL>.

3. Valavanidis A. Dietary supplements: Beneficial to human health or just peace of mind? A critical review on the issue of benefit/ risk of dietary supplements. Pharmakeftiki [Internet]. 2016;28(2):60–83. Available from: <URL>.

4. Hassan S, Egbuna C, Tijjani H, Ifemeje JC, Olisah MC, Patrick-Iwuanyanwu KC, et al. Dietary supplements: Types, health benefits, industry and regulation. In: Functional Foods and Nutraceuticals [Internet]. Cham: Springer International Publishing; 2020. p. 23–38. Available from: <URL>.

5. Liu Z, Ren Z, Zhang J, Chuang CC, Kandaswamy E, Zhou T, et al. Role of ROS and nutritional antioxidants in human diseases. Front Physiol [Internet]. 2018 May 17;9. Available from: <URL>.

6. Yahia EM, García-Solís P, Celis MEM. Contribution of fruits and vegetables to human nutrition and health. In: Postharvest Physiology and Biochemistry of Fruits and Vegetables [Internet]. Elsevier; 2019. p. 19–45. Available from: <URL>.

7. Jideani AIO, Silungwe H, Takalani T, Omolola AO, Udeh HO, Anyasi TA. Antioxidant-rich natural fruit and vegetable products and human health. Int J Food Prop [Internet]. 2021 Jan 1;24(1):41–67. Available from: <URL>.

8. Rudrapal M, Khairnar SJ, Khan J, Dukhyil A Bin, Ansari MA, Alomary MN, et al. Dietary polyphenols and their role in oxidative stress-induced human diseases: Insights into protective effects, antioxidant potentials and mechanism(s) of action. Front Pharmacol [Internet]. 2022 Feb 14;13:806470. Available from: <URL>.

9. Rahaman MM, Hossain R, Herrera-Bravo J, Islam MT, Atolani O, Adeyemi OS, et al. Natural antioxidants from some fruits, seeds, foods, natural products, and associated health benefits: An update. Food Sci Nutr [Internet]. 2023 Apr 13;11(4):1657–70. Available from: <URL>.

10. Shaik MI, Hamdi IH, Sarbon NM. A comprehensive review on traditional herbal drinks: Physicochemical, phytochemicals and pharmacology properties. Food Chem Adv [Internet]. 2023 Dec;3:100460. Available from: <URL>.

11. Chibuye B, Singh I Sen, Ramasamy S, Maseka KK. Natural antioxidants: A comprehensive elucidation of their sources, mechanisms, and applications in health. Next Res [Internet]. 2024 Dec;1(2):100086. Available from: <URL>.

12. Guo M. Antioxidants and antioxidant-rich foods. In: Functional Foods [Internet]. Elsevier; 2025. p. 7–53. Available from: <URL>.

13. El Guiche R, Tahrouch S, Amri O, Mehrach K, Hatimie A. Antioxidant Activity and Total Phenolic and Flavonoid Contents of 30 Medicinal and Aromatic Plants Located in the South of Morocco. Int J New Technol Res [Internet]. 2015;1(3):7–11. Available from: <URL>.

14. Embuscado ME. Spices and herbs: Natural sources of antioxidants – A mini review. J Funct Foods [Internet]. 2015 Oct;18:811–9. Available from: <URL>.

15. Stagos D. Antioxidant activity of polyphenolic plant extracts. Antioxidants [Internet]. 2019 Dec 24;9(1):19. Available from: <URL>.

16. Siddiqui RA, Moghadasian MH. Nutraceuticals and nutrition supplements: Challenges and opportunities. Nutrients [Internet]. 2020 May 29;12(6):1593. Available from: <URL>.

17. Puri V, Nagpal M, Singh I, Singh M, Dhingra GA, Huanbutta K, et al. A comprehensive review on nutraceuticals: Therapy support and formulation challenges. Nutrients [Internet]. 2022 Nov 3;14(21):4637. Available from: <URL>.

18. Dwyer J, Coates P, Smith M. Dietary supplements: Regulatory challenges and research resources. Nutrients [Internet]. 2018 Jan 4;10(1):41. Available from: <URL>.

19. Sarma N, Giancaspro G, Venema J. Dietary supplements quality analysis tools from the United States Pharmacopeia. Drug Test Anal [Internet]. 2016 Mar 9;8(3–4):418–23. Available from: <URL>.

20. Carvalho AV, Ferreira Ferreira da Silveira T, Mattietto R de A, Padilha de Oliveira M do S, Godoy HT. Chemical composition and antioxidant capacity of açaí (*Euterpe oleracea*) genotypes and commercial pulps. J Sci Food Agric [Internet]. 2017 Mar 5;97(5):1467–74. Available from: <URL>.

21. Santiago-Saenzcésar YO, López-Palestinajorge CU, Gutiérrez-Tlahque J, Monroy-Torres R, Pinedo-Espinoza JM, Hernandez-Fuentes AD. Nutritional and functional evaluation of three powder mixtures based on mexican quelites: alternative ingredients to formulate food supplements. Food Sci Technol [Internet]. 2020 Dec;40(4):1029–37. Available from: <URL>.

22. Akyıldız İE, Raday S, Erdem Ö, Acar S, Coşkun İ, Damarlı E. Analytical investigation of active compound contents of *Panax ginseng* C.A. meyer and *Ginkgo biloba* L. supplements fortified with apitherapy products. Int J Second Metab [Internet]. 2021 Jun 15;8(2):70–93. Available from: <URL>.

23. Gupta M, Dey S, Marbaniang D, Pal P, Ray S, Mazumder B. Grape seed extract: Having a potential health benefits. J Food Sci Technol [Internet]. 2020 Apr 30;57(4):1205–15. Available from: <URL>.

24. Nieto G, Ros G, Castillo J. Antioxidant and antimicrobial properties of rosemary (*Rosmarinus officinalis*, L.): A review. Medicines [Internet]. 2018 Sep 4;5(3):98. Available from: <URL>.

25. Tan HF, Gan CY. Polysaccharide with antioxidant, α-amylase inhibitory and ACE inhibitory activities from Momordica charantia. Int J Biol Macromol [Internet]. 2016 Apr;85:487–96. Available from: <URL>.

26. Belwal T, Giri L, Bahukhandi A, Tariq M, Kewlani P, Bhatt ID, et al. Ginkgo biloba. In: Nonvitamin and Nonmineral Nutritional Supplements [Internet]. Elsevier; 2019. p. 241–50. Available from: <URL>.

27. Brown AC. An overview of herb and dietary supplement efficacy, safety and government regulations in the United States with suggested improvements. Part 1 of 5 series. Food Chem Toxicol [Internet]. 2017 Sep;107:449–71. Available from: <URL>.

28. Fibigr J, Šatínský D, Solich P. Current trends in the analysis and quality control of food supplements based on plant extracts. Anal Chim Acta [Internet]. 2018 Dec;1036:1–15. Available from: <URL>.

29. Shipkowski KA, Betz JM, Birnbaum LS, Bucher JR, Coates PM, Hopp DC, et al. Naturally complex: Perspectives and challenges associated with Botanical Dietary Supplement Safety assessment. Food Chem Toxicol [Internet]. 2018 Aug;118:963–71. Available from: <URL>.

30. Hertog MGL, Hollman PCH, Venema DP. Optimization of a quantitative HPLC determination of potentially anticarcinogenic flavonoids in vegetables and fruits. J Agric Food Chem [Internet]. 1992 Sep 1;40(9):1591–8. Available from: <URL>.

31. Apak R, Güçlü K, Özyürek M, Karademir SE. Novel total antioxidant capacity index for dietary polyphenols and vitamins C and E, using their cupric ion reducing capability in the presence of neocuproine: CUPRAC method. J Agric Food Chem [Internet]. 2004 Dec 1;52(26):7970–81. Available from: <URL>.

32. Re R, Pellegrini N, Proteggente A, Pannala A, Yang M, Rice-Evans C. Antioxidant activity applying an improved ABTS radical cation decolorization assay. Free Radic Biol Med [Internet]. 1999 May 1;26(9–10):1231–7. Available from: <URL>.

33. Singleton VL, Orthofer R, Lamuela-Raventós RM. Analysis of total phenols and other oxidation substrates and antioxidants by means of folin-ciocalteu reagent. In 1999. p. 152–78. Available from: <URL>.

34. Yıldız L, Başkan KS, Tütem E, Apak R. Combined HPLC-CUPRAC (cupric ion reducing antioxidant capacity) assay of parsley, celery leaves, and nettle. Talanta [Internet]. 2008 Oct;77(1):304–13. Available from: <URL>.

35. Karaman Ş, Tütem E, Sözgen Başkan K, Apak R. Comparison of total antioxidant capacity and phenolic composition of some apple juices with combined HPLC–CUPRAC assay. Food Chem [Internet]. 2010 Jun;120(4):1201–9. Available from: <URL>.

36. Karaman Ş, Tütem E, Başkan KS, Apak R. Comparison of antioxidant capacity and phenolic composition of peel and flesh of some apple varieties. J Sci Food Agric [Internet]. 2013 Mar 15;93(4):867–75. Available from: <URL>.

37. Gengaihi S El, Baker DHA. Grape seeds extract as brain food: A review. Int J Pharm Clin Res [Internet]. 2017 Mar 24;9(1):77–85. Available from: <URL>.

38. Gad AS, Sayd AF. Antioxidant properties of rosemary and its potential uses as natural antioxidant in dairy products—A review. Food Nutr Sci [Internet]. 2015;06(01):179–93. Available from: <URL>.

39. Lee SH, Jeong YS, Song J, Hwang KA, Noh GM, Hwang IG. Phenolic acid, carotenoid composition, and antioxidant activity of bitter melon (*Momordica charantia*L.) at different maturation stages. Int J Food Prop [Internet]. 2017 Dec 31;20(sup3):S3078–87. Available from: <URL>.

40. Wang L, Clardy A, Hui D, Gao A, Wu Y. Antioxidant and antidiabetic properties of Chinese

and Indian bitter melons (*Momordica charantia* L.). Food Biosci [Internet]. 2019 Jun;29:73–80. Available from: <URL>.

41. López-Gutiérrez N, Romero-González R, Vidal JLM, Frenich AG. Quality control evaluation of nutraceutical products from *Ginkgo biloba* using liquid chromatography coupled to high resolution mass spectrometry. J Pharm Biomed Anal [Internet]. 2016 Mar;121:151–60. Available from: <URL>.

42. Rimkiene L, Kubiliene A, Zevzikovas A, Kazlauskiene D, Jakstas V. Variation in flavonoid composition and radical-scavenging activity in *Ginkgo biloba* L. due to the growth location and time of harvest. J Food Qual [Internet]. 2017;2017:6840397. Available from: <URL>.

43. Apak R, Güçlü K, Özyürek M, Çelik SE. Mechanism of antioxidant capacity assays and the CUPRAC (cupric ion reducing antioxidant capacity) assay. Microchim Acta [Internet]. 2008 Apr 21;160(4):413–9. Available from: <URL>.

44. Özcan MM, Al Juhaimi F, Gülcü M, Uslu N, Geçgel Ü. Determination of bioactive compounds and mineral contents of seedless parts and seeds of grapes. South African J Enol Vitic [Internet]. 2017 Oct;38(2): 212-20. Available from: <URL>.

45. Krasteva D, Ivanov Y, Chengolova Z, Godjevargova T. Antimicrobial potential, antioxidant activity, and phenolic content of grape seed extracts from four grape varieties. Microorganisms [Internet]. 2023 Feb 3;11(2):395. Available from: <URL>.

46. Amorati R, Valgimigli L. Advantages and limitations of common testing methods for antioxidants. Free Radic Res [Internet]. 2015 May 4;49(5):633–49. Available from: <URL>.

47. Olah NK, Osser G, Câmpean RF, Furtuna FR, Benedec D, Filip L, et al. The study of polyphenolic compounds profile of some *Rosmarinus officinalis* L. extracts. Pak J Pharm Sci [Internet]. 2016;29(6):2355–61. Available from: <URL>.

48. Saeed F, Afzaal M, Niaz B, Arshad MU, Tufail T, Hussain MB, et al. Bitter melon (*Momordica charantia*): A natural healthy vegetable. Int J Food Prop [Internet]. 2018 Jan 1;21(1):1270–90. Available from: <URL>.

49. Alper M, Özay C. Antioxidant activity and phenolic composition of ethanol extracts of *Momordica charantia* and *Datura stramonium*. Kahramanmaraş Sütçü İmam Üniversitesi Tarım ve Doğa Derg [Internet]. 2022 Feb 28;25(1):1–9. Available from: <URL>.

50. Anilakumar KR, Kumar GP, Ilaiyaraja N. Nutritional, pharmacological and medicinal properties of *Momordica charantia*. Int J Nutr Food Sci [Internet]. 2015;4(1):75-83. Available from: <URL>.

51. Akyüz E, Türkoğlu S, Sözgen Başkan K, Tütem E, Apak MR. Comparison of antioxidant capacities and antioxidant components of commercial bitter melon (*Momordica charantia* L.) products. Turkish J Chem [Internet]. 2020 Dec 16;44(6):1663–73. Available from: <URL>.

52. Savsatli Y, Seyis F. Determination of suitable solvents for extraction of different fruit parts of bitter melon (*Momordica charantia* L. Int J Agric Nat Sci [Internet]. 2016;9(1):18–22. Available from: <URL>.

53. Hussain A, Fatima H, Komal M, Kauser S, Yaqub S, Akram S, et al. Evaluation of peel, flesh and seeds of bitter gourd (*Momordica charantia* L.) for biologically active components, through development of powders and ethanolic extracts. Discov Appl Sci [Internet]. 2024 Aug 6;6(8):432. Available from: <URL>.

54. Gayathry KS, John JA. A comprehensive review on bitter gourd (*Momordica charantia* L.) as a gold mine of functional bioactive components for therapeutic foods. Food Prod Process Nutr [Internet]. 2022 Dec 25;4(1):10. Available from: <URL>.

55. Koczka N, Ombódi A, Móczár Z, Stefanovits-Bányai E. Total phenolic content and antioxidant capacity of ginkgo teas. Acta Aliment [Internet]. 2016 Mar;45(1):77–84. Available from: <URL>.

56. Aybastier Ö. Determination of antioxidant properties of *Ginkgo biloba* in different forms. Eur J Sci Technol [Internet]. 2020 Apr 1;18:206–12. Available from: <URL>.

57. Xiao J. Dietary flavonoid aglycones and their glycosides: Which show better biological significance? Crit Rev Food Sci Nutr [Internet]. 2017 Jul 15;57(9):1874–905. Available from: <URL>.

JOTCS A Journal of the Turkish Chemical Society Section: A Chemistry

TURKISH CHEMICAL SOCIETY

Microstructure-Mechanical Properties of Mg-xCa Alloys Produced by Mechanical Alloying-Hot Pressing Process and Their Optimization Using Central Composite Design Method

Lütfiye Feray Güleryüz[1*], Rasim İpek[1]

[1]Department of Mechanical Engineering, Faculty of Engineering Ege University, Bornova, 35040, İzmir, Türkiye.

Abstract: In the study, Mg-xCa alloys with high mechanical performance were developed using a statistical model central composite design (CCD) method to predict the mechanical properties of Mg and Ca powders produced by powder metallurgy. Powder metallurgy (TM) is a production method that offers great advantages over other production methods. However, there are limited studies in the literature on the production of alloying Ca to eliminate the high degradation rate of pure Mg loss. Mg and Ca powders were subjected to the alloying process for different times as 11.99-14.43-18-21.5-24 h, and after mechanical alloying (MA), grain size measurements of the powders and XRD and SEM-EDS analyses were performed. After MA, the powders were sintered at different temperatures, such as 325-370-437-504-549°C in an argon gas environment under 46 MPa pressure, and samples were obtained. The microstructures, mechanical properties, compressive strength, density values, and XRD-SEM results showed that the secondary phase Mg_2Ca increased with increasing Ca content, which indicates the increasing hardness of Mg-xCa alloy. Using the CCD method, the sample's compressive strength, hardness, and density results with optimal values produced from Mg-xCa alloys were determined as 251 MPa, 146 Brinell, and 1.7 g/cm^3, respectively. The compatibility of the experimental results with the Regression formula confirms the reliability of the equation.

Keywords: Powder metallurgy; CCD method; XRD; SEM-EDS; Mg-xCa alloys.

Submitted: January 30, 2025. **Accepted:** May 10, 2025.

Cite this: Güleryüz LF, İpek R. Microstructure-Mechanical Properties of Mg-xCa Alloys Produced by Mechanical Alloying-Hot Pressing Process and Their Optimization Using Central Composite Design Method. JOTCSA. 2025;12(2): 141-154.

DOI: https://doi.org/10.18596/jotcsa.1630114

***Corresponding author's E-mail:** ferayguleryuz@hotmail.com

1. INTRODUCTION

Central Composite Design (CCD) is a widely used five-level fractional factorial design, originally developed by Box and Wilson (1). The structure of CCD typically includes a 2^n full factorial design, 2 × n axial designs, and m central designs. In this setup, the axial designs are similar to the central designs, with the exception of one factor that takes levels either above the high level or below the low level of the 2^n full factorial design (2). One of the main advantages of CCD is its ability to estimate the nonlinearity of dependent variables effectively. Furthermore, it provides maximum information with a minimal amount of experimental data and reduces the number of experiments needed to predict quadratic terms in a second-order model. In addition to these benefits, CCD is highly effective in simultaneously evaluating mathematical and statistical data, making it a powerful tool for optimizing experimental conditions. This method enables researchers to manipulate multiple input factors at once and understand their individual and combined effects on a desired output. Due to these capabilities, CCD has become one of the most popular experimental designs in research fields that require precise modelling and optimization. Its efficiency and flexibility make it especially useful in developing predictive models and improving system performances with fewer experiments (6-9).

Mechanical alloying (MA) is a very widely used method in powder metallurgy production (10-12). Compared to other traditional metallurgical techniques, it is possible to produce alloys that are difficult to produce with the MA technique. Moreover, the MA method has an economic advantage since it enables the production of alloys with different

melting temperatures without reaching high temperatures (13). The powder metallurgy process is carried out in the solid state due to the absence or minimization of undesirable interface reactions between the matrix and the reinforcement element. Therefore, the MA method, which is a solid-state processing technique, is especially preferred in the production of magnesium matrix and calcium-reinforced alloys (14). The hexagonal close-packed structure of Mg (c/a = 1.624) forms solid solutions with many elements (15). Because the mechanical properties of alloying elements such as Mg can be further strengthened by solid solution, precipitation hardening, and grain refinement hardening (15), on the other hand, the superior properties of Mg–Ca alloys are reported (16), and their strength, surface corrosion, fatigue, biocompatibility, and allergic reaction properties of tissues are reported in different studies (17-20). Compared to traditional cold press sintering processes, the Joule sintering process is a process that minimizes porosity in the structure. The Joule heating technique requires a shorter time, less power, and a lower temperature. In addition, higher densities are obtained in this technique compared to cold press-sintering. Another advantage of this system is the sintering time, which does not require a long time as in other cold press processes (21-23).

In this study, the structural, morphological, and mechanical properties of Mg-xCa alloys produced by the mechanical alloying-hot pressing method were examined, and mechanical properties of Mg-xCa alloys produced by the mechanical alloying-hot pressing method were discussed, and statistical modeling was performed using the CCD method. Mg-xCa alloys with improved mechanical properties were successfully developed using the central composite design (CCD) method. The application of powder metallurgy and mechanical alloying at different times, followed by sintering at various temperatures, enabled precise control of microstructure and phase formation. The results showed that increasing Ca content promoted the formation of Mg_2Ca, leading to higher hardness and compressive strength. The strong correlation between the experimental results and the regression model confirmed the reliability of the CCD approach. The structural, morphological, and mechanical properties were determined using XRD, SEM-EDS analysis, and compressive strength-hardness tests.

2. EXPERIMENTAL

In the study, 9 different powder mixtures were prepared according to the CCD method for the mechanical alloying process, as seen in Table 1.

Table 1: Prepared mechanical alloying powders.

Sample no.	MA time (h)	Ca content (%)
Pure-Mg	0	0
1	11.99	4.7
2	14.43	2.7
3	14.43	6.7
4	18	1.33
5	18	4.7
6	18	8
7	21.57	2.7
8	21.57	6.7
9	24	4.7

The powders were subjected to a planetary ball milling process with 10 mm diameter stainless steel balls having 20:1 (ball/powder) weight ratio and 160 rpm rotation speed at different hours during mechanical milling. Then, a high-strength graphite mold with a 10 mm inner diameter and 60 mm height was used for the sample fast sintering process. Mg powder with 99% purity, an irregular grain shape, and an average grain size of 125 µm was used as reinforcement material, and calcium powder with 99.98% purity was used as matrix material. To prevent excessive cold welding, 2% by weight zinc stearate ($C_{36}H_{70}O_4Zn$) was added as a process control element in all samples. A mechanical alloying process was carried out to obtain Mg-xCa alloy.

Nine mechanically alloyed samples were subjected to a sintering process for 20 samples using five different temperatures according to CCD modeling. The ball-milled powders were placed in a graphite mold and hot press sintered under 46 Mpa pressure in an argon atmosphere. Different sintering temperatures (325-370-437-504-549 °C) and mechanical milling times (11.99-14.43-18-21.5-24 h) were carried out. Standard metallographic techniques were used to prepare the samples for microstructural examination. Metallographic samples were prepared from cross-sections of the investigated composites. All samples were gently ground.

In the CCD method, the selected factors are the Mg-xCa ratio, sintering temperature, and MA time. Independent variables are coded as -1 and +1, representing a two-level full factorial design. It has eight factorial points. The pivot point represents the high and low points of each factor. In the present study, CCD consists of $2k+2k+n$ runs. k is the number of factors. $2k$ is the number of factorial points, 2k is the number of axial points, α is the distance between the axial point and the center point, and α value is the coded value determined by the number of factors. It was obtained from the following Eq. (1):

$$\alpha = 2k^{1/2} \quad (1)$$

where the six axial points were located at (±α, 0, 0), (0, ±α, 0), (0, 0, ±α), and the six replicates were at the center (Figure 1).

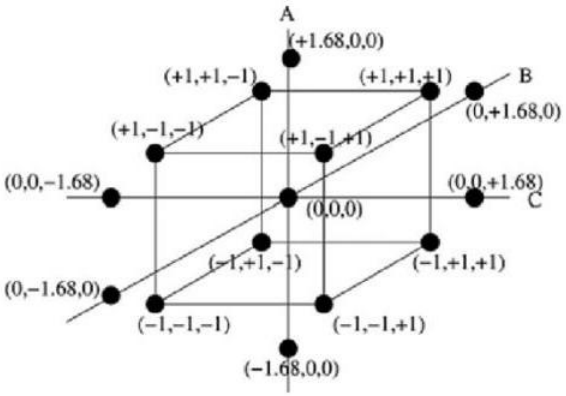

Figure 1: CCD design with 3 factors and 5 levels.

The phase structure of the samples was examined by XRD (X-ray diffractometer; D2 PHASER, Bruker Corp., Germany) using Cu-K_α (1.5406 Å) radiation in between 2θ=30-75 °C with scan speed 2 °C/min. The average crystallite sizes were determined from Scherrer Eq. (2) (24,25):

$$D = \frac{k \cdot \lambda}{\beta \cdot Cos\ \theta} \quad (2)$$

where D represents the crystallite size in nanometers, while k is considered a constant, typically valued at 0.9, CuKα denotes the wavelength (λ = 0.15406 Å), and β signifies the full width at half maximum measured in radians.

The surface morphology, microstructure, and phase detection of powders were performed by scanning electron microscopy (SEM; Jeol JSM 5910LV) equipped with energy dispersive spectroscopy (EDS; Oxford Instruments Inca X-Sight 7274). Hardness tests were performed on all samples using a Brinell hardness method with a 2.5 mm diameter ball indenter and 62.5 kgf load. For the compressing test, the cylindrical samples were determined by ASTM test method B 925-08 using a Zwick Roel Model 2100 tensile testing machine with a 0.5 mm/min testing speed.

3. RESULTS AND DISCUSSION

3.1. XRD-SEM Results of Mechanical Alloying Powders

Figure 2 shows the X-ray diffraction results of the powders after mechanical alloying. As seen in the XRD results, in addition to the Mg phase (JCPDS card no. 65-3583), a small amount of Mg_2Ca phase (JCPDS card no. 89-4244) was formed. Also, some MgO occurred due to the oxidation of Mg during MA. As seen in Figure 2, since mechanical alloying was done in an air environment, increasing the temperature with the milling time from 11.99 to 24 h increased the oxidation effect and, therefore, the MgO peak intensity in the XRD pattern. The mechanical alloying process ensures material homogenization and also leads to a reduction in grain size. From the XRD results, the crystallite size and Ca content-MA time relationship in the powders after the MA process were examined using the Scherrer equation, and the results are given in Table 2. While the initial grain size was 49 nm for pure Mg, it was found to be approximately 42 and 37 nm at 11.99 and 14.43 h MA times, respectively. The grain size continued to decrease and reached the lowest value of roughly 33 nm at the end of 18 h. The grain size tended to increase again after the 18 h MA process and was determined to be approximately 37 and 41 nm at 21.57 and 24 h MA times, respectively. During the MA process, grain growth is reported at long MA times (26-28), in which the dislocation mechanism is dominant at the beginning, and work hardening and temperature increase during MA effective. In addition, the present results showed that the duration of the mechanical alloying process is significantly effective compared to the Ca ratio.

Table 2: Crystallite sizes of mechanical alloying powders calculated from the Scherrer method and Ca amounts.

Sample no.	MA time (h)	Ca content (%)	Criystallite size (nm)
Pure-Mg	0	0	49
1	11.99	4.7	42
2	14.43	2.7	36
3	14.43	6.7	38
4	18	1.33	33
5	18	4.7	32
6	18	8	33
7	21.57	2.7	37
8	21.57	6.7	38
9	24	4.7	41

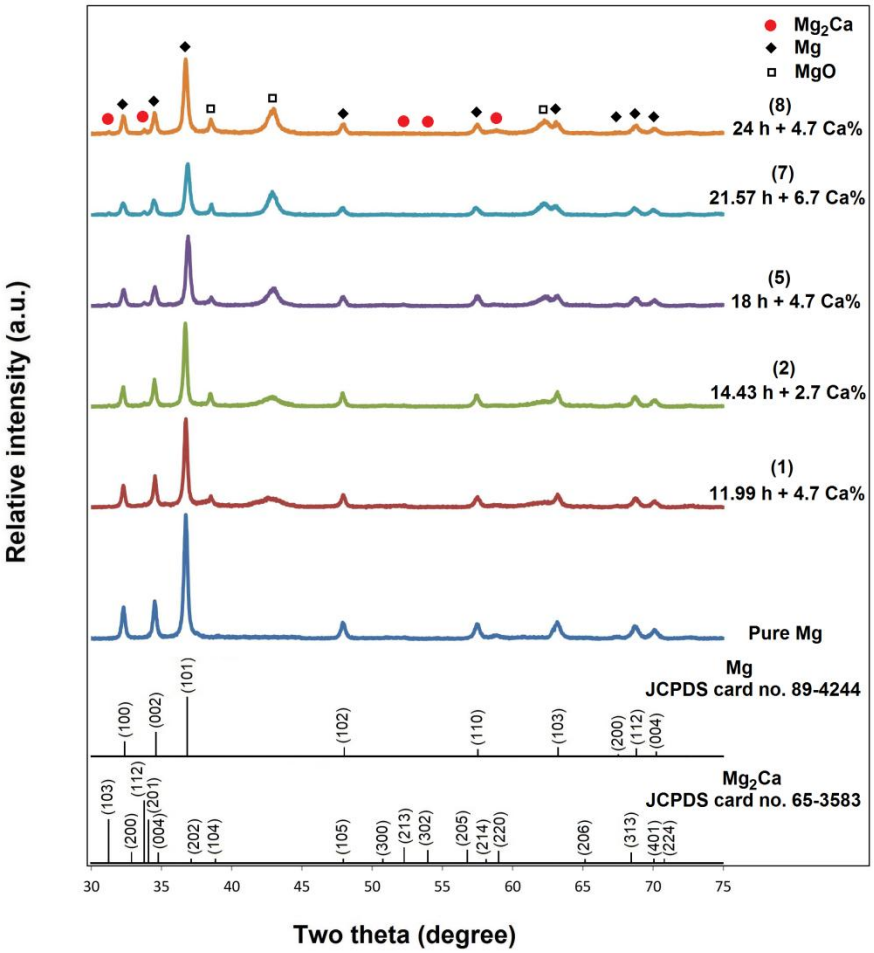

Figure 2: X-ray diffraction results of powders produced by adding Ca to pure Mg powder at different rates (between 1.33% and 8%) and performing MA for periods between 11.99 and 24 h.

Figure 3(a-e) shows the SEM images at x20000 magnification, showing the changes in the surface morphologies of the powders subjected to the mechanical alloying process at different MA times with different Ca contents. The SEM microstructure image of powder number 1 or code 4.7/11.99 is given in Figure 3a, where the grain shapes became significantly amorphous after 11.99 h mechanical grinding, consistent with the XRD result. In the SEM image of the 3-6.7/14.43 coded or powder number 3, whose MA time is 14.43 h and is given in Figure 3b, it was observed that the tendency for coalescence in the particles continued and the size decrease continued due to the shrinking amorphous particle structure. In Figure 3c, it was determined that the powder and grain sizes of the 4.7/18 coded powder number 5 subjected to an 18 h MA process were at the smallest values, which is the expected result of the grinding-boiling-breakage cycles in the mechanical grinding mechanism, in accordance with the literature. In addition, the breaking mechanism is effective here, and the grains are spherical. The powders given in Figure 3d and Figure 3e at 21.57 h (6.7/21.57 coded or powder number 7) and 24 h (4.7/24 coded or powder number 9) tended to cluster (plaque-like stratification) and grain growth was observed, respectively. It is seen from the SEM results that the agglomeration-clustering tendency continued to increase with the increase in grinding time. Additionally, the presence of Ca is likely to contribute to some tendency towards amorphization in the structure.

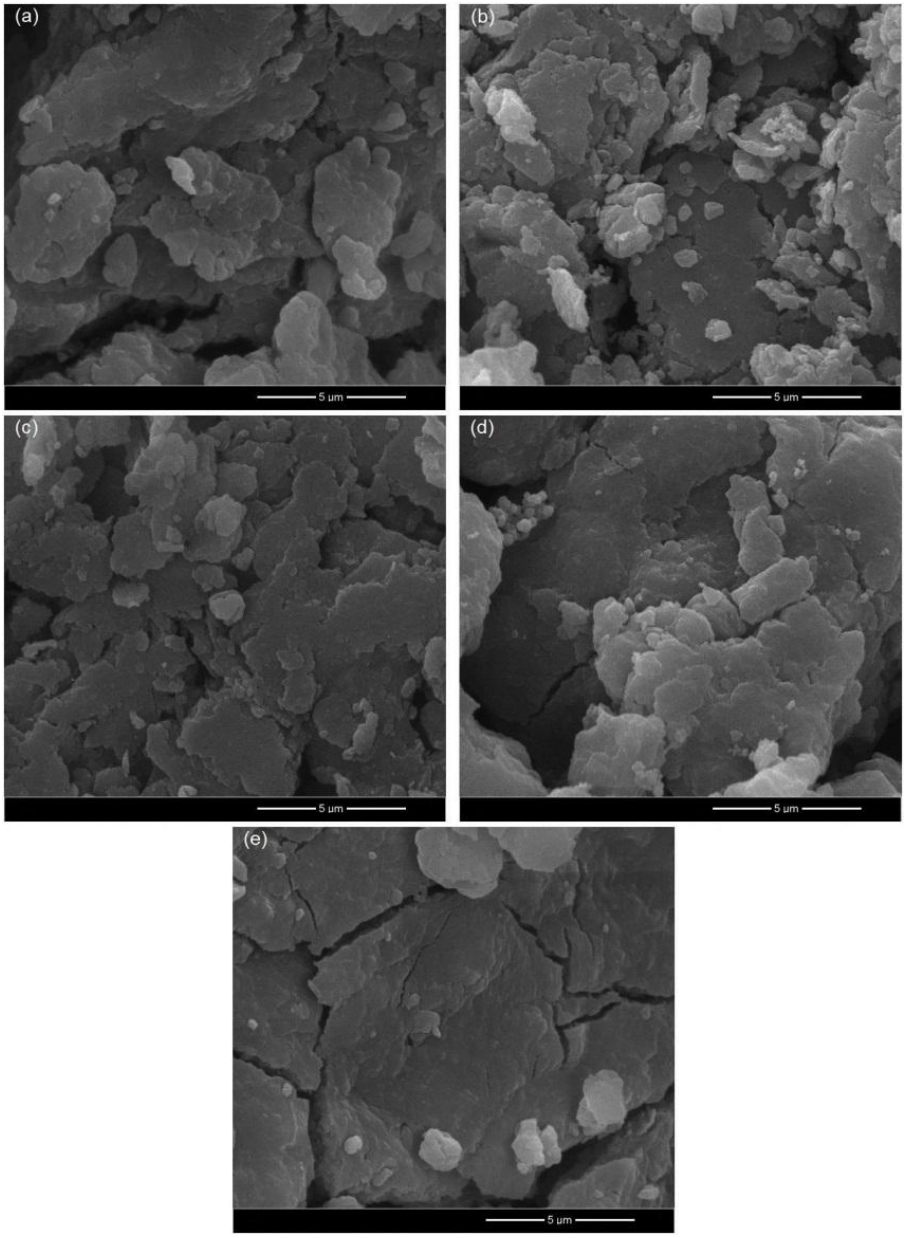

Figure 3: SEM micrographs at x20000 magnification of the powders mechanically alloyed at different times and Ca concentrations (a) 4.7/11.99, (b) 3-6.7/14.43, (c) 1-4.7/18, (d) 6-(6.7/21.57 and (e) 9-4.7/24, respectively.

3.2. XRD, SEM-EDS, Porosity, Mechanical Testing Results of Hot-Pressing Samples

The XRD results of the hot-pressing samples are given in Figure 4. As seen in the XRD results, in addition to the Mg main phase of the samples subjected to the sintering process at different temperatures, the Mg_2Ca phase formed during the MA process. In addition, as seen in Figure 4, the MgO phase formed during mechanical alloying is also present in the structure after the hot pressing process. While the broad MgO peaks in Figure 2 correspond to low crystallite size and amorphization, the sharpened peaks in Figure 4 can be associated with the crystallinity developing in the MgO phase and the increase in crystallite size.

Figure 5(a-f) shows the EDS results along with the SEM images for the hot-pressing samples. In the SEM images, the regions indicated by the red arrow indicate the regions where the Mg-xCa phase is present. The EDS results of the area where the entire SEM micrograph is scanned in Figure 5(a, b) and the blue framed region in Figure 5c are given in Figure 4d, e, and f, respectively. In EDS results, the Ca% contents of the samples vary between 2.65, 6.40, and 9.25% by weight and 1.49, 3.84, and 5.54 atomic % amounts, respectively. The theoretical contents of the samples have 1.33%, 4.7%, and 8% Ca, which are compatible with the amounts obtained as a result of elemental analysis, respectively. When the XRD and SEM-EDS results are evaluated together, the presence of oxygen in the EDS results is associated with some MgO phase in the Mg matrix formed during mechanical milling, as seen in the X-ray diffraction pattern. Moreover, depending on the presence of the Mg_2Ca phase in the XRD results, the grains with high atomic contrast in both the SEM backscattered electron images and the presence of the Ca element in the EDS results confirm the Mg_2Ca phase.

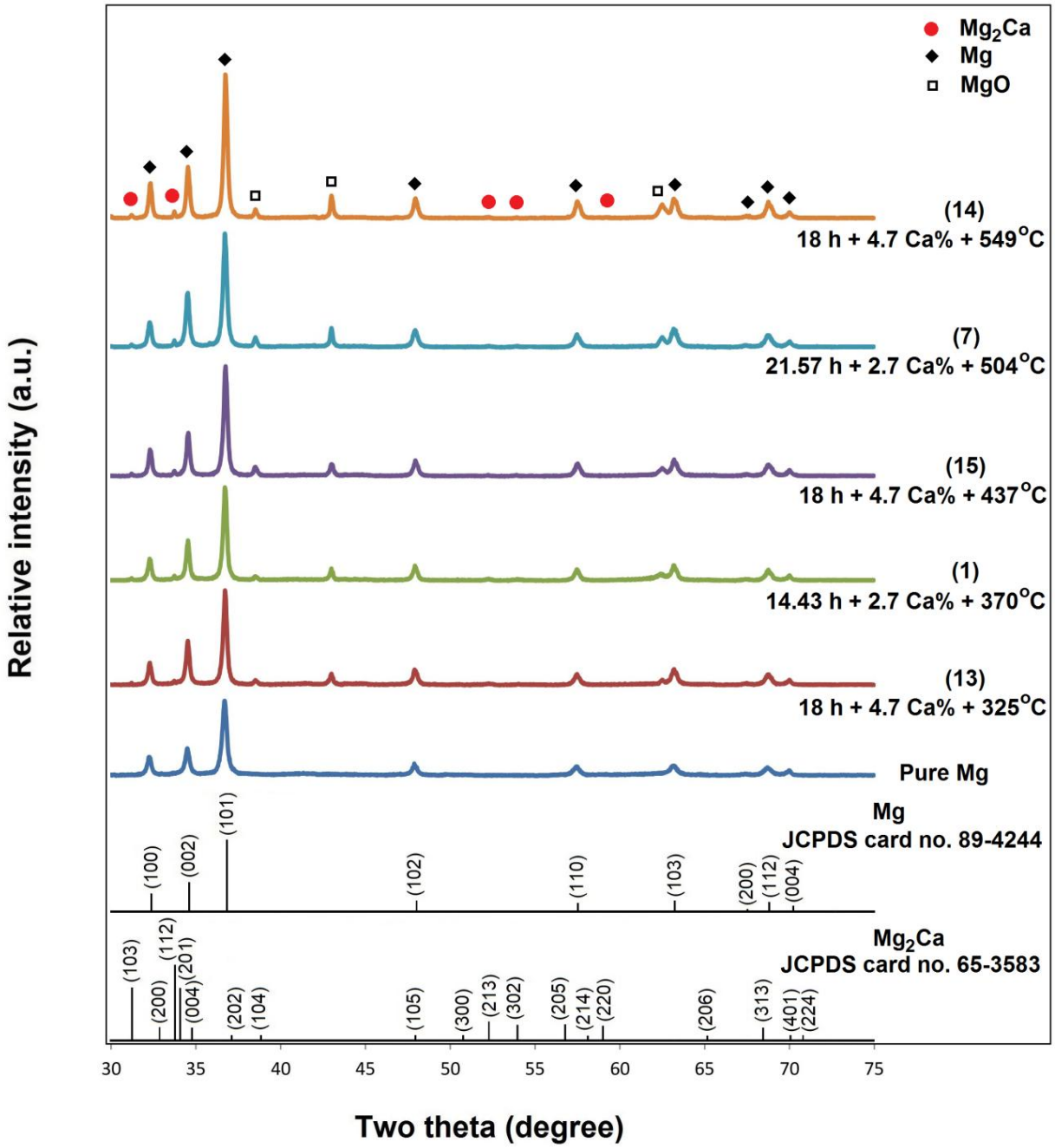

Figure 4: X-ray diffraction results of hot-pressing samples subjected to sintering at different temperatures.

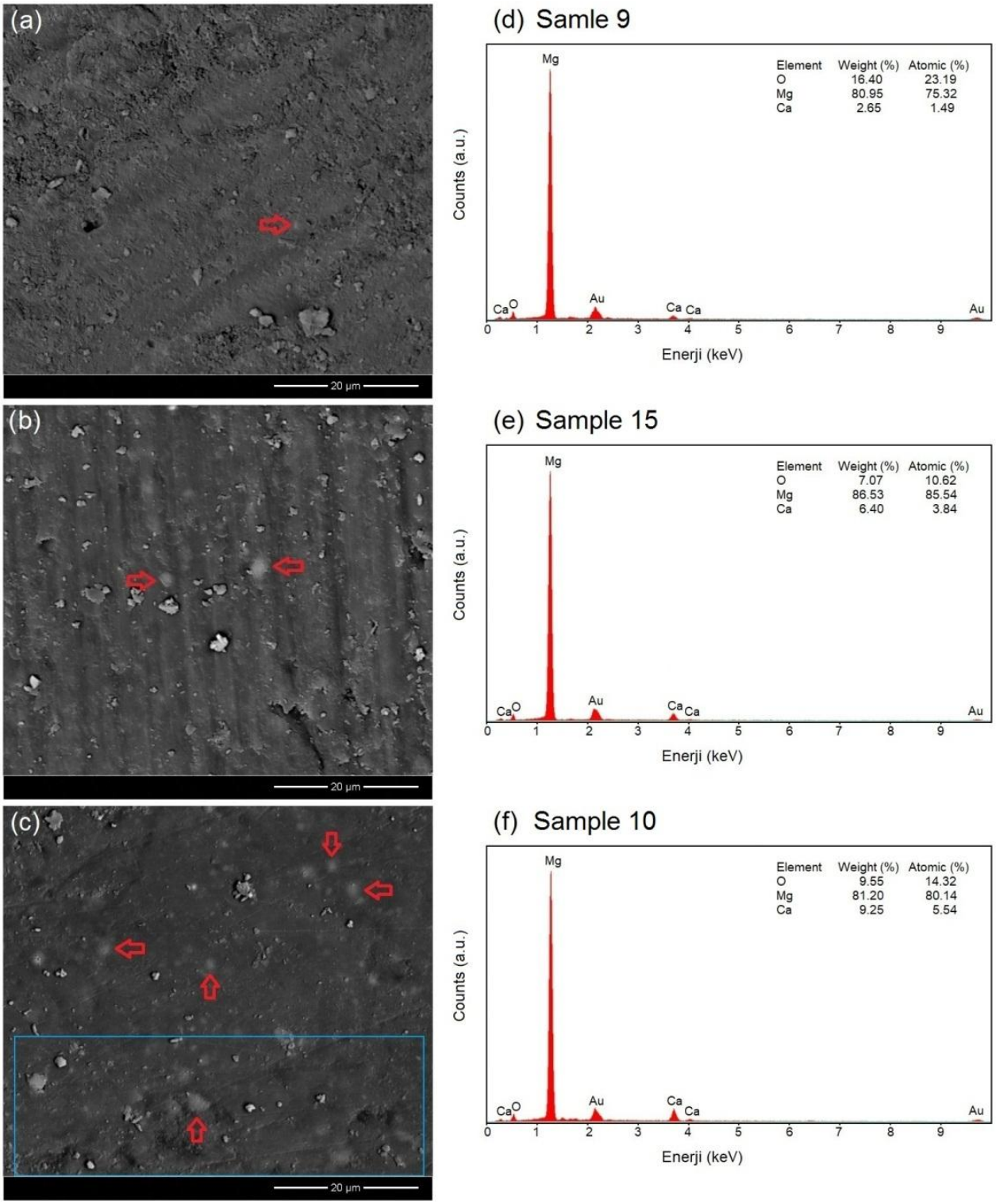

Figure 5: SEM (backscattered electron) images at x5000 magnification and EDS spectra for the hot-pressing samples (a)-(d) 1.33/18/437, (b)-(e) 4.7/18/437, (c)-(f) 8/18/437, respectively.

Theoretical, real densities and porosity amounts of hot-pressing samples are given in Table 3, where real densities and porosity amounts vary between 1.546-1.700 g/cm^3 and 1.6-11%, respectively. Compared with the theoretical values in Table 2, the actual densities and porosities of the samples vary depending on the Ca% ratio, MA time, and sintering temperature. The porosity results of the samples were examined based on the Ca ratio, MA time, and temperature factors and are given in Figure 6(a-c). The MA time reached the lowest porosity value around 18 h. At the same time, the Ca ratio showed a low porosity of 97, around 4.7%, where amounts above 4.7% Ca can be associated with an increase in the Mg_2Ca phase and deterioration in parameters. Another parameter, temperature, showed the lowest porosity around 437 °C (Figure 6c). Based on the obtained data, it is seen that the sintered samples achieved optimum porosity values at 18 h MA time, 4.7% Ca ratio, and 437 °C heat treatment temperature.

Table 3: Theoretical density, real density, and porosity results of hot-pressing samples.

Sample number	Sample code	Theoretical density-ρt (g/cm^3)	Real density-ρg (g/cm^3)	Porosity (%)
1	2.7/14.43/370	1.7329	1.609	7.1
2	6.7/14.43/370	1.7250	1.593	7.6
3	2.7/21.57/370	1.7329	1.603	7.5
4	6.7/21.57/370	1.7250	1.546	11
5	2.7/14.43/504	1.7329	1.643	5
6	6.7/14.43/504	1.7250	1.607	7
7	2.7/21.57/504	1.7329	1.655	4
8	6.7/21.57/504	1.7250	1.571	9
9	1.33/18/437	1.7350	1.690	3
10	8/18/437	1.7230	1.608	7
11	4.7/11.99/437	1.7290	1.569	10
12	4.7/24/437	1.7290	1.650	5
13	4.7/18/325	1.7290	1.615	7
14	4.7/18/549	1.7290	1.641	5
15	4.7/18/437	1.7290	1.682	2
16	4.7/18/437	1.7290	1.662	3
17	4.7/18/437	1.7290	1.666	3
18	4.7/18/437	1.7290	1.700	1.6
19	4.7/18/437	1.7290	1.690	2
20	4.7/18/437	1.7290	1.662	3

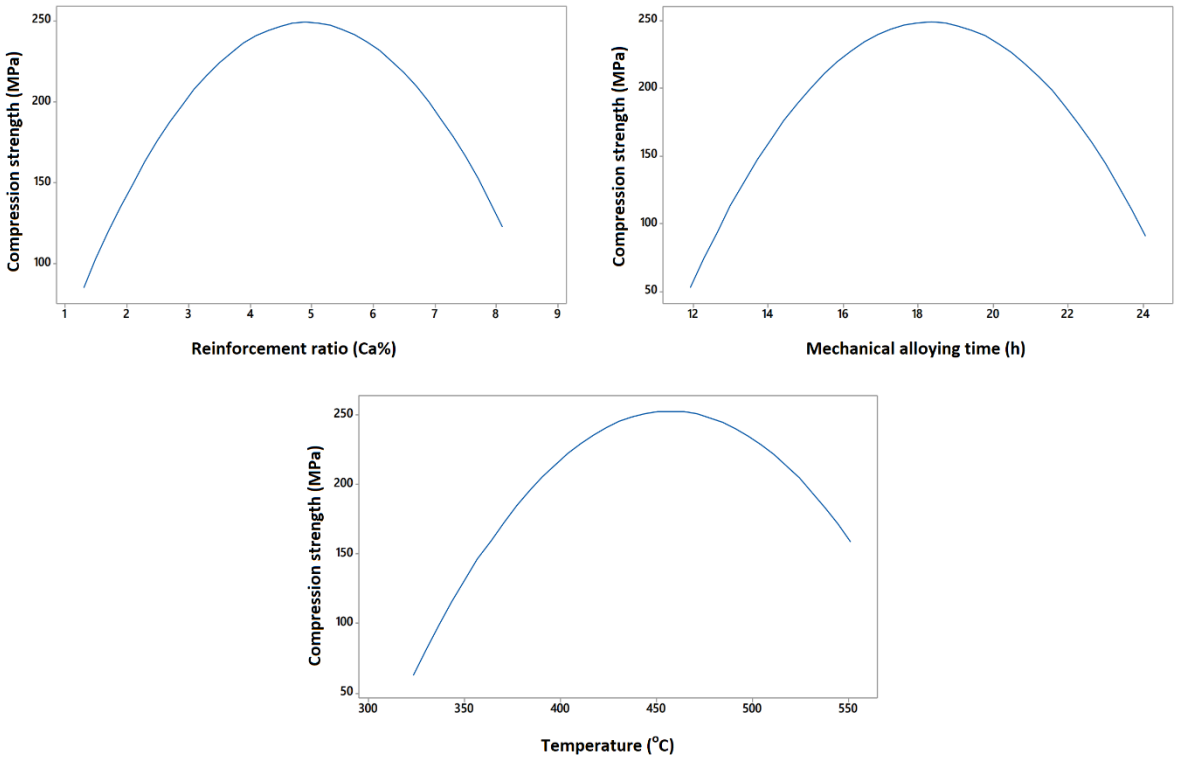

Figure 6: (a) %Ca ratio-porosity, (b) MA time-porosity, (c) Temperature-porosity results.

The hardness and compression test results of the samples subjected to hot pressing are summarized in Table 4. While the hardness values of the samples vary between 44-146 HB, the compression test values range between 38-251 MPa. In Table 4, it is seen that the hardness and compression test results are at high values for the sample with optimum values (sample coded 18-4.7/18/437), and these results are consistent with the literature data, which is given in Table 5. As seen in Table 5, in the study

conducted by Yahşi and İpek, compressive strength is 307 MPa for Mg/MgO structure after 18 h of milling and sintering at 550 °C (29). In another study by Hirata et al., compressive strength is 150 MPa for Al_2O_3 alloy after 24 h milling time and 1300 °C sintering (30). Yahşi et al. (31) reported compressive strength values of 195 and 192 MPa, respectively, at short milling times by adding 10% and 20% of PVA (polyvinyl alcohol) to the Mg matrix.

Table 4: Brinell hardness and compressive strength results of hot-pressing samples.

Sample number	Sample code	Brinell hardness (kg/mm^2)	Compressive strength (MPa)
1	2.7/14.43/370	44	38
2	6.7/14.43/370	52	39
3	2.7/21.57/370	52	76
4	6.7/21.57/370	45	108
5	2.7/14.43/504	108	94
6	6.7/14.43/504	91	132
7	2.7/21.57/504	69	75
8	6.7/21.57/504	60	116
9	1.33/18/437	127	102
10	8/18/437	123	125
11	4.7/11.99/437	58	58
12	4.7/24/437	46	106
13	4.7/18/325	49	52
14	4.7/18/549	131	188
15	4.7/18/437	143	250
16	4.7/18/437	143	245
17	4.7/18/437	145	249
18	4.7/18/437	146	251
19	4.7/18/437	144	245
20	4.7/18/437	143	220

Table 5: Study results and literature data.

MA time (h)	Sintering temperature (C^o)	Matrix	Additive	Content (%)	Brinell hardness (kg/mm^2)	Compressive strength (MPa)	Ref.
18	437	Mg	Mg	4.7	146	251	This study
18	550	Mg	Mg	-	35	307	(29)
24	1300	AKP50	AKP20	1-100	-	150	(30)
0.5	400	Mg	PVA	10	-	195	(31)
1	400	Mg	PVA	20	-	192	(31)

3.3. Evaluation of Hot-Pressing Samples with Statistical Model Central Composite Design (CCD) Method

Table 6 presents the regulated version of the samples produced according to different Ca% (X1), MA (X2), and temperature (X3) parameters according to the CCD experimental design method.

To determine the experimental factors (A, B, C) and the interactions between the factors (A*A, B*B, C*C, A*B, A*C, B*C) and to test the reliability of the experiments, ANOVA analysis was performed using the data in Table 6 with the help of the Minitab 17 program. The results obtained are summarized in Table 7.

Table 6: Regulation of hardness, porosity, and compressive strength parameters of hot-pressing samples according to CCD method.

Std. ord.	Run ord.	Coded Variables			Uncoded Variables			Hardness (HB)	Porosity (%)	Comp. Strength (MPa)
		X1	X2	X3	X1	X2	X3			Y
1	1	-1	-1	-1	2.7	14.43	370	44	7.1	38
2	7	1	-1	-1	6.7	14.43	370	52	7.6	39
3	16	-1	1	-1	2.7	21.57	370	52	7.5	76
4	12	1	1	-1	6.7	21.57	370	45	11	108
5	9	-1	-1	1	2.7	14.43	504	108	5	94
6	2	1	-1	1	6.7	14.43	504	91	7	132
7	20	-1	1	1	2.7	21.57	504	69	4	75
8	8	1	1	1	6.7	21.57	504	60	9	116
9	13	-1.68179	0	0	1.33	18	437	127	3	102
10	19	1.68179	0	0	8	18	437	123	7	125
11	11	0	-1.68179	0	4.7	12	437	58	10	58
12	3	0	1.68179	0	4.7	24	437	46	5	106
13	5	0	0	-1.68179	4.7	18	325	49	7	52
14	18	0	0	1.68179	4.7	18	549	131	5	188
15	10	0	0	0	4.7	18	437	143	2	250
16	17	0	0	0	4.7	18	437	143	3	245
17	15	0	0	0	4.7	18	437	145	3	249
18	14	0	0	0	4.7	18	437	146	1.6	251
19	4	0	0	0	4.7	18	437	144	2	245
20	6	0	0	0	4.7	18	437	143	3	220

Table 7: ANOVA analysis of hot-pressing samples.

Analysis of variance (ANOVA) of CCD model					
Source	Degrees of Freedom (DF)	Sum of squares	Mean square	F value	P value
MODEL	9	114047	12671.9	42.81	0.000 significant
LINEAR	3	14208	4736.1	16.00	0.000
A	1	1663	1662.5	5.62	0.039
B	1	1708	1708.0	5.77	0.037
C	1	10838	10838.0	36.61	0.000
SQUARE	3	96909	32303.0	109.13	0.000
A*A	1	33819	33819.0	114.25	0.000
B*B	1	51156	51156.4	172.82	0.000
C*C	1	30686	30686.4	103.67	0.000
2-Way interaction	3	2930	976.5	3.30	0.066
A*B	1	145	144.5	0.49	0.501
A*C	1	264	264.5	0.89	0.367
B*C	1	2521	2520.5	8.52	0.015
Resudial error	10	2960	296.0		
Lack of fit	5	2275	454.9	3.32	0.107 significant
Pure error	5	685	137.1		
Total	19	117007			
R-sq	97.47 %				

In Table 7, when the model is evaluated in terms of F and P-value, the model created is statistically significant because the P-value for the F-value of 42.81 is less than 0.05 (0.000<0.05). On the other hand, when the model is evaluated in terms of Lack of fit and P-value, it is not significant because the lack of fit is 0.107>0.05. The lack of fit test determines whether the mathematical form of the obtained model is suitable for representing the experimental data (32). As a result, the lack of fit value is insignificant in the adjusted model. Therefore, the removal of two-way interactions (A*B,

A*C, B*C) components in Table 7 does not affect the model reliability.

Table 8: ANOVA analysis result data.

Adeq-precision	16.7556
R-Sq	%97.12
R-Sq (adj)	%95.44
R-Sq(pred)	%88.50

In Table 8, Adeg-precision measures the signal/noise ratio, which becomes significant when it is greater than 4. For this model, Adeg-precision=16.7556 is a suitable value and shows a sufficient signal/noise ratio. RSq value and RSq (adj) values are 97.12% and 95.44%, respectively. The R Sq value is close to 97.12%, indicating that the deviation in the distribution of the experiments is low. The RSq (adj) value is 95.44%. The R Sq (pred) value is expected to be close to RSq (adj), and 88.5% is a reasonable value. As a result, when all three parameters are considered, the most effective factor is temperature. In addition, the MA-temperature interaction is relatively more effective than the MA-Ca ratio and the temperature-Ca ratio. The following Regression Eq. (3) was obtained using the Minitab 17 program.

$$C8 = 243.72+11.03*A + 11.18*B + 28.17\ C - 48.44\ A*A - 59.58\ B*B - 46.14\ C*C - 17.75\ B*C \quad (3)$$

The regression equation is 97.80%. R-Sq (adj) value is 95.44% and close to 97.80%. Here, C8 gives the estimated value. A, B, and C show the coded factors. The (+) values seen here show that the increase in reinforcement ratio, MA time, and temperature increases the compressive strength. It is seen that the most effective of the main factor values is temperature. It is understood that the interaction between the factors (A*A, B*B, C*C) is more effective than the main effects (A, B, C). The regression Eq. (3) confirms that it can be used to estimate compressive strength within the limit values. The comparison of the experimental results according to the regression equation is shown in the graph in Figure 7. As seen in the graph, the experimental results are in good agreement with the results calculated according to the Regression equation.

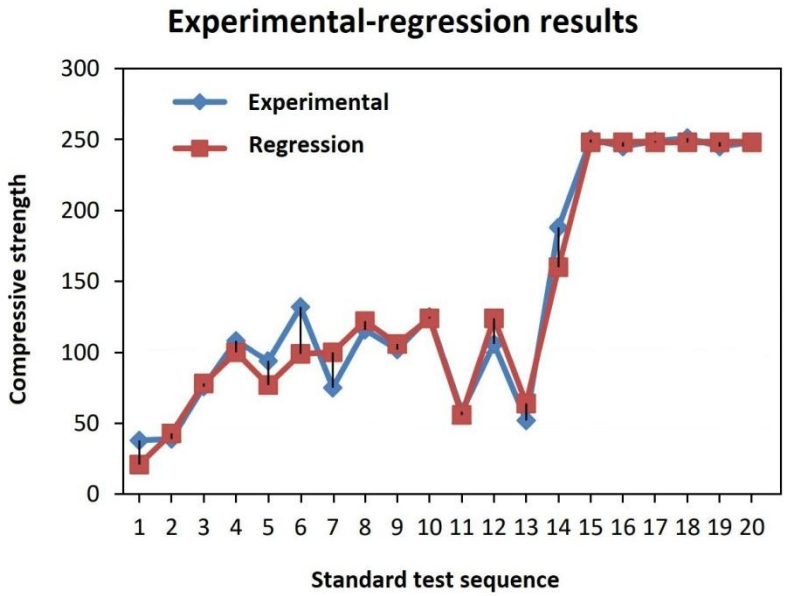

Figure 7: Regression equation and experimental results comparison graph.

4. CONCLUSION

In this study, the mechanical performance of Mg-xCa alloys was systematically investigated by applying the Central Composite Design (CCD) methodology. CCD enabled the optimization and prediction of mechanical properties by controlling two critical process parameters: mechanical alloying time and sintering temperature, where Mg and Ca powders were subjected to mechanical alloying for varying durations (11.99, 14.43, 18, 21.5, and 24 hours), followed by sintering at different temperatures (325°C, 370°C, 437°C, 504°C, and 549°C) under an argon atmosphere at 46 MPa pressure. XRD, SEM-EDS analyses, and grain size measurements revealed that prolonged alloying time and higher sintering temperatures promoted the formation of the Mg_2Ca secondary phase. The presence of this phase contributed significantly to the enhancement of mechanical properties. The experimental results indicated a clear increase in compressive strength, hardness, and density with increasing Ca content. The maximum compressive strength, hardness, and density obtained were 251 MPa, 146 Brinell hardness, and 1.7 g/cm^3, respectively. Using the CCD model, regression equations were derived that accurately predicted the experimental outcomes. The close correlation between the experimental data and the model predictions validated the reliability of the CCD approach in optimizing the mechanical performance of Mg-xCa alloys. Moreover, the findings confirm that fine-tuning processing parameters through statistical modelling can significantly enhance the mechanical behavior of magnesium-based alloys produced by powder metallurgy. This study demonstrates that CCD is an effective and reliable method for process optimization in developing high-performance Mg

alloys with controlled degradation rates, which is crucial for biomedical and structural applications.

5. CONFLICT OF INTEREST

There is no conflict of interest.

6. REFERENCES

1. Box GEP, Wilson KB. On the experimental attainment of optimum conditions. In: Kotz S, Johnson NL, editors. Breakthroughs in Statistics [Internet]. Springer, New York, NY; 1992. p. 270–310. Available from: <URL>.

2. Kuehl RO. Design of experiments: statistical principles of research design and analysis. Duxbury Press; 2000.

3. Wang J, Wan W. Experimental design methods for fermentative hydrogen production: A review. Int J Hydrogen Energy [Internet]. 2009 Jan;34(1):235–44. Available from: <URL>.

4. Li Z, Lu D, Gao X. Optimization of mixture proportions by statistical experimental design using response surface method - A review. J Build Eng [Internet]. 2021 Apr;36:102101. Available from: <URL>.

5. O-Thong S, Prasertsan P, Intrasungkha N, Dhamwichukorn S, Birkeland NKå. Optimization of simultaneous thermophilic fermentative hydrogen production and COD reduction from palm oil mill effluent by *Thermoanaerobacterium*-rich sludge. Int J Hydrogen Energy [Internet]. 2008 Feb;33(4):1221–31. Available from: <URL>.

6. Mohapatra S, Pradhan N, Mohanty S, Sukla LB. Recovery of nickel from lateritic nickel ore using *Aspergillus niger* and optimization of parameters. Miner Eng [Internet]. 2009 Feb;22(3):311–3. Available from: <URL>.

7. Solanki N, Saini S, Singh SK, Paudel KR, Goh BH, Dua K, et al. Central composite designed boswellic acids loaded nanoparticles for enhanced cellular uptake in human lung cancer cell line A549. J Drug Deliv Sci Technol [Internet]. 2025 Mar;105:106591. Available from: <URL>.

8. Ndlovu A, Cornish LA, Sithebe HSL. Relationship between sintering pressure and leach rate of polycrystalline diamond compacts (PDCs) using central composite design (CCD) modelling. Int J Refract Met Hard Mater [Internet]. 2024 Nov;124:106854. Available from: <URL>.

9. Verma S, Verma B. Optimizing carbon nanotube-doped ternary composite for high-energy-density hybrid supercapacitors: A comprehensive electrochemical assessment through central composite design. J Ind Eng Chem [Internet]. 2024 Dec;140:354–63. Available from: <URL>.

10. Zhao H, Wang W, Fu Z, Wang H. Thermal conductivity and dielectric property of hot-pressing sintered AlN–BN ceramic composites. Ceram Int [Internet]. 2009 Jan;35(1):105–9. Available from: <URL>.

11. İlhan M, Mergen A, Yaman C. Removal of iron from $BaTa_2O_6$ ceramic powder produced by high energy milling. Ceram Int [Internet]. 2013 Jul;39(5):5741–50. Available from: <URL>.

12. İlhan M, Mergen A, Yaman C. Mechanochemical synthesis and characterisation of $BaTa_2O_6$ ceramic powders. Ceram Int [Internet]. 2011 Jul;37(5):1507–14. Available from: <URL>.

13. Suryanarayana C, Ivanov E, Boldyrev V. The science and technology of mechanical alloying. Mater Sci Eng A [Internet]. 2001 May;304–306:151–8. Available from: <URL>.

14. Song SG, Shi N, Gray GT, Roberts JA. Reinforcement shape effects on the fracture behavior and ductility of particulate-reinforced 6061-Al matrix composites. Metall Mater Trans A [Internet]. 1996 Nov;27(11):3739–46. Available from: <URL>.

15. Bamberger M, Dehm G. Trends in the development of new Mg alloys. Annu Rev Mater Res [Internet]. 2008 Aug 1;38(1):505–33. Available from: <URL>.

16. Li Z, Gu X, Lou S, Zheng Y. The development of binary Mg–Ca alloys for use as biodegradable materials within bone. Biomaterials [Internet]. 2008 Apr;29(10):1329–44. Available from: <URL>.

17. Bronzino JD. Medical devices and systems, the biomedical engineering handbook [Internet]. Bronzino JD, editor. CRC Press; 2006. Available from: <URL>.

18. Park JB, Lakes RS. Biomaterials [Internet]. New York, NY: Springer New York; 2007. Available from: <URL>.

19. Chen Y, Xu Z, Smith C, Sankar J. Recent advances on the development of magnesium alloys for biodegradable implants. Acta Biomater [Internet]. 2014 Nov;10(11):4561–73. Available from: <URL>.

20. Zberg B, Uggowitzer PJ, Löffler JF. MgZnCa glasses without clinically observable hydrogen evolution for biodegradable implants. Nat Mater [Internet]. 2009 Nov 27;8(11):887–91. Available from: <URL>.

21. Carney CM, Mah T. Current isolation in spark plasma sintering of conductive and nonconductive ceramics. J Am Ceram Soc [Internet]. 2008 Oct;91(10):3448–50. Available from: <URL>.

22. Song X, Liu X, Zhang J. Neck formation and self-adjusting mechanism of neck growth of conducting powders in spark plasma sintering. J Am Ceram Soc [Internet]. 2006 Feb 14;89(2):494–500. Available from: <URL>.

23. Jha SK, Raj R. The effect of electric field on sintering and electrical conductivity of titania. Chen I -W., editor. J Am Ceram Soc [Internet]. 2014 Feb 13;97(2):527–34. Available from: <URL>.

24. İlhan M, Ekmekçi MK, Güleryüz LF. Effect of boron incorporation on the structural, morphological, and spectral properties of $CdNb_2O_6:Dy^{3+}$ phosphor synthesized by molten salt process. Mater Sci Eng B [Internet]. 2023 Dec;298:116858. Available from: <URL>.

25. İlhan M, Güleryüz LF, Ekmekci MK. Structural properties, photoluminescence, and judd-ofelt parameters of Eu^{3+}-doped $CoNb_2O_6$ phosphor. J Turkish Chem Soc Sect A Chem [Internet]. 2023 Aug 30;10(3):745–56. Available from: <URL>.

26. Yoon KH, Park HS, Cho JY, Kim ES. Microwave dielectric properties of $(Pb_{0.4}Ca_{0.6})(Fe_{0.5}Ta_{0.5})O_3$ ceramics prepared by mechanochemical processing. J Eur Ceram Soc [Internet]. 2003 Jan;23(14):2579–82. Available from: <URL>.

27. Mergen A. Mechanochemical synthesis of $MgTa_2O_6$ ceramic. Ceram Int [Internet]. 2009 Apr;35(3):1151–7. Available from: <URL>.

28. Moure A, Castro A, Tartaj J, Moure C. Mechanosynthesis of perovskite $LaGaO_3$ and its effect on the sintering of ceramics. Ceram Int [Internet]. 2009 Sep;35(7):2659–65. Available from: <URL>.

29. Yahşi Y, İpek R. Effect of ball milling time on microstructural properties of Mg/MgO. Hacettepe J Biol Chem [Internet]. 2022 Aug 1;50(3):269–74. Available from: <URL>.

30. Hirata Y, Fujita H, Shimonosono T. Compressive mechanical properties of partially sintered porous alumina of bimodal particle size system. Ceram Int [Internet]. 2017 Feb;43(2):1895–903. Available from: <URL>.

31. Yahsi Y, Yusan S, Akgol S, Ipek R. Experimental investigation of sinterability of PVA-coated Magnesium powders via mechanical milling using electric field-assisted sintering technique. Kov Mater Mater [Internet]. 2024 Nov 6;62(4):211–22. Available from: <URL>.

32. Myers RH, Montgomery DC. Response surface methodology: Process and product optimization using designed experiment [Internet]. John Wiley & Sons. Inc.; 1995. Available from: <URL>.